NUMERICAL MODELLING OF DISPERSION OF ATMOSPHERIC POLLUTION IN AND ABOVE URBAN CANOPIES

By Vasiliki Assimakopoulos

Thesis completed at Imperial College of Science, Technology and Medicine for the fulfillment of the requirements for a PhD degree of the University of London

London, 2001

BIBL. LONDN. UNIV.

To my precious family

ACKNOWLEDGEMENTS

The completion of this Ph.D. thesis required lots of personal effort and devotion, but could not be possible without the continuous support and encouragement of certain people who I would like to thank from the bottom of my heart.

My two supervisors, Professor Helen M. ApSimon and Professor Nicolas Moussiopoulos two remarkable teachers and scientists, who inspired me and guided me through the manifold issues of atmospheric pollution. Their continuous guidance, encouragement and faith in me was the driving force that kept me going.

Dr. Roy Colville, the third person in the progress review panel, who would always lent a sympathetic ear and provide support and valuable advice at all times.

Dr. Scaperdas, Antonio, Helen, Jason Teresa, Emma, Amber, from the Environmental Modelling, Measurement and Assessment group, for being patient with me and extremely helpful at all times.

Dr. Jan Ehrhardt from the Institute of Technical Thermodynamics of the University of Karlsruhe, for his vital contribution regarding microscale modelling.

Dr. Chauvet from the Laboratory of Heat Transfer and Environmental Engineering, for generously providing me with useful advice and ideas. Also Peter Sahm for the technical support provided concerning mesoscale modelling.

The System Administrators from both the EMMA group and LHTEE for keeping the computers running.

Christos for sharing my joy or frustration and for being superbly patient, sweet and supportive during the most difficult period of my efforts.

I could never find the right words to thank properly the dearest and most important people in my life, my father Makis, my mother Kaiti and my little sister Margarita. Their unconditional love, their continuous support and encouragement made all this possible.

ABSTRACT

In the past decade, the degradation of air quality in urban and therefore highly populated areas has attracted the interest of researchers. The concentration of emissions from cars, heating, industry and other activities especially in areas of insufficient ventilation such as street canyons, often leads to exceedances of air quality standards set by WHO, the EU and the local government. This situation has led to the need for improved numerical models, which are able to relate emissions to concentrations of pollutants, and which are therefore able to predict urban air quality and indicate areas of high pollution.

This thesis is concerned with the modelling of wind and turbulent fields both within the urban canopy where dispersion is limited by single or clusters of buildings and over surrounding areas, using the computational fluid dynamics code. MIMO (MIcroscale MOdel).

More specifically, using MIMO, the two-dimensional modelling of wind field and pollutant dispersion within parallel arrays of streets was performed and results were compared with available wind tunnel experimental data. The sensitivity of vortex structures to various street geometries were investigated illustrating significant departures from the traditional street canyon concept.

Since fast chemistry between ozone and oxides of nitrogen can affect concentrations of nitrogen dioxide, an urban pollutant proven to have adverse effects on health, the MIMO model has been extended to incorporate this.

Some investigation has also been undertaken on wind fields for three-dimensional building configurations. Attention has also been given to how microscale models such as MIMO can be linked to city scale models such as an Eulerian, non-hydrostatic model MEMO (MEsoscale MOdel).

Table of Contents

Acknowledgements 3

Abstract 4

List of Tables 8

List of Figures 10

Executive Summary 15

1 Introduction 20

1.1 Air quality management and the need for air pollution modelling 20

1.2 Scope of project 24

2 Theoretical background 27

2.1 Outline of existing modelling techniques 27

2.1.1 Diagnostic models 28

2.1.2 Prognostic models 29

2.2 Description of dispersion processes 31

2.2.1 Dispersion processes 31

2.2.2 Urban Boundary Layer 33

2.2.3 Modelling techniques 35

2.2.4 Characteristics of air flow in street canyons 37

2.2.4.1 Previous Studies 37

2.2.4.2 Experimental work 39

3 Microscale Model Description 45

3.1 Introductory remarks 45

3.2 Classification scheme of predicting turbulent flows 46

3.3 MIcroscale MOdel structure, MIMO 47

3.3.1 Model equations and numerical solution 48

3.3.2 Turbulence modelling 48

3.3.3 MIMO model initial and boundary conditions 50

3.3.3.1 Initial conditions 50

3.3.3.2 Boundary conditions 52

3.3.4 Solution Procedure 55

3.3.5 Model structure 58

4 Two dimensional calculations employing MIMO ` 63

4.1 Two-dimensional calculations 63

4.1.1	*Description of wind tunnel experiment*	*63*
4.1.2	*Computational domain*	*66*
4.1.3	*Inflow profiles and boundary conditions*	*67*
4.1.4	*Comparison of computed concentrations against measured*	*72*
4.1.5	*Optimisation of results*	*75*
4.1.6	*Results*	*80*
4.2	*Effects of street canyon geometry to dispersion of pollutants*	*84*
4.2.1	*Step-up notch results-aspect ratio 1*	*85*
4.2.2	*Step-down notch results-square*	*93*
4.2.3	*Step-up notch results (deep case)*	*101*
4.2.4	*Step-down notch results (deep case)*	*107*
4.2.5	*Aspect ratio effect on dispersion*	*111*
4.2.6	*Effect of upwind characteristics*	*123*
5	*Fast chemistry*	*126*
5.1	*Introductory remarks*	*126*
5.2	*MIMO Photochemical Routine*	*129*
5.3	*MIPHOR results*	*130*
5.3.1	*Night-time chemistry*	*130*
5.3.2	*Day-time chemistry*	*136*
5.4	*Concluding remarks*	*138*
6	*Three-dimensional calculations*	*140*
6.1	*Description of wind tunnel experiment*	*141*
6.2	*Computational domain*	*141*
6.3	*Inflow profiles and Boundary Conditions*	*145*
6.4	*Results*	*148*
7	*Mesoscale calculations- The London case*	*155*
7.1	*The non-hydrostatic mesoscale model MEMO*	*156*
7.1.1	*Model Equations*	*156*
7.1.2	*Transformation to Terrain-Following Coordinates*	*158*
7.1.3	*Numerical Solution of the Equation System*	*158*
7.1.4	*Parameterisations*	*159*
7.2	*Initial and Boundary Conditions*	*160*
7.3	*Eulerian dispersion model*	*162*
7.4	*Calculations performed*	*163*

7.4.1 Area of investigation and emission inventory *163*
7.4.2 Background meteorological information *171*
7.4.3 London Air Pollution Monitoring Network *172*
7.4.4 MEMO results *173*
7.5 Preliminary conclusions *183*
8 Discussion of results and suggestions for further work *185*
8.1 Discussion of results *185*
8.1.1 MIMO results, the 2 D case. *186*
8.1.2 The Fast Chemistry Module *189*
8.1.3 MIMO results, the 3D case. *190*
8.1.4 The Inert MEMO Results. *190*
8.2 Suggestions for further work *192*
REFERENCES *194*
APPENDIX A *206*

List of Tables

Table 4.1. Dimensionless concentrations as computed by MIMO for the roof of the upwind building for the square step-up notch configuration. 115
Table 4.2. Dimensionless concentrations as computed by MIMO for the roof of the upwind building for the square step-down notch configuration. 116
Table 4.3. Dimensionless concentrations as computed by MIMO for the roof of the upwind building for the deep step-up notch configuration. 116
Table 4.4. Dimensionless concentrations as computed by MIMO for the roof of the upwind building for the deep step-down notch configuration. 116
Table 4.5. Dimensionless concentrations as computed by MIMO for the upwind building wall for the square step-up notch configuration. 117
Table 4.6. Dimensionless concentrations as computed by MIMO for the upwind building wall for the square step-down notch configuration. 117
Table 4.7. Dimensionless concentrations as computed by MIMO for the upwind building wall for the deep step-up notch configuration. 118
Table 4.8. Dimensionless concentrations as computed by MIMO for the upwind building wall for the deep step-down notch configuration. 118
Table 4.9. Dimensionless concentrations as computed by MIMO for the downwind building wall for the square step-up notch configuration. 119
Table 4.10. Dimensionless concentrations as computed by MIMO for the downwind building wall for the square step-down notch configuration. 120
Table 4.11. Dimensionless concentrations as computed by MIMO for the downwind building wall for the deep step-up notch configuration. 120
Table 4.12. Dimensionless concentrations as computed by MIMO for the downwind building wall for the deep step-down notch configuration. 120
Table 4.13. Dimensionless concentrations as computed by MIMO for the downwind building roof for the square step-up notch configuration. 121
Table 4.14. Dimensionless concentrations as computed by MIMO for the downwind building roof for the square step-down notch configuration. 121
Table 4.15. Dimensionless concentrations as computed by MIMO for the downwind building roof for the deep step-up notch configuration. 122
Table 4.16. Dimensionless concentrations as computed by MIMO for the downwind building roof for the deep step-down notch configuration. 122
Table 4.17. Dimensionless concentrations computed by MIMO for different aspect ratios when the emission source is placed close to the upwind building. 122

Table 4.18. Dimensionless concentrations computed by MIMO for different aspect ratios when the emission source is placed close to the downwind building. 123

Table 7.1. Brief description of characteristics of stations chosen for comparison purposes. 179

List of Figures

Figure 1.1. Simplified Flowchart of an Air Quality Management System. 22

Figure 2.1. Side view of a simplified street canyon structure. 34

Figure 3.1. Illustration of how the power law is implemented as input for the street canyon case. 51

Figure 3.2. Schematic representation of the structure of the microscale model MIMO. 59

Figure 4.1. Illustration of the two-dimensional experimental set up. 64

Figure 4.2. Non-dimensional concentrations of the tracer gas emitted measured at the positions indicated. 65

Figure 4.3. Plan view of the two-dimensional computational domain of the square canyon case. 68

Figure 4.4. Plan view of the two-dimensional computational domain of the deep canyon. 68

Figure 4.5a. Inlet profile of velocity. 70

Figure 4.5b. Inlet profile of turbulent kinetic energy. 70

Figure 4.5c. Inlet profile of the rate of dissipation of t.k.e. 71

Figure 4.6a. Wind field computed by MIMO for the square canyon case. 73

Figure 4.6b. Wind field computed by MIMO for the deep canyon case. 73

Figure 4.7a. Comparison between measured and computed dimensionless concentrations for the square canyon case. 74

Figure 4.7b. Comparison between measured and computed dimensionless concentrations for the deep canyon case. 74

Figure 4.8a. Wind field computed by MIMO for the square canyon case. 81

Figure 4.8b. Wind field computed by MIMO for the deep canyon case. 81

Figure 4.9. Comparison between measured and computed non-dimensional concentrations for the square street canyon cases. 82

Figure 4.10. Comparison between measured and computed non-dimensional concentrations for the deep canyon case. 83

Figure 4.11a. Wind field and pollutant dispersion, as computed by MIMO for upwind building height of 0.06m. 87

Figure 4.11b. Wind field and pollutant dispersion, as computed by MIMO for upwind building height of 0.055m. 87

Figure 4.11c. Wind field and pollutant dispersion, as computed by MIMO for upwind building height of 0.05m. 88

Figure 4.11d. Wind field and pollutant dispersion, as computed by MIMO for upwind building height of 0.045m. 88

Figure 4.11e. Wind field and pollutant dispersion, as computed by MIMO for upwind building height of 0.04m. 89

Figure 4.11f. Wind field and pollutant dispersion, as computed by MIMO for upwind building height of 0.035m. 89

Figure 4.11g. Wind field and pollutant dispersion, as computed by MIMO for upwind building height of 0.03m. 90

Figure 4.11h. Wind field and pollutant dispersion, as computed by MIMO for upwind building height of 0.025m. 90

Figure 4.11i. Wind field and pollutant dispersion, as computed by MIMO for upwind building height of 0.02m. 91

Figure 4.11j. Wind field and pollutant dispersion, as computed by MIMO for upwind building height of 0.015m. 91

Figure 4.11k. Wind field and pollutant dispersion, as computed by MIMO for upwind building height of 0.01m. 92

Figure 4.11l. Wind field and pollutant dispersion, as computed by MIMO for upwind building height of 0.005m. 92

Figure 4.11m. Wind field and pollutant dispersion, as computed by MIMO for upwind building height of 0.0m. 93

Figure 4.12a. Wind field and pollutant dispersion, as computed by MIMO for downwind building height of 0.055m. 96

Figure 4.12b. Wind field and pollutant dispersion, as computed by MIMO for downwind building height of 0.05m. 96

Figure 4.12c. Wind field and pollutant dispersion, as computed by MIMO for downwind building height of 0.045m. 97

Figure 4.12d. Wind field and pollutant dispersion, as computed by MIMO for downwind building height of 0.04m. 97

Figure 4.12e. Wind field and pollutant dispersion, as computed by MIMO for downwind building height of 0.035m. 98

Figure 4.12f. Wind field and pollutant dispersion, as computed by MIMO for downwind building height of 0.03m. 98

Figure 4.12g. Wind field and pollutant dispersion, as computed by MIMO for downwind building height of 0.025m. 99

Figure 4.12h. Wind field and pollutant dispersion, as computed by MIMO for downwind building height of 0.02m. 99

Figure 4.12i. Wind field and pollutant dispersion, as computed by

MIMO for downwind building height of 0.015m. 100

Figure 4.12j. Wind field and pollutant dispersion, as computed by MIMO for downwind building height of 0.01m. 100

Figure 4.12k. Wind field and pollutant dispersion, as computed by MIMO for downwind building height of 0m. 101

Figure 4.13a. Wind field and pollutant dispersion as computed by MIMO for upwind building height of 0.06m (deep canyon). 103

Figure 4.13b. Wind field and pollutant dispersion as computed by MIMO for upwind building height of 0.05m (deep canyon). 104

Figure 4.13c. Wind field and pollutant dispersion as computed by MIMO for upwind building height of 0.04m (deep canyon). 104

Figure 4.13d. Wind field and pollutant dispersion as computed by MIMO for upwind building height of 0.03m (deep canyon). 105

Figure 4.13e. Wind field and pollutant dispersion as computed by MIMO for upwind building height of 0.02m (deep canyon). 105

Figure 4.13f. Wind field and pollutant dispersion as computed by MIMO for upwind building height of 0.01m (deep canyon). 106

Figure 4.13g. Wind field and pollutant dispersion, as computed by MIMO for upwind building height of 0m (deep canyon). 106

Figure 4.14a. Wind field and pollutant dispersion, as computed by MIMO for downwind building height of 0.05m (deep canyon). 108

Figure 4.14b. Wind field and pollutant dispersion, as computed by MIMO for downwind building height of 0.04m (deep canyon). 109

Figure 4.14c. Wind field and pollutant dispersion, as computed by MIMO for downwind building height of 0.03m (deep canyon). 109

Figure 4.14d. Wind field and pollutant dispersion, as computed by MIMO for downwind building height of 0.02m (deep canyon). 110

Figure 4.14e. Wind field and pollutant dispersion, as computed by MIMO for downwind building height of 0.01m (deep canyon). 110

Figure 4.14f. Wind field and pollutant dispersion, as computed by MIMO for downwind building height of 0.0m (deep canyon). 111

Figure 4.15a. Wind field and pollutant dispersion, from the upwind side as computed by MIMO for the aspect ratio of 3. 112

Figure 4.15b. Wind field and pollutant dispersion, from the downwind side as computed by MIMO for the aspect ratio of 3. 113

Figure 4.15c. Wind field and pollutant dispersion, from the upwind side as computed by MIMO for the aspect ratio of 1.5. 113

Figure 4.15d. Wind field and pollutant dispersion, from the downwind side as computed by MIMO for the aspect ratio of 1.5. 114
Figure 4.16. Comparison of concentrations for the square canyon cases. 125
Figure 4.17. Comparison of concentrations for the deep canyon cases. 125
Figure 5.1. Distribution of total NO_x along the street before fast chemistry is activated. 131
Figure 5.2. Distribution of total NO along the street before fast chemistry is activated. 131
Figure 5.3. Distribution of total NO_2 along the street before fast chemistry is activated. 132
Figure 5.4. Distribution of total NO_2 along the street after fast chemistry is activated. 133
Figure 5.5. Distribution of total O_3 along the street after fast chemistry is activated. 133
Figure 5.6. NO_2/NO_x ratio formed after fast chemistry is activated indicating percentage increase of NO_2. 134
Figure 5.7. Average NO_2/NO_x ratio versus background O_3 concentration as computed by MIMO for the upwind wall. 135
Figure 5.8. Average NO_2/NO_x ratio versus background O_3 concentration as computed by MIMO for the centre of the canyon. 135
Figure 5.9. Average NO_2/NO_x ratio versus background O_3 concentration as computed by MIMO for the downwind wall. 136
Figure 5.10. Average NO_2/NO_x ratio versus background O_3 concentration as computed by MIMO for the upwind wall. 137
Figure 5.11. Average NO_2/NO_x ratio versus background O_3 concentration as computed by MIMO for the centre of the canyon. 137
Figure 5.12. Average NO_2/NO_x ratio versus background O_3 concentration as computed by MIMO for the downwind wall. 138
Figure 5.13. NO_2/NO_x ratio varying with background ozone concentration, averaged across the street canyon domain. 138
Figure 6.1. Plan view (left) and side view (right) of the square buildings indicating their dimensions. 142
Figure 6.2. Plan view of the experimental layout. 143
Figure 6.3. Plan view of the computational domain. 144
Figure 6.4. Plot of the inflow profile of the horizontal velocity. 146
Figure 6.5. Plot of the inflow profile of the turbulent kinetic energy. 146

Figure 6.6. Plot of the inflow profile of the rate of dissipation of turbulent kinetic energy. 147

Figure 6.7. A comparison of measured vertical profile of velocity against vertical profile of velocity as computed by MIMO. 149

Figure 6.8. Computed flow field established at a height of Z/H=1/3. 151

Figure 6.9. Measured flow field established at a height of Z/H=1/3. 151

Figure 6.10. Side view of wind field established at location A. 152

Figure 6.11. Side view of wind field established at location B. 152

Figure 6.12. Flow field established at a height of Z/H=1/3 154

Figure 6.13. Simulated vertical profile of velocity for wind at angle of 45 degrees against vertical profile of velocity for zero degrees wind direction. 154

Figure 7.1a. The CORINE Level 3 classification for the London greater area. 164

Figure 7.1b. 165

Figure 7.2. Chart of the mean sea level pressure analysis for 00:00LST on the 30th of July 1999. 167

Figure 7.3. Chart of the mean sea level pressure analysis for 00:00LST on the 31st of July 1999. 168

Figure 7.4. Analysis of the 1000-5000 Pa thickness layer of the 31st of July 1999 at 00:00LST. 169

Figure 7.5. Analysis of the Temperature, Relative Humidity and Wind of the 31st of July 1999 at 00:00LST. 170

Figure 7.6. Map of the Greater London Area indicating the locations of the selected monitoring stations. 173

Figure 7.7. MEMO simulations of the wind field flows and NO_x concentrations over the GLA on the 30th of July 1999. 177

Figure 7.8. MEMO simulations of the wind field flows and NO_x concentrations over the GLA on the 31st of July 1999. 178

Figure 7.9. Hourly variation of NO_x concentrations for the 30th and the 31st of July 1999 for the stations of Bexley, Bloomsbury, Brent and London Bridge, (moving from the top downwards). The pink points indicate the computed concentrations. 182

Figure 7.10. Scatter diagram of the model concentrations against the LAQMN measurements for the 30th and the 31st of July 1999. 183

Executive Summary

The present work was performed within the frame of a PhD thesis of the Imperial College of Science, Technology and Medicine. It was technically supported by the Environmental Measurement, Modelling and Assessment Group (EMMA, former Air Pollution Group) of Imperial College and the Laboratory of Heat Transfer and Environmental Engineering (LHTEE), of the Aristotle University of Thessaloniki.

The subject of the thesis is, **"The numerical modelling of dispersion of atmospheric pollution in and above urban canopies".**

The need to investigate numerically the flow and dispersion properties in and above urban canopies, especially those in densely populated cities, was recognised. This field could not be covered by mesoscale models including those that could run nested. On the other hand the relatively recent wind tunnel experimental data on street canyon simulations, proved to be very interesting indicating flows with special characteristics and areas of high concentrations. All these could not easily be understood without the proper theoretical support.

Having this in mind it was decided to target the following main objectives:

- **Select** and **adjust** a microscale model able to resolve wind flow and pollutant dispersion in a densely built environment.

- **Develop** such a model in order to accommodate chemical processes such as the ones taking place within street canyons immediately after pollutants are emitted from vehicle exhausts.

- **Investigate** source-receptor relationships, especially over short distances and under certain wind conditions.

- **Validate** the performance of the model against available wind tunnel experimental data, since scarce field experimental data exist.

- **Select** a mesoscale model able to resolve wind flow and pollutant dispersion over the greater area of a densely populated city.

- **Perform** a preliminary sensitivity analysis in order to investigate its capability to accommodate topographical details, surface characteristics and local dispersion properties.

- **Examine** the possibility of performing model cascade in order to optimise the performance of both the mesoscale and microscale model

In order to successfully complete the above objectives it was necessary to overcome certain difficulties, a summary of which is given.

a) The lack of experience regarding the extended use of microscale models for the reconstruction of flows within densely built-up areas.

b) The development of algorithms able to represent the chemical processes taking place in areas of high pollutant production with photochemical pollutants characterised by their fast chemical cycles.

c) Lack of systematic field experimental data, which could be used for validation purposes of the algorithms. However, some relevant wind tunnel experimental data were identified some of which were used for the present thesis.

d) The numerous different building configurations and building shapes met in an urban area produced even greater difficulties since the number of possible different combinations was large. Thus, deciding which to choose proved difficult.

The above difficulties were dealt with the good and imminent support provided by the EMMA group and LHTEE. The support included provision of the necessary computing power, the knowledge regarding models and modelling and supervision.

The main conclusions drawn from the completed work can be summarised as follows:

1) The importance of the processes taking place within a densely built-up urban environment, was highlighted by the fact that certain flows were detected of a complex nature, such as a double vortex system, corkscrew vortices etc.

2) Treating the emitted pollutants as inert was proven wrong, since from the calculations performed fast chemical reactions with implications for the concentrations of certain pollutants dangerous to health, were demonstrated.

3) Regarding the two-dimensional multiple canyon cases studied numerically, the concentration fields predicted were in good agreement with the available wind tunnel experimental data. It must be noted that the wind fields predicted for the two classical cases of a square and a deep canyon configuration, came in excellent agreement with already published results.

4) Having established satisfactory performance of the numerical model used, further work was performed in order to study the effects of different geometrical configurations on the wind field and dispersion characteristics. When the upwind conditions were altered, the incident flow characteristics were distinctively affected.

5) Despite the necessary simplifications and assumptions imposed in order to perform three-dimensional computations, the simulations indicated very good agreement between the computed wind field and the wind tunnel measurements.

6) Of interest was the case when the wind came at an angle to the street canyon, where unfortunately there were no wind tunnel experimental data for comparison. The wind field remained almost the same as the case above, although certain characteristics were slightly affected, e.g., vortex location and size, slight destruction of vortex shape etc.

7) The nested mesoscale model wind field simulations, gave quite interesting results, which compared well with synoptic observations.

8) MEMO NO_x inert dispersion simulations for a weekend case, which maintains special traffic emission characteristics, showed good agreement in both average values and trends measured in the field by the London Air Quality Monitoring Network.

The thesis is structured in eight chapters the content of which is presented below:

CHAPTER 1: An introduction to the manifold character of air pollution is given. A brief description of the different scales affected by and producing air pollution is provided and the writer focuses on the current air quality status in urban areas. Within that frame, the need for air pollution modelling and management is pointed out.

CHAPTER 2: An insight into the various models used for air quality studies is given. The theoretical background of the atmospheric boundary layer and the effects imposed by the urban environment is also included. Finally, the work performed in the microscale by previous researchers and progress made is reported.

CHAPTER 3: A mathematical description of the selected microscale model is given, together with the details of its structural organisation. Furthermore, general comments made by other researchers on the specific type of models and their utility and reliability is provided.

CHAPTER 4: The two-dimensional calculations performed with the microscale model are presented and compared to the available wind tunnel experimental data. Having established its satisfactory performance, an analysis is done to study the effects of different geometrical configurations on the pollutant dispersion characteristics. Furthermore, the upwind conditions were altered and the internal boundary layer development was investigated in relation to the different wind fields and pollutant concentration distributions observed.

CHAPTER 5: A fast-chemical module is implemented within the microscale model and the effects of this chemical cycle on the concentration of NO_2, a pollutant harmful to human health, is investigated. Daytime and night-time computations are performed while, the importance of the processes taking place in the microscale is discussed.

CHAPTER 6: In this chapter three-dimensional calculations performed with the microscale model are presented. In this respect, three-dimensional wind tunnel experimental data are used in order to validate the microscale model's performance for a more complicated case. Despite the simplifications made before initialisation, the model performed very well. The three-dimensional characteristics of the flow are analysed and the interrelation between three and two-dimensional characteristics of wind flow along a three-dimensional set-up is pointed out. Furthermore, the wind direction is altered and the effects on the wind field patterns observed are analysed.

CHAPTER 7: The mesoscale model work is reported here. A mathematical description together with the relevant previous published work completed with the model is also given. Computations of the flow field patterns, which were performed for the Greater London Area are presented. These focused on selected meteorological conditions under which air pollution episodes could occur. The flow field patterns were used by an Eulerian dispersion model in order to calculate NO_x inert concentrations over the area of interest. The results obtained over the central area of London and without taking into consideration background pollution levels, were good..

CHAPTER 8: The purpose of this chapter is to summarise the results obtained and the conclusions drawn as well as to give a good description of further work envisaged.

1 Introduction

The degradation of ambient air quality has become a leading problem of countries of the developed and developing world, especially in urban and therefore overpopulated areas, where most activities are concentrated. Urban areas are therefore those, which consist of the main sources of pollution from industrial units, transportation, heating of buildings and other small-scale sources (Fenger, 1999). These form the pollution levels in inhabited areas, which in several occasions exceed the limits set by the EU, the World Health Organisation (WHO)[1] and the local government. Nevertheless, pollution is a phenomenon belonging to different scales with urban areas being the most important sources. Urban pollution transported in the free atmosphere forms the mesoscale pollution level in the greater environmental area.

Over the past decade considerable improvement has been made in reducing the levels of pollutants such as sulphur dioxide, lead and particulates as a result of the use of the so-called "green technologies". On the other hand, the levels of the so-called photochemical pollutants, nitrogen oxides, non-methane volatile organic compounds, carbon monoxide and ozone still remain high in most European cities despite a decline in emissions. Exceedances of the short-term WHO-AQG are recorded in the majority of the large European cities. Ozone concentrations in particular, show extreme seasonal and even diurnal variations. Road traffic emissions constitute the dominant source category for this form of air pollution.

1.1 Air quality management and the need for air pollution modelling

From the above it has become obvious that quality of life for people living in large metropolitan areas can not be accomplished unless several measures are taken to manage the air quality environmental pressures. In particular, the simple approach, taking place in all big cities, of setting up a simple air quality monitoring network, allowed only for the late diagnosis of an air quality episode, without giving enough

---

[1] http://www.who.int/environmental_information/Air/Guidelines/aqguide3.pdf

time to the local managers for prediction and for taking the necessary measures for its reversal. More recently several research efforts focused their attention on the design and the implementation of urban air quality management programs (SCAQMD, 1994A; SCAQMD, 1994B). The main target of such programs was to cover an urban area typically of a size 15x15 km. This approach partially solved the problem since it studied the greater urban area without giving the necessary insight on the microscale part of the problem. However, these approaches have given some good results, as they were able to deal with the complexities of the urban environment and the corresponding meteorological features.

In order for these models to perform satisfactorily it was necessary to provide them with the appropriate historical and on-line meteorological and air quality data, emission inventory and topography information. A typical example illustrating an air quality management system is shown in Figure 1.1.

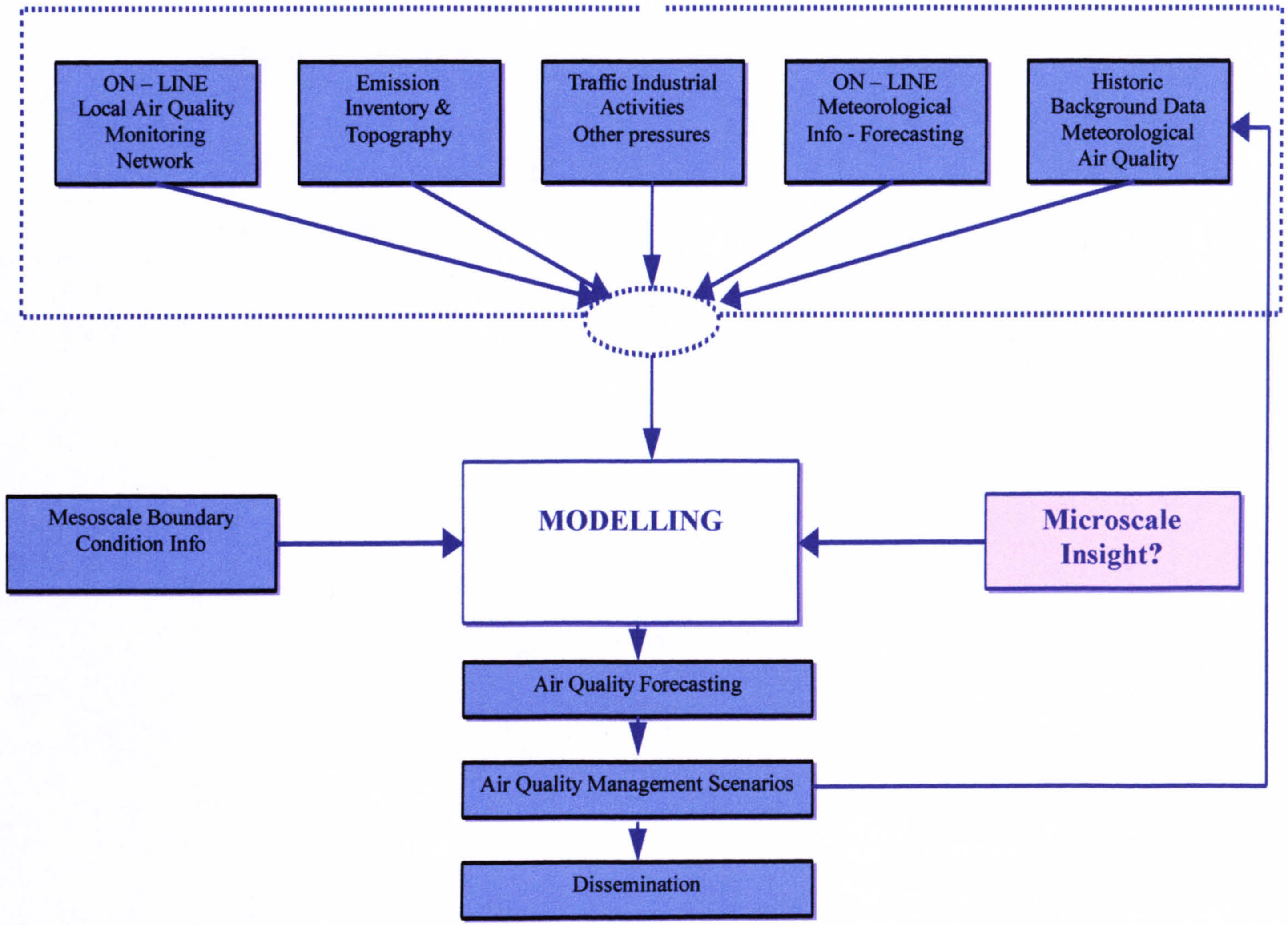

Figure 1.1. Simplified Flowchart of an Air Quality Management System.

As seen from Figure 1.1 the modelling routines are the core of the system, which in order to function properly require an organised input database. This should include an on-line connection to present-time meteorological conditions, a well informed emission inventory database as well as information on traffic, industrial activities and other environmental pressures, topographical data and last but not least access to a historic background database of meteorology and air quality. The appropriate meteorological boundary conditions are provided by a mesoscale model, which runs nested. The output of such a modelling system would give a prognosis of the air quality above the urban area and give information about which pollutants are exceeding the relevant limits. This output in turn is used to select the appropriate environmental management scenario and dissemination of the relevant information is done. The air quality data as well as the air quality management scenarios are given as feedback to the historic background database.

From Figure 1.1, the contribution of microscale insight is considered critical since the dispersion of pollutants in urban environments is dominated by the wind flow around complex building structures. Down-wash phenomena and increased local turbulence strongly influence not only the mean flow field but also the diffusion parameters. A typical configuration is the so-called street canyon, formed along a street in a densely built urban area. At the bottom of a street canyon, the vehicles emit gaseous pollutants. Under certain conditions, e.g. for non-zero wind component perpendicular to the street, higher concentration levels are observed on the leeward than on the windward side of the street canyon, assuming the street canyon is infinitely long. Due to their rather coarse resolution, mesoscale models can not predict these influences accurately and, therefore, in the recent years microscale models have been developed which explicitly take into account the building structure and provide a much more detailed insight into urban dispersion. Nevertheless, atmospheric flow and pollutant dispersion over urban areas is affected by phenomena belonging to different scales. Regional transport and the flow in the upper part of the planetary boundary layer are mainly determined by mesoscale phenomena. There exists however, a gap between mesoscale and microscale models, which is difficult to bridge, since the connection between the street canyon scale and the mesoscale is difficult to accomplish. The difficulty lies in the non-existence of the relevant mathematical formulae, but also on the complications of creating such routines. Nevertheless, an effort to create

multiscale model systems is currently on the way, starting at local-to-regional scale and going down to the microscale. This attracts the interest of many researchers and European funding agencies. An example of such a model system is ZEUS, which is currently under development at the Aristotle University of Thessaloniki, based on the mesoscale model MEMO and the microscale model MIMO.

1.2 Scope of project

Since cars are accepted to be the major emission source of air pollutants in urban areas, and a further increase of city traffic is expected, investigations of dispersion processes in street canyons have become a focal point in environmental research, (Leitl and Meroney, 1997; Delaunay et al, 1997; Gerdes and Olivary, 1999; Herbert et al, 1998; Huang et al, 2000; Johnson and Hunter, 1998, 1999; Kamenetsky and Vieru, 1995; Lakehal et al, 1995; Lanzani and Tamponi, 1995; Oliveira and Younis, 2000; Green et al, 2001; Marquez and Smith, 1999). Following recent work published by several researchers one may identify some important points and suggestions:

- The increase of vehicular traffic within densely populated cities adds further pressures on an already deteriorating urban air-quality. To develop strategies for reversing this trend a satisfactory understanding is necessary on the linkage between the air flowing above the urban canopy and that recirculating in the urban street canyons. This knowledge is not only needed below the level of the roofs, to predict urban air quality, but also above, as it assists the mesoscale and microscale wind circulation and pollution dispersion modeller to describe more accurately the effect of the buildings in such models (Rafailidis, 1997; Macdonald et al, 1998; Vignati et al, 1996).

- In order to control these pollution levels, administrative organisations need to carry out measurements in the streets (Scaperdas and Colvile, 1999). According to EU directive 85/203/EEC, pollution caused by road traffic should be measured where maximum concentrations are expected. These locations can be determined either through physical modelling in a boundary layer wind tunnel or by application of a numerical transport and diffusion model (Croxford and Penn, 1998). Both methods have their specific

advantages and disadvantages. Although numerical models usually allow the study of many scenarios in a shorter time and at lower cost, so far only the wind tunnel experiment provides sufficiently accurate results for very complex building configurations, (Goetting et al., 1997; Uehara et al, 2000). For such building configurations the existing microscale models are still being validated (Theodoridis and Moussiopoulos, 1999; Theurer, 1999).

- The fluid motion governing the dispersion process is highly turbulent and influenced by both large-scale meteorological conditions and small-scale gravitational and thermal effects. To analyse these turbulent buoyant flows, it is therefore important to develop specific techniques and reliable tools, (Sini et al., 1996).

- The increasing trend in using numerical urban pollution dispersion models for regulatory purposes intensifies the need to adopt the most appropriate model for each specific purpose. This entails reliable prior validation of the candidate models, normally based on experimental data from either physical modelling or field observations, (Rafailidis, 1998; Olesen, 1995).

- Air pollution models may be applied for the optimisation of control strategies and for short-term predictions of smog episodes as well as for the investigation of different emission scenarios and their impacts on air quality.[2] Especially at the urban scale, simulation models have already been successfully used to address questions related to the atmospheric environment, although a full evaluation of such models is still lacking. Recent activities facilitate defining how to quantify the uncertainties of air pollution models. A basic requirement in this respect is the availability of detailed experimental datasets for model evaluation (Moussiopoulos, 1995; Mayer, 1999; Pearlmutter et al, 1999).

The above selected papers and main conclusions, indicate the trends and potential in urban air quality research. In this respect it was decided to proceed and work in this field incorporating an already existing microscale model. Such a model with the

---

[2] http://reports.eea.eu.int/TEC11a/en/page011.html

ability to resolve wind flow and dispersion characteristics in urban areas, and with the possibility for further development is MIMO, which was developed at the University of Karlsruhe (Ehrhardt, 2000). More information regarding the model will be given within the next chapters. Furthermore, in order to improve the performance of MIMO, the possibility of linking it with a mesoscale model was studied in order to obtain more accurate boundary and initial conditions. In this respect the MEMO model was also selected, developed at the Laboratory of Heat Transfer and Environmental Engineering, where the appropriate knowledge and technical support was provided. It must be noted here that a successful linking of models belonging to different scales would open a new dimension to the accurate prediction of air quality, in areas where the complexity of the terrain, the building structure and the sources distribution coexist.

The main objectives of the present thesis can be summarised as follows:

- **Select** and **adjust** a microscale model able to resolve wind flow and pollutant dispersion in a densely built-up environment.

- **Develop** such a model in order to accommodate chemical processes such as the ones taking place within street canyons immediately after pollutants are emitted from vehicle exhausts.

- **Investigate** source-receptor relationships, especially over short distances and under certain wind conditions.

- **Validate** the performance of the model against available wind tunnel experimental data, since scarce field experimental data exist.

- **Select** a mesoscale model able to resolve wind flow and pollutant dispersion over the greater area of a densely populated city.

- **Perform** a preliminary sensitivity analysis in order to investigate its capability to accommodate topographical details, surface characteristics and local dispersion properties.

- **Examine** the possibility of performing model cascade in order to optimise their performance.

2 Theoretical background

Modelling is a basis for better understanding and prevention of air pollution. In order to better understand these phenomena, several different modelling techniques have been applied in this field that are well known.

In the last decades, the mechanisms of air pollutant transport and transformation are the subject of intense scientific research. One of the principle aims of this research is to establish source/receptor relationships, i.e., to quantify to what extent various emissions sources contribute to the occurrence of air pollution episodes. Nowadays most of the physical and chemical processes leading to high air pollution levels seem to be understood. Nevertheless, air pollution still causes serious problems in many countries all over the world. Such problems may be classified depending on their characteristic length scale. Usually, global, continental, regional and local scale problems are distinguished.

Observational evidence is only rarely sufficient to describe atmospheric transport and transformation of pollutants. For this reason mathematical models have been developed to simulate wind flow and the dispersion of chemically reacting pollutants in the atmosphere. Over the past few years there has been considerable progress in the practical applications of mathematical models at all above-mentioned scales.

2.1 Outline of existing modelling techniques

A particularly serious problem that overpopulated areas have to face is environmental degradation that comes from photochemical pollution. This kind of pollution appears with the presence in the atmosphere of oxidant substances such as ozone, nitrogen dioxide, PAN,etc., as a result of the photochemical oxidation of the mixture of the nitrogen oxides (NO_x) and of the hydrocarbons, (HC) which are emitted from point and area sources (industrial units, highways), under the influence of the sun radiation. The observed atmospheric concentrations of oxidants, (secondary pollutants), are a result of complicated chemical reactions and products which have to do with the general situation of the atmosphere, such as meteorological conditions, radiation etc

and thus their relationship with the concentrations of the primary pollutants are not linear, (NO_x, HC).

For these reasons the interest in dealing with the air pollution problem is centred in the development of a methodology, which will be able to forecast the concentration of pollutants in a certain area and their dependence on changes in the concentrations of the primary pollutants, with the ultimate aim of determining a proper procedure of controlling the pollution. Simple techniques based on the view that the minimisation of the emissions of primary pollutants will bring the analogous minimisation of oxidants seem to have failed due to the non-linearity of the chemistry of the oxidants and the dependence of the behaviour of the system on the initial conditions.

The development of a proper methodology for the study and controlling of air pollution demands always a forecasting scheme or a model based on a simple or more complicated mathematical procedure and which combines three parameters: meteorology, emissions and chemistry.

It should be mentioned here that, models vary considerably in type and complexity according to requirements. The most complex models may take too long to run, or to acquire the required input data, in a real emergency, in which case a simple model may be much more practical and provide the answers needed at that time. It also has to be said that complex models may not be significantly more accurate than simpler ones, unless the quality of physics and the quality of the input data matches the model's complexity. Air quality data may be divided in two categories:

- Diagnostic or empirical models
- Prognostic or deterministic models

2.1.1 Diagnostic models

These are statistical descriptions. They include empirical relations based on data from measurements in the atmosphere or in special chambers simulating the atmospheric mixture and which provide data of concentration of pollutants not depending on time. Their major disadvantage is that they are readily dependent with the data from which

they are derived and for this reason they can not be used in independent from them applications.

2.1.2 Prognostic models

These models are based on a description of the atmospheric workings from the basic physicochemical equations such as the equation of dispersion in a turbulent medium. The appropriate mechanisms which describe atmospheric chemistry and which provide information both for the spatial and the time dependent distribution of the concentrations of the pollutants are used

The main categories of prognostic models include the following:

- ***Gaussian models***

Such models calculate the horizontal distribution of a pollutant considering it may approach a Gaussian form assuming the diffusivity is constant over uniform terrain. However, the range of eddy sizes is so large that the bigger eddies are always incompletely sampled so that the distribution can never be truly Gaussian.

Assuming a point source, such as s stack, the concentration of a pollutant plume at any (x,y,z) location can be computed from the following diffusion equation:

$$C(x,y,z)=\frac{Q}{2\pi\sigma_y\sigma_z U}\exp\left[-\frac{1}{2}\left(\frac{y}{\sigma_y}\right)^2\right]\exp\left[-\frac{1}{2}\left(\frac{z}{\sigma_z}\right)^2\right]$$

Where: Q is the pollutant release rate (kg/s), U is the wind speed (m/s), σ_y and σ_z is the lateral and vertical eddy diffusivity respectively (in m).

- ***Box models***

These are the most simple arithmetic air quality models. The area of the model is one cell or 'box', which may cover an area of several hundreds of square kilometres. The primary pollutants emitted in the 'box' from the sources within the area covered by the model, follow an instantaneous and homogeneous mixing. Under this assumption the concentration of the pollutants can be described by a simple equality between the

rates of transfer in and out of the box, the rates of emission from the sources in the box and the rates of chemical production or destruction of pollutants.

Because of their structure, box models can predict quite well only the temporal change of the mean concentration in the box for each pollutant. Since they do not provide a spatial analysis they can not be used in cases where the meteorological magnitudes and the emissions differ a lot along the area of the model.

- ***Lagrangian trajectory models***

An imaginary column of air is used which is defined by the ground and by the height of the inversion, if this exists, which is transported by the wind and can be transformed by time.

Moving around the area of interest of the model, the air column is enriched with primary pollutants, which are emitted by sources existing within the trajectory of the column. In many cases the pollutants are chemically transformed while others are inert.

The assumptions made during the forming of trajectory models tend in general to diminish their usefulness. Their basic characteristics, i.e., the use of one moving column of air with wind being constant with respect to height and without taking into account the convergence or divergence of the wind field, can lead to a non-realistic representation of the situation in the atmosphere in cases where there exist large point sources inhomogeneously distributed or the wind presents serious spatial differences, e.g., with complex terrain.

- ***Gridded models***

In this case the computational domain is subdivided into smaller areas (cells), which compose the grid. In every point of the grid the dispersion equation is solved with mass continuity for every pollutant within a medium, where turbulent flow and advection dominate transport and pollutants are subjected to chemical transformation. The grid used in the model can be two-dimensional or three-dimensional depending on the demands of the application and the structure of the model. In general there are both practical and theoretical limitations concerning the dimensions or the number of

the cells in which the sector of the model is subdivided. The form of the grid to be used for a certain case is dependent on the degree of detail of the available input data (wind, parameters of turbulent flow, temperature, emissions etc.) and the available computational potential.

The study of transport, diffusion and deposition in a large scale of components such as SO_2, which lead to the formation of oxides and also the study of aerosols is usually performed with such models. Also nested grid models have been developed in order to use a denser grid above sensitive areas.

- ***Other modelling tools***

Such a tool, rarely used in air pollution modelling, is that of neural networks, which are widely used in other fields such as pattern recognition, speech recognition and synthesis, financial forecasting, etc, (Boznar and Mlakar, 1995; Gardner and Dorling, 1999).

The Monte Carlo simulation approach has already been shown to be a very powerful method for modelling pollutant dispersion over a complex terrain because the complications there, namely the inhomogeneity of the mean flow and turbulence, can in principle be easily accommodated, (Tombrou et al., 1995 and 1998).

Finally empirical models have been developed for pollution management and prediction purposes. Some interesting examples are, the model AEOLIUS developed by Buckland and Middleton (1999), following the Environment Act of 1995, which required local authorities to review past and assess future air quality. Their model predicts concentration levels within a specific street canyon under certain climatic and emission conditions. Similar work is also reported by Ashie et al (1999).

2.2 Description of dispersion processes

2.2.1 Dispersion processes

Normally pollutants are emitted at relatively low level, most often within the boundary layer. If the effluent is very hot, there will be a significant plume rise due to buoyancy. Most of the material may penetrate into the free troposphere, thus leaving behind only a remnant in the atmospheric boundary layer. Due to deviations from the

ideal structure and uncertainties in the details of the emissions (especially in accidental releases) it is often very difficult to specify the initial vertical distribution of the pollutant with any certainty. The situation is easier with pollutants with little buoyancy released near the ground. However, if the boundary layer is very shallow, or the effective source height is high enough, the plume may be incorporated into the growing boundary layer as the surface fluxes increase, due perhaps to increased solar heating of the ground. Although the boundary layer is usually well mixed by the turbulence over a timescale of less than an hour, vertical gradients of pollution, moisture and wind can persist at any locality because of markedly different origins of the air at different heights.

The importance of the wind field: The vertical movement of pollutants in the boundary layer is largely controlled by the prevailing stability conditions, and therefore the air temperature stratification. Free convection is an important means of diffusing material into a large volume, and the depth of the mixed layer sets an upper limit to the vertical dimension. Therefore, from a convective standpoint the best conditions for pollutant dispersion usually occur with strong instability and a deep mixed layer. This is characteristic of sunny, daytime conditions, especially in summer. Conversely, the worst conditions for dispersion occur when there is a temperature inversion and the boundary layer is stable. Turbulence is then suppressed and upward motion is effectively eliminated.

Dispersion patterns: The emission height is very important when talking about dispersion in the boundary layer. The higher the point of injection the smaller will be the ground-level concentrations downwind, because eddy diffusion will have had a longer time to dilute the plume contents. Tall stacks are therefore usually of help in combating poor air quality near the point of release. The effective height of release can also be increased if the effluent emerges at a high velocity and at a temperature well above that of the environmental air so that it possesses buoyancy. The plume then ascends well above the stack exit before bending-over and proceeding downwind. On the meteorological side the effect of increasing wind speed is to 'push' the plume over progressively and to diminish the amount of plume rise; and the environmental lapse rate is important because instability encourages upward penetration whereas stability produces a restraining influence, (Oke, 1988).

For continuous releases when the plume is sampled over an hour or more, the concentration profiles in the vertical and to a lesser extent in the horizontal begin to assume rather smooth shapes since the statistical irregularities evident at shorter times are increasingly ironed out. The distribution shows a peak in the centre with the concentration falling away to zero on either side.

After its initial rise the form of the plume downwind is largely governed by the prevailing structure of turbulence. Using atmospheric stability it is possible to classify the most characteristic plume patterns: *Looping, Coning, Fanning, Lofting and Fumigation.*

2.2.2 Urban Boundary Layer

The urban boundary layer, UBL, is that portion of the ABL whose climatic characteristics are modified by the presence of a city at the surface. As air flows from the countryside to the city, it encounters a new and very different set of boundary conditions. Thus, an internal boundary layer develops downwind from the leading edge of the city. In comparison with the surrounding landscape the city usually provides a rougher, warmer, and perhaps drier set of surface conditions (Stull, 1988, Oke, 1987). The UBL normally extends over the surface and the free convection layers. The UBL is a local to mesoscale phenomenon whose characteristics are governed by the nature of the general urban surface. The roughness elements of a city are mainly its buildings. These relatively tall, sharp-edged and inflexible objects make cities the roughest of all aerodynamic boundaries. The wind profile equations should include a zero-displacement height to allow for the upward movement of the effective ground. The effects of increased roughness on moderate or strong airflow are the increased drag and turbulence results in a deeper zone of frictional influence within which wind speeds are reduced in comparison with those at the same height in the country. This local slowing of the airflow causes it to 'pile-up' (i.e. converge) over the city, and this is relieved by uplift. The vertical motion induced is in addition to that brought about by the heat island effect, and may be sufficient to cause the UBL to 'dome' up over the city by about 250m in the daytime, (Oke, 1987; Stull, 1988). Beneath roof level is the urban canopy layer (UCL), which is produced by micro-scale processes operating in the streets (canyons) between the buildings. Its climate is an amalgam of microclimates, each of which is dominated by the characteristics of its

immediate surroundings. The principal unit of the urban canopy layer is the urban canyon consisting of the walls and ground (usually a street) between two adjacent buildings.

A "street canyon" represents a relatively narrow street between buildings that line up continuously along both sides. It simulates the basic geometry of the labyrinth confining the urban canopy layer of the city centres. This layer is vertically bounded by the ground surface and the roof level and maintains a distinct climate where microscale meteorological processes dominate. This arrangement recognises the three dimensional nature of the urban canopy, and allows the inclusion of the interaction between buildings rather than treating them as isolated objects, in Figure 2.1 a side-view of an almost square street canyon is provided. In a city with a grid-like street pattern there are often two canyon orientations offset by 90 degrees. Each one possesses a different microclimate as a result of differences in the angle of solar incidence and the angle-of-attack of the wind. Such differences are in addition to those created by the radiative, thermal and moisture characteristics of their construction materials and the canyon geometry, (Oke, 1987).

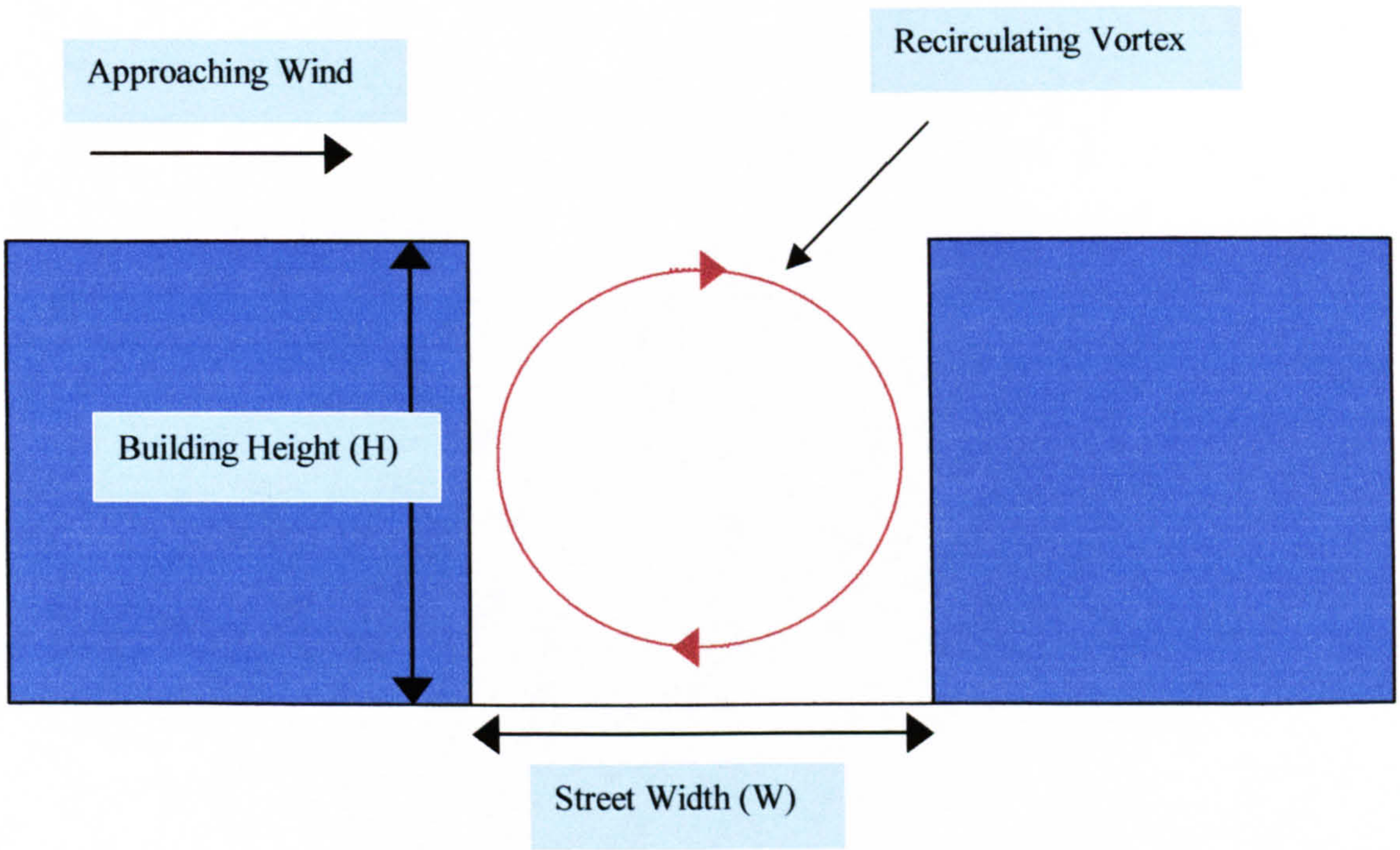

Figure 2.1: Side view of a simplified street canyon structure.

2.2.3 Modelling techniques

A simplified description of the wind field developed in a square street canyon was attempted first by Hotchkiss and Harlow (1973), which although quite simplified reflects the basic properties of wind circulation in street canyons. One of the earliest street pollution models is the STREET model by Johnson and Hunter, (1995). It is an empirical model derived from analysis of measurements in certain streets. A quite different approach was introduced by Yamartino and Wiegand (1986) in their Canyon Plume-Box Model (CPBM). The model is essentially the combination of a plume model for the direct impact of vehicle-emitted pollutants with a box model, which enables computation of the additional impact due to pollutants recirculated within the street. The performance of this model was found to be better than the one of the STREET model mainly because it was not an empirical one with a wider range of application potential.

An empirical approach was also used to determine traffic pollution in Dutch city streets, the CAR model (Calculation of Air pollution from Road traffic). It was based on a series of wind tunnel experiments (Eerens et al., 1993). Only annual average concentrations are calculated and other statistical means are estimated based on empirical relationships, derived from measurements in the national pollution network. An international version of model also exists (Boeft et al., 1996).

The OSPM or Operational Street Pollution Model by Berkowicz et al., (1996) and Berkowicz et al. (1997), is a robust and simple operational model. It uses concepts previously developed by Yamartino and Wiegand (1986). OSPM was tested with hourly concentrations of pollutant from selected sites in Denmark, Norway and the Netherlands. Concentrations of exhaust gases are calculated using a combination of a plume model for the direct contribution and a box model for the recirculating part of the pollutants in the street. OSPM makes use of a simplified parameterisation of flow and dispersion conditions in a street canyon. This parameterisation was deduced from extensive analysis of experimental data and model tests. Results of these tests were used to improve the model performance, especially with regard to different street configurations and a variety of meteorological conditions.

Furthermore, several small-scale turbulence models have been developed able to represent successfully the wind flow and pollution dispersion characteristics within single or clusters of obstacles (CHENSI Sini et al., 1996, MIMO Ehrhardt, 2000).

Moving to the urban scale several models have been developed in this respect. ADMS-Urban model is a steady state new generation Gaussian type model, which was originally developed for point source applications (UK-ADMS). It is characterised by the use of boundary layer similarity profiles to parameterise the variation of turbulence with height within the boundary layer. The model has since been developed as a multi-source dispersion modelling system for air quality management applications. The model has been tested with an urban emissions inventory in two areas of London, Central London and East London and was used to examine and evaluate the consideration of both local effects and emissions from the Greater London Area (Carruthers et al., 1996, Carruthers et al., 1999). Another example of an urban scale model is UDM-FMI (Karpinnen et al., 1998) and CAR-FMI (Kukkonen et al., 2001). Another example of an urban scale model is the Urban Airshed Model (UAM), EPA, 1990.

In general, urban scale models should be able to allow for the various local scale effects, i.e., influence of buildings and obstacles, downwash phenomena and plume rise, together with chemical transformation and deposition. However, since these models are based on the Gaussian theory, they can not allow for the detailed structure of buildings and obstacles. Usually the concentrations computed may be interpreted as spatially averaged values, while inside a street canyon pollutant concentrations vary significantly. Nevertheless, urban scale models can provide easily with hourly time series of meteorological and emission conditions for one year. Street scale models on the other hand, are able to represent concentrations distributions inside a street canyon and to account for building structure, but if they had to be applied for consecutive streets such as to cover a larger area high computational time would be required making this attempt not practical.

Finally, meteorological models covering a greater urban area and its surroundings and providing also urban scale models with the appropriate meteorological and pollution background boundary values are available. One such example is the MEMO model (Moussiopoulos et al., 1995). These models have a coarse resolution, compared to

urban scale or small-scale models, and use average values to represent ground situation. However, they can take into account synoptic conditions, which also play an important role for air quality above an urban area.

2.2.4 Characteristics of air flow in street canyons

The dynamic characteristics of airflow patterns observed in a street canyon reflect the near field geometry, and depend on the canyon shape and the neighbouring roof configuration. This influences the canyon ventilation and results in different pollution dispersion patterns for each case, (Rafailidis, 1997, and 1998; Meroney et al., 1999). Before proceeding with previous published work it is useful to define certain parameters. The aspect ratio for a canyon in terms of its geometrical characteristics is defined as the building height (H) over the street width (W). Furthermore, it is also of importance to define the street canyon's frontal aspect ratio, building length (L) over building height (H), when studying three-dimensional flow characteristics.

If a building is part of an urban area the flow pattern depends upon the geometry of the array, especially the height to width ratio (H/W). When the buildings are relatively widely spaced (H/W<0.4 for cubic and <0.3 for row buildings) their flow pattern appears almost the same as if they were isolated (Isolated Roughness Flow, IRF). At closer spacing (H/W up to about 0.7 for cubes and 0.65 for rows) the wake of any building interferes with that of the next downstream leading to a complicated pattern (Wake Interference Flow, WIF). At spacings closer than those the main flow starts to skim over the building tops and drives a lee vortex in the cavity (often a street) (Skimming Flow, SF). This is a lee eddy characteristically found in separated flow behind sharp obstacles, but here it is reinforced by the downward deflection produced by the windward face of the succeeding obstacle.

2.2.4.1 Previous Studies.

Early field observations, (DePaul and Sheih, 1986; Nakamura and Oke, 1988; Oke 1987), suggested that, in order to sustain stable vortices in street canyons, a critical velocity of the order of 2 m/s is required at roof level, being perpendicular to the street canyon axis. In addition, however, oblique winds also induce a parallel contribution, which results in simultaneous advection of pollutants along and across the street. Furthermore, parallel winds transport downwind pollution evenly

dispersed around the canyon cross-section. In practice, however, town street canyons are regularly intersected by other streets which feed them with fresh or more polluted air, thus leading to complex dispersion patterns (Hoydysh and Dabberdt, 1988; Kastner-Klein et al., 1997). In fact Hoydysh and Dabberdt, (1988) in their earlier work indicated that the cross canyon gradient of concentration of pollutants when the free stream winds are perpendicular to the canyon axis, for symmetric and step up canyon configurations, are a factor of two or more greater for the leeward than the windward façade.

Significant components of the street canyon microclimate are their characteristic wind-induced flow patterns. They are significant because airflows often directly affect the comfort of the city inhabitants, (Bottema, 1999). Several studies dealing with the canyon flow regimes as a function of the geometrical ratios W/H and L/H aimed at identifying optimum urban canyon geometries for efficient dispersion of pollutants, (De Paul and Sheih, 1986; Hunter et al., 1992; Hussain and Lee, 1980; Lee and Park, 1994; Nakamura and Oke, 1988; Oke, 1987). The air-flow in the canyon is also responsible for the transport of other properties such as heat and moisture.

Nearly all previous studies reported here gave emphasis on the supposed two-dimensional nature of the flows and the assumption made that most of the important features can be explained in these terms. For example, in numerical studies the threshold H/W ratios for the transition between flow regimes have been evaluated by investigating changes in flow patterns in vertical cross-sections. This has involved repeated observations of the flow regimes with increasing canyon width, necessitating many numerical experiments each of which is computationally expensive. Part of the reason for this approach is that, genuine three-dimensional numerical models have become available relatively recently and thus most existing numerical experiments are limited to two dimensions, (Hunter et al., 1992).

Knowledge of threshold height/width (H/W) ratios for the transition between flow regimes is important if the problems associated with urban canyon climates, such as high pollution concentrations or channelling of air flow, are to be identified.

When the above roof wind direction is perpendicular to the axis of the canyon DePaul and Sheih (1986) showed that one or more vortices can develop within the canyon, their strength and location being essentially dependent on the ratio W/H.

Sini et al., 1996, compared his simulations with previous studies. In this study the isothermal wind fields are simulated for aspect ratios ranging from 0.33 to 14.82. The asymptotic value W/H infinity is also simulated, by combining the simulations of the backward and forward facing step flows. The aim was to investigate two key factors, namely the street canyon aspect ratio and the differential heating of the wall surfaces, and their influence upon the in-street flow structure. He found that differential heating of walls could have a large influence on the in-street flow and its vertical transport capabilities. He further suggested that investigation of the three-dimensional nature of flow within urban canyons suggests that the maintenance of a vortex circulation, associated with skimming flow, is dependent on the extent of the double-eddy circulation near the corners of the lee face of the canyon.

The transition to wake interference flow occurs for canyons sufficiently wide that the double-eddy circulation is fully formed. It is the change from skimming to wake interference flow that is the most significant to urban climatologists since skimming flow, a feature of narrow canyons, provides minimal flushing of the canyon and is relatively ineffective in removing pollutants, heat and moisture.

The structure of the lowest atmospheric layer over the canopy, often called 'roughness sublayer', (Rotach, 1995) also depends on the ratio W/H, from that of a weakly disturbed 'constant flux' atmospheric surface layer for small values of W/H, up to that of a series of internal layers developing on each line of obstacles.

2.2.4.2 Experimental work.

Wind tunnel experiments: In wind tunnel experiments the urban situation to be studied is reproduced at small scale and the experimental device is a wind tunnel (Plate, 1999). Wind tunnel applications for urban areas include three typical cases:

- Wind force and wind pressure determinations on buildings and other structures such as bridges.

- Pedestrian comfort which is studied by identifying local high winds induced by geometry of the buildings by virtue of sand erosion.

- Finally the most important contribution of wind tunnel studies to urban planning is in the field of pollution from different sources, point or line sources.

An important early wind-tunnel study is that of Hussain and Lee, (1980) for a large number of street-like geometrical arrangements of long building models. Although the authors mainly measured pressure distributions, their systematic measurements have allowed Oke's (1987) further analysis in terms of three flow regimes, depending on height-to-width and length-to-height ratios of the buildings.

Although many wind tunnel simulations of flow around isolated buildings have been validated by on-site measurements, the extremely small number of in-street detailed flow structure measurements allows only very partial validation of the simulations, (Rotach, 1995).

A novel 2-D wind tunnel experiment was performed by Rafailidis, (1997). In this study the effect of the street canyon geometry and roof shape both on the mean flow field and on the dispersion of pollutants was studied. Data from this experiment were also provided from the web, thus they were available for other researchers to use for validation purposes, (http://www.mi-uni-hamburg.de). At present at the same web address an extensive data base of both 2-D and 3-D experiments is also available.

Wind tunnel tests performed by Pearce and Baker (1999), on the dispersion of vehicular pollutants in an urban area, were focused on the urban planning point of view. Their main aim was to investigate the relationship between high-speed wind to assist in dispersion and ventilation of low-level gaseous pollutants while maintaining an environment that is both comfortable and safe for pedestrians. A limitation to this, the authors argue, is posed by the lifting of particulates into the air so that increases in speed can increase pollutant levels for certain pollutants. Thus, the measurement of both the wind and concentration fields at pedestrian level was attempted, which constituted the novelty of these sets of experiments. The wind tunnel model scaled down a real street from a city in the UK. Amongst their findings, the irregularity of

roof heights enhanced ventilation at the pedestrian level, thus producing a general first relationship between changes in mean wind speed and mean tracer concentration.

In another wind tunnel study, Gayev and Savory (1999), attempted to treat a city as a penetrable roughness structure placed in the flow and to derive the definition of an urban canopy. Thus, they placed three penetrable fences in the form of three rows of vertical cylinders within a simple 2D square street canyon in order to investigate effects on the flow. The placement of internal obstacles produced distributions and fluctuations of velocity similar to these existing in real urban canopies. Furthermore, in certain locations vortex mixing resulted in homogeneous flow distributions. Finally, indications were found that fences of interior roughness might be deliberately applied in order to aid the ventilation of street canyons. They suggested that further work should be done in order to assess the effects on the flow field of size and distribution of the internal roughness and other parameters in order to assess effect of roughness on dispersion of pollutants within the urban canopy.

An interesting and important series of wind tunnel experiments were performed by Gerdes and Olivary (1999). Their aim was to investigate pollutant contamination of a 2D urban street canyon, altering the landscape upstream of the canyon, the ratio between the upstream and downstream canyon walls and the spacing between the canyon walls. They not only measured mean concentrations but also the statistical properties of the concentration field, which serves for instantaneous values for the concentration for exposure studies. Their experimental results showed a strong influence of the landscape on the pollutant dispersion, whereby higher concentrations inside the canyon area were observed for an urban roughness upwind area compared to an open landscape upstream area. When the downwind building of the canyon was made taller than the upwind it affected the flow field much more than the characteristics of the upwind building and in fact enhanced ventilation. It was also found that the distance between the buildings of the canyon played no important role.

Another interesting aspect, which is thought to influence the dispersion of pollutants within street canyons, is the so-called car induced turbulence. Several researchers have been preoccupied with this issue amongst them Kastner-Klein et al., (1999) who after performing a series of wind tunnel experiments – without traffic, and with traffic- found that the lateral component of the mean flow displayed great dependence

on the traffic arrangement in the canyon. In the case of two-way traffic the concentration distribution was found to be approximately symmetric, however mean transport of pollutant along the canyon was negligibly small. In the case of one-way traffic in the canyon the along-canyon concentration distribution of pollutant was strongly influenced, with concentration values increasing in the direction of flow.

A more recent wind tunnel experiment performed by Pavageau and Schatzmann (1999), examined some turbulent characteristics and statistical properties of the concentration field developing from the steady state release of a tracer gas at street level in a canyon amidst urban roughness. The concept behind such an experimental campaign lies on the fact that previous wind tunnel experimentalists have been focused mainly on mean concentration levels and their spatial distribution. Thus, the probabilistic aspect of the problem, together with its turbulent characteristics has been neglected. Therefore, time series of fluctuating concentrations were recorded at a large number of points within a street canyon. Amongst their most interesting findings are: Near the source and at the leeward wall there exist large concentration gradients, such that by displacing slightly the measurement instrument large deviations in the measured values occur. Thus, the EU directive 85203/EEC indicating that sensors should be placed at the locations of maximum concentrations should not be followed according to Pavageau and Schatzmann, (1999), but rather at areas of smooth concentration gradients such as the windward wall. They also found, in accordance to the field experiment performed by Louka et al., (2000), that there exists a main street vortex which oscillates around its mean position yielding a region of strong interface at the roof between the turbulence inside the street and the boundary layer aloft.

Yet another wind tunnel experiment done by Kastner-Klein et al., (1999) of a single street canyon, showed the effect of altering the geometrical characteristics of the street canyon and the upwind characteristics. It was found that adding more buildings upwind of a single-street canyon increases concentration of pollutants emitted within it. This is attributed to the perturbation of the flow as an internal boundary layer forms due to the existence of the buildings. This was also found by Pavageau et al., (1999). Furthermore, geometry affects dispersion either by enhancing it or by depressing it.

Field experiments: Vakeva et al., (1999) performed a field study in order to measure and compare street level and rooftop concentrations of submicron aerosols and gaseous pollutants in an urban street canyon in Finland. The field experiment was based on the idea that emissions and thus also concentrations of primary pollutants have extremely strong spatial and temporal variations and the characterisation of urban air pollution is fairly complicated. The concentrations of pollutants in urban areas are controlled by a balance between those factors, which lead to pollutant accumulation and those which lead to pollutant dispersion. There are usually strong gradients of gaseous and particulate pollutants both in the vertical and horizontal directions due to activities of emission sources, rapid mixing and dilution of street level emissions. Their study was performed following several studies done by other researchers who measured the horizontal and vertical gradients of CO and NO_x within a street canyon. Their measurements showed an average vertical difference of approximately a factor of two for both CO and NO_x between street level and the rooftop, (approximately 25-m high). They also found that during low wind speed conditions, the differences in concentrations between the leeward and windward side of the road are small, but quite different from the centreline concentrations. Furthermore, Zoumakis (1995) fitted semi-empirical curves to experimental data measured by himself and other investigators and found that the average vertical profile of vehicular pollutant concentrations follows the general exponential form.

On the contrary the highest ozone concentrations were measured at rooftop height whereas street level concentrations were up to eight times lower. It was also found that approximately 20% of NO_x was NO_2 at a distance 6m from the kerb, during the times of strongest emissions (Vakeva et al., 1999). This fact comes to support numerical calculations done by Moussiopoulos et al., (1998) with a computational fluid dynamics code, which showed very little O_3 in the street canyon and maximum levels outside. Finally the analysis illustrated that traffic is the dominant factor affecting street level pollution and that the source of street level ozone is transportation from upper parts of the boundary layer during night-time Similar work was reported by Michallef et al, 1998.

Early full-scale experimental observations of flow within urban streets to validate these more idealised studies are reported by DePaul and Sheih (1986). They

demonstrated qualitatively that there is a re-circulation within a narrow street when the mean wind above the roof is greater than 2 m/s. Later Nakamura and Oke (1988) studied the thermal effects during daytime conditions on the re-circulation patterns within street canyons. Rotach (1995) in an interesting sequence of papers presents profiles of mean wind and turbulence measured in the upper levels of a street above the roofs in the centre of Zurich. The geometry of the buildings surrounding this site is highly complex and the data plotted by Rotach is averaged over a range of directions. Hence, the results should not be interpreted in terms of individual street and building geometry. On the contrary Rotach's measurements were designed to characterise flow over a large number of buildings and thereby answer questions such as the height above the roofs where the buildings can be considered to be roughness. A comprehensive programme of measurements of the wind field in a full-scale single street canyon were required. Results of such measurements are presented by Louka et al., (2000). Based on the conception that in most European cities the street canyon aspect ratio is large enough that skimming flow with a recirculation develops, measurements were obtained of the airflow within and above two long farm buildings for a wind perpendicular, to the street canyon axis. It was found that the recirculation pattern within the street was unsteady; thus the turbulent fluctuations were dominant the mean flow being the residual. Most importantly Louka et al.(2000), identified a shear layer shed from the upstream roof that becomes unstable through Kelvin-Helmholtz instability. This layer forces the unsteady recirculation within the street and transports air from within the street upwards to the boundary layer aloft. It was also found that pitched roofs are associated with more energetic eddies thus, affecting the strength and depth of the shear layer. From these field measurements of the flow field it was deduced that such a mechanism transports automobile emissions around the recirculation path and ejects them upwards across the shear layer. In a similar manner pollutants from the boundary layer aloft or from neighbouring street canyons may be entrained into the street of interest.

3 Microscale Model Description

3.1 Introductory remarks

Computational Fluid Dynamics or CFD is the analysis of systems involving fluid flow, heat transfer and associated phenomena such, as chemical reactions by means of computer-based simulation. The technique is very powerful and spans a wide range of industrial and non-industrial application areas (Gossman, 1999; Kim and Boysan, 1999; Lee et al, 1997a). CFD codes are structured around the numerical algorithms that can tackle fluid flow problems. All codes contain the following three main elements:

1. **Pre-processor:** Consists of the input of a flow problem to a CFD program. This involves defining the geometry of the computational domain. Moreover, all necessary input parameters related to the physical and chemical phenomena are specified. Finally, the appropriate boundary conditions are specified. The accuracy of a CFD solution is dependent on by the number of cells in the grid. In general, the larger the number of cells the better the solution accuracy. Both the accuracy of a solution and its cost in terms of necessary computer hardware and calculation time are dependent on the fineness of the grid. Optimal meshes are often non-uniform: finer in areas where large variations occur from point to point and coarser in regions with relatively little change.

2. **Solver:** There exist three different numerical solution techniques for solving the model equations. The one used in the present work is the finite volume method. The numerical method, which forms the basis of the solver, includes the approximation of the unknown flow variables by means of simple functions, the discretisation by substitution of the approximations into the governing flow equations and subsequent mathematical manipulations and finally the solution of the algebraic equations. The finite volume numerical algorithm consists of the following steps: Formal integration of the governing equations of fluid flow over all the finite control volumes of the solution domain. Discretisation involves the substitution of a variety of finite-difference-type approximations for the terms in the integrated equation representing flow processes such as convection, diffusion and sources. This converts the integral

equations into a system of algebraic equations. Solution of the algebraic equations by an iterative method. The control volume integration, distinguishes the finite volume method from all other techniques described above and the resulting statements express the exact conservation of relevant properties for each finite size cell. The clear relationship created between the numerical algorithm and the underlying physical conservation principle makes the finite volume method the most popular form of numerical solution.

3. **Post-processor:** In this part data visualisation tools are utilised in order to display the domain geometry and the grid, vector plots, contour plots, view manipulation (translation e.g.), particle tracking etc. The ability to assess the numerical solution, i.e., whether it has been successful or not is of great importance. This can be done with the use of three mathematical concepts: convergence, consistency and stability.

3.2 Classification scheme of predicting turbulent flows

In engineering applications most flows are turbulent. In addition to that the flows to be resolved involve such difficulties as complex geometry. The most common methods, used for the solution of such complex problems include the following widely recognised approaches:

- Methods based on equations obtained by averaging the equations of motion over time if the flow is statistically steady, over a co-ordinate in which the mean flow does not vary, or over an ensemble of realisations (an imagined set of flows in which all controllable factors are kept fixed). This approach is called one point closure and leads to a set of partial differential equations called the Reynolds averaged Navier-Stokes (or RANS) equations. These equations do not form a closed set, so this method requires the introduction of approximations, (turbulence models).

- Large Eddy Simulation solves for the largest scale motions of the flow while modelling only the small-scale motions. It can be regarded as a kind of compromise between one-point methods and direct numerical simulation. The large scale motions are generally much more energetic than the small scale ones and their size and strength make them by far the most effective transporters of the conserved properties. The small scales are usually much weaker, and provide little transport of these

properties. Large eddy simulations are three dimensional, time dependent and expensive but much less costly than a DNS of the same flow. In general, because it is more accurate, DNS is to be preferred. LES is the preferred method for flows in which the Reynolds number is too high or the geometry is too complex for the application of DNS.

- Finally there is direct numerical simulation, in which the Navier-Stokes equations are solved for all of the motions in a turbulent flow. The most exact approach to turbulence simulation is to solve the Navier-Stokes equations without averaging or approximation other than the necessary numerical discretisations whose errors can be estimated and controlled. In such simulations, all of the motions contained in the flow are resolved. The result is equivalent to a single realisation of a flow or a short duration laboratory experiment. The domain on which the computation is performed must be at least as large as the largest turbulent eddy. A useful measure of this scale is the integral scale L of the turbulence. Each linear dimension of the domain must be at least as large as a few times the integral scale. It must also capture all of the kinetic energy dissipation. This, however, occurs on the smallest scales, the ones on which the viscosity is active, so the size of the grid must be no larger than a viscously determined scale, (the Kolmogoroff scale). Since the number of points to be employed in each of the three co-ordinate directions, and the time step is related to the grid size, the cost of a simulation typically scales as Re_L^3. Where the Reynolds number is based on the magnitude of the velocity fluctuations and the integral scale. Since the number of grid points in a computation is limited by the processing speed and memory of a machine, direct numerical simulation is possible only at low Reynolds numbers, or for homogeneous turbulence (Ferziger, Peric, 1997; Versteeg and Malalasekera, 1995).

3.3 MIcroscale MOdel structure, MIMO

The increasing interest in the prediction of wind flow and pollutant dispersion over built-up areas and major advances in computer technologies have led to the development of efficient numerical models as an alternative or complementary approach to laboratory and field experiments. The microscale model MIMO, (Winkler, 1995; Ehrhadt, 2000) was developed at the Institut fur Technische Thermodynamik on the basis of the non-hydrostatic mesoscale model MEMO (Flassak, 1990, Kunz and Moussiopoulos, 1995). Finally the microscale model MIMO

has been applied and validated for several case studies, such as to simulate flow around obstacles with simple geometries like a surface-mounted cube (Ehrhard et al. 1998) and a U-shaped building (Goetting et al, 1997). The results from these simulations were compared with results from wind tunnel experiments. Moreover, the model was applied successfully to predict plumes rising from cooling towers and dispersion of pollutants in built-up areas.

3.3.1 Model equations and numerical solution

Governing equations

MIMO solves the conservation equations for mass, momentum, energy and scalar quantities such as the humidity or the concentration of pollutants. The general form of the conservation equation is given by:

$$\frac{\partial(\rho\phi)}{\partial t}+\frac{\partial(\rho U_j\phi)}{\partial x_j}=\frac{\partial}{\partial x_j}(\rho\Gamma\frac{\partial\phi}{\partial x_j})+S_\phi \qquad (3.1)$$

The source term S of quantity ϕ takes the appropriate form for momentum, energy, turbulent kinetic energy, dissipation rate, concentration and the exchange coefficient Γ. U_i denotes the mean velocity and x_i the Cartesian co-ordinates. θ is the potential temperature. The mean state is assumed to be in hydrostatic equilibrium, i.e. $dp/dz = -\rho g$. Usually the density fluctuations ρ' are small compared to the mean density ρ_o. Assuming $\rho' \ll \rho_o$, the conservation equation for momentum takes the following form where density variations in the inertia term are neglected, but retained in the buoyancy term, (Boussinesq approximation).

$$\frac{\partial(\rho_o U_i)}{\partial t}+\frac{\partial(\rho_o U_i U_j)}{\partial x_j}=-\rho' g_i-\frac{\partial p}{\partial x_i}-\frac{\partial(\rho_o\overline{u_i u_j})}{\partial x_j} \qquad (3.2)$$

3.3.2 Turbulence modelling

Numerical modelling of turbulence is of importance for providing accurate microscale wind fields, which are necessary for transport and dispersion calculations of pollutants in the vicinity of buildings. To solve the conservation equations it is necessary to

model the unknown Reynolds stresses, which arise from the time averaging of the non-linear transport equations for momentum. This leads to the eddy viscosity model:

$$-\rho\overline{u_i' u_j'} = \mu_t\left(\frac{\partial \overline{u_i}}{\partial x_j}+\frac{\partial \overline{u_j}}{\partial x_i}\right)-\frac{2}{3}\rho\delta_{ij}k \qquad (3.3)$$

Where k is the turbulent kinetic energy: $k=\frac{1}{2}\overline{u_i' u_i'}$

Usually the turbulence models are based on the eddy viscosity hypothesis by Boussinesq, which states that the Reynolds stresses $\tau_{ij}= -\rho (uiuj)$ are proportional to the mean strain rate S_{ij}:

$$\tau_{ij}=2\mu_t S_{ij}-2/3\rho k\delta_{ij} \qquad (3.4)$$

The Einstein summation convention was also applied. It is of importance to note that the eddy viscosity μ_t is not a property of the fluid but a property of the flow field and it is usually expressed in terms of the velocity and length scales of the turbulent motion.

Although the eddy viscosity hypothesis is not correct in detail, it is easy to implement and can provide reasonably good results for many flows. In the simplest description, turbulence can be characterised by its kinetic energy, k and a length scale L. Mixing length models are also known as zero-equation models.

The difficulty in prescribing the turbulence quantities suggests the use of partial differential equations for their calculation. Since a velocity and a length scale are needed, a model based on two such equations is a logical choice. In its most usual form, this equation is:

$$\frac{\partial(\rho\varepsilon)}{\partial t}+\frac{\partial(\rho u_j\varepsilon)}{\partial x_j}=C_{\varepsilon 1}P_k\frac{\varepsilon}{k}-\rho C_{\varepsilon 2}\frac{\varepsilon^2}{k}+\frac{\partial}{\partial x_j}\left(\frac{\mu_t}{\sigma_\varepsilon}\frac{\partial\varepsilon}{\partial x_j}\right) \qquad (3.5)$$

In this model, the eddy viscosity is expressed as:

BIBL. LONDIN.

$$\mu_t = \rho C_\mu \sqrt{k} L = \rho C_\mu \frac{k^2}{\varepsilon} \qquad (3.6)$$

The model based on equations (3.5) and (3.6) is called the k-ε model. This model contains five parameters; the most commonly used values are:

C_μ=0.09; $C_{\varepsilon 1}$=1.44; $C_{\varepsilon 2}$=1.92; σ_k=1.0; σ_ε=1.3

The most commonly used k-ε two-equation turbulence model, is the one by Jones and Launder (1972). It determines the velocity and length scales of the turbulent motion by solving for the transport equations of the turbulent kinetic energy k and the dissipation rate, ε. To account for buoyancy effects the production of turbulent kinetic energy and dissipation is augmented by an additional buoyancy term depending on the Richardson number Ri.

The k-ε models are numerically robust and efficient, however they are known to have deficiencies in describing turbulent flows with body force effects arising from streamline curvature and Reynolds stress differences, which are not predicted correctly. Therefore, their application to highly complex flows can lead to considerable inaccuracies, thus certain improvements and corrections have been applied (Burr, et al, 1998; Lakehal and Rodi, 1997; Maurizi, 2000; Park and Sung, 1995; Lakehal, 1998). Following that, Ehrhardt, 2000 proceeded to the development of non-linear stress-strain relationships that transcend the Boussinesq hypothesis, without increasing the complexity of the structure. These non-linear eddy viscosity models are also used for other engineering applications and have been proven quite useful (Bauer, et al, 1998).

3.3.3 MIMO model initial and boundary conditions

3.3.3.1 Initial conditions

In the model MIMO two different possibilities for the initialisation are included. The first is to couple the microscale model MIMO with MEMO (Kunz et al., 1998), or to calculate the velocity from measured data or by implementation of the power law:

$$U(z) = U_r (z / z_r)^{\alpha}$$

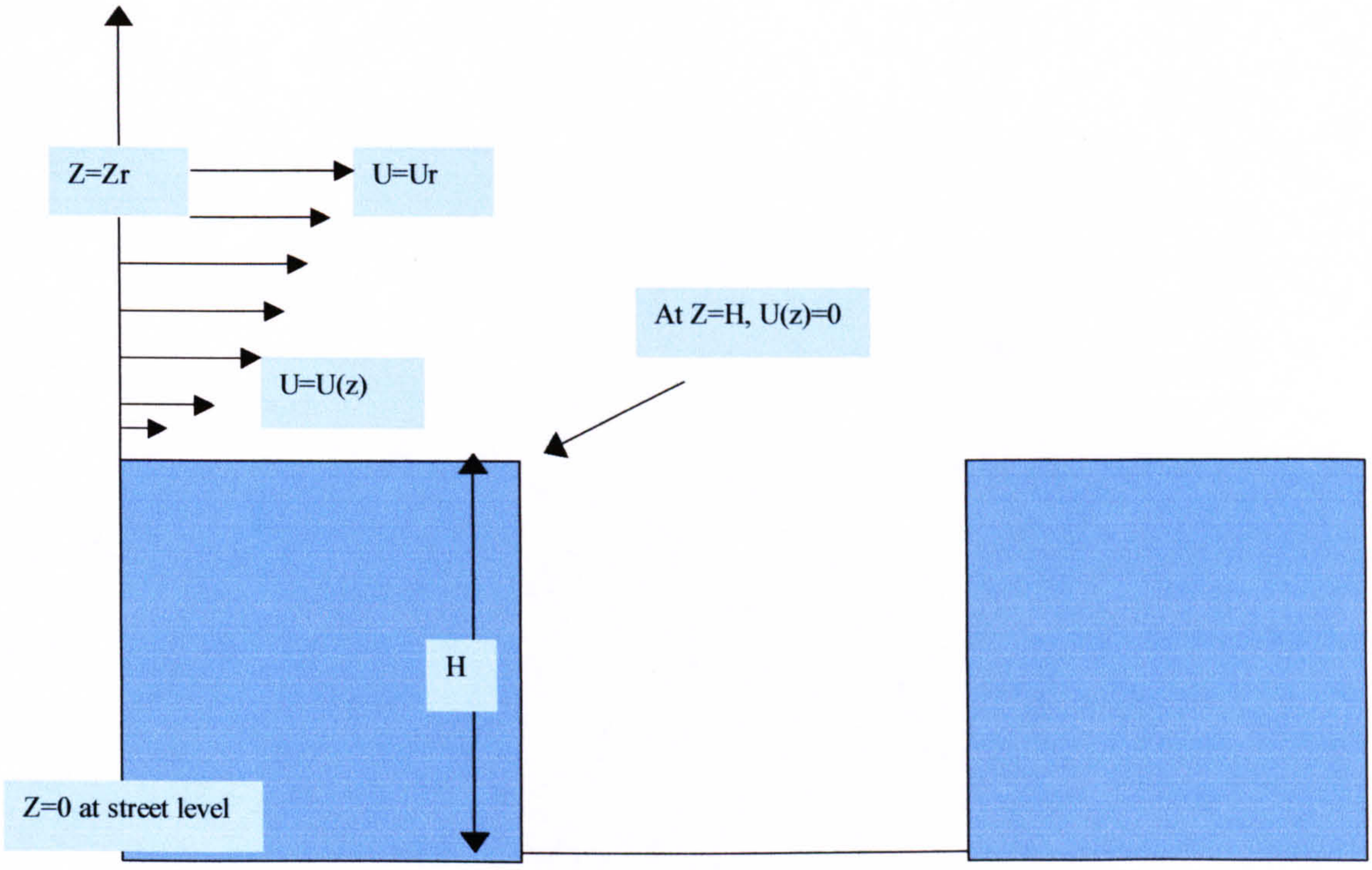

Figure 3.1. Illustration of how the power law is implemented as input for the street canyon case.

Herein Ur denotes the reference velocity at the corresponding height z_r. The exponent 'α' depends on the thermal stratification. The temperature is initialised on the basis of measured profiles or by a constant gradient. Initialisation of the pressure follows the thermal stratification according to the hydrostatic equation.

The turbulent kinetic energy, k, is either computed from experimental data or from theoretical profiles, the same applies for the calculation of the rate of its dissipation ε.

In exploratory design calculations the detailed boundary condition information required to operate the model may not be available. Industrial CFD users rarely have measurements of k and ε at their disposal. Progress can be made by entering values of k and ε from the literature and subsequently exploring the sensitivity of the results to these inlet distributions. If no information is available at all, crude approximations for the inlet distributions for k and ε in internal flows can be obtained from the turbulence intensity T_I and a characteristic length L of the equipment by means of the following simple assumed forms:

$$k = \frac{3}{2}\left(U_{ref} T_i\right)^2 ; \varepsilon = C_\mu^{3/4} \frac{k^{3/4}}{\ell} ; \ell = 0.07L \qquad (3.7)$$

3.3.3.2 Boundary conditions

The turbulence model equations for k and ε are elliptic by virtue of the gradient diffusion term. Their behaviour is similar to the other elliptic flow equations. Thus, the following boundary equations are needed, which are grouped with respect to the physical behaviour of the flow:

- Lateral inflow and outflow
- Internal openings
- Solid walls and planes of symmetry

At boundary nodes where variable values are given, i.e., Dirichlet conditions, no equation is needed. When the boundary conditions involve derivatives, Neumann conditions, the boundary condition must be discretised to provide the required equation. At lateral inflow boundaries Dirichlet conditions are imposed for all main quantities except for the pressure, which must be of Neumann type. Internal openings are distinguished into easily penetrable obstacles, i.e. open factory buildings with stacks emitting pollutants. In the latter case the initial wind velocity is prescribed according to the mass flux at the emission exhaust. The flow inside an easily penetrable obstacle is resolved explicitly.

On a symmetry plane the following conditions prevail:

a) Zero vertical velocity (i.e., w) and

b) Zero gradient of the variables vertical to this plane. At a symmetry plane the shear stress is zero, but the normal stress is not since:

$$\left(\frac{\partial u}{\partial y}\right)_{sym} = 0; \left(\frac{\partial v}{\partial y}\right)_{sym} \neq 0$$

The pressure is not required at boundaries (except if a pressure at a boundary is specified). This is due to the fact that the nearest control volume for the velocity component normal to the boundary extends only up to the centre of the scalar control volume, where the pressure is calculated.

The boundary conditions for the pressure-correction equation are also important. When the mass flux through a boundary is prescribed, the mass flux correction in the pressure correction equation is also zero there. This condition should be directly implemented in the continuity equation when deriving the pressure correction equation. It is equivalent to specifying a Neumann boundary condition (zero gradient) for the pressure correction. At the outlet, if the inlet mass fluxes are given, extrapolation of the velocity to the boundary (zero gradient) can usually be used for steady flows when the outflow boundary is far from the region of interest and the Reynolds number is large. The extrapolated velocity is then corrected to give exactly the same total mass flux as at inlet (this can not be guaranteed by any extrapolation). The corrected velocities are then considered as prescribed for the following outer iteration and the mass flux correction at the outflow boundary is set to zero in the continuity equation. This leads to the pressure-correction equation having Neumann conditions on all boundaries and makes it singular. To make the solution unique, one usually takes the pressure at one point to be fixed, so the pressure correction calculated at that point is subtracted from all the corrected pressures. Another choice is to set the mean pressure to some value.

Wall boundary conditions prohibit fluid flow across the boundary surface. Additionally the fluid is assumed to be at rest on the wall boundary surface (no-slip condition). The wall boundary condition for the velocity components implemented, the boundary value of turbulent kinetic energy next to solid walls and the rate of turbulent dissipation at the first grid point adjacent to the wall are implemented by virtue of three different schemes explained in the next chapter. At a wall the no-slip boundary condition applies, i.e. the velocity of the fluid is equal to the wall velocity, a Dirichlet boundary condition. However, there is another condition that can be directly imposed in a finite volume method:

The normal viscous stress is zero at a wall, this follows from the continuity equation, e.g. for a wall at y=0:

$$\left(\frac{\partial u}{\partial x}\right)_{wall}=0\Rightarrow\left(\frac{\partial v}{\partial y}\right)_{wall}=0\Rightarrow\tau_{yy}=2\mu\left(\frac{\partial v}{\partial y}\right)_{wall}=0$$

At high Reynolds numbers the standard k-ε model avoids the need to integrate the model equations right through to the wall by using wall functions, which rely on the existence of a logarithmic region in the velocity profile. If y is the co-ordinate direction normal to a solid wall, the mean velocity at a point y_p with $30<y_p^+<500$ satisfies the log-law and measurements of turbulent kinetic energy budgets indicate that the rate of turbulence production equals the rate of dissipation. Using these assumptions, the fact that the flow is in local equilibrium, i.e., the production and dissipation are nearly equal, and the eddy viscosity formula, it is possible to develop the following wall functions:

$$u^+=\frac{U}{u_\tau}=\frac{1}{\kappa}\ln(Ey_p^+)$$

$$k=\frac{u_\tau^2}{\sqrt{C_\mu}}$$

$$\varepsilon=\frac{u_\tau^3}{\kappa y}$$

Von Karman's constant $\kappa = 0.41$ and the wall roughness parameter $E = 9.8$ for smooth walls.

Using the above equations one can derive an expression connecting the velocity at the first grid point above the wall and the wall shear stress:

$$\tau_w=\rho u_\tau^2=\rho C_\mu^{1/4}\kappa\sqrt{k}\frac{u_t}{\ln(n^+E)}$$

where $E=e^{\kappa B}$.

When these laws of the wall boundary conditions are used, the diffusive flux of k through the wall is usually taken to be zero, yielding the boundary condition that the normal derivative of k is zero. The dissipation boundary condition is derived by assuming equilibrium i.e., balance of production and dissipation in the near wall region. The production in the wall region is computed from:

$$P_k = \tau_w \frac{\partial \overline{u_t}}{\partial n}$$

The above equation is valid near the wall because the shear stress is nearly constant in this region. The dissipation is needed at the midpoint of the control volume near the wall. The velocity derivative required can be derived from the logarithmic velocity profile:

$$\left(\frac{\partial \overline{u_t}}{\partial n}\right)_P = \frac{u_\tau}{\kappa n_P} = \frac{C_\mu^{1/4}\sqrt{k_P}}{\kappa n_P}$$

which provides a second equation relating the wall shear stress and the velocity at the first grid point. From these two equations, both quantities may be computed.

When the above approximations are used, the equation for ε is not applied in the control volume next to the wall; instead, ε is at the control volume centre, set equal to:

$$\varepsilon_P = \frac{C_\mu^{3/4} k_P^{3/2}}{\kappa n_P}$$

It should be noted that the above boundary conditions are valid when the first grid point is within the logarithmic region, i.e. when $y_P^+ > 30$. Problems arise in separated flows; within the recirculating region and, especially, in the separation and reattachment regions, the above conditions are not satisfied. Usually the fact that wall functions are not valid in these regions is ignored and they are applied everywhere. However, if the above conditions are violated over a large portion of wall boundaries, serious modelling errors result. Low Reynolds number versions of the models should be used in such regions but their accuracy for a wide range of flows has not yet been demonstrated.

3.3.4 Solution Procedure

The governing equations described in the previous section are solved numerically on a staggered grid by using a finite volume (FV) discretisation procedure. The FV method uses the integral form of the conservation equations. The solution domain is subdivided into a finite number of control volumes (CV's), and the conservation

equations are applied to each CV. At the centroid of each CV lies a computational node at which the variable values are calculated. Interpolation is used to express variable values at the CV interface in terms of the nodal values. As a result, one obtains an algebraic equation for each CV. The FV method can accommodate any type of grid, so it is suitable for complex geometries. The method is conservative, provided that surface integrals are the same for the CV's sharing the boundary. The FV method is perhaps the simplest to understand and to program. The disadvantage of FV methods is that methods of higher than second are more difficult to develop in 3D. This is due to the fact that the FV approach requires two levels of approximation: interpolation and integration.

There is no need for all variables to share the same grid; a different arrangement may turn out to be advantageous. In Cartesian co-ordinates, the staggered grid arrangement offers several advantages over the collocated arrangement, where all the variables are stored at the same set of grid points. Several terms that require interpolation with the collocated arrangement, can be calculated without interpolation. Both the pressure and diffusion terms are approximated by central difference approximations without interpolation, since the pressure nodes lie at CV face centres and the velocity derivatives needed for the diffusive terms are computed at the CV faces. The biggest advantage of the staggered grid arrangement is the strong coupling between the velocities and pressure. This helps to avoid some types of convergence problems and oscillations in pressure and velocity fields. The numerical approximation on a staggered grid is also conservative of kinetic energy.

Scalar quantities such as the pressure or the potential temperature are defined at the centre of a cell while velocity components are specified at the centre of the appropriate interfaces between two cells. A co-ordinate transformation x=x(x1), y=y(x2) and z=z(x3) is applied in the three spatial dimensions to allow for higher resolution, e.g. near buildings or near the surface.

The conservation equation of mass is formulated in terms of the pressure yielding an elliptic differential equation. When a flow has a region of recirculation, information may travel upstream as well as down stream. As a result, one can not apply conditions only at the upstream end of the flow. The problem then acquires elliptic character. This situation occurs incompressible flows and makes solution of the equations

difficult. An important feature of elliptic problems is that a disturbance in the interior of the solution, changes the solution everywhere. Consequently the solutions to physical problems described by elliptic equations are always smooth even if the boundary conditions are discontinuous. A unique solution to elliptic equations can be obtained by specifying conditions on the dependent variable on all the boundaries of the solution domain. Problems requiring data over the entire boundary, such as the one solved in the present work, are called boundary value problems. Usually, solution of the Navier-Stokes equations is complicated by the lack of an independent equation for the pressure, whose gradient (pressure difference), contributes to each of the three momentum equations. Furthermore, the continuity equation does not have a dominant variable in incompressible flows. Mass conservation is a kinematic constraint on the velocity field rather than a dynamic equation. One way out of this is to construct the pressure field so as to guarantee satisfaction of the continuity equation.

$$\frac{\partial}{\partial x_i}\left(\frac{\partial p}{\partial x_i}\right) = -\frac{\partial}{\partial x_i}\left[\frac{\partial\left(\rho u_i u_j\right)}{\partial x_j}\right]$$

The discrete form of the elliptic equation is solved using a preconditioned conjugate gradient method. This is a technique for solving non-linear equations. Non-linear solvers can be divided into two broad categories: Newton-like methods and global methods. Newton methods converge very quickly if an accurate estimate of the solution is available but may fail if the initial guess is far from the solution. Global methods on the other hand are guaranteed to find the solution but are not very fast. Combinations of the two methods are often used. The conjugate gradient method is based on the following: It is possible to minimise a function with respect to several directions simultaneously while searching in one direction at a time. Each new search direction is required to be conjugate to all the preceding ones. The conjugate gradient method is an iterative method. The rate of convergence of this method depends on the condition number κ of the matrix where $\kappa = \lambda_{max}/\lambda_{min}$, and λ_{max} and λ_{min} are the largest and smallest eigevalues of the matrix. The condition numbers of matrices that arise in CFD problems are usually approximately the square of the maximum number of grid points in any direction. For example with 100 grid points in each direction, the condition number should be about 10^4 and the standard conjugate gradient method would converge slowly. This method can be improved by replacing the problem

whose solution we seek by another one with the same solution but a smaller condition number. This is called preconditioning.

In problems where fluid flow plays an important role one must account for the effects of convection. Diffusion always occurs alongside convection so they are predicted combined. Assuming the velocity field and fluid properties are known at all locations, the convective and diffusive fluxes are calculated. In order to do so, the value of the transported quantity ϕ and its gradient normal to the cell face at one or more locations on the CV face are required. The numerical treatment of advective transport a three-dimensional second order total variation diminishing (TVD) scheme is implemented. Furthermore, a second order flux corrected transport (FCT) scheme can be applied. Both schemes are positive, transportive, conservative and they are characterised by a low level of numerical diffusion. Diffusion terms are treated by a second order central difference scheme.

3.3.5 Model structure

The microscale model MIMO is written in FORTRAN 90 programming language and is installed on a UNIX server. Compilation and execution takes place on a Vector Parallel Processor machine. It must be noted here that the grid generator is installed on a different UNIX server, on which the plotting packages are also located. In figure 3.1 an overview of the structure of MIMO is given. As seen from the figure, the code is divided into two main sub-directories, the source and the bin. In each sub-directory is further divided as follows:

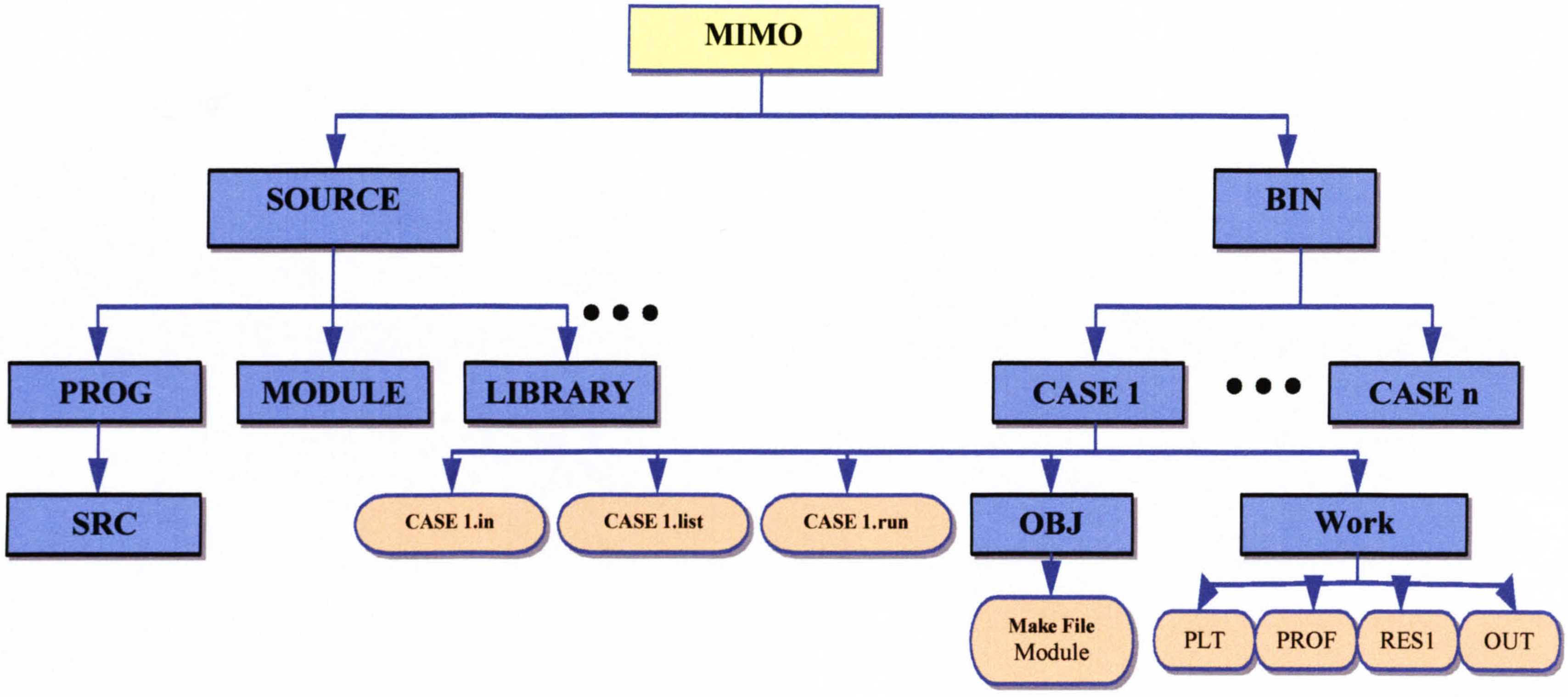

Figure3.2. Schematic representation of the structure of the microscale model MIMO

1. Source: In this directory there exist in different sub-directories all the files, which consist the core of the model (sub-directories: PROG, MODULE, LIBRARY). In more detail the necessary libraries of equations, public files, modules, solution of Helmholtz equations applying Fourier transforms related to boundary conditions files, files relevant with temperature calculations and solar radiation and buoyancy, files used for transforming output data to be compatible to a plotting package named TECPLOT. Most importantly a sub-directory containing the model files including the main routine and all the subroutines needed for the calculations are contained (SRC).

2. Bin: In this part of the code the three necessary subdirectories for pre-processing, executing and post-processing exist. Within sub-directory **case**, files for initialisation and execution exist. These files are usually named after the case studied, for instance if a canyon configuration is studied the case may be named **"canyon"**. Thus, the input file, named e.g. **"canyon.in"**, contains all the important information for initialisation, such as which boundary conditions are to be used, which velocity profile will be implemented, the number of desired iterations etc. The list file containing the grid constructed and the positions of buildings, named e.g. **"canyon.list"**. Finally the executable file, named e.g. **"canyon.run"**, which contains the names of the relevant input and list files used for the specific run. In sub-directory **work** all output files are stored by the model after completion of the computations. These are used for post-processing the results, plotting, studying the convergence etc.

Order of calculations - description of code

Input files description

All important input parameters before execution are specified in the input file. It usually takes the name of the case as well for organisation reasons. Within the input file the following parameters are specified:

General input data such as: the version to be run, that is a pure flow calculation, or additionally potential temperature, humidity, heat flux and radiation as well as concentration of pollutants. This is specified by positive integers. Furthermore, the file format of the selected geometry file is specified as well as for the recovery files in case a recovery run is attempted.

The **boundary conditions** are set for both the vector and scalar quantities on all the boundaries of the computational domain, north, south, east, west, top, bottom. Moreover, boundary conditions are set for the walls, in case buildings exist, and the floor.

Before any run it is essential to provide vertical distribution of **inflow profiles** for the horizontal velocity, the turbulent kinetic energy and the rate of dissipation of turbulent kinetic energy. Moreover, inflow profiles maybe provided for temperature, humidity and concentration of pollutants if required. It is possible to specify these inflow profiles from measurements provided by wind tunnel or field experiments or certain laws and finally from coupling of MIMO to MEMO a mesoscale model.

In the case where temperature and humidity play an important role then parameters such as floor temperature, temperature gradient, relative humidity, floor air pressure need be specified.

In the input file another important step is the setting of the **time-step** for initialisation and also the number of iterations to be performed by the elliptic solver. Furthermore, the selection or not of a local time stepping and the **turbulence model** to be used is made. The turbulence models implemented in the model are either one-equation or two-equation turbulence closure models or finally non-linear turbulence closure models (Ehrhard, 1999).

Finally, the number of desired iteration steps and the step at which the output files containing the results should be created are specified. Furthermore, the format of the output file is chosen.

Main run

In the mimo.f90 routine the main program is written, and the calculations are organised in the following manner:

Pre-process: This is the first stage of the calculations where the model reads the selected grid, the selected input parameters, performs inflow profile initialisation by means of interpolating.

First part of main run, turbulent exchange coefficients are calculated and also the time step is determined.

Second part of main run, change of velocity components and pressure force calculations.

Third part of main run, change of scalar quantities.

Post-process, computation of residuals.

Output to printer and file.

An increase to the number of cells (which could mean literally decreasing their dimensions so that they are able to describe small-scale phenomena) implies an increase of the computational power and of the degree of analysis of the required input data. Today there have developed enough types of gridded models, which are different from each other depending on their physical and chemical workings that they include, and the way they deal with these workings concerning the approaches done and the arithmetic procedures to solve the equations of diffusion.

Grid models as they have developed up to now have the ability to compute the concentrations of pollutants in the microscale. Thus, phenomena such as the destruction of ozone from NO nearby highways or hot spots very close to the emission sources are covered by an average value within the cell. This problem is related both with the demands in computing power and with the available data to be used as boundary values.

4 Two dimensional calculations employing MIMO

4.1 Two-dimensional calculations

The work performed so far aims at supporting the assumptions made earlier and it is of twofold character. Firstly the validity of the microscale model MIMO is checked against experimental data from a wind tunnel experiment consummated at the Meteorological Institute of Hamburg (Rafailidis and Schatzmann, 1995 and Rafailidis, 1997). Secondly certain sensitivity analyses are performed in order to ascertain the effect of altering important features of street canyon geometry, on the wind field and pollutant dispersion characteristics within urban areas. The results are expected to reveal how significant the alterations of the street canyon geometry are to the dispersion of pollutants, using as a reference the wind tunnel experimental data.

Thus, the intention of the author is to divide the two-dimensional calculations completed, into two parts. The first part being the validation of the model and the second part, the analysis of the influence of street canyon geometry to the dispersion of pollutants.

4.1.1 Description of wind tunnel experiment

The experiment consisted of a detailed wind-tunnel study, by Rafailidis and Schatzmann (1995), and Rafailidis (1997)[1], of the three-dimensional time-averaged velocity and turbulence characteristics above a model city, under neutral stratification conditions. It also aimed at providing a simulation of toxic emissions from vehicle exhausts in a street canyon within an urban environment. In particular, an investigation was made on the effect of different street widths and different shapes of the roofs of nearby buildings on measured concentrations.

The wind tunnel test section was 1.5m wide, 1m high, and 4m long. The experimental domain for the tests is two-dimensional, extending from one side of the tunnel to the opposite, and consisting of many parallel streets enclosed by pairs of blocks simulating buildings at a 1:500 geometric scale. Between two of the buildings, in a street canyon of breadth B a steady line source S is placed, also extending across the

---

[1] http://www.mi.uni-hamburg.de/technische_meteorologie/windtunnel/street02/overview.html

tunnel. The wind is orthogonal to the direction of the street, and there are buildings of square cross-section, with both height and side H, at regular intervals both upstream and downstream of the street containing the source. To simulate an urban roughness 20 upstream and 7 downstream- from the measurement area -street canyons were included. Tests were performed with B/H = 1 and with B/H = 1/2. A side view of the wind tunnel showing equally spaced buildings (in this case with flat roofs) simulating an urban environment is shown in Figure 4.1.The wind direction is indicated by the arrow.

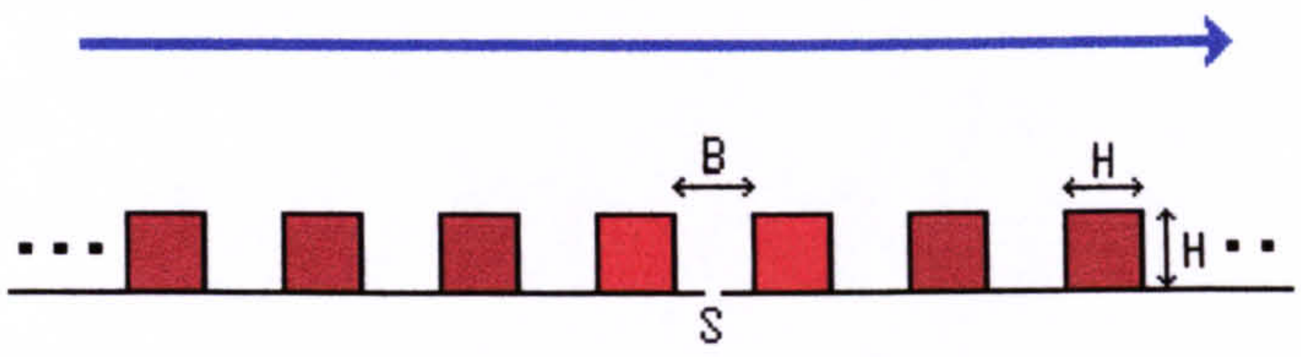

Figure 4.1. Illustration of the two-dimensional experimental set up.

The flow measurements were made with either a two-dimensional laser Doppler anemometer (LDA) or a hot film anemometer system above the middle of the roof of the building taken as the inlet. The concentrations were measured in the symmetry plane of the set-up at the positions shown in Figure 4.2, using a Laser light sheet visualisation method with different combinations of roofs neighbouring the street containing the source. The measurements were thus taken on several points on the roof of the upwind building (**up-roof**), the upwind (**up-wall**) and downwind building walls (**down-wall**) of the street canyon and on the roof of the downwind building (**down-roof**). No measurements were taken on the floor where the source was placed and in fact the ones taken on the up-wall and down-wall locations were 15 mm or more above the floor. A more detailed description of the wind tunnel experiments and the physical model is given in Rafailidis, 1997.

According to Leitl and Meroney, 1997, a significant lateral flow structure was detected and measured in the street canyon, where the flow was expected to be quasi two-dimensional. Since the secondary flow structure obviously causes a concentration gradient in the lateral direction, it was also expected to affect the concentration measurements in the symmetry plane. Extensive flow visualisation experiments using a Laser light sheet visualisation set-up and Laser-Doppler-Velocimeter measurements were performed in order to locate the source, but a final statement about what was

causing the 3D flow structure and how to minimise the influence of lateral flow within the street canyon could not be made. Furthermore, it was difficult to predict the magnitude of the influence of the second order flow on mean concentrations measured in the centre plane of the street canyon.

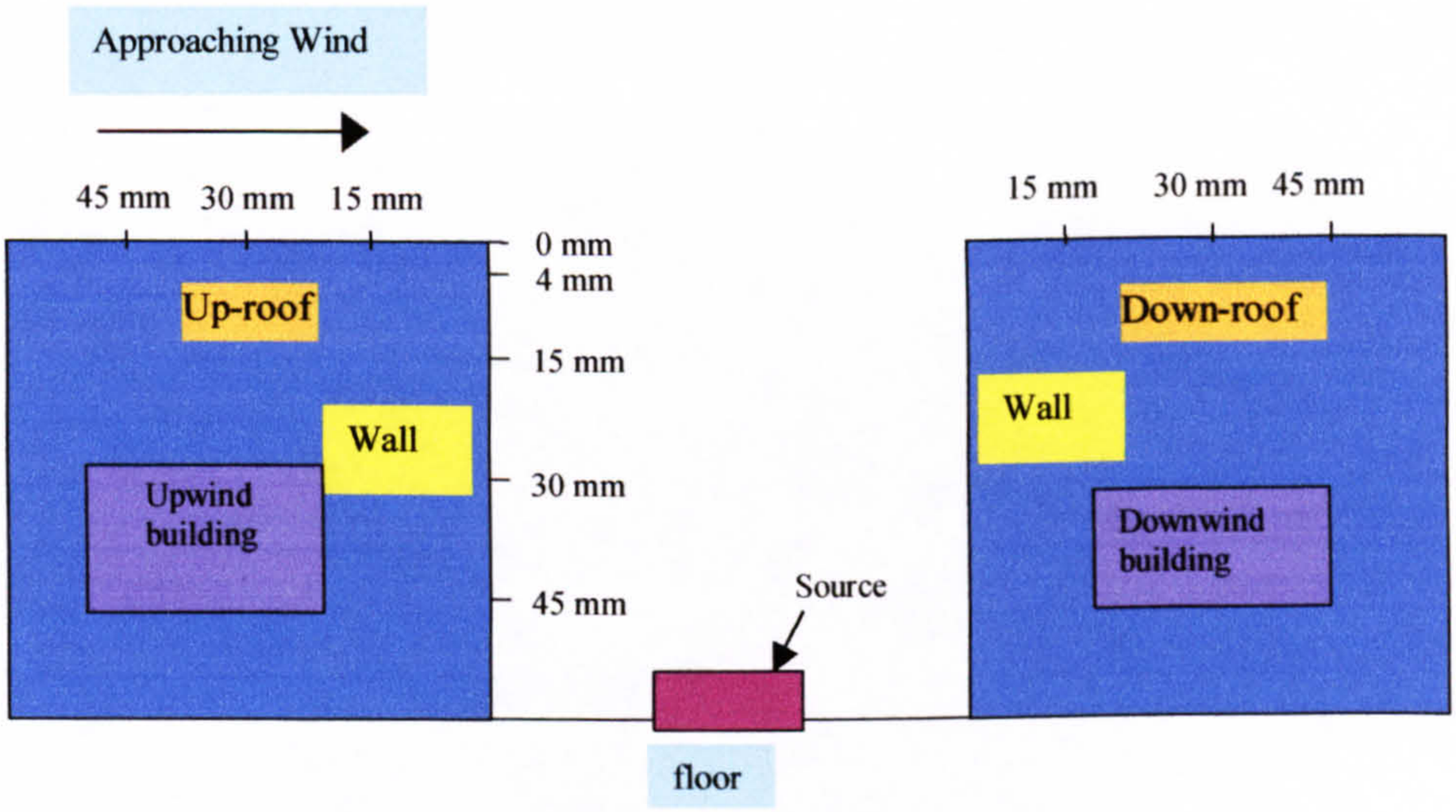

Figure 4.2.The non-dimensional concentrations of the tracer gas emitted were measured at the positions indicated.

The experimental details were:

- Wind tunnel test section height = 1m approximately.
- Wind velocity U = 5m/s (measured in the free stream 0.50m above the tunnel floor).
- Line source length = 0.9 m (across the flow)
- Height of building H = 0.06m characteristic length scale of the experiment

The Reynolds number, which corresponds to this experimental set-up, is 30.000, which means that the flow field and concentration patterns are independent of the wind velocity. The length scale of the experiment is defined by H and by the velocity scale U, which are used for the Reynolds number calculation. The relevant dimensionless groups are therefore B or W/H and Q/(LHU). Linearity of turbulent passive dispersion and dimensional considerations imply that the measured concentration at any position x relative to the source will be of the form:

$$C(x) = [q/(HU)] \,.\, Ki(x/H, B/H, h_0/H, u_0/U)$$

for some functions K_i, where the values i=1,2,3... enumerate the different combinations of upstream and downstream roof geometries studied. If the dilution mechanism is dominated by the turbulence in the ambient wind tunnel flow then, except very close to the source, the last two dimensionless arguments (which are both small), will not be important. In this case we expect essentially

$$C(x) = [Q/(LHU)] \cdot K_i(x/H, B/H)$$

The presented form, CUHL/Q (=CUH/q), of the concentration therefore represents a scale independent number for any given street geometry B or W/H, roof geometry i, and position x expressed as a multiple of the building size.

It must be noted here that wind tunnel experimental data are a good source of data results for validation of microscale models. Firstly, because different complexity cases may be simulated (from a single street canyon to a more complex urban area) and secondly because the boundary conditions set may be kept constant for a long time, thus making it possible to simulate steady-state dispersion.

4.1.2 Computational domain

The flow in the street canyon was assumed to be two-dimensional. MIMO is a 3-D model but for this case it was stripped down to 2-D, by having 4 cells on the lateral direction. The set-up of the computational domain is very important since the more refined the grid the better accuracy one may achieve. On the other hand this may result in exhaustion of computational capabilities and more time will be required before convergence. Several grids with different cell sizes were tested as well as different laws of the wall before choosing the one which required less time and memory, but which also gave quite accurate results.

It is common practice amongst modellers to commence by constructing the geometrical configuration with the smallest aspect ratio (i.e., B/H=1/2, where B=street width and H=building height) configuration. It is well known that an aspect ratio of 0.5, will give rise to a more complex field than an aspect ratio of 1. Consequently, for the construction of the computational domain for a wider street canyon, the grid independence approach was adopted.

The minimum cell size was kept constant, while the buildings were moved in order to achieve the desired aspect ratio. For the deep canyon case (B/H=0.5) equal sized cells were made with dimensions 3mm x 2mm x 2mm, thus embodying 10 cells in the horizontal direction and 30 in the vertical (inside the canyon). The physical domain was 450 mm x 480 mm x 8 mm for the 0.5 aspect ratio and 600 mm x 480 mm x 8 mm for the aspect ratio of 1. It should be noted here that several domains with different cell sizes were tested in order to find the one, which was both economical and gave accurate results, and by altering it further the results remained almost the same.

Thence, and in order to test how different canyon geometries may alter the flow field and the dispersion characteristics the buildings would be moved while keeping the cell size the same. The computational domain embodies five street canyons and six buildings. The width of the buildings is equal to the building height for all buildings except the inlet and outlet ones which are half the original width. The inlet boundary (left side) was defined at the middle of the third upstream building where the wind profile was measured during wind tunnel experiments. In figures 4.3 and 4.4, plan views of the computational domain constructed for the square and deep canyon cases are illustrated.

4.1.3 Inflow profiles and boundary conditions

The initial wind field was calculated from velocity and turbulence intensity profiles that were measured along vertical lines over the roof of the inlet building. The boundary conditions set were the following:

Inlet boundary: At the inlet boundary, the profiles of the horizontal velocity u, the turbulent kinetic energy k and its rate of dissipation ε are specified, such as to match the corresponding experimental conditions, while zero values are assigned to the vertical wind velocity w and the concentration C. Dirichlet conditions apply here.

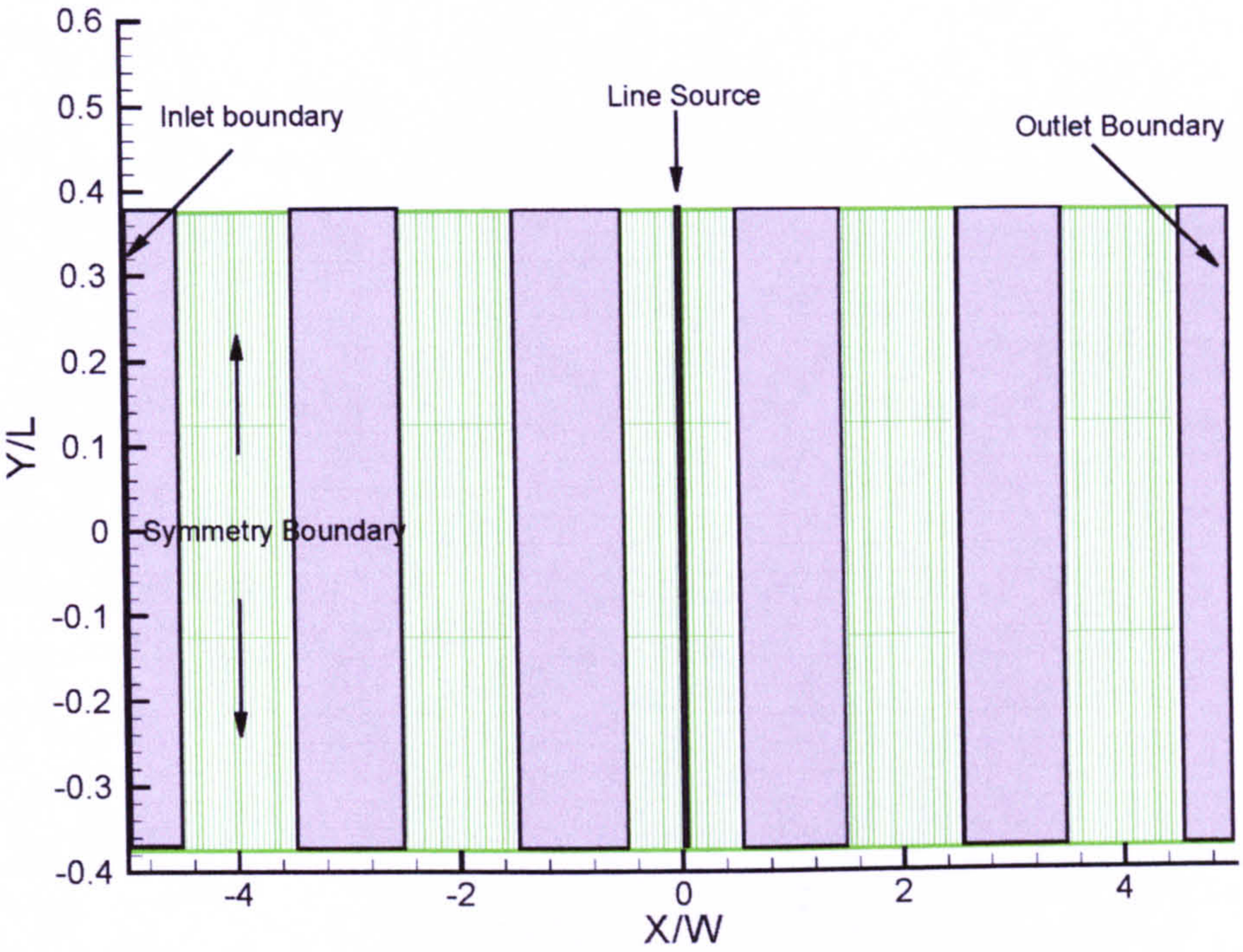

Figure 4.3. Plan view of the two-dimensional computational domain of the square canyon case

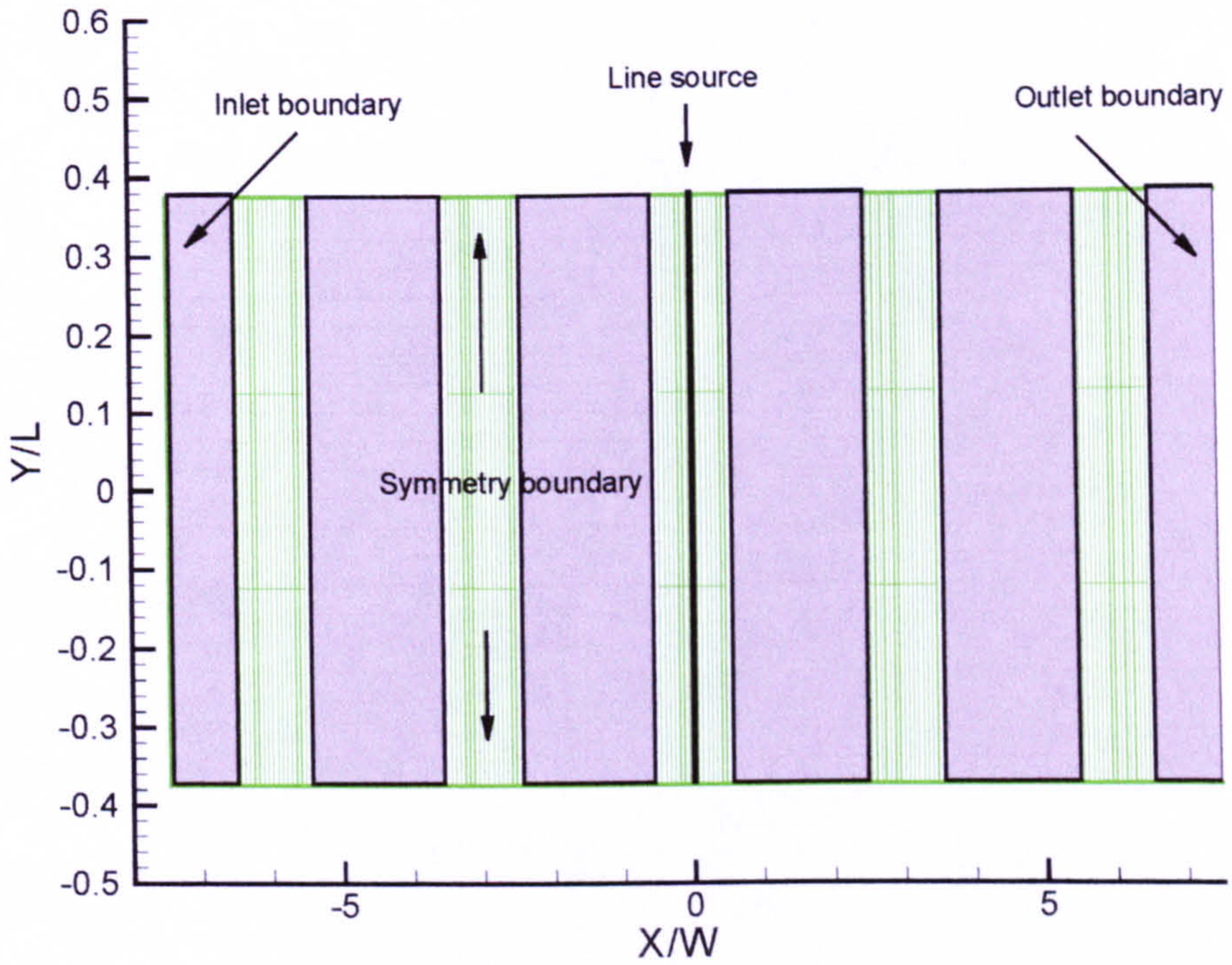

Figure 4.4. Plan view of the two-dimensional computational domain of the deep canyon case.

The inlet values of turbulent kinetic energy k and the rate of its dissipation ε, were calculated from the measured horizontal velocity profiles (LDA U) and turbulent intensities T_uU [%] as follows:

$$k_2 = ((\frac{T_uU}{100}) \times LDA(U))^2 + ((\frac{T_uW}{100}) \times LDA(U))^2 / 2 \qquad (4.1)$$

Thus, the measured turbulent intensity is divided by 100 and then it is multiplied by the local U both in the X and Z directions. Consequently the rate of dissipation is calculated by:

$$\varepsilon = \frac{u^{*3}}{\kappa y} \qquad (4.2)$$

Where:

- $U^* = C_\mu{}^{1/4} * k^{1/2}$ (the friction velocity), and C_μ is a dimensionless constant equal to 0.09 and k (turbulent kinetic energy) is at position z = 80 mm i.e., the first measurement taken above the building.
- y is the vertical distance from the roof of the buildings where measurements are taken, thus the first measurement is taken at 20 mm away from the roof of the building.
- κ is the von Karman constant equal to 0.4.

The input profiles of velocity, turbulent kinetic energy and its dissipation used for the numerical simulation are shown in figures 4.5a, 4.5b and 4.5c respectively.

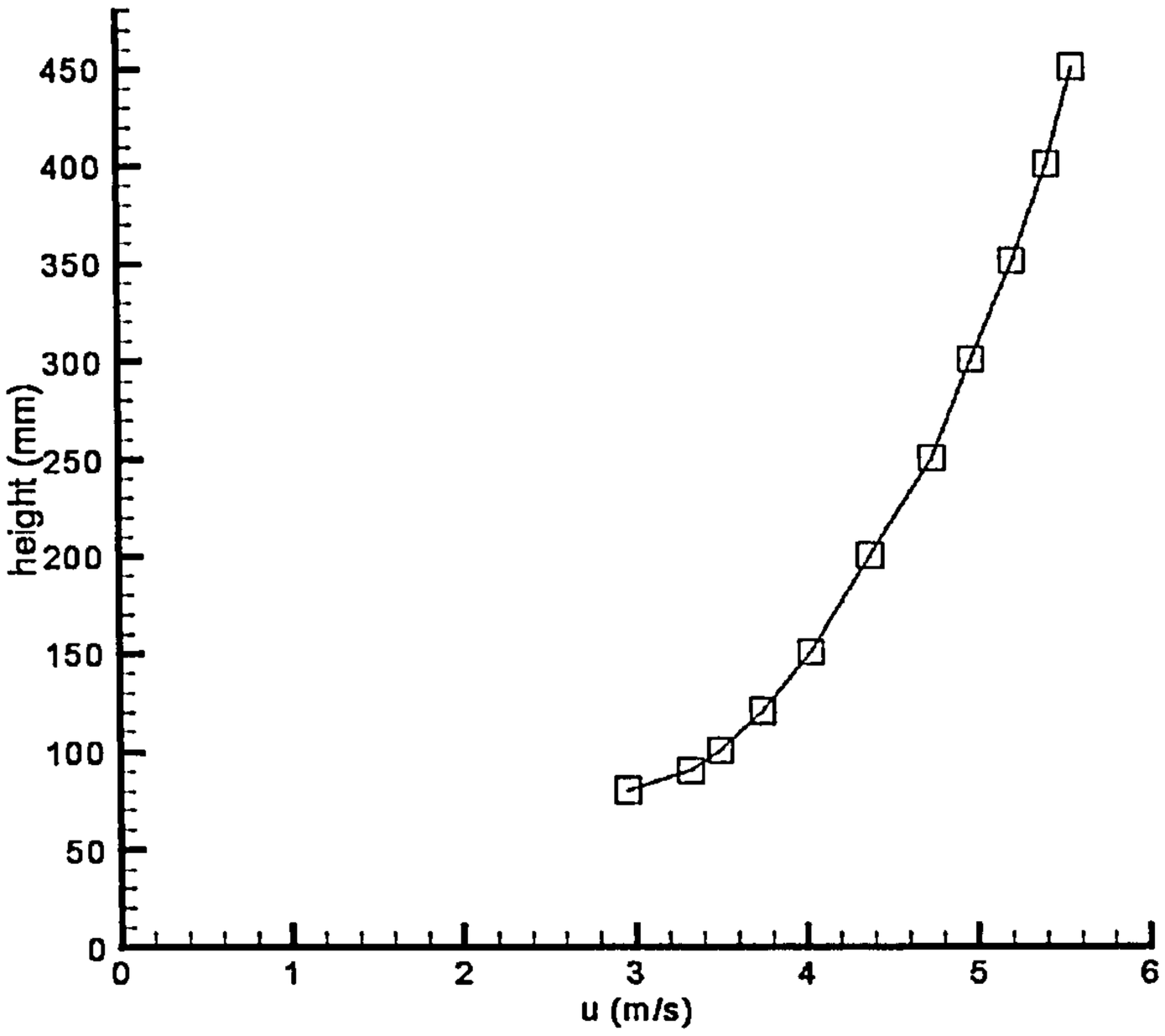

Figure 4.5a. Inlet profile of velocity.

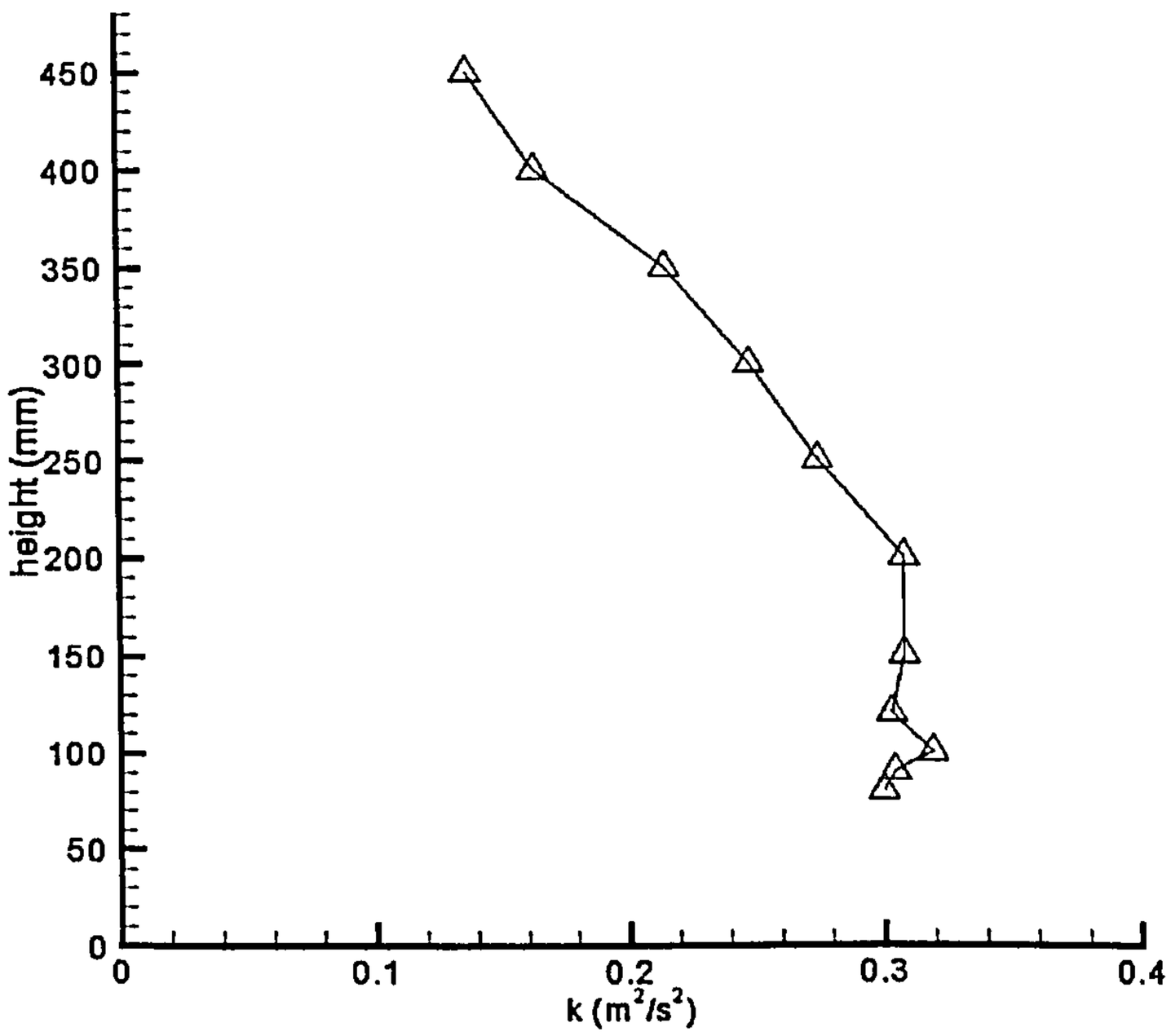

Figure 4.5b. Inlet profile of turbulent kinetic energy.

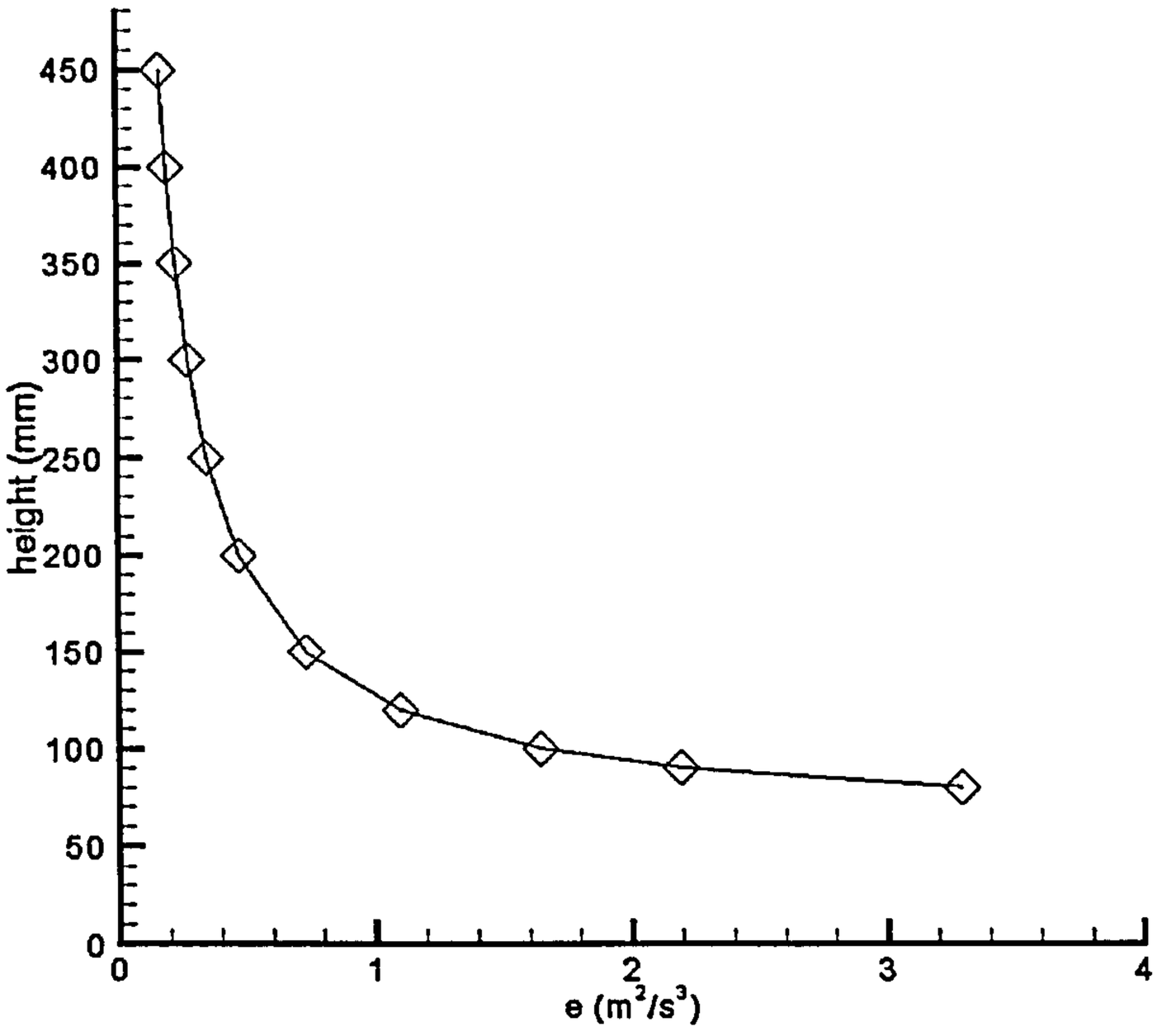

Figure 4.5c. Inlet profile of the rate of dissipation of t.k.e.

Since the wind tunnel results of concentration measurements were provided in a non-dimensional form all calculated concentrations, C were normalised as: K=CULH/Q, where C [vol/vol] denotes the tracer concentration, U [m/s] is the free stream velocity, H [m] is the building height, L [m] is the length of the line source and Q [vol/s] the source strength.

Outlet boundary: At the outlet boundary, the gradients with respect to the streamwise direction are set to zero. Neumann boundary conditions apply here.

Symmetry boundary: At the free-stream horizontal boundary, placed at a distance of 7 H over the flat building roofs, symmetry boundary conditions are applied. Thus zero vertical velocity conditions apply as well as zero gradients for all the other variables.

Wall boundary: Launder and Spalding (Standard law of the wall)

At high Reynolds number the standard k-e model (Launder and Spalding, 1974) avoids the need to integrate the model equations right through to the wall by making use of the universal behaviour of near wall flows. If y is the co-ordinate direction normal to a solid wall, the mean velocity at a point y with $30<y^+<500$ satisfies the log-law.

Within MIMO it is implemented explicitly. In spite of its advantages the assumption that the logarithmic law holds for the whole of the turbulent boundary layer is wrong.

Using these assumptions and the eddy viscosity formula ($\mu_t=\rho C_\mu k^2/\varepsilon$), it is possible to develop the following wall functions to be used as boundary conditions for the velocity, the turbulent kinetic energy and its rate of dissipation respectively:

$$u^+ = \frac{1}{\kappa}\ln(Ey^+) \tag{4.3}$$

$$k = \frac{u_\tau^2}{\sqrt{C_\mu}} \tag{4.4}$$

$$\varepsilon = \frac{u_\tau^3}{\kappa y} \tag{4.5}$$

4.1.4 Comparison of computed concentrations against measured

The cases studied at this stage were the following:

- B/H = 1, with flat roofed buildings
- B/H = ½, with flat roofed buildings

The flow fields obtained for both the square and deep canyons are presented in figures 4.6a and 4.6b respectively. From these figures, one can observe the single main vortex established in the square canyon, which results in a wind direction close to the source, from the down-wall to the up-wall, thus indicating maximum concentration levels at the up-wall close to the street level. The flow field developed for the deep canyon case however, disagrees completely with previously published work. It indicates the existence of a single main vortex circulation pattern, the same as in the case of B/H=1.

The dimensionless concentrations computed by MIMO are compared to the ones measured in the wind tunnel, for the square and deep canyon cases in Figures 4.7a and 4.7b, respectively. Comparison begins from the top corner of the upwind building and ends at the end corner of the downwind building's roof. From Figure 4.7a, it may be seen that the model has underestimated the concentration levels by more than 30% for the peak value. It has however, indicated the correct location of the maximum concentration as well as followed the general trend of the distribution of pollutants within the street canyon. The model has performed worse for the deep canyon case

since it failed to indicate the location of maximum concentration, on the lower upwind rather than the lower downwind building corner, according to measurements and current literature (Figure 4.7b). Additionally, it shows a significant over estimation of the measured concentrations. As these results could not be characterised as satisfactory, a finer grid was constructed but still the quality of computed results remained poor.

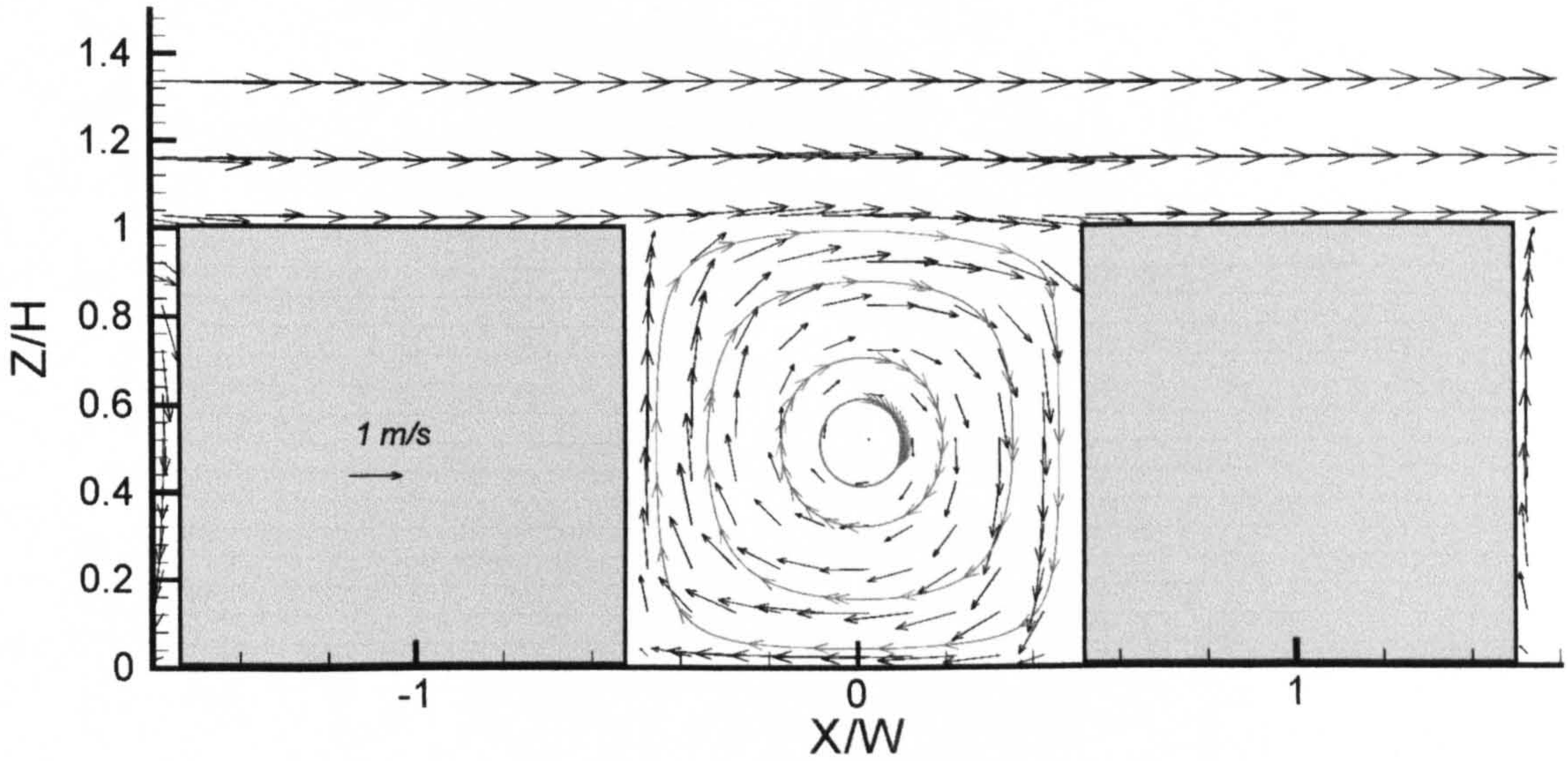

Figure 4.6a. Wind field computed by MIMO for the square canyon case.

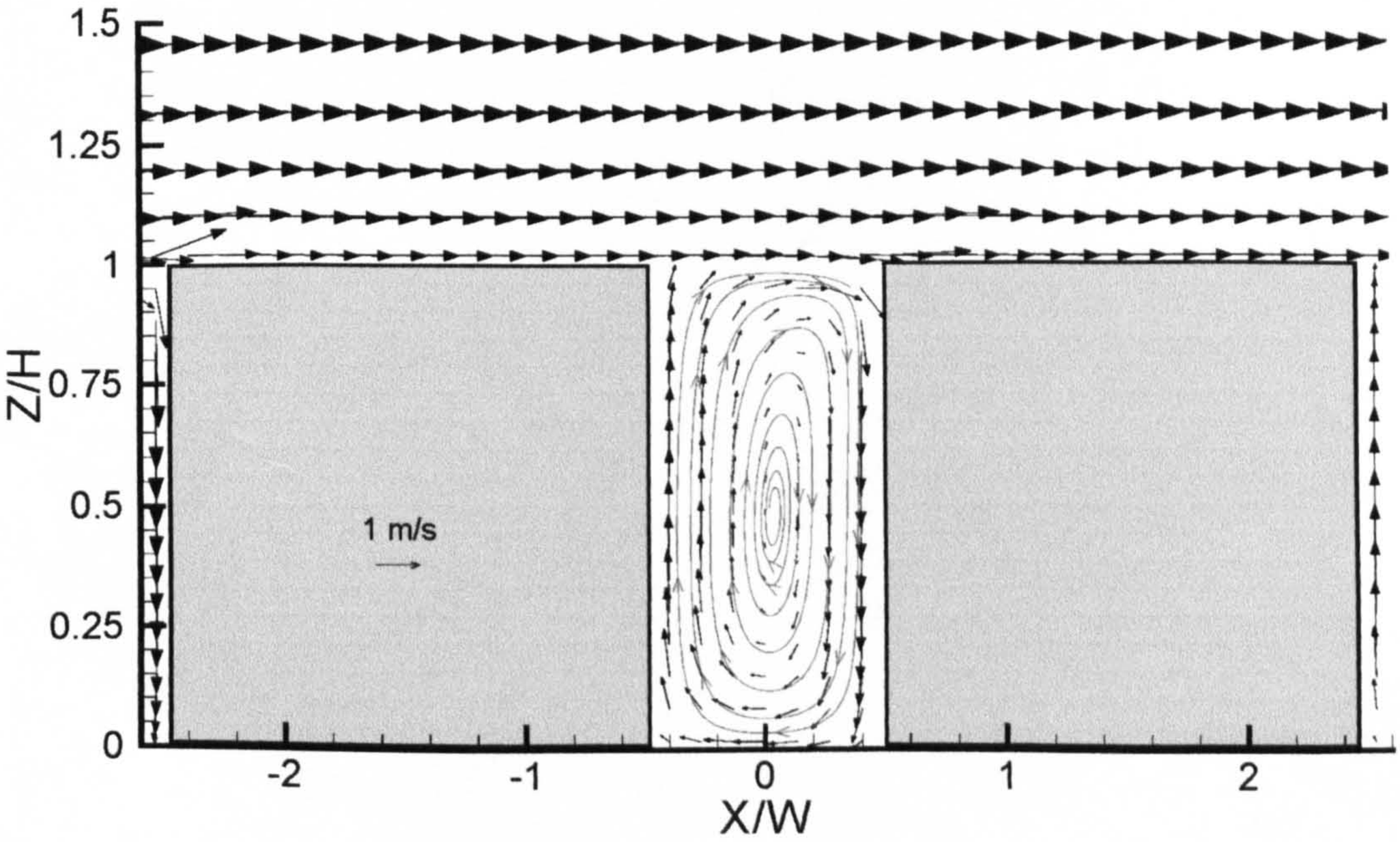

Figure 4.6b. Wind field computed by MIMO for the deep canyon case.

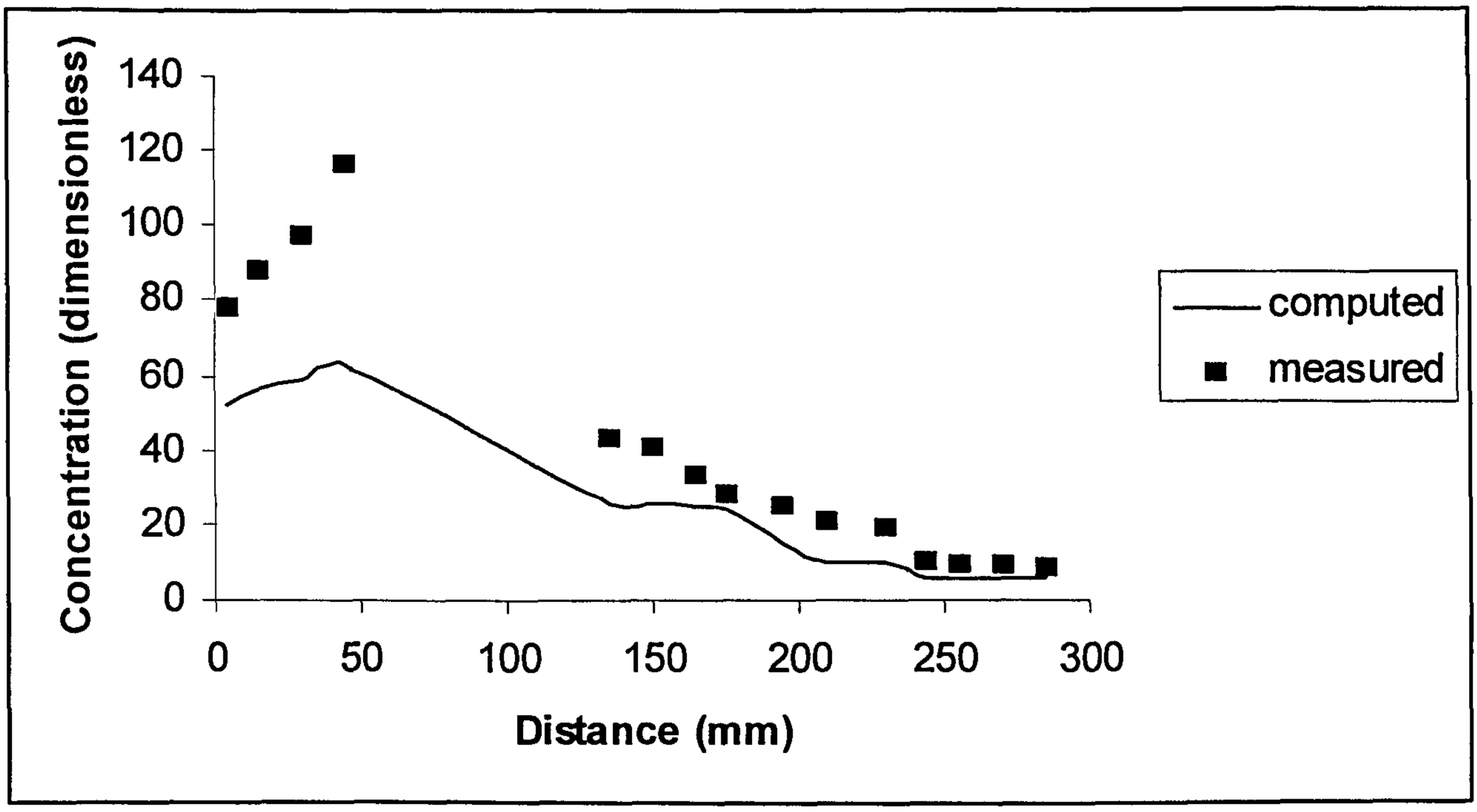

Figure 4.7a. Comparison between measured and computed dimensionless concentrations for the square canyon case.

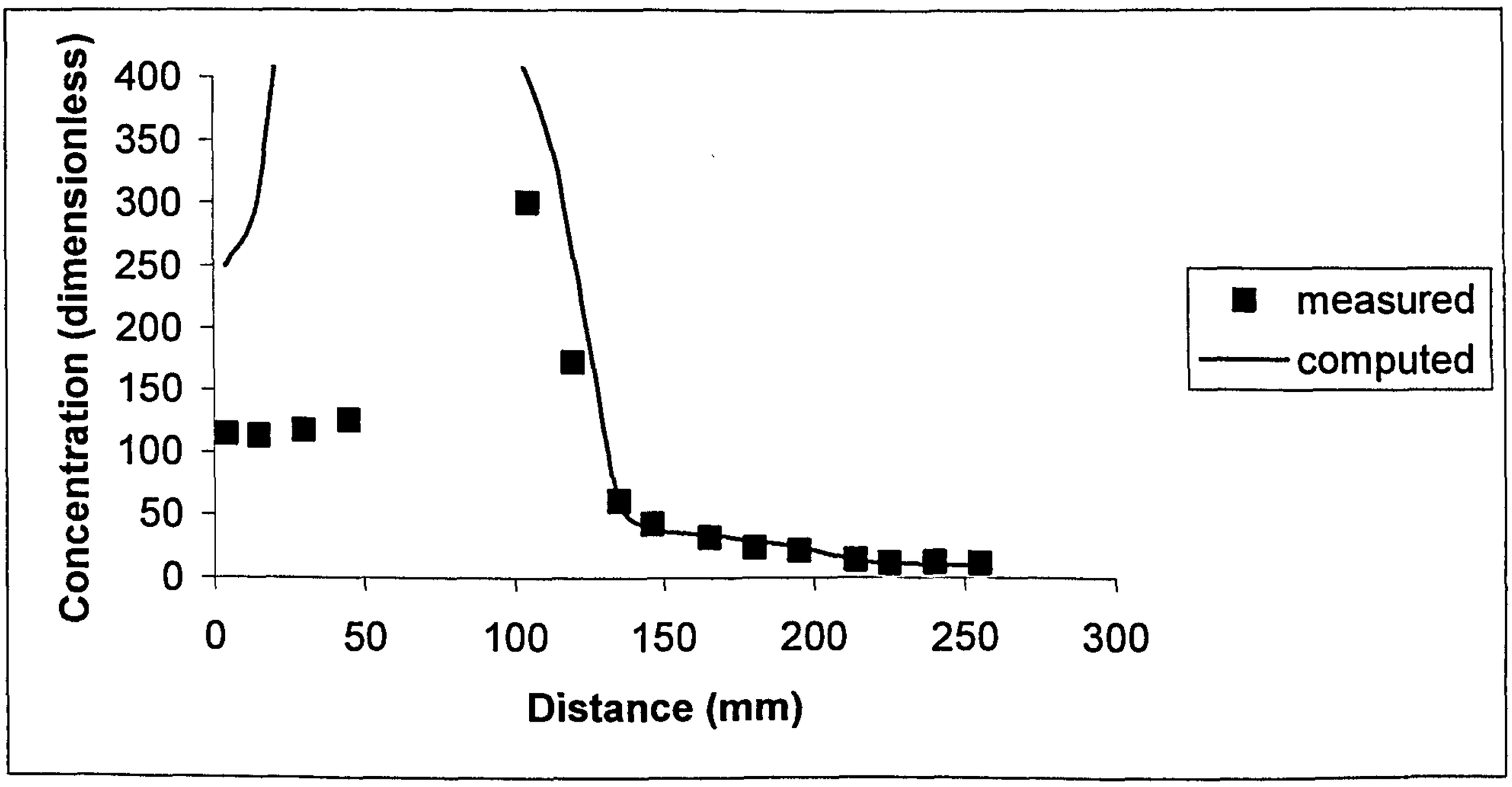

Figure 4.7b. Comparison between measured and computed dimensionless concentrations for the deep canyon case.

4.1.5 Optimisation of results

The main objective of the optimisation process was to improve the model performance over complex geometries. To achieve this objective it was thought necessary to select different wall laws suitable for this purpose. In this respect, the following two well documented cases were selected:

- The semi-empirical law of the wall proposed by Reichardt, 1951
- The revised standard law of the wall produced by Sondak and Pletcher, 1995

The following geometrical configurations were studied:

- B/H = 1 with flat roofs
- B/H = 1/2 with flat roofs

It is well understood that the wall is the most common boundary encountered in confined fluid flow such as in the present case, where the flow is confined between two buildings. In cases of turbulent flows near solid walls, the flow behavior and turbulence structures are considerably different from the ones of free turbulent flows. Dimensional analysis has shown that in turbulent thin shear layer flows, a Reynolds number based on a length scale L in the flow direction, is always very large (e.g. U = 1m/s, L = 0.1m and $\nu = 10^{-6}$ m^2/s gives $Re = 10^5$). This implies that inertia forces are overwhelmingly larger than the viscous forces at these scales. If a Reynolds number based on a distance y away from the wall is formed, such that $Re = Uy/\nu$, it then becomes obvious that if y is of the order of L then the above argument holds true. Hence, inertia forces dominate in the flow far away from the wall. As one comes closer to the wall, y decreases to zero and the same happens to the Reynolds number. Just before y reaches zero there will be a range of values of y for which the Reynolds number is of the order of 1. At this distance from the wall and closer the viscous forces will be equal in order of magnitude to the inertia forces or larger. In flows along solid boundaries there is usually a substantial region of inertia-dominated flow far away from the wall and a thin layer within which, viscous effects predominate over turbulent ones. However, the number of mesh points required to resolve all the details in a turbulent boundary layer would be prohibitively large and that is why wall functions are commonly employed in order to represent the effect of the wall boundaries.

The structure of the turbulent boundary layer, develops as follows:

a) Linear sub-layer

A fluid layer in contact with a smooth wall, where at the solid surface the fluid is stationary. Turbulent eddying motions must also stop very close to the wall. In the absence of turbulent (Reynolds) shear stress effects, the fluid closest to the wall is dominated by viscous shear. This layer is in practice extremely thin ($y^+ < 5$) and one may assume that the shear stress is approximately constant and equal to the wall shear stress τ_w throughout the layer. Thus

$$\tau(y) = \mu \frac{\partial U}{\partial y} \cong \tau_w \qquad (4.6)$$

After integration with respect to y and application of boundary condition U = 0 if y = 0, a linear relationship is obtained between the mean velocity and the distance from the wall:

$$U = \frac{\tau_w y}{\mu} \qquad (4.7)$$

After some simple algebra and making use of the definitions of u^+ and y^+:

$$y^+ = \frac{\rho u_\tau y}{\mu} \qquad (4.8)$$

$$u^+ = \frac{U}{u_\tau} \qquad (4.9)$$

This leads to:

$$u^+ = y^+ \qquad (4.10)$$

Because of the linear relationship between velocity and distance from the wall the fluid layer adjacent to the wall is often known as the linear sub-layer.

b) Log-law layer

Outside the viscous sublayer, ($30<y^+<500$), a region exists where viscous and turbulent effects are both important. The shear stress τ varies slowly with distance from the wall and within this inner region it is assumed to be constant and equal to the

wall shear stress. One further assumption regarding the turbulence length scale $l_m=\kappa y$, allows us to derive a dimensionally correct form of the functional relationship between u^+ and y^+

$$u^+ = \frac{1}{\kappa}\ln y^+ + B \qquad (4.11)$$

Numerical values for the universal constants are found from measurements, with κ the von Karman constant equal to 0.41 and B equal to 5.5 for smooth walls. Because of the logarithmic relationship between u^+ and y^+ the above formula is called the log-law and the layer the log-law layer.

c) The outer layer

This is the inertia-dominated region far away from the wall. According to experimental measurements the log-law is still valid in the region $0.02<y/\delta<0.2$, where δ is the turbulent boundary layer thickness. For larger values of y the velocity defect law provides the correct form:

$$\frac{U_{max}-U}{u_\tau} = g(\frac{y}{\delta}) \qquad (4.12)$$

The turbulent boundary layer adjacent to a solid surface is therefore, composed of two regions:

The inner region, 10% to 20% of the thickness of the wall layer, where the shear stress is almost constant and equal to the wall shear stress. Within this region there are three zones, in order of increasing distance from the wall:

- linear sub-layer: viscous stresses dominate the flow adjacent to the surface
- buffer layer: viscous and turbulent stresses are of similar magnitude
- log-law layer: turbulent (Reynolds) stresses dominate.

The outer region or law-of-the-wake layer, the inertia-dominated core flow far from wall, free from direct viscous effects.

The standard high-Reynolds-number k-ε model, such as MIMO in this case, requires modification for flow near walls to account for damping of velocity fluctuations

normal to the wall and for viscous effects. It has been suggested by Sondak and Pletcher (1995), that three common approaches are the addition of low-Reynolds-number terms, patching-in a simpler model near the wall, and using wall functions.

However, it must be noted here that in the low-Reynolds-number-model case, terms are added to the standard model, some of which typically contain exponential damping functions. These models require fine grid resolution near the walls, resulting in a relatively large total number of grid points. The equations are difficult to solve numerically due to their stiffness, and results from these models are often disappointing when compared with experimental data. Concerning patching in a simpler model at the wall, such as an algebraic model or a one-equation model has been shown to yield good results for some flow fields, but more testing is required before it may be fully assessed. A disadvantage of the patched models is that they also require fine grid spacing at the wall. Finally the use of wall functions is based on the idea that knowledge of the basic structure of turbulent boundary layers, (as described above), may be applied to flow near walls. The entire turbulent boundary layer need not be resolved, and large grid spacing may be used at the wall. Since the rate at which the grid may stretch away from the wall is limited by most numerical solution schemes, wall functions result in a large saving in the total number of grid points required. The reduced memory and CPU time required when using wall functions can be extremely important for the computation of complex three-dimensional flow fields even those involving rough walls, (Sondak and Pletcher, 1995). That is why up to now wall functions are still quite popular in CFD modeling.

One disadvantage of wall functions is that the log equation, which is fundamental to them, is not accurate for some flow fields, such as those with regions of separated flow. Even with this limitation, wall functions have been shown to yield results comparable, and often superior, to those obtained with low-Reynolds-number models, including computations of some complex flow fields.

A short description of the laws used follows:

1. Sondak and Pletcher (1995)

In reality the Sondak and Pletcher law of the wall is an improvement to the standard law of the wall derived by Launder and Spalding (1974), thus, the present method is

valid for points in the viscous sub layer as well as points in the log region. This is too implemented explicitly within MIMO.

According to Sondak and Pletcher, first the friction velocity u^* and the wall shear stress τ_w are computed as functions of the mean flow variables. Values of k and ε are then computed at the grid point adjacent to the wall and are used for the boundary conditions for the turbulence transport equations. Finally the wall shear stress is forced into the Navier-Stokes equations.

In the log region, the velocity profile is given by equation (4.8 in wall coordinates) and in the linear sub-layer by equation (4.7). Depending on whether the grid point adjacent to the wall falls in the log region or the viscous sub-layer the appropriate equation is used for calculating the velocity. This is done by neglecting the buffer region. The boundary conditions for the turbulent kinetic energy and the dissipation are given as follows:

For the log layer:

$$k = \frac{u_\tau^2}{\sqrt{C_\mu}} \tag{4.13}$$

$$\varepsilon = \frac{u_\tau^3}{\kappa y} \tag{4.14}$$

For the viscous sublayer:

$$k = \frac{u_*^2}{\sqrt{C_\mu}} \left(\frac{y^+}{y_c^+}\right)^2 \tag{4.15}$$

$$\varepsilon = \frac{k^{2/3}}{l_\varepsilon} \tag{4.16}$$

2. Reichardt

This generalised semi-empirical law of the wall was derived by Reichardt after conducting an experiment on turbulent exchange of momentum of flow in tubes and pipes. This formula for the friction velocity gives a complete representation of the

velocity distribution commencing from the viscous sublayer and extending out to the outer layer of a turbulent boundary layer. This is an implicit procedure and thus contrary to the above is considered to be time consuming. The formula for this case is given below:

$$u^* = \frac{|U|}{\frac{1}{\kappa}\ln(1+0.4y^+)+7.8(1-\exp(-\frac{y^+}{11})-\frac{y^+}{11}\exp(-0.33y^+))} \quad (4.17)$$

4.1.6 Results

As already mentioned above the following 2-dimensional street canyon configurations were studied:

- A square one (B/H = 1) with all roofs flat
- A deep one (B/H = ½) with all roofs flat

The inlet profiles used are the same as in figures 4.5a, 4.5b, 4.5c. All other boundary conditions remain the same. In Figures 4.8a and b the flow field established for the B/H = 1 and B/H = ½ cases are illustrated. In the square canyon case a single primary vortex is established. In the deep canyon case the corresponding main vortex covers approximately the top 2/3 of the street canyon total depth. On the contrary, almost stagnant conditions are established near the street level, due to the existence of a weak counter-rotating vortex. This comes in good agreement with current literature.

Figure 4.9, shows the comparison between the measured and computed non-dimensional concentrations for the square canyon case and for all three wall functions.

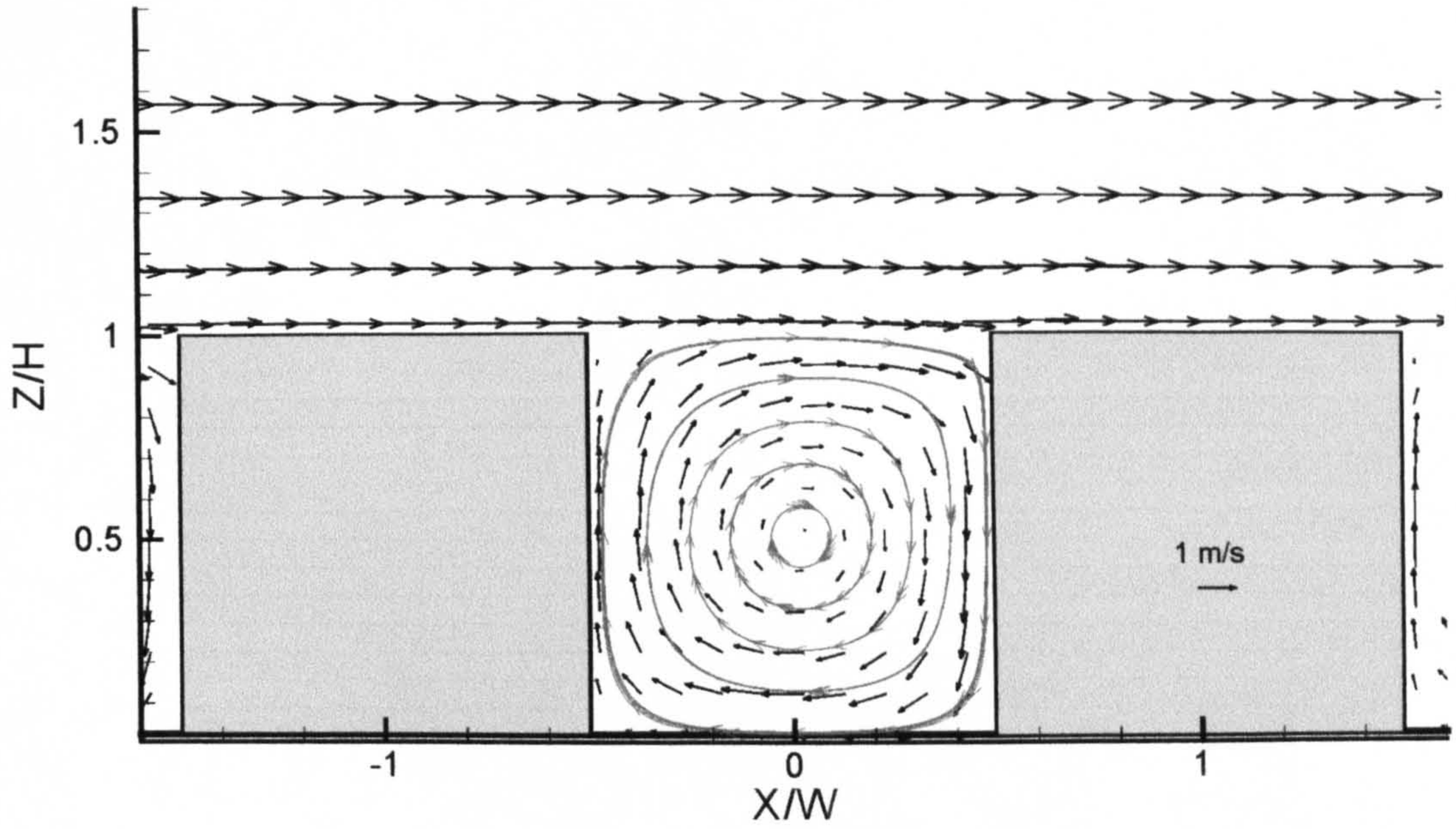

Figure 4.8a. Wind field computed by MIMO for the square canyon case.

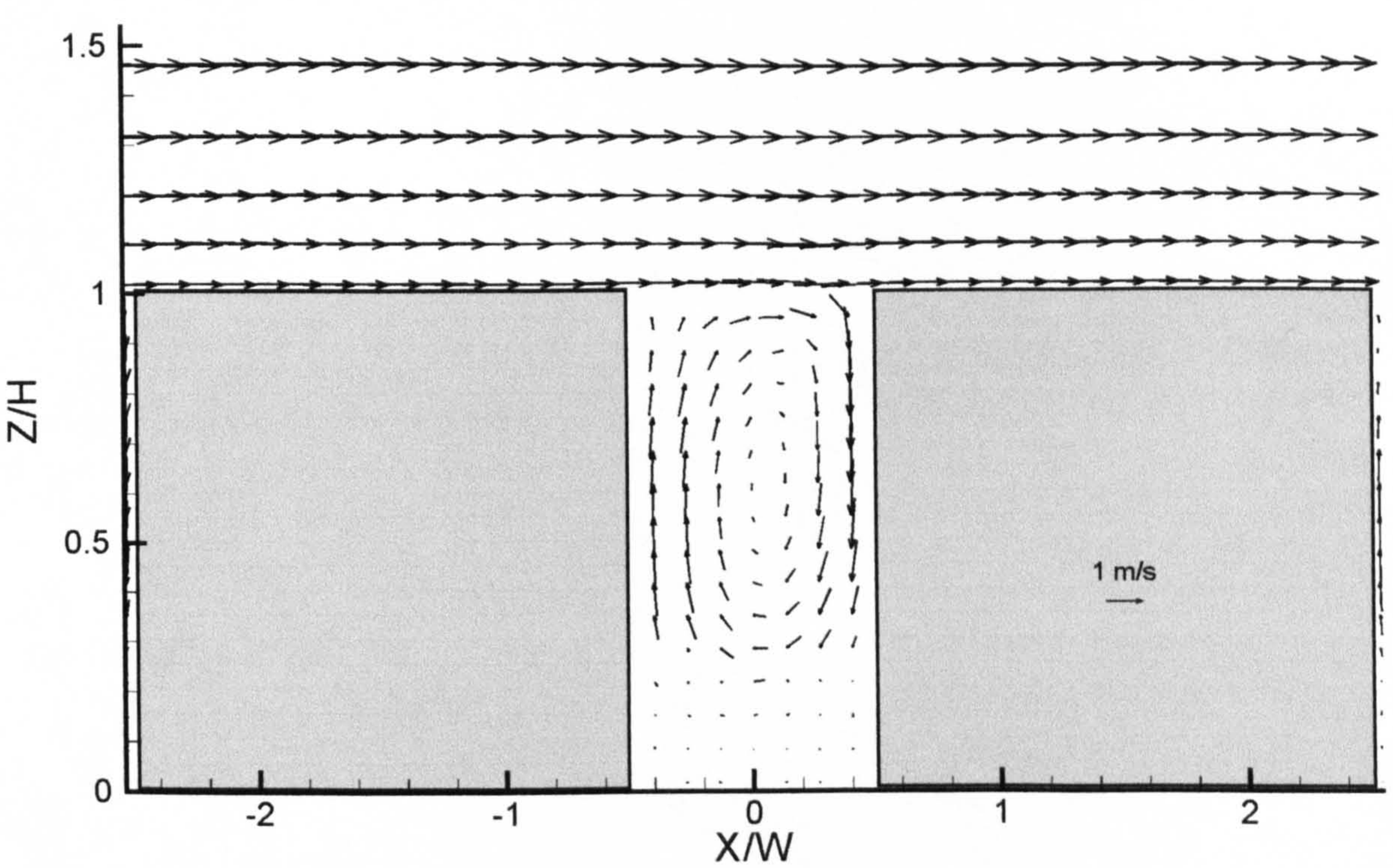

Figure 4.8b. Wind field computed by MIMO for the deep canyon case

From the results one can observe that indeed the dispersion of the pollutants is influenced quite significantly by using the three different wall functions. More specifically in all three cases the maximum concentrations appear on the up-wall

(distance 0-60mm on the graph), due to the combined action of the primary and corner vortices. However, for the Launder and Spalding case (in the graph marked as L-S) the model seems to have underestimated quite significantly, of the order of 30-40% for the up-wall, the concentration levels within the street canyon. Concerning the Sondak and Pletcher (marked as S-P in the graph) and the Reichardt (marked as R in the graph) cases the model seems to be performing better, but still the concentration levels on the up-wall are underestimated to a lesser extent (of the order of 20%).

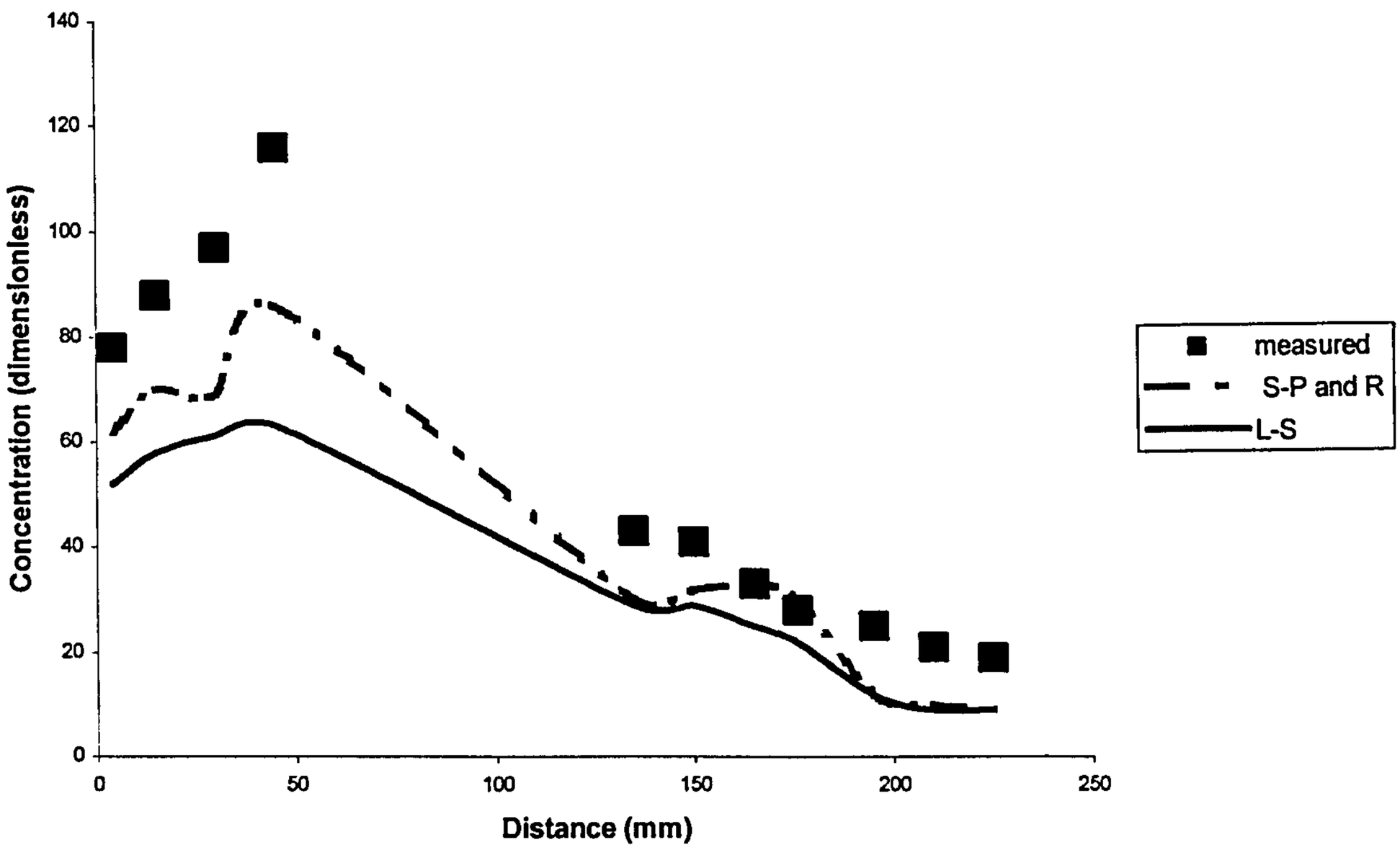

Figure 4.9.Comparison between measured and computed non-dimensional concentrations for the square street canyon cases.

Figure 4.10, shows the results from the comparison between the measured and computed non-dimensional concentrations for the deep canyon case and for all three wall functions. For the S-P case maximum concentrations appear on the down-wall (distance 120-180mm on the graph) due to the action of the weak counter-rotating vortex at the bottom the street canyon. One can observe here the overestimation of the peak concentration levels in contrast to the underestimation, which occurred for the square canyon case. However, for both configurations the agreement between the computed and measured concentrations is quite good. Calculations performed for the Reichardt wall function have given similar results to the Sondak and Pletcher case. For the L-S case the results indicate not only a great overestimation of concentrations,

but total absence of the double vortex system since the position of maximum concentrations appears on the up-wall.

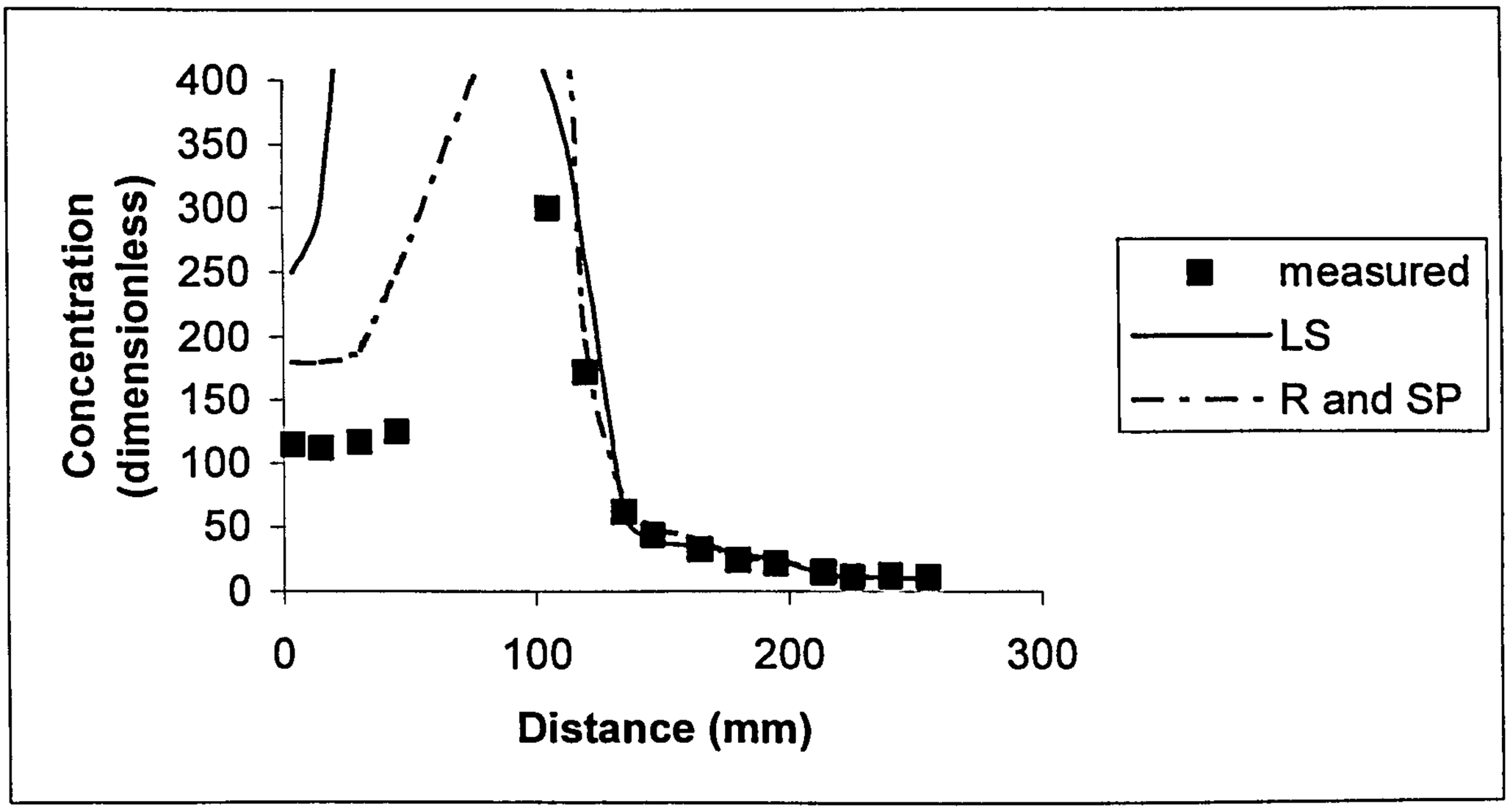

Figure 4.10.Comparison between measured and computed non-dimensional concentrations for the deep canyon case.

MIMO did perform satisfactory and the influence of using different wall functions was evident. The Sondak and Pletcher (SP), and Reichardt (R) cases produced more accurate results since according to the above they are valid for both the linear sub-layer and the log-law layer and the velocity at the first grid point from the wall is estimated more accurately. The Launder and Spalding procedure suggests that the model avoids computing the friction velocity in the linear sub-layer, which is a source of error if the first grid point falls in this layer. With this exception, the agreement between computed and measured results is quite good. Therefore, the Sondak and Pletcher wall function formulation was adopted for further calculations as the Reichardt wall function, being implicit required more computational time.

The differences observed between the computed and measured non-dimensional concentrations, could be explained as follows:

- The experiment allowed for three-dimensional effects to develop. This was not the case for the two-dimensional set-up of the algorithm, which obviously, neglected the lateral component of the flow. This omission could easily lead to

an error of 10-15%, which is in many cases reported in full scale atmospheric experiments.

- Experimental imperfections which, were pointed out by the same experimental team lead to 10-15% differences when the experiment was repeated in another laboratory (private communication with Rafailidis team).
- The profiles and the characteristics of the input flows used were purely statistical approximations of the real profiles used in the wind tunnel. This introduced errors, especially at the inlet region of the computational domain.

The MIMO performance is considered satisfactory, taking into account the very recent published results by the dedicated European Program TRAPOS model intercomparison exercise[2].

4.2 Effects of street canyon geometry to dispersion of pollutants

In this partition of the work, special attention was paid to the wind field developed and consequently to the dispersion of pollutants in relation to certain geometrical features of the street canyon. This topic is of great importance to urban planners who are interested in locating areas of high pollutant concentration and also of optimum street canyon configurations. The work presented here, involved changing the geometrical configuration of the street canyon containing the source and altering the upwind and/or downwind characteristics of the multiple-street canyon configuration with respect to the source of pollution. This procedure would provide the necessary detailed information of an **'urban cell'**, which is the basic unit of a greater **'urban background area'**, the characteristics of which are needed for a large number of applications. The selection of this approach was made on the ground, that the computational domain of an **'urban cell'** could be extended so that to bridge the gap between the **'urban cell'** and the **'urban background area'**.

As a reference case the experimental set-up and experimental results produced by Rafailidis (1997) were used as in the first partition of the work, where satisfactory

---

[2] http://www.dmu.dk/TRAPOS

performance of the model was established. Thus, the computational domain remains the same as described above. The velocity, turbulent kinetic energy and the dissipation inlet profiles used are given in figures 4.3a, 4.3b, and 4.3c respectively.

The flow field evolved and also the dispersion of the pollutants emitted at the street canyon floor are appreciated. In Europe the typical street-width to building-height aspect ratio is close to 1. Furthermore, not all street-canyons are symmetric in the sense that the street is not bounded by a continuous array of equal height buildings from both sides, but buildings vary in height and in roof shape.

The geometrical characteristics of the buildings of the street canyon containing the source were altered as follows:

- First the height of the upwind building was decreased gradually thus creating a **step-up notch** for both an aspect ratio of 1 and 0.5.

- Then the height of the downwind building was decreased gradually, thus creating a **step-down notch** for both an aspect ratio of 1 and 0.5.

- The flow field and dispersion of pollutants was studied for the street canyon containing the source, for **different aspect ratios** ranging from 3 to 0.5. In this case two lanes of traffic were used either separately or together to simulate close to reality situations of heavily trafficked roads.

In general the intention of these calculations was to investigate pollutant dispersion patterns under different geometrical configurations, under the effect of upstream or downstream situations. Also the percentage of pollutant concentration that reaches downstream street canyons was checked.

4.2.1 Step-up notch results-aspect ratio 1

A step-up notch is formed when the upwind building is shorter than the downwind building. The width of the street canyon was set at 60 mm thus the original configuration was that of a square street canyon, (aspect ratio of 1). Instead of a typical single rotating vortex for the square canyon case and a double vortex system for the deep case, an asymmetric geometrical configuration gives rise to interesting variations of the air flow. These changes affect both the distribution of concentration

of pollutants within the street canyon and also the location of peak concentrations. In Figure 4.11a, the symmetric case where both buildings are of equal size is illustrated and in Figures 4.11b-m, the wind field developed and the dispersion of pollutants for all the cases studied is illustrated. As seen from the figures the upwind building becomes gradually shorter, the main vortex, once covering the whole street canyon, is now displaced with its centre shifted towards the downwind building side of the canyon and the vortex itself stretching along an imaginary diagonal line, which connects the lower upwind building corner to the upper downwind building corner (Figures 4.11b-h). Because of the distortion and the tilt of the main vortex a secondary weaker vortex hardly depicted in the figures, emerges at the lower upwind building corner. Furthermore, in the same location a high pollutant concentration area develops, which is gradually extended from the upwind building side towards the centre of the canyon, (Figures 4.11b-g). Due to the lowering of the upwind building the flow is accelerated above the cavity and the ventilation inside the canyon is reduced following the weakening of the vortex. When the upwind building acquires a height of 30mm, the vortex from the upstream canyon has covered almost the entire up-roof, (Figure 4.11g). By further decreasing the building height, the vortex of the canyon upstream having shifted upwards and over the upwind building roof, clearly shows a tendency to merge with both the general flow and the vortex of the step-up notch, (Figures 4.11h-l). This is also associated with the formation of a return flow, over the roof of the upwind building and into the canyon upstream. Finally, when the building height reduces further to 5mm, a single extended vortex is clearly formed between the downwind building and the upwind building of the canyon upstream, coupled with a stronger downdraft on the down-wall and a further reinforcement of the return flow, which passes over the roof of the upwind building. When the upwind building is absent (Figure 4.11m) the same wind field as above is established and pollutants are dispersed towards the canyon upstream.

From the above findings it may be concluded that concerning the pollutant levels, high concentrations occur when the consecutive buildings' height ratio is almost 1/2 (Hupwind / Hdownwind). The centre of the pollution cell appears on the lower upwind building corner. Further increase of this ratio leads to a better ventilation scheme of the canyon area and reduction of pollution levels.

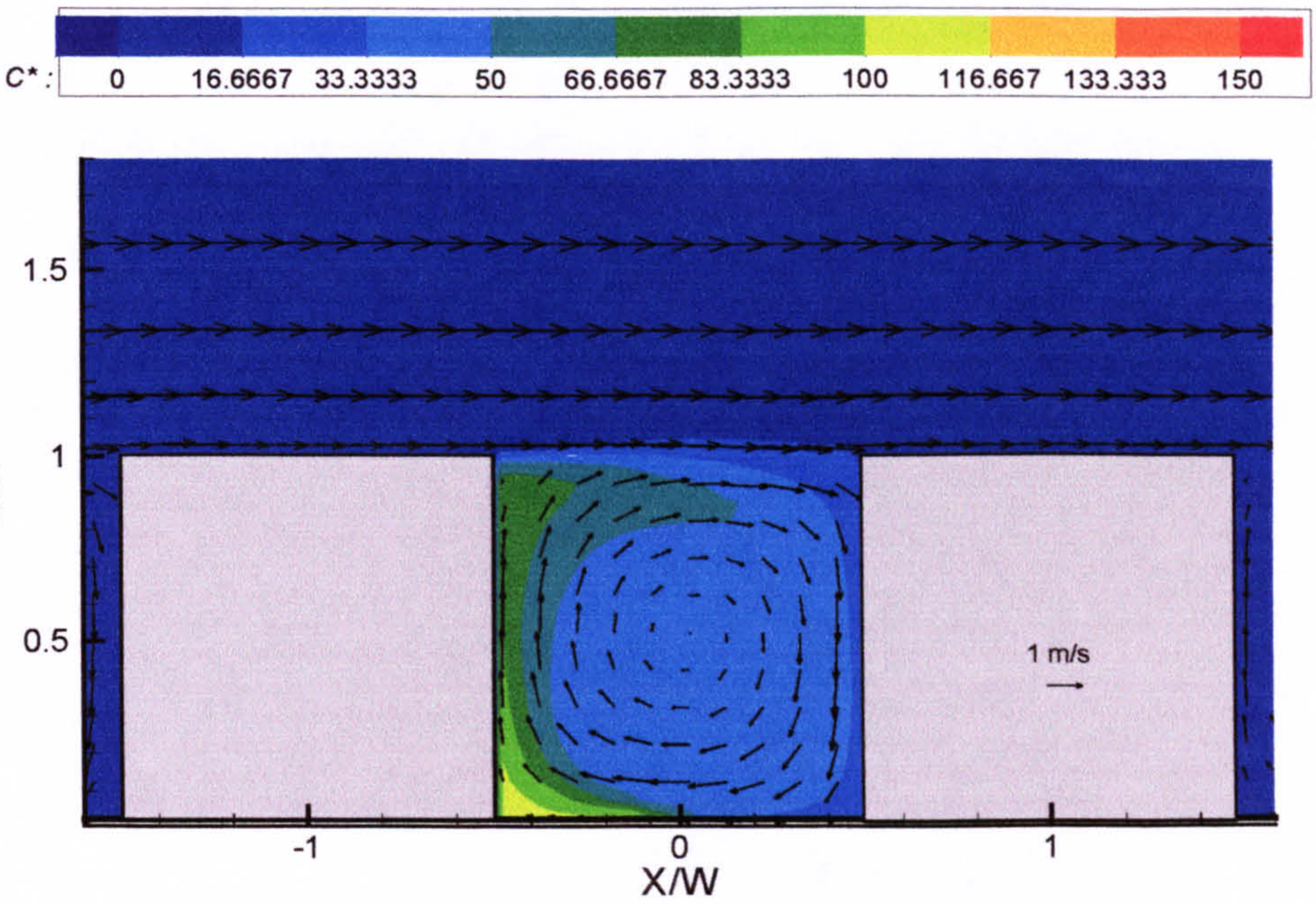

Figure 4.11a. Wind field and pollutant dispersion, as computed by MIMO for upwind building height of 0.06m.

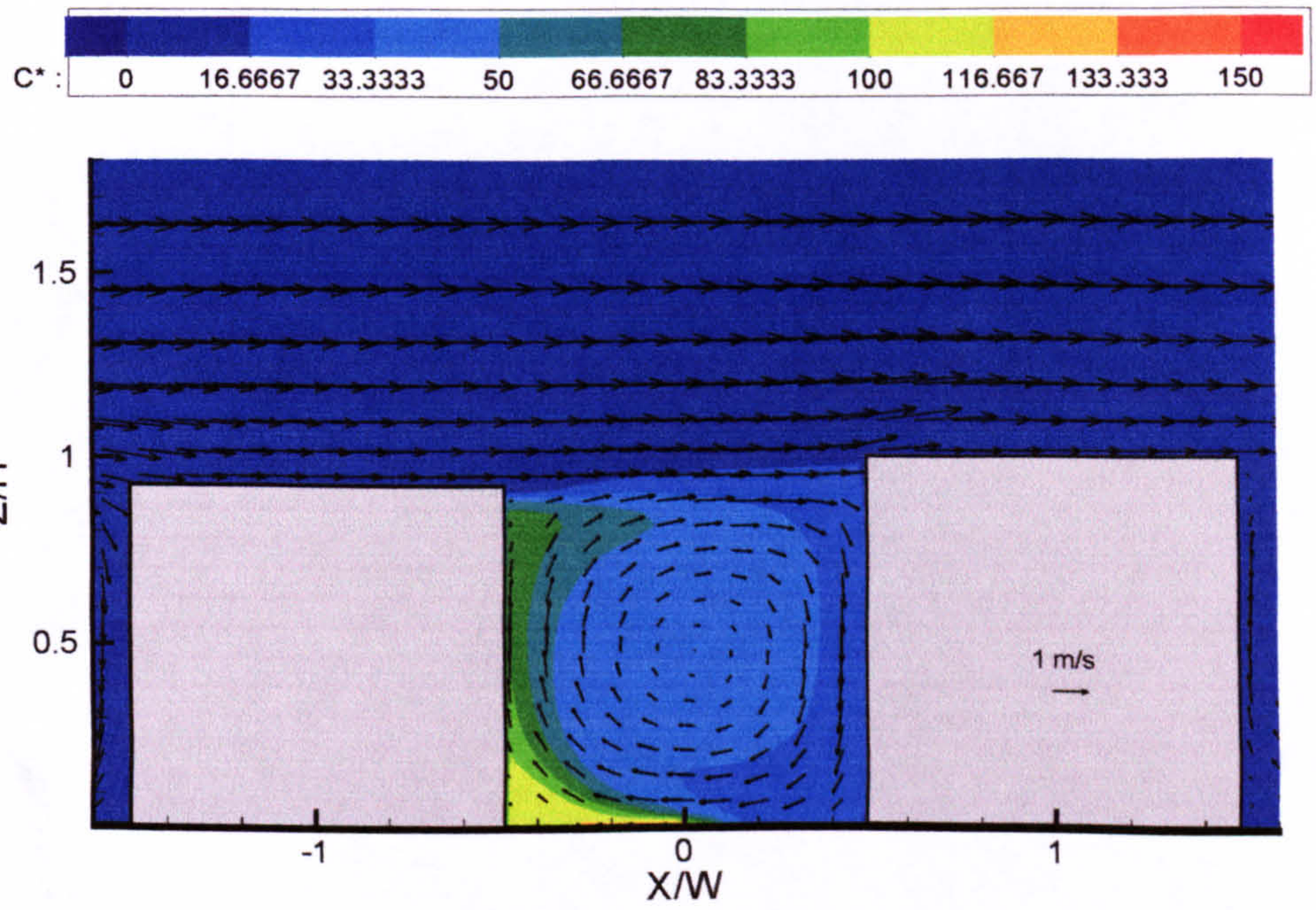

Figure 4.11b. Wind field and pollutant dispersion, as computed by MIMO for upwind building height of 0.055m.

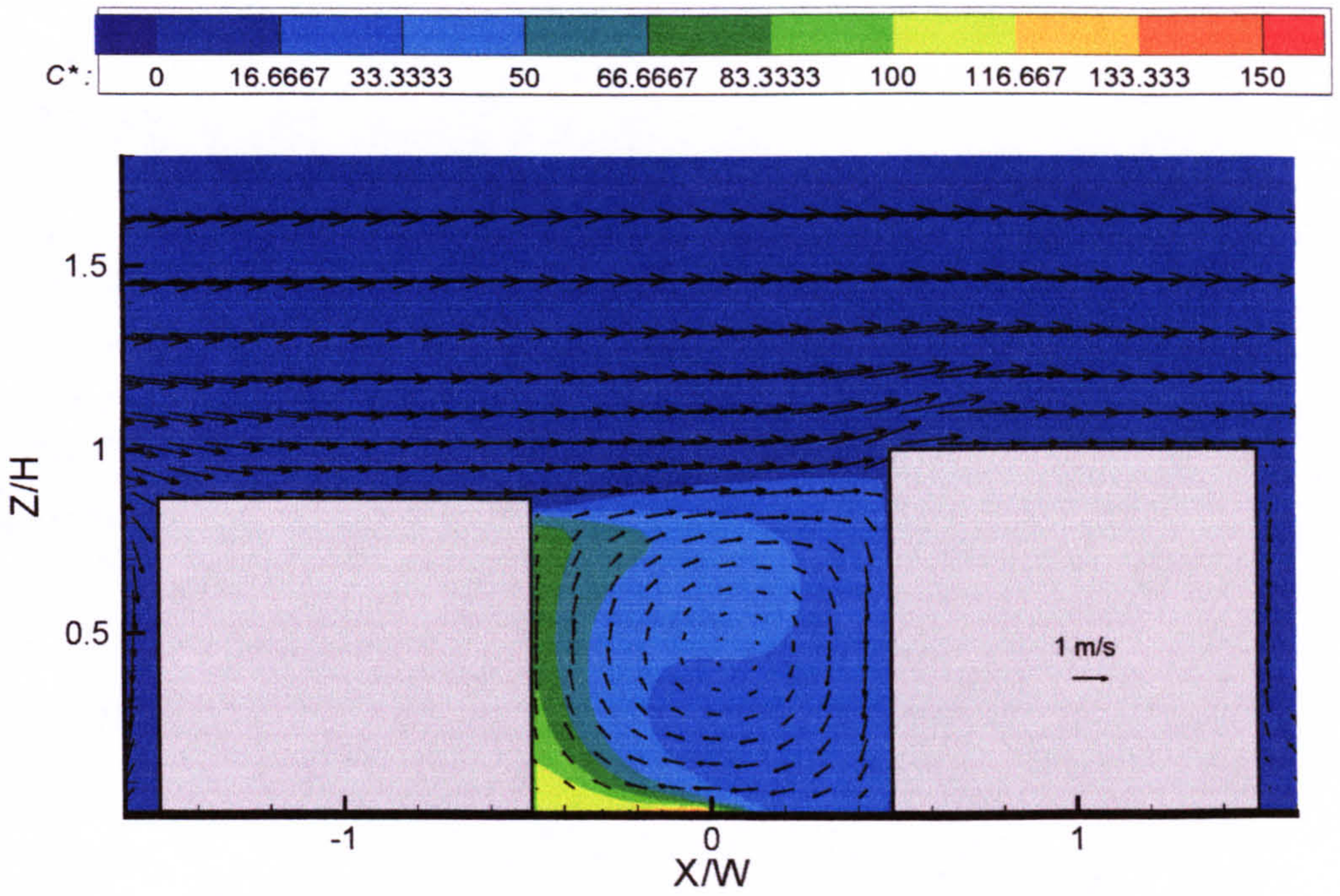

Figure 4.11c. Wind field and pollutant dispersion, as computed by MIMO for upwind building height of 0.05m.

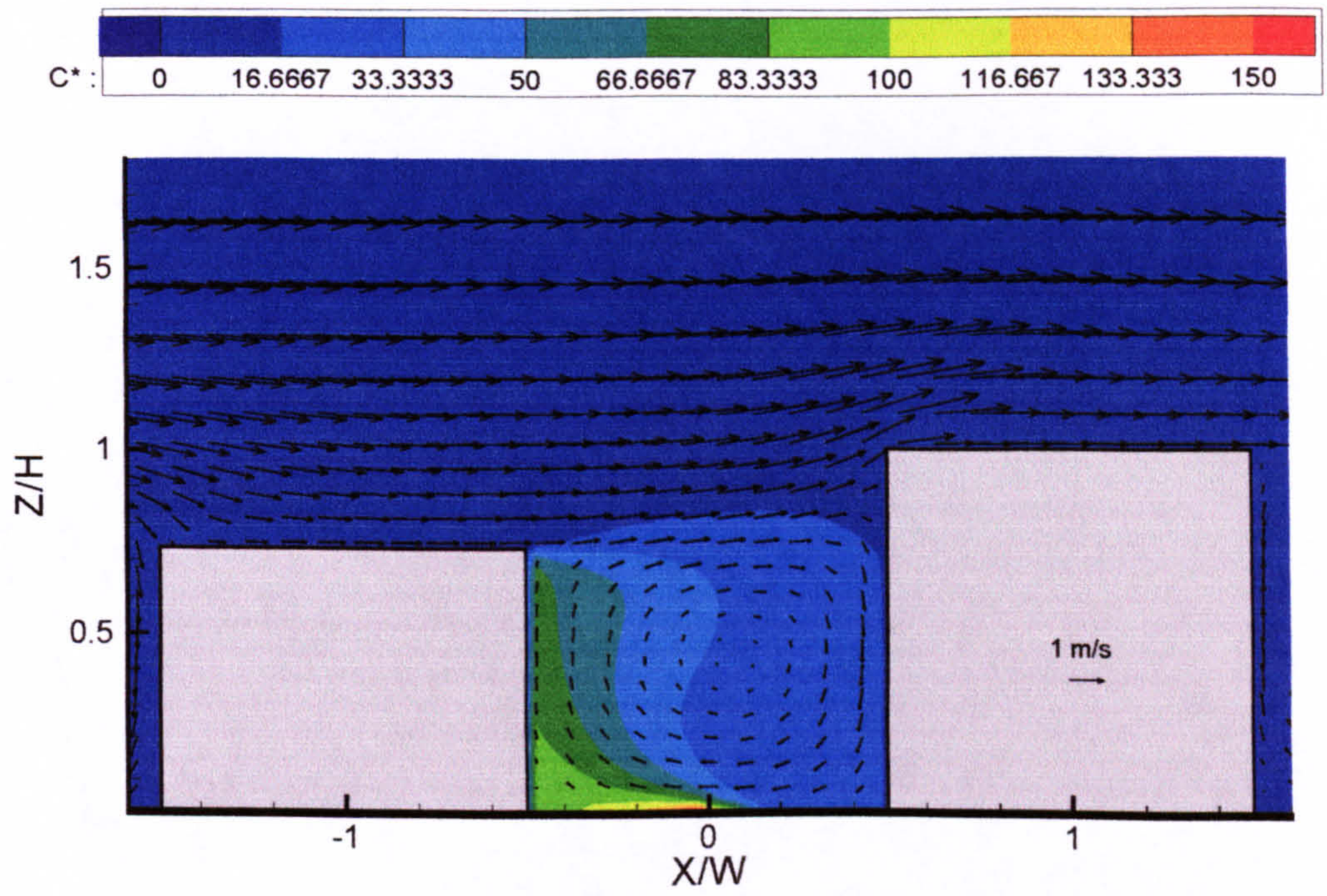

Figure 4.11d. Wind field and pollutant dispersion, as computed by MIMO for upwind building height of 0.045m.

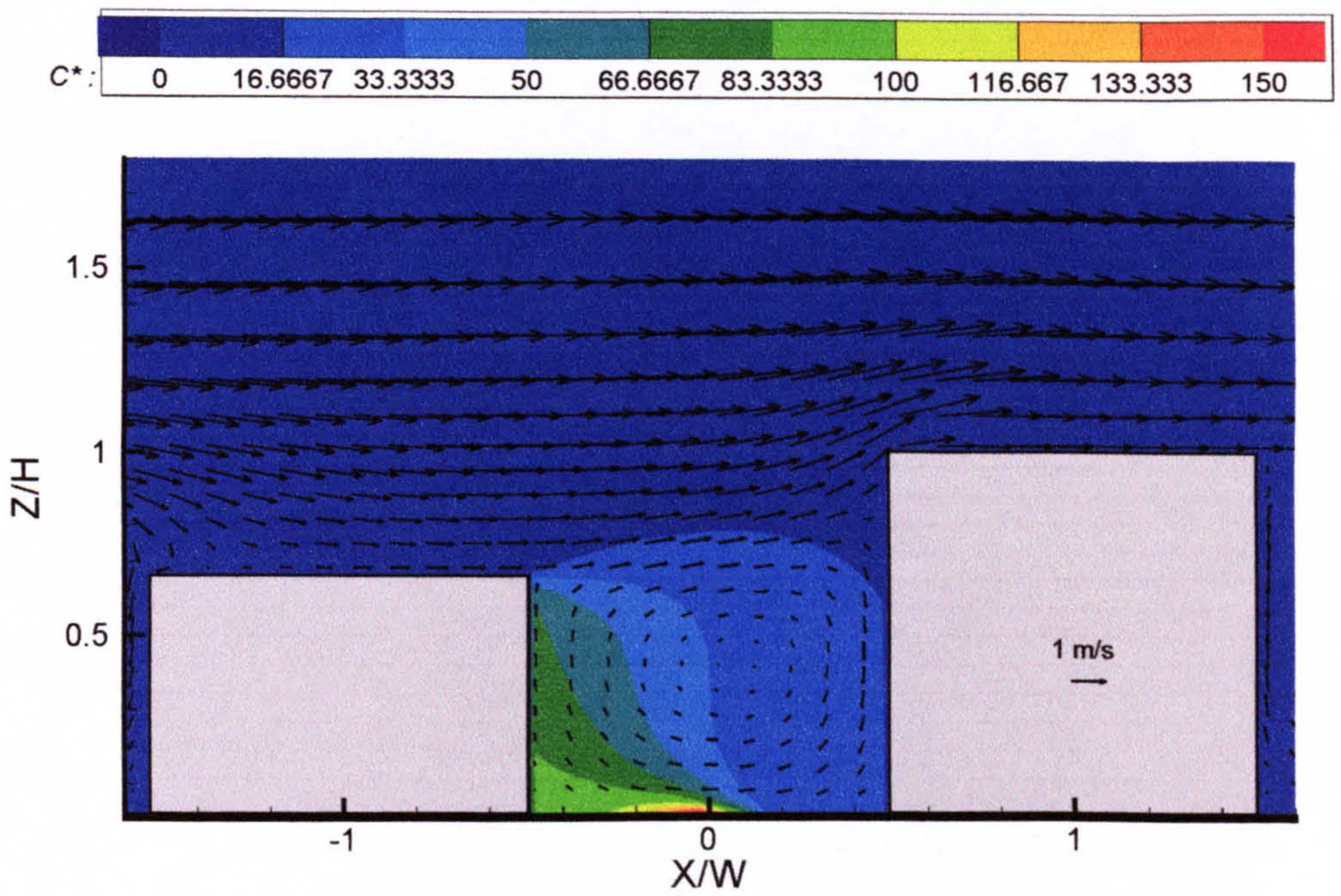

Figure 4.11e. Wind field and pollutant dispersion, as computed by MIMO for upwind building height of 0.04m.

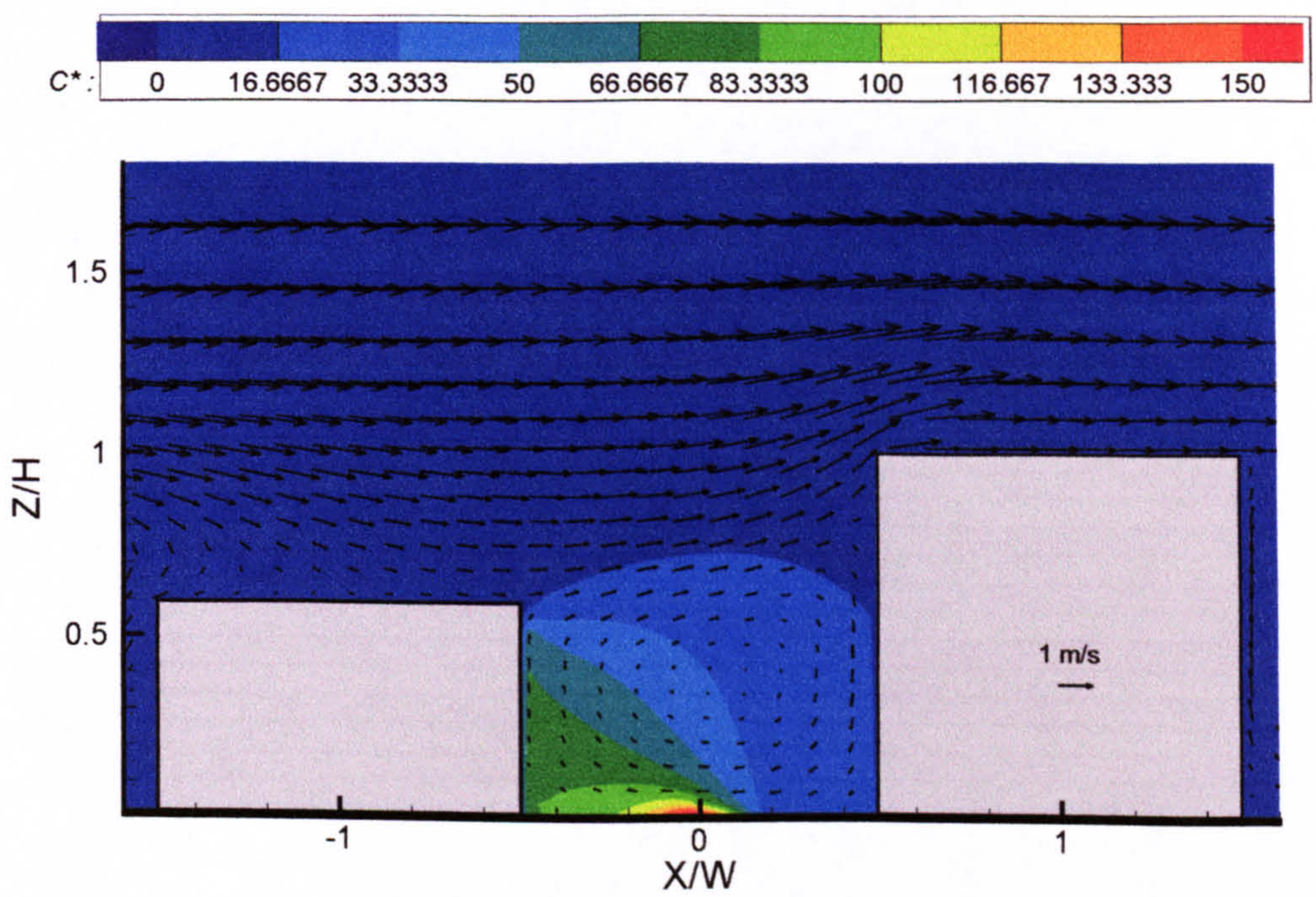

Figure 4.11f. Wind field and pollutant dispersion, as computed by MIMO for upwind building height of 0.035m.

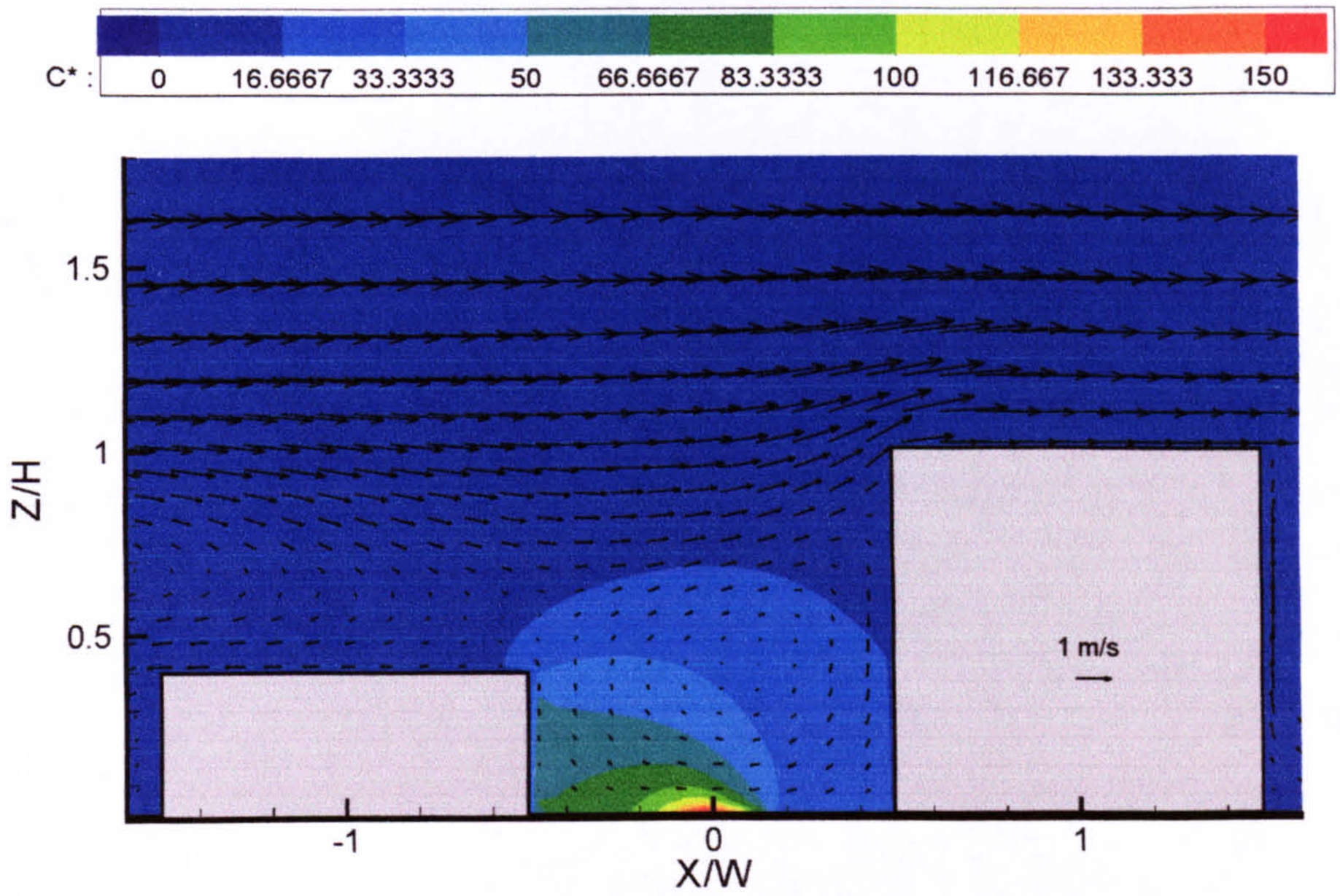

Figure 4.11g. Wind field and pollutant dispersion, as computed by MIMO for upwind building height of 0.03m.

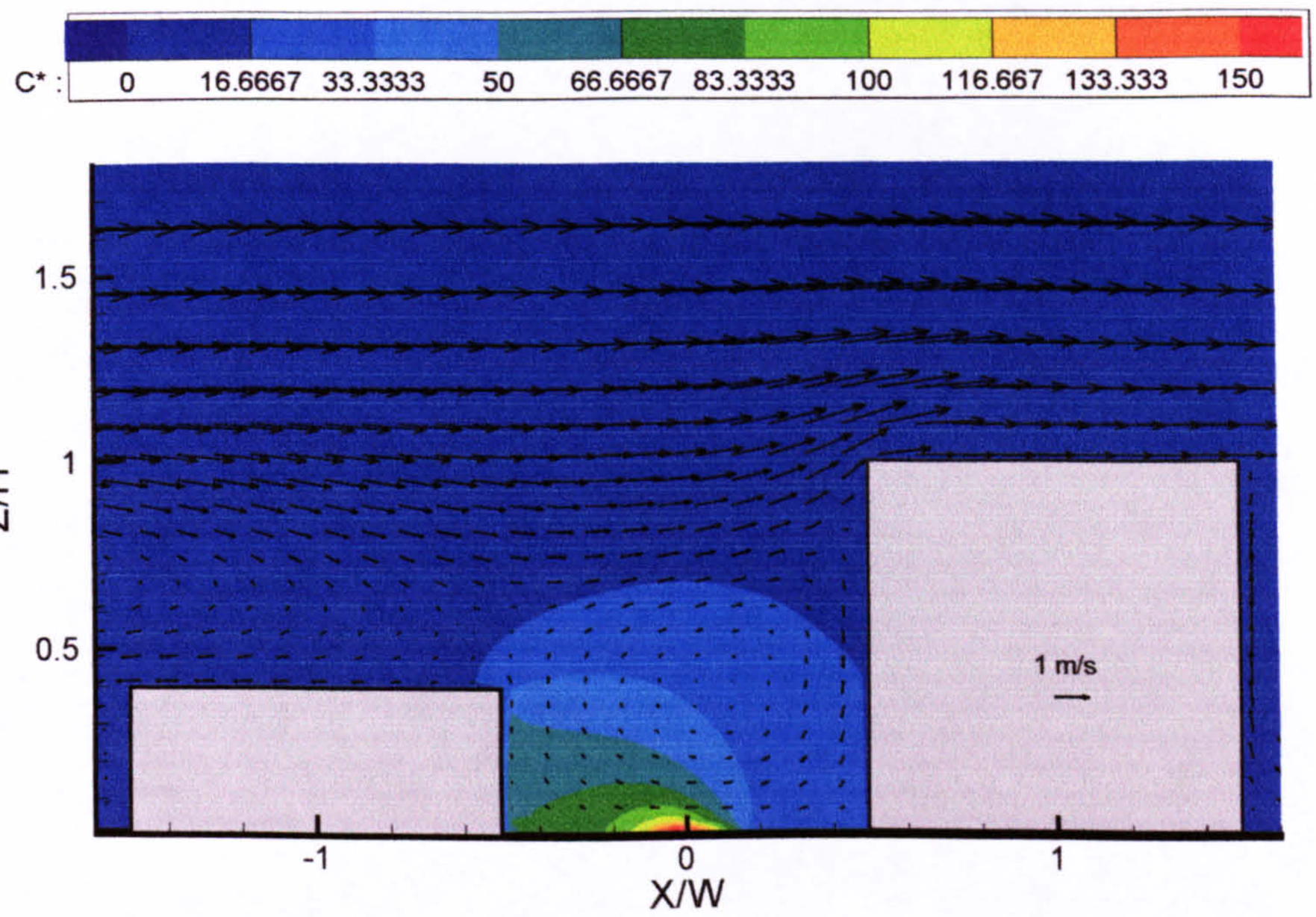

Figure 4.11h. Wind field and pollutant dispersion, as computed by MIMO for upwind building height of 0.025m.

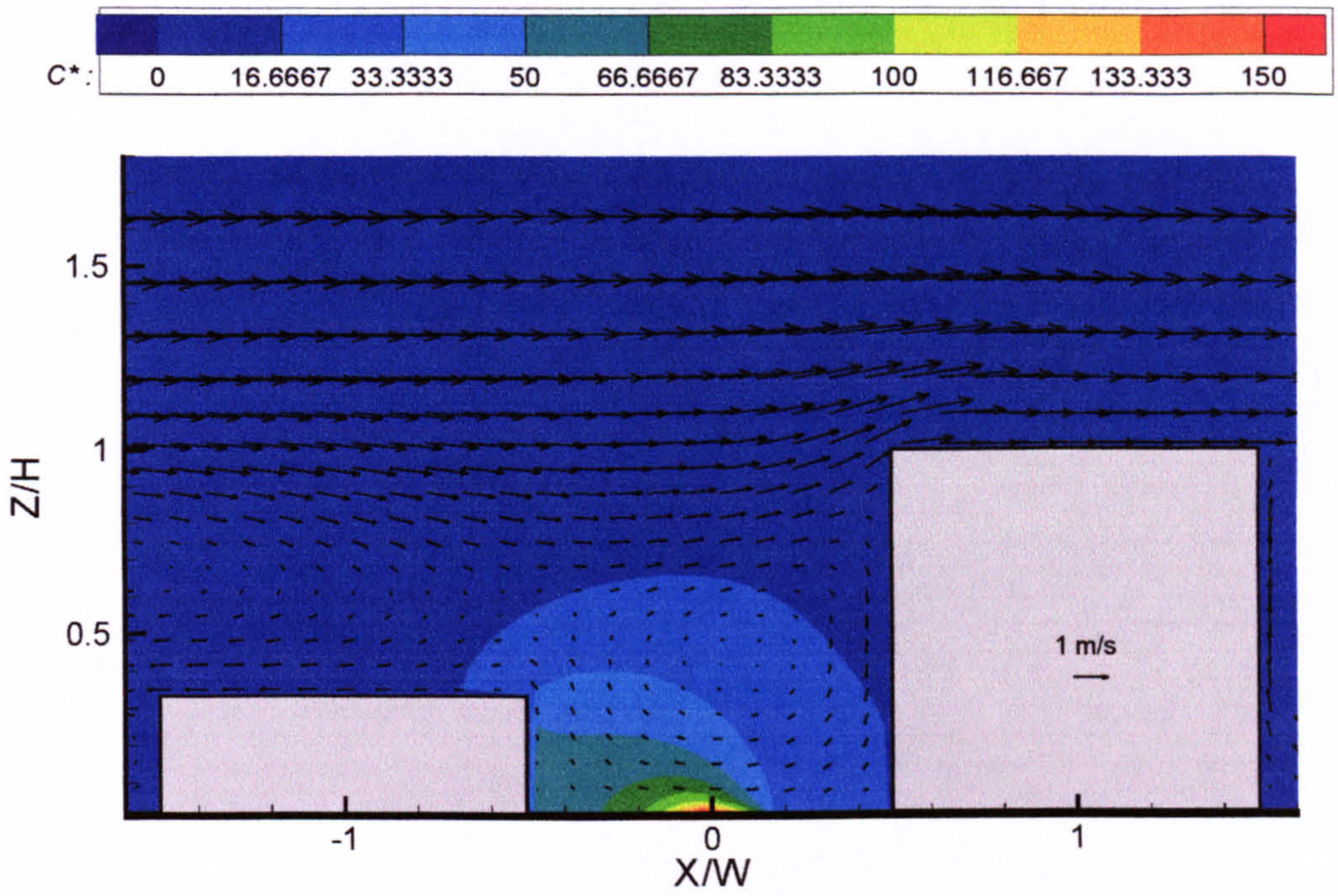

Figure 4.11i. Wind field and pollutant dispersion, as computed by MIMO for upwind building height of 0.02m.

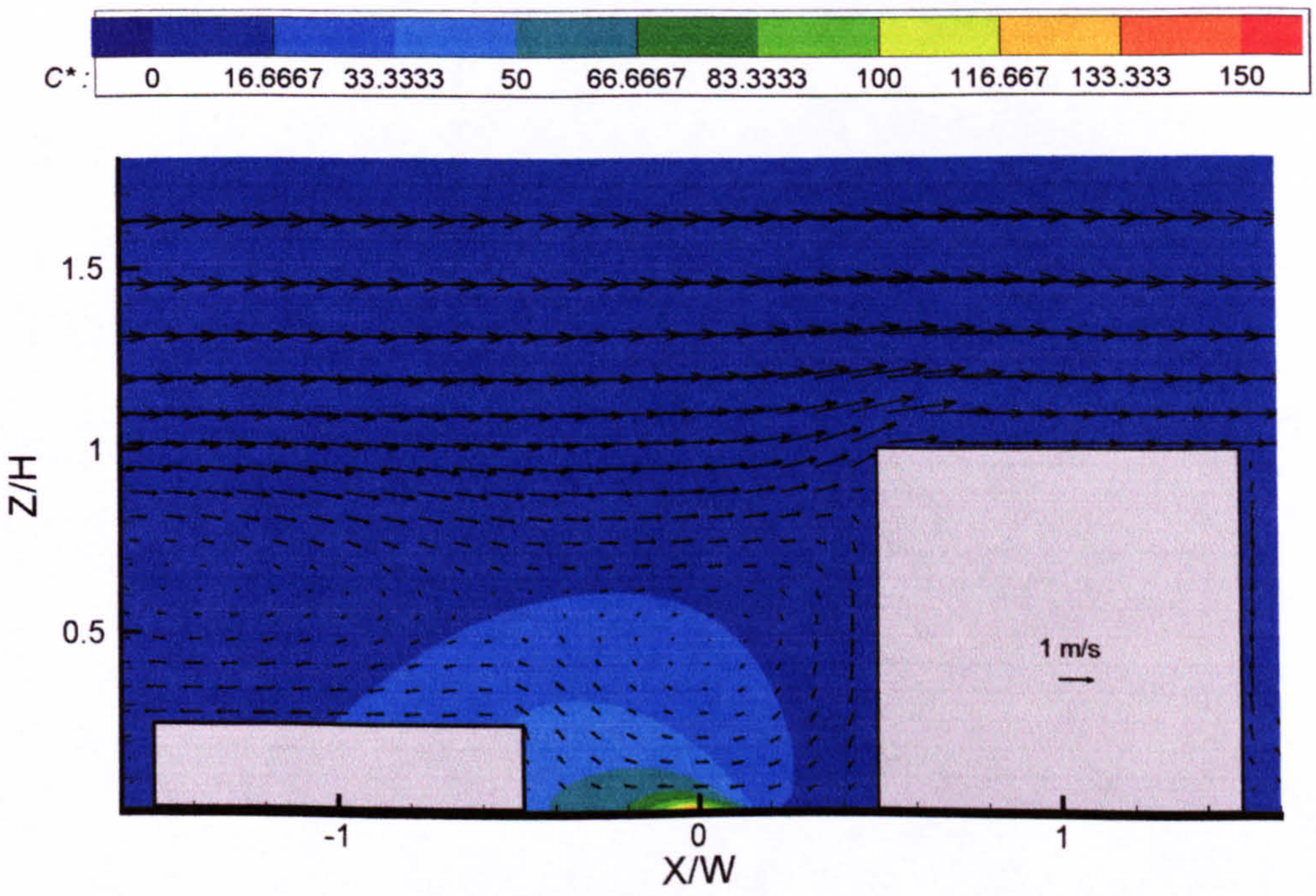

Figure 4.11j. Wind field and pollutant dispersion, as computed by MIMO for upwind building height of 0.015m.

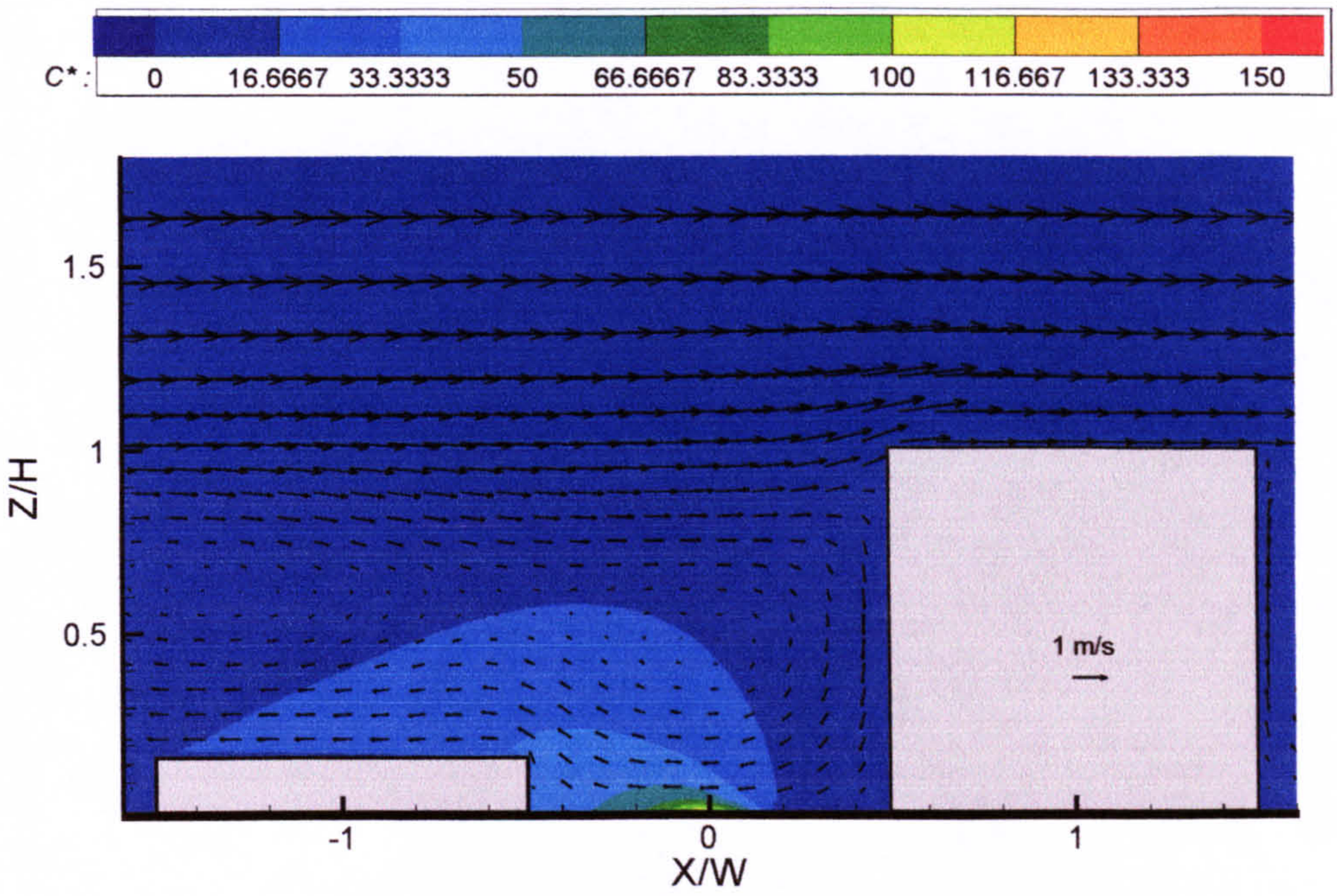

Figure 4.11k. Wind field and pollutant dispersion, as computed by MIMO for upwind building height of 0.01m.

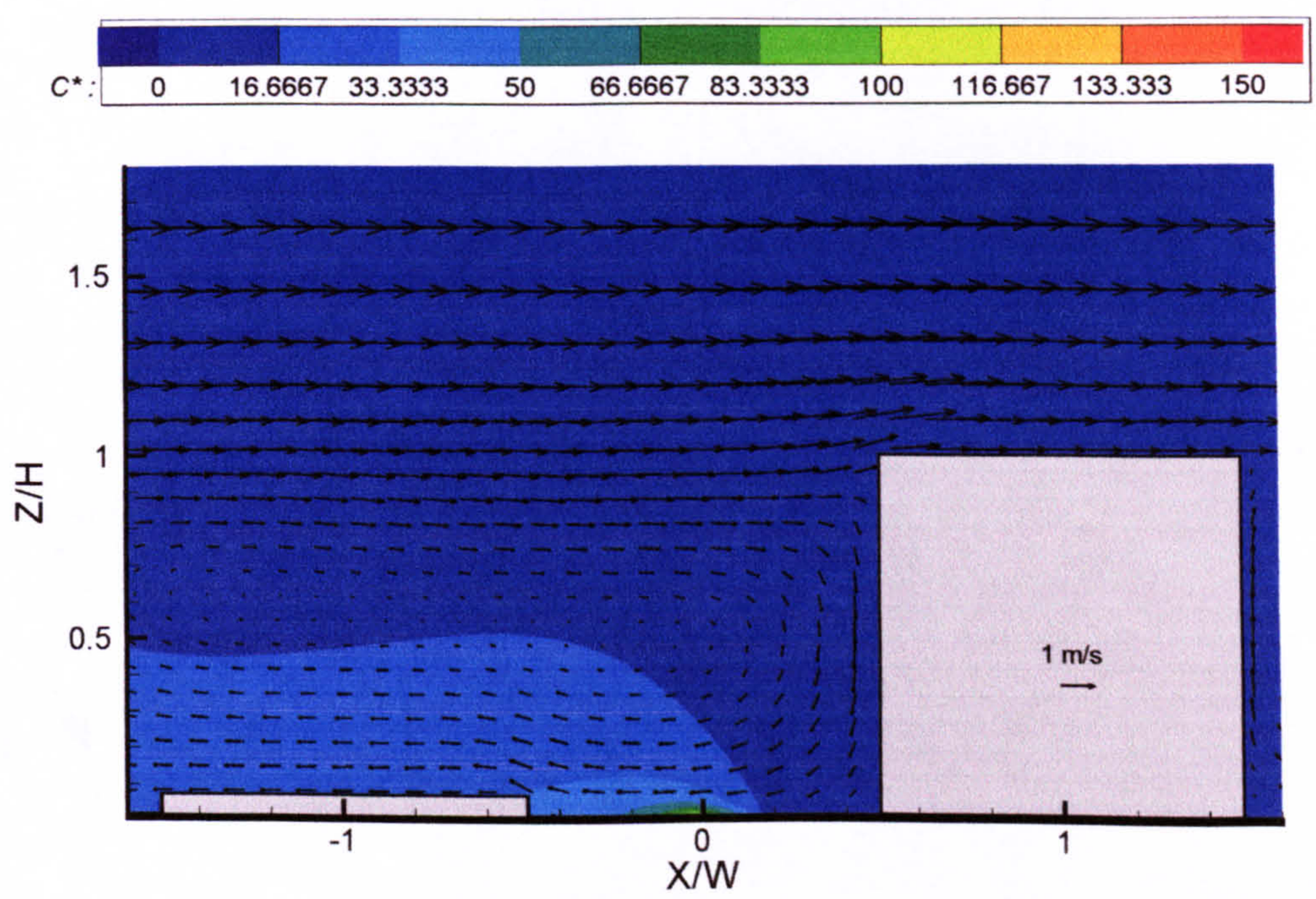

Figure 4.11l. Wind field and pollutant dispersion, as computed by MIMO for upwind building height of 0.005m.

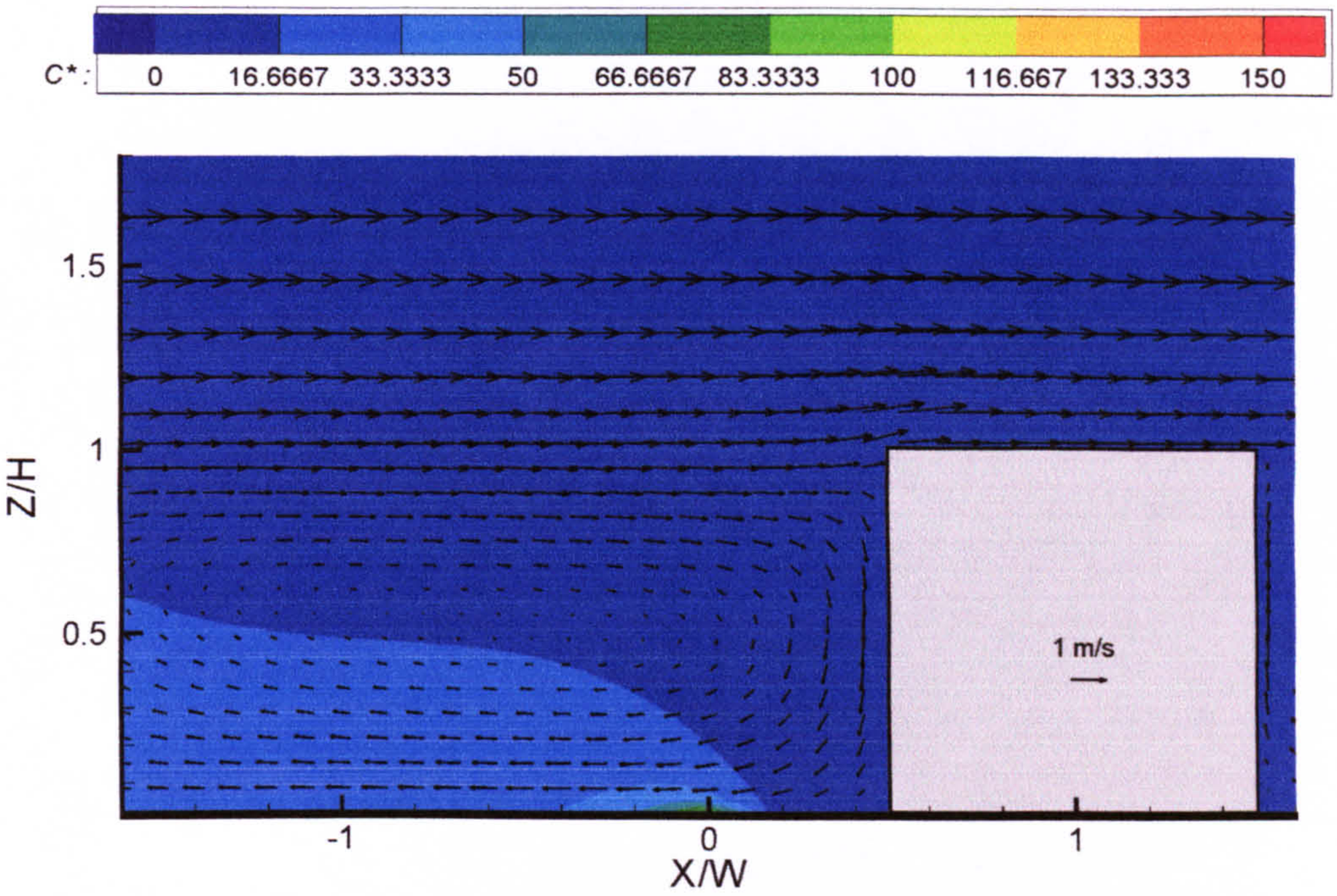

Figure 4.11m. Wind field and pollutant dispersion, as computed by MIMO for upwind building height of 0.0m.

4.2.2 Step-down notch results-square

The step-down notch configuration is formed when the downwind building is lower in height from the upwind one. For this set of simulations the height of the downwind building was reduced in 5mm steps. The width of the street canyon was set at 60 mm thus the original configuration was that of a square street canyon, (aspect ratio of 1).

As seen in Figures 4.12a and b, the flow from above the cavity gives rise to the development of a strong isolated vortex. This does not allow escape of pollutants over the building roofs, thus a local increase of concentrations is observed. The main vortex formed does not seem to change in shape compared to the symmetric case shown earlier, neither does the vortex centre.

Further decrease of the downwind building height, (lower than 45 mm) results in a weakening of the vortex strength, a shifting of its centre upwards and an increase of the pollution region both on the up wind building wall and at the floor of the cavity, Figures 4.12c and d. This situation changes dramatically when the downwind building

height reduces to 35 mm, where the following remarks can be made, (Figures 4.12e and f):

- Creation of a secondary vortex at the lower downwind building corner of the cavity, of opposite circulation flow to the main vortex.

- Weakening of the strength and shifting of the centre of the main vortex above the roof of the downwind building.

- Elimination of the pollution from the upwind building side and

- Creation of a pollution cell at the floor of the cavity centred at the location of emission of pollutants.

Following the above pattern, a further decrease of the downwind building height (Figures 4.12g and h) leads to the development of an elongated vortex above the downwind building height. Moreover, the pollution pattern changes showing a shrinking tendency and a preference to the downwind building corner. The vortex established at the downwind building corner remains unchanged.

When the downwind building height reduces further, (15 or 10 mm) the following are observed:

- The main vortex remains above the downwind building roof and is further elongated. Its downstream end begins to merge with the vortex downstream.

- The pollution cell shows a clear tendency of detachment from the downwind building wall and shifts towards the upwind building of the cavity.

- The secondary vortex at the downwind building corner weakens and it is hardly visible in the case of 10 mm height.

- There is a return flow from the canyon downstream to the canyon of interest, through which the backward transport of pollutants is possible.

Finally, as seen from Figures 4.12i, j and k, where the downwind building becomes even smaller or removed, the following remarks can be made:

- Practically a single elongated vortex is well established inside the canyon as expected, presenting, as in the case step-up notch configuration, a strong downdraft flow at the downwind building wall of the canyon downstream.

- High pollutants concentration has returned to the upwind building wall of the canyon of interest, indicating a maximum at the bottom part close to the lower upwind building corner.

Summarising the main points of the results presented above, the following conclusions could be drawn:

- The location of maximum pollution concentration varies with the different downwind building heights, shifting from one side of the canyon studied to the other.

- A secondary vortex appears when the downwind building height is almost half the upwind building height. This is also of importance since this vortex supports the creation of a localised air pollution concentration cell.

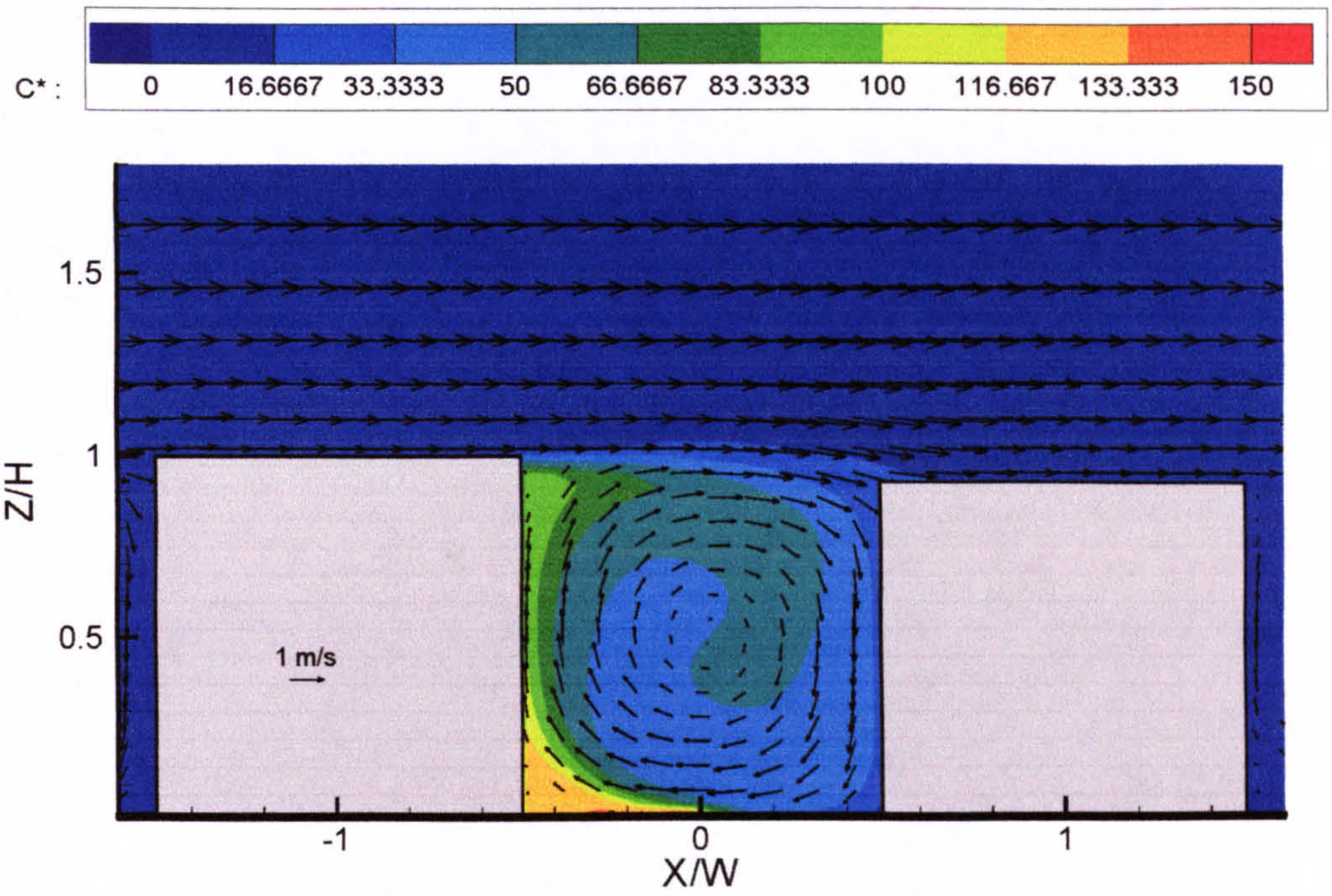

Figure 4.12a. Wind field and pollutant dispersion, as computed by MIMO for downwind building height of 0.055m.

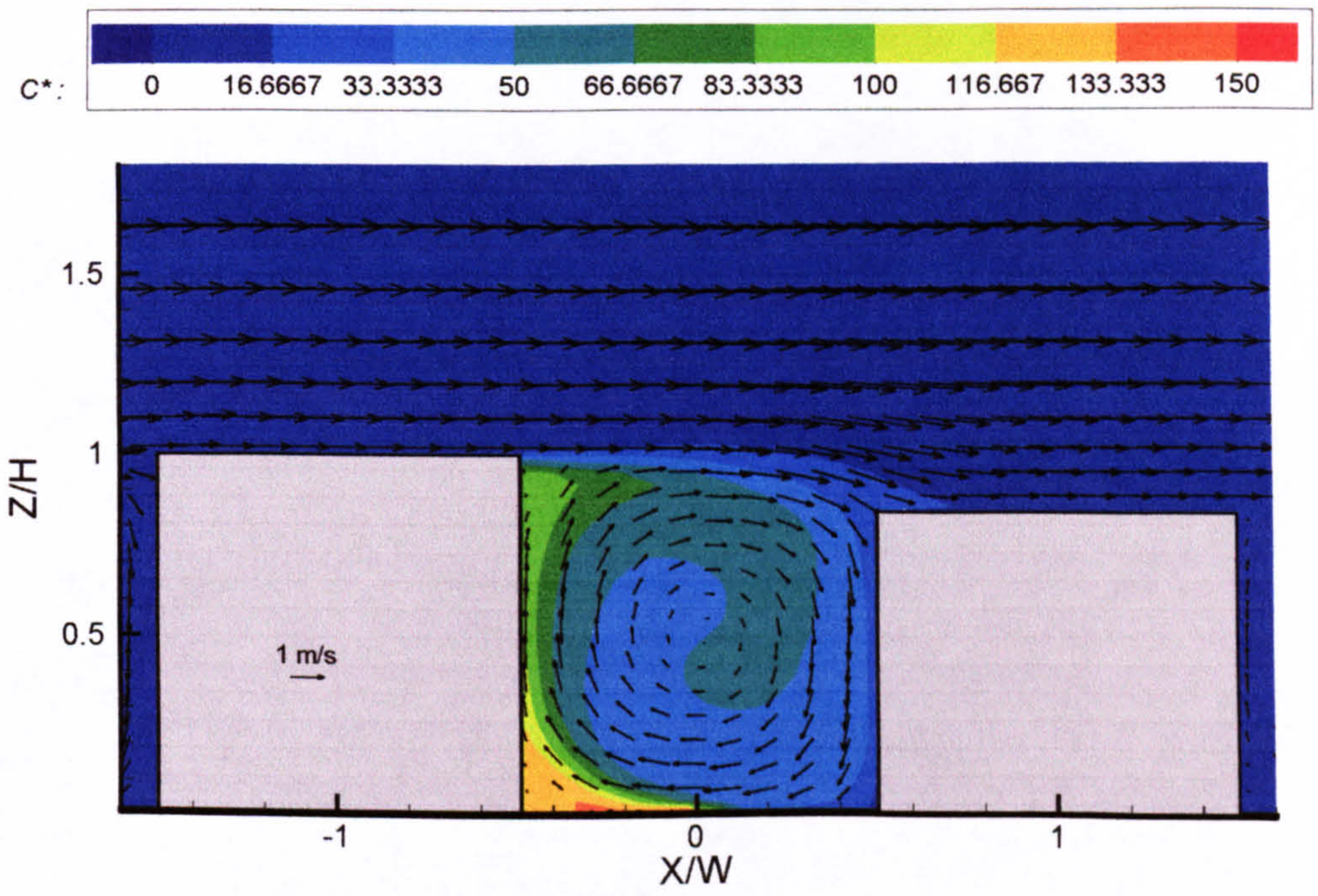

Figure 4.12b:Wind field and pollutant dispersion, as computed by MIMO for downwind building height of 0.05m.

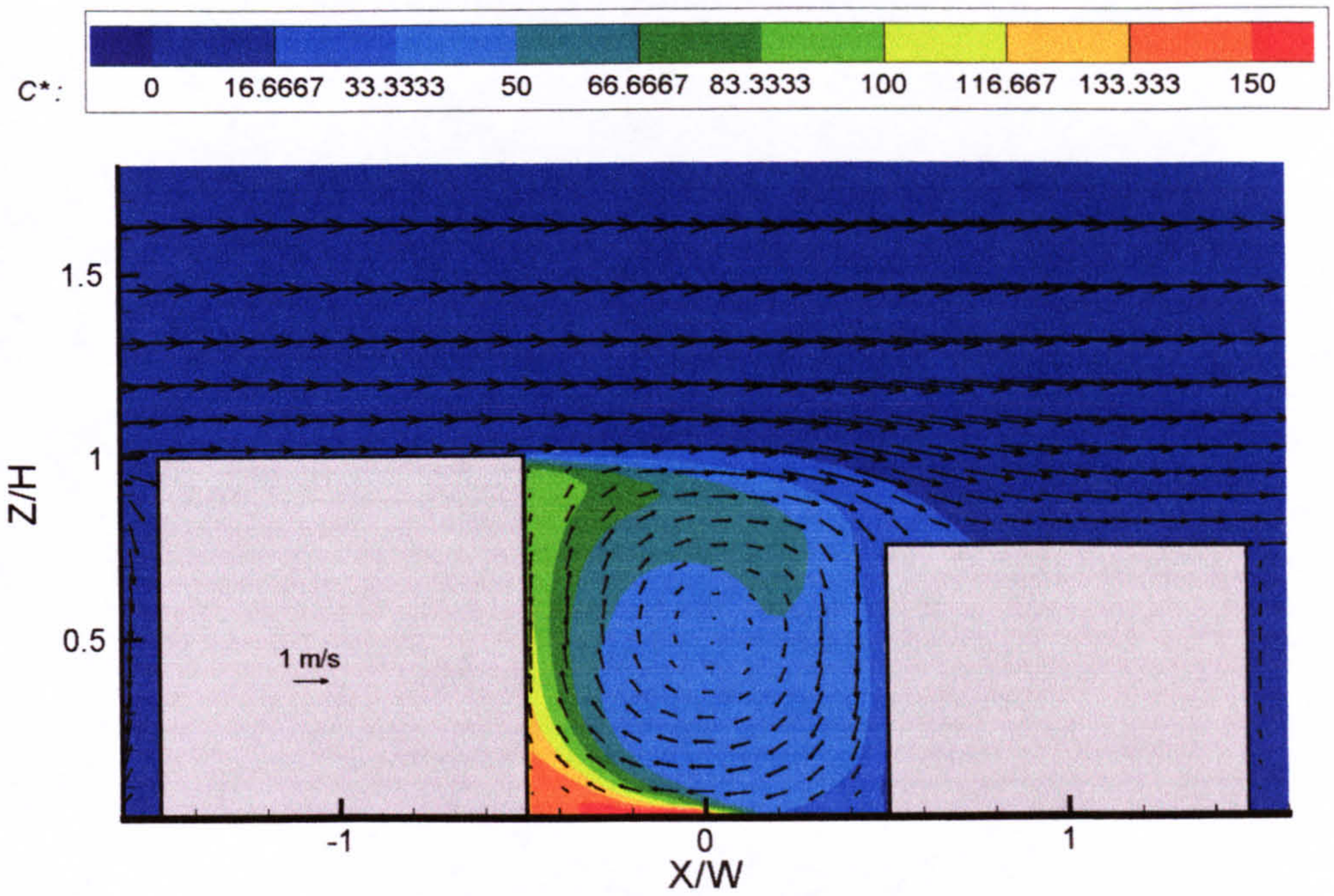

Figure 4.12c. Wind field and pollutant dispersion, as computed by MIMO for downwind building height of 0.045m.

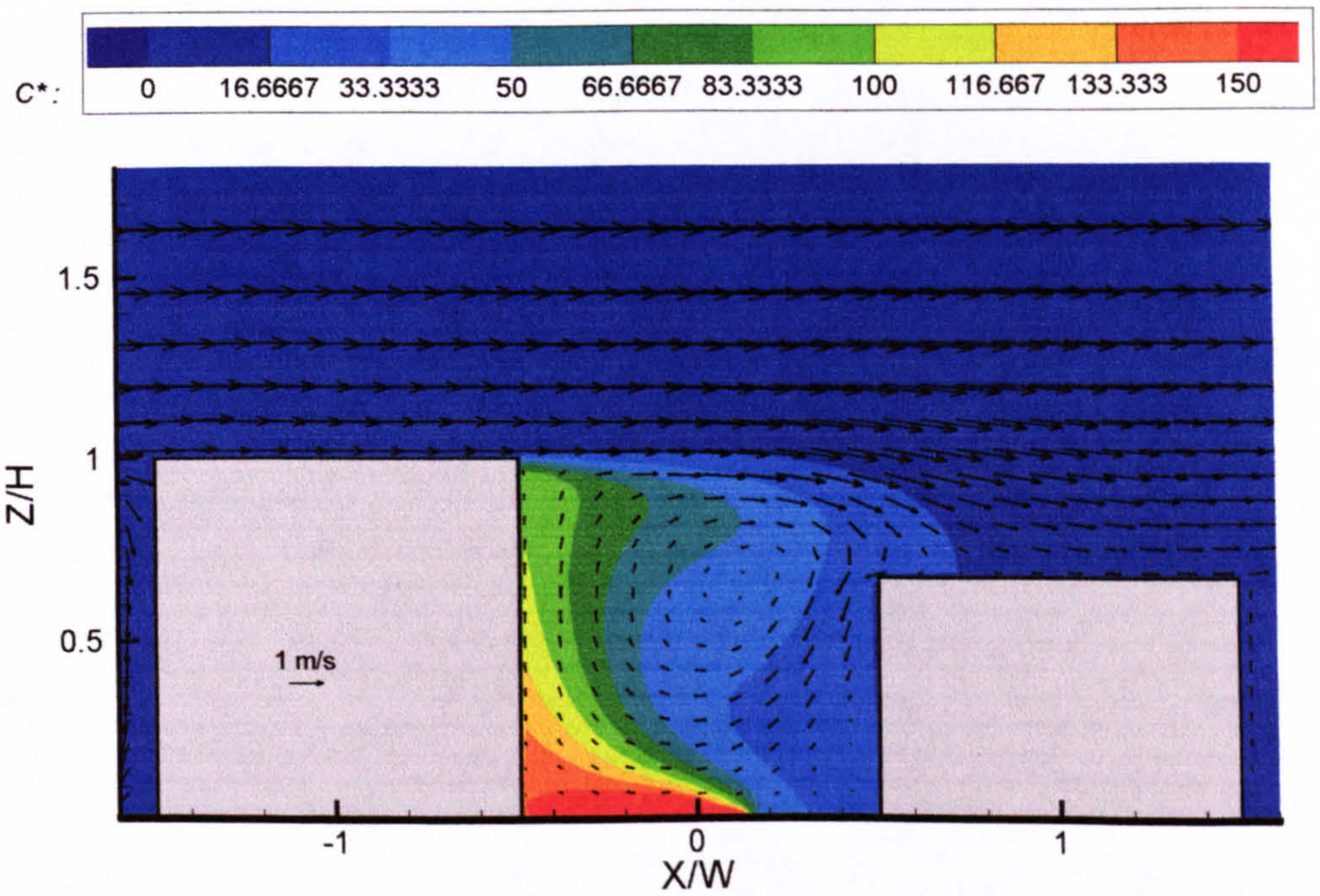

Figure 4.12d. Wind field and pollutant dispersion, as computed by MIMO for downwind building height of 0.04m.

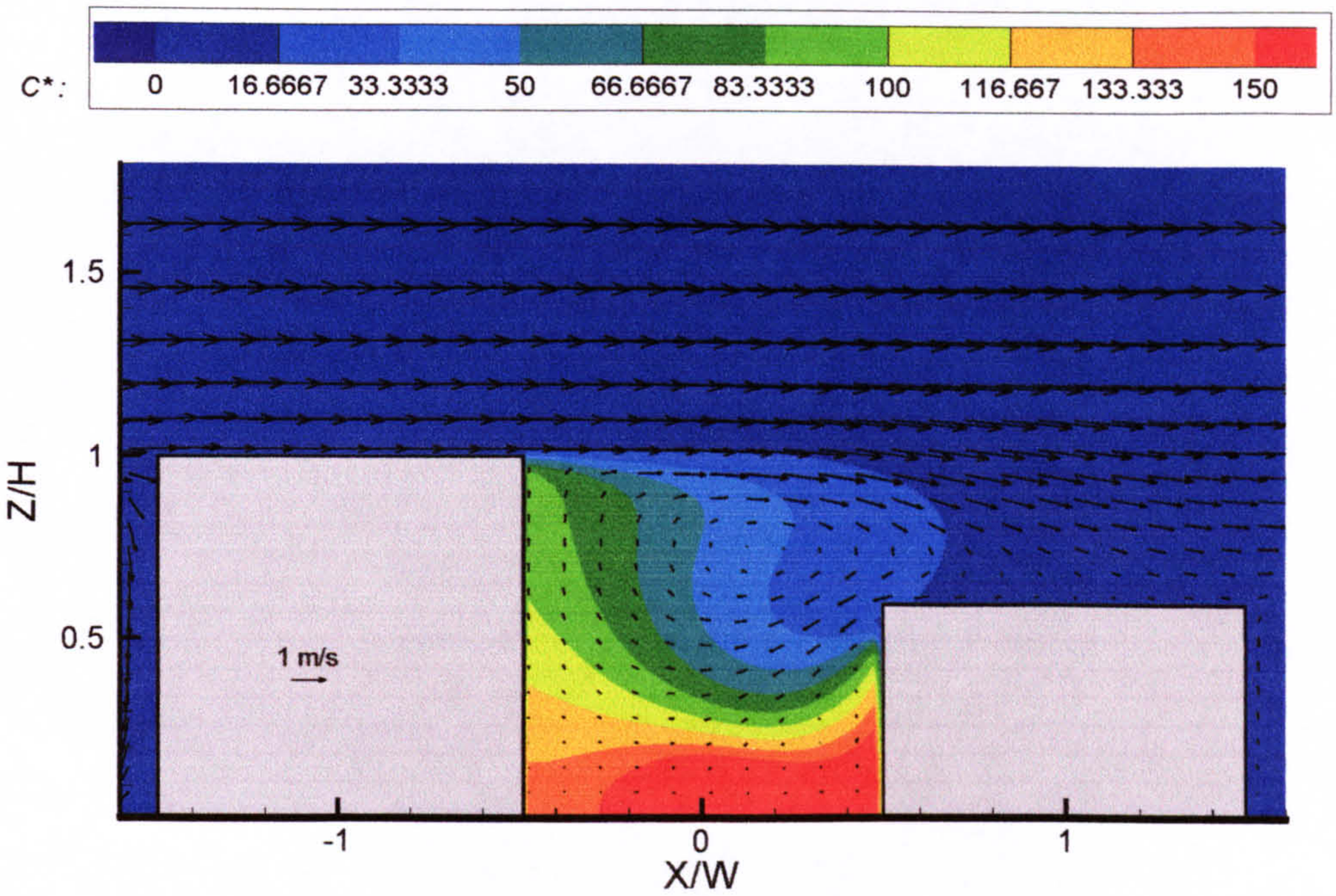

Figure 4.12e. Wind field and pollutant dispersion, as computed by MIMO for downwind building height of 0.035m.

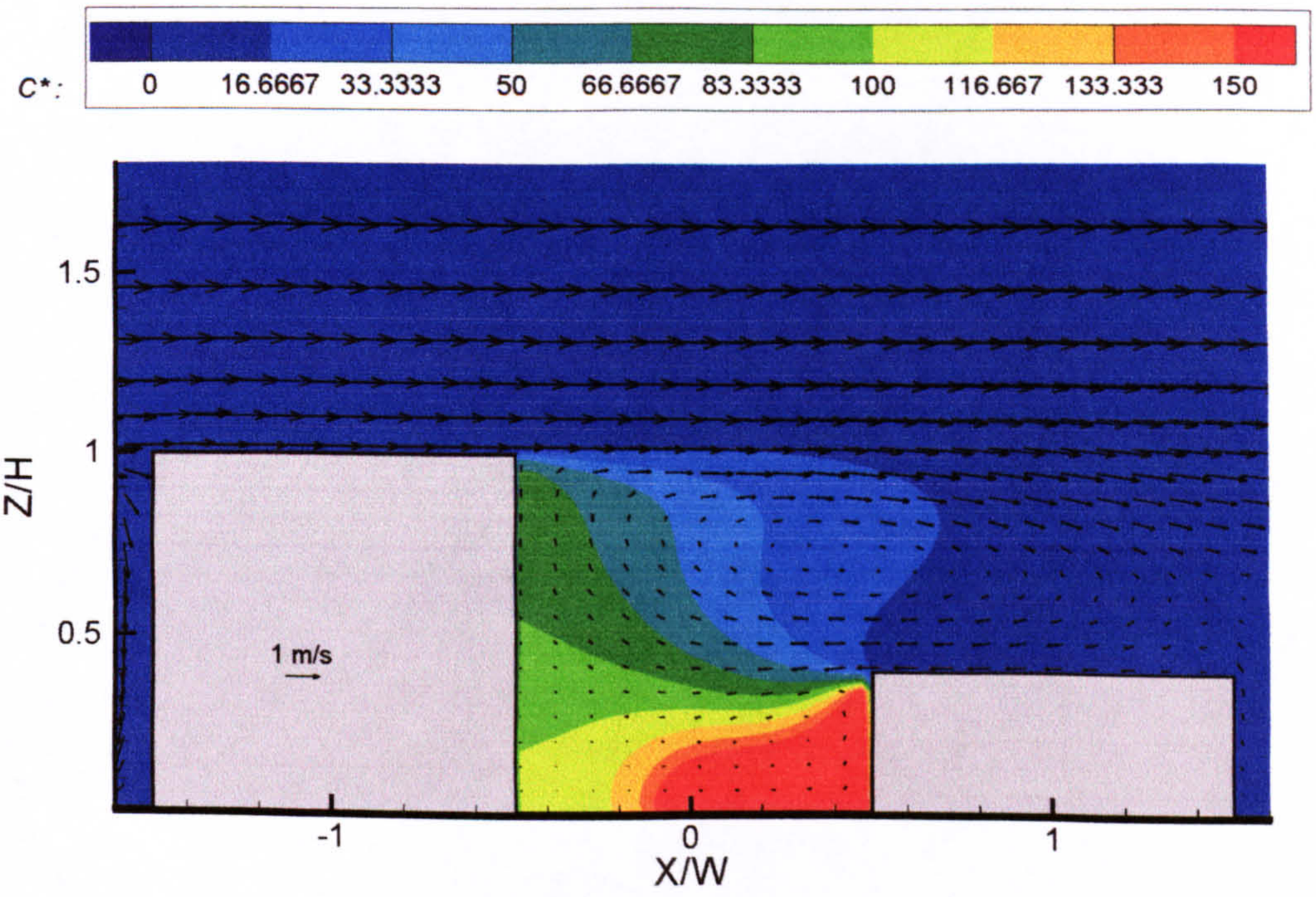

Figure 4.12f. Wind field and pollutant dispersion, as computed by MIMO for downwind building height of 0.03m.

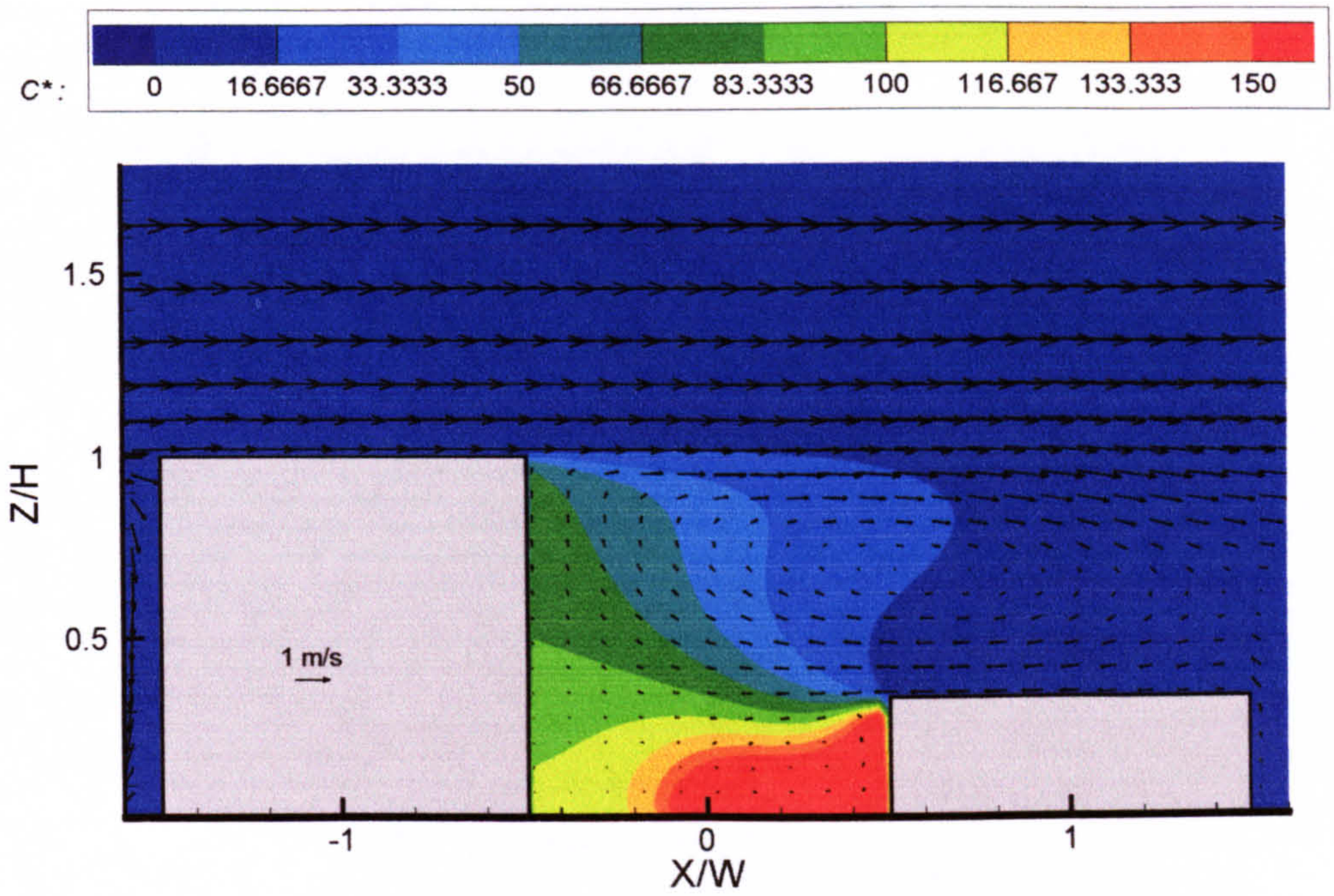

Figure 4.12g. Wind field and pollutant dispersion, as computed by MIMO for downwind building height of 0.025m.

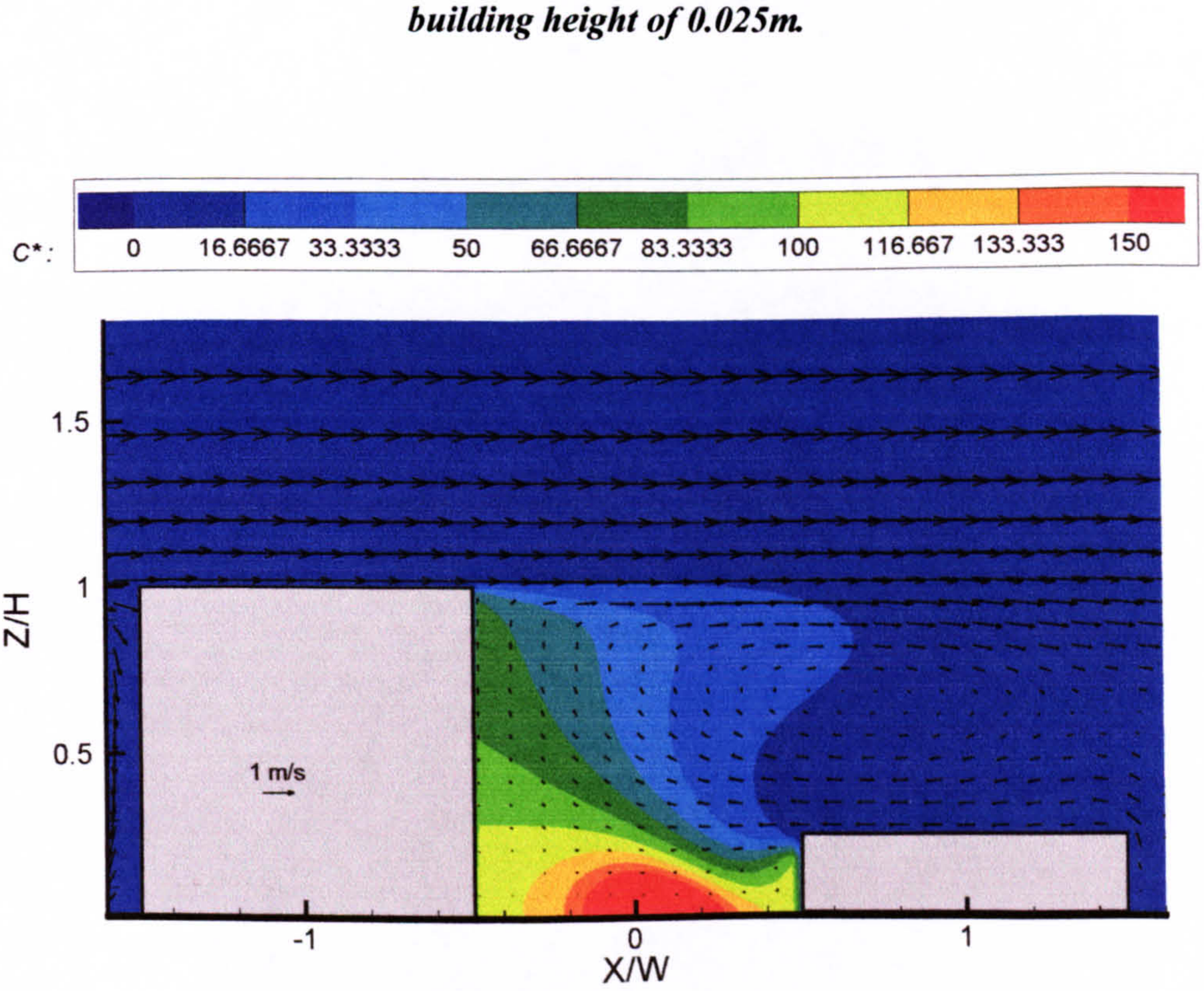

Figure 4.12h. Wind field and pollutant dispersion, as computed by MIMO for downwind building height of 0.02m.

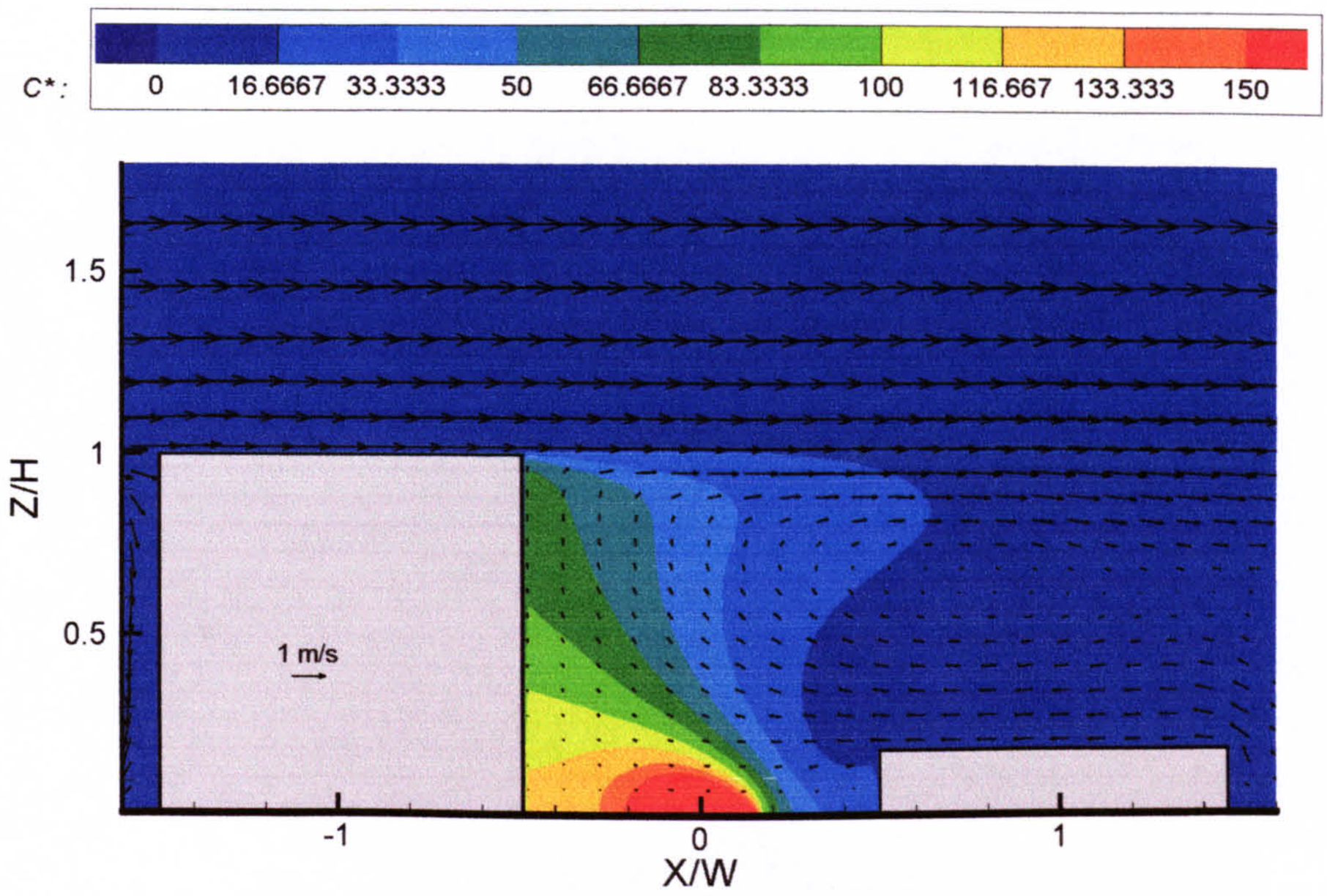

Figure 4.12i. Wind field and pollutant dispersion, as computed by MIMO for downwind building height of 0.015m.

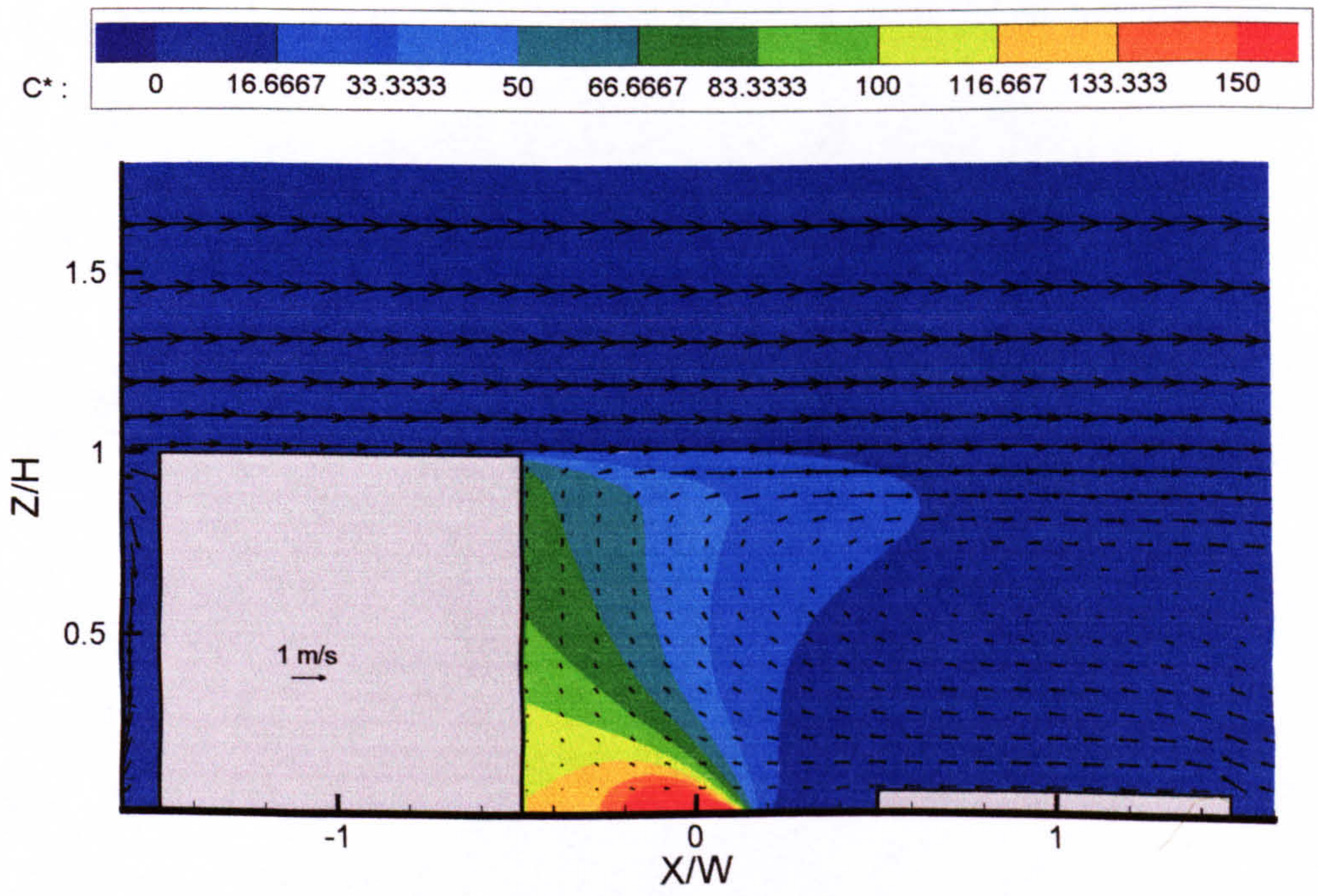

Figure 4.12j. Wind field and pollutant dispersion, as computed by MIMO for downwind building height of 0.01m.

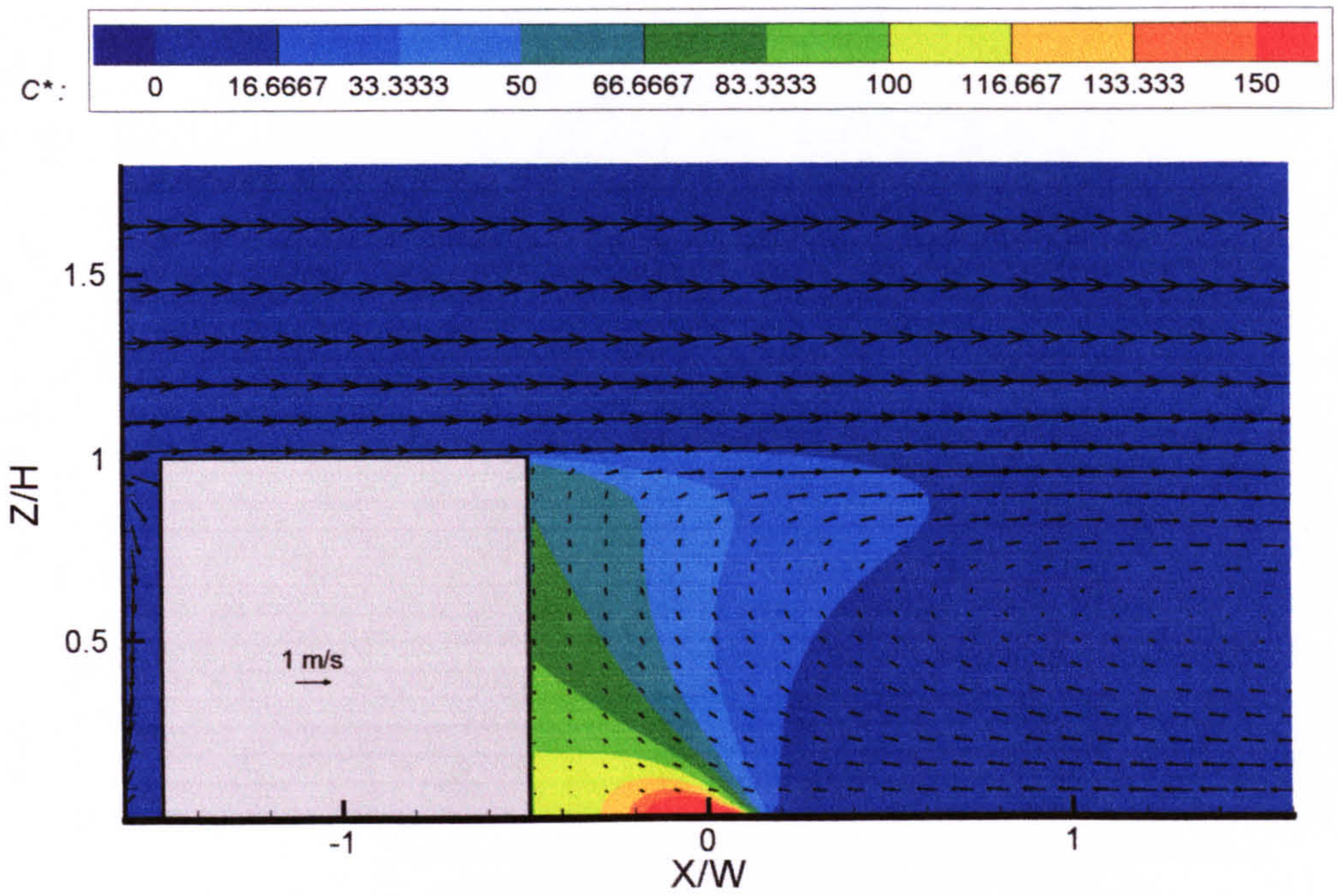

Figure 4.12k. Wind field and pollutant dispersion, as computed by MIMO for downwind building height of 0m.

4.2.3 Step-up notch results (deep case)

The step-up notch configuration is formed when the upwind building is lower in height from the downwind one. For this set of simulations the height of the upwind building was reduced in 10mm steps. The width of the street canyon was set at 30 mm thus the original configuration was that of a deep street canyon.

As seen in Figure 4.13b, the main vortex now extends down to more than 2/3 of the depth of the street canyon, while below that height almost stagnant conditions prevail. The centre of the vortex is shifted upwards and to the right. The top of the main vortex reaches the roof of the upwind building since the flow above suppresses it, which then hits on the part of the downwind building wall which protrudes and accelerates up and downstream. The wind velocity is larger on the downwind building wall due to the shifting of the centre of the main vortex, which combined with the effect of the enlargement of the vortex aids in aeration of the canyon. The pollutants escape from the upwind building wall due to the action of the vortex and concentration levels start to rise on that wall. Simultaneously concentrations decrease

at the downwind building corner. It is worth noting, that although there exist strong downdrafts on the right side of the vortex, there is a pollution cell at the cavity floor.

When the upwind building height decreases further (Figures 4.13c) the following changes are marked:

- The main vortex is maintained and stretches up towards the upward downwind building corner, while its centre shifts downwards and to the right. The thickness of the stagnant regime below is slightly reduced.

- The pollution cell at the bottom of the canyon is almost eliminated since pollutants diffuse upwards, and disperse following the vortex pattern. Thus, a background pollution regime is formed extending over a good part of the canyon.

In Figure 4.13d, where the upwind building is 30 mm and the downwind building is 60 mm high, the following important features can be detected:

- The main vortex has lifted almost entirely above the roof of the upwind building and almost entirely above the remaining street canyon.

- The flow within the canyon is isolated from the flow above since the vortex acts as a cup. The wind inside the canyon is almost stagnant and the pollutants diffuse in an upward manner. This results to a further in-canyon dispersion of pollution compared to the previous case.

Finally, when the upwind building height reduces further to 10 mm and then vanishes (Figures 4.13e-g), a single extended vortex is clearly formed between the downwind building of the canyon studied and the upwind building of the canyon upstream, which is coupled with a stronger downdraft on the downwind building wall. Moreover, a further reinforcement of the return flow, which passes over the roof of the upwind building, is observed. Following this flow pattern it is obvious that pollution dispersion is at its best, without indicating any preference in the canyon.

Summarising the main points of the results presented above, the following conclusions could be drawn:

- In the deep canyon case, where the main vortex lifts up out of the canyon, almost stagnant conditions prevail at the bottom of the cavity and diffusion of pollutants occurs. Thus, pollutants do not indicate a preference to a certain location of the canyon and their concentration is almost uniform across the street width.

- There is a continuous weak circulation pattern observed at the bottom of the street canyon for all geometric configurations.

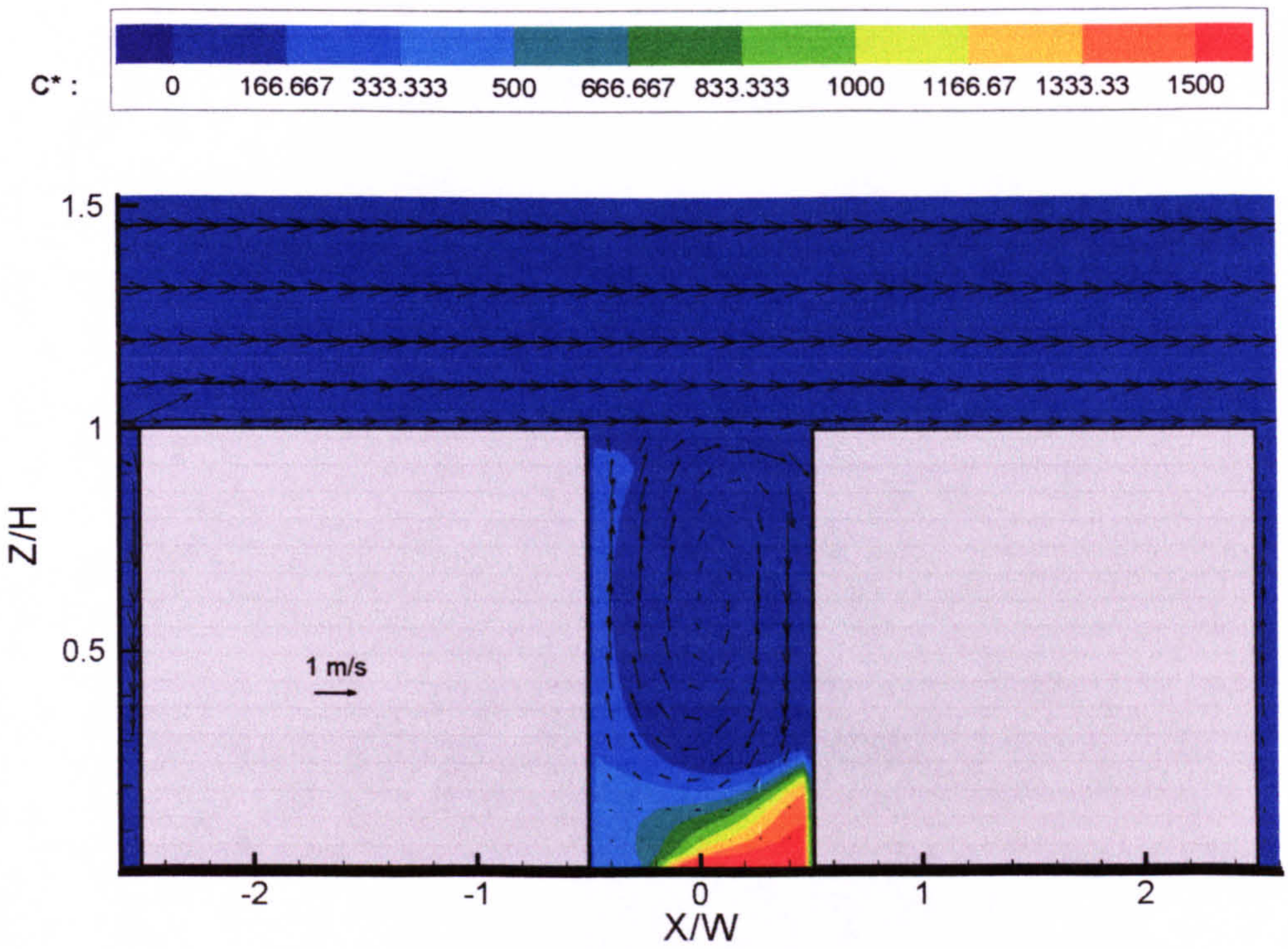

Figure 4.13a. Wind field and pollutant dispersion as computed by MIMO for upwind building height of 0.06m (deep canyon).

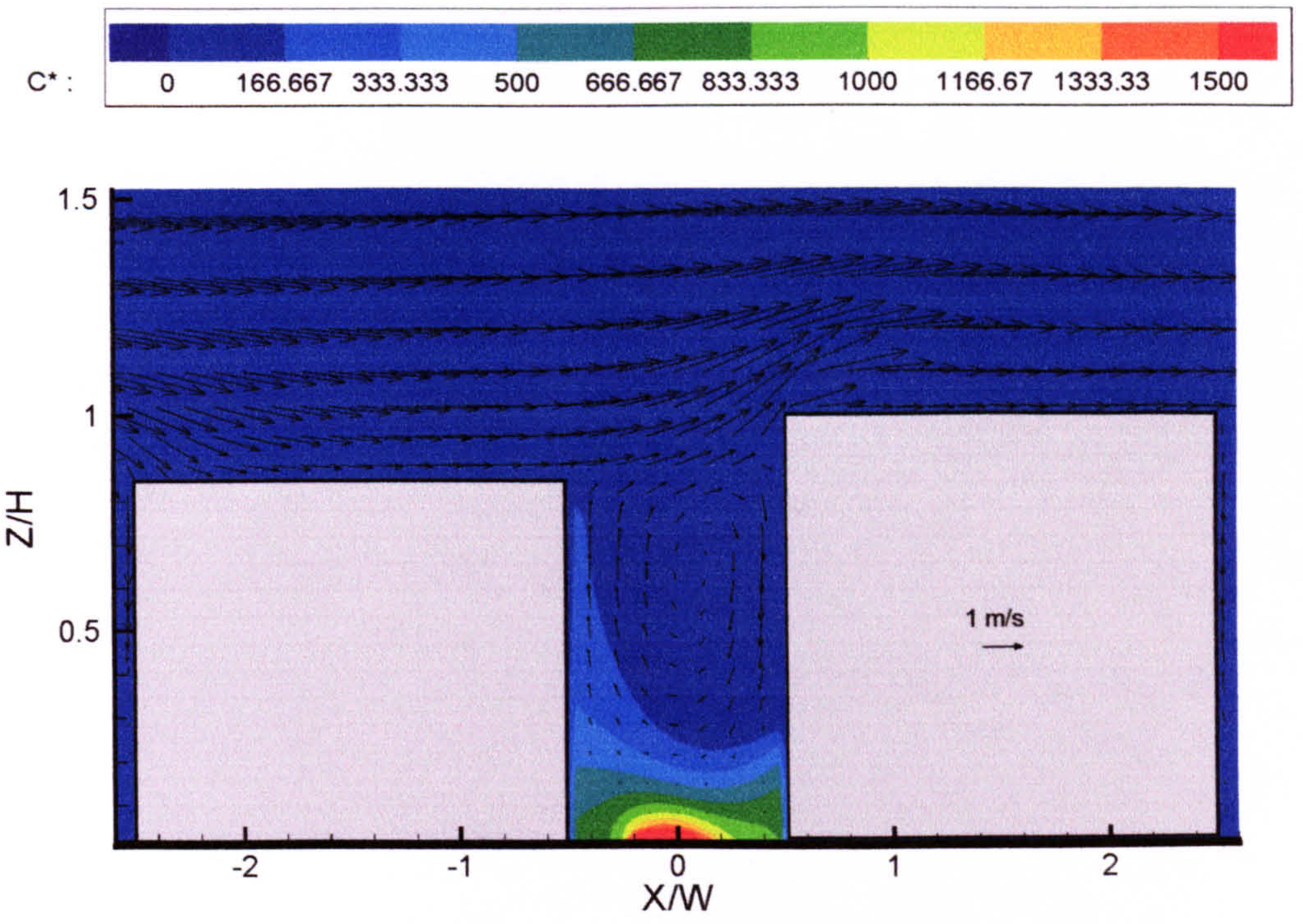

Figure 4.13b. Wind field and pollutant dispersion, as computed by MIMO for upwind building height of 0.05m (deep canyon).

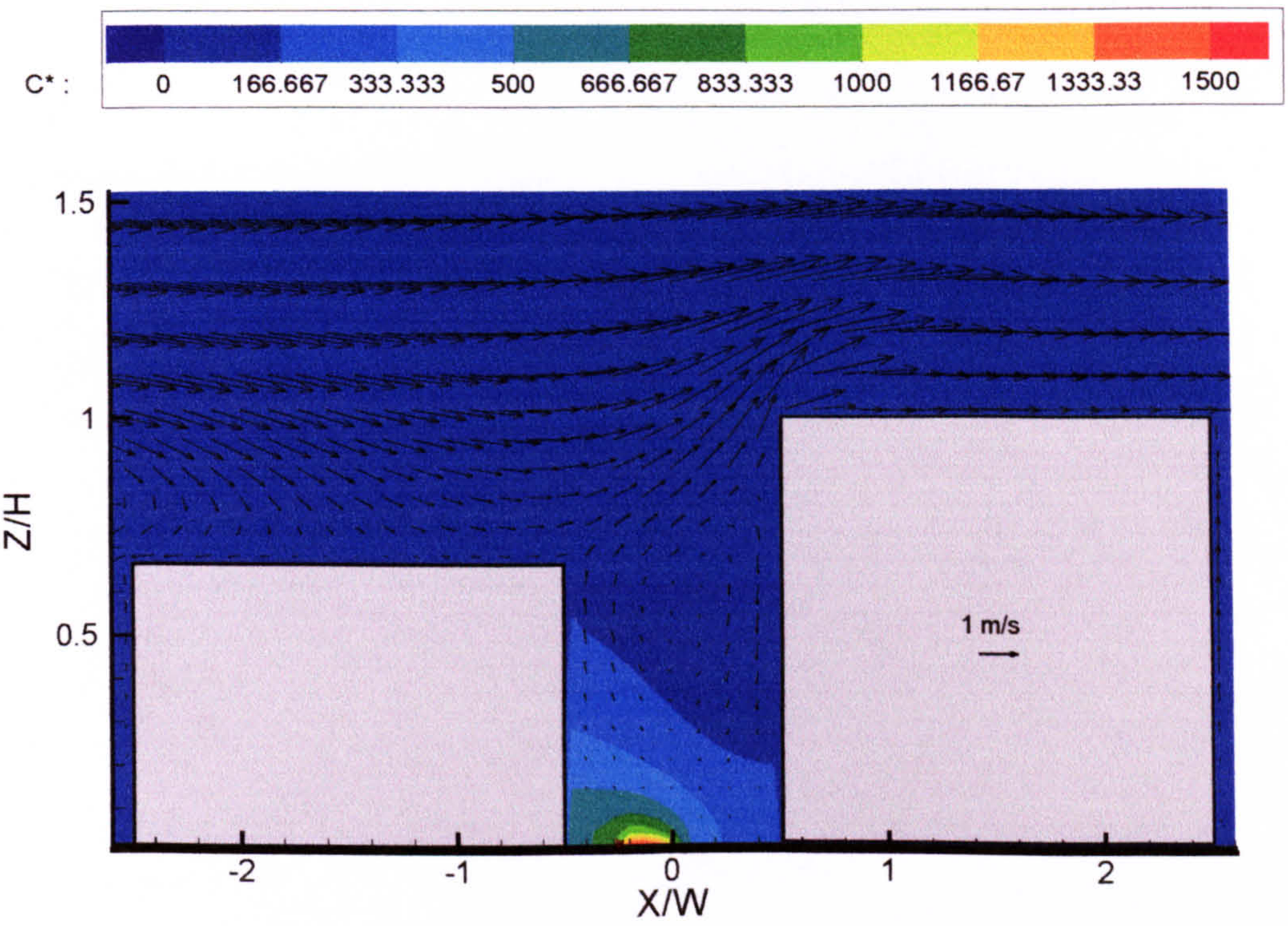

Figure 4.13c. Wind field and pollutant dispersion, as computed by MIMO for upwind building height of 0.04m (deep canyon).

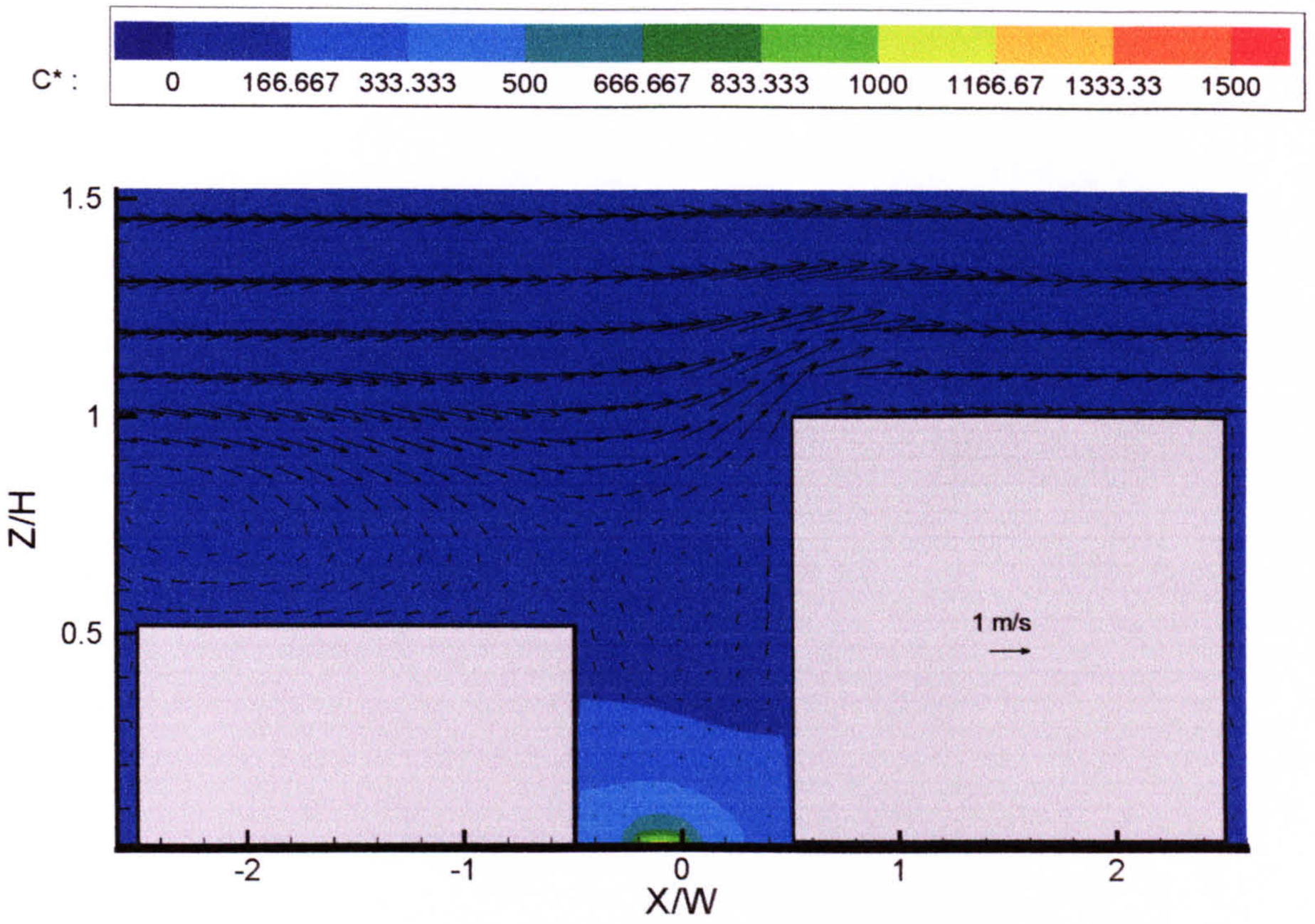

Figure 4.13d. Wind field and pollutant dispersion, as computed by MIMO for upwind building height of 0.03m (deep canyon).

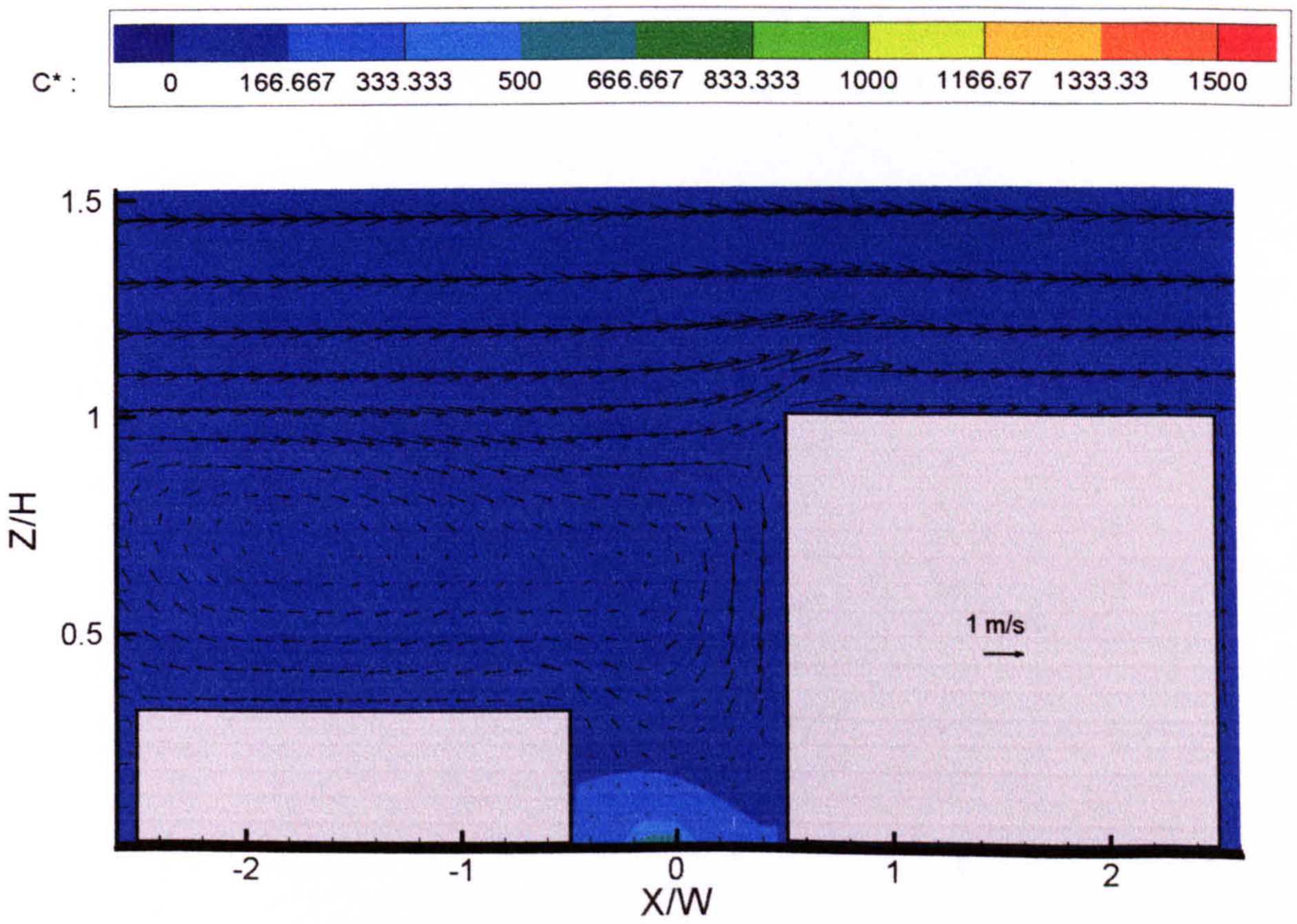

Figure 4.13e. Wind field and pollutant dispersion, as computed by MIMO for upwind building height of 0.02m (deep canyon).

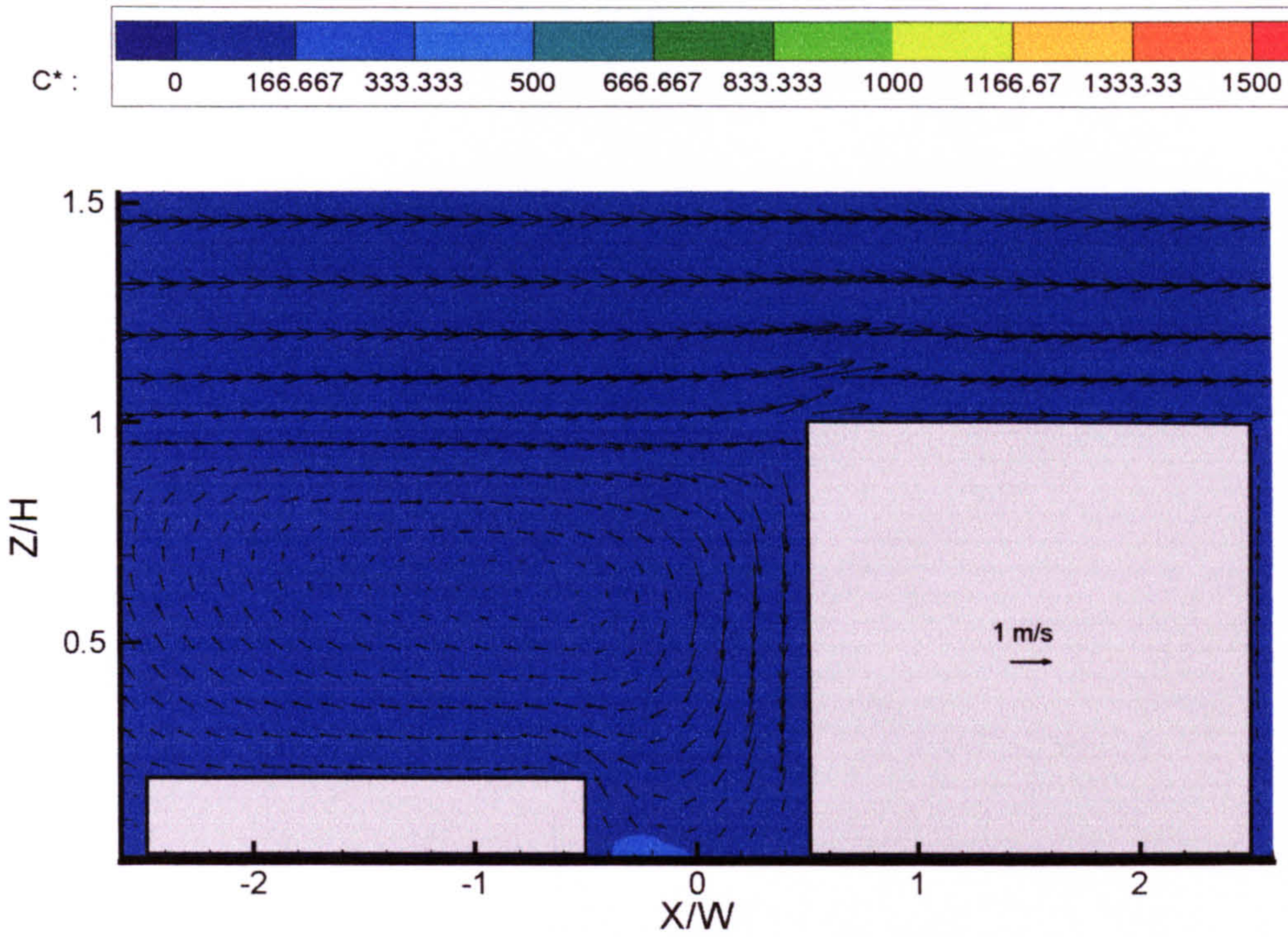

Figure 4.13f. Wind field and pollutant dispersion, as computed by MIMO for upwind building height of 0.01m (deep canyon).

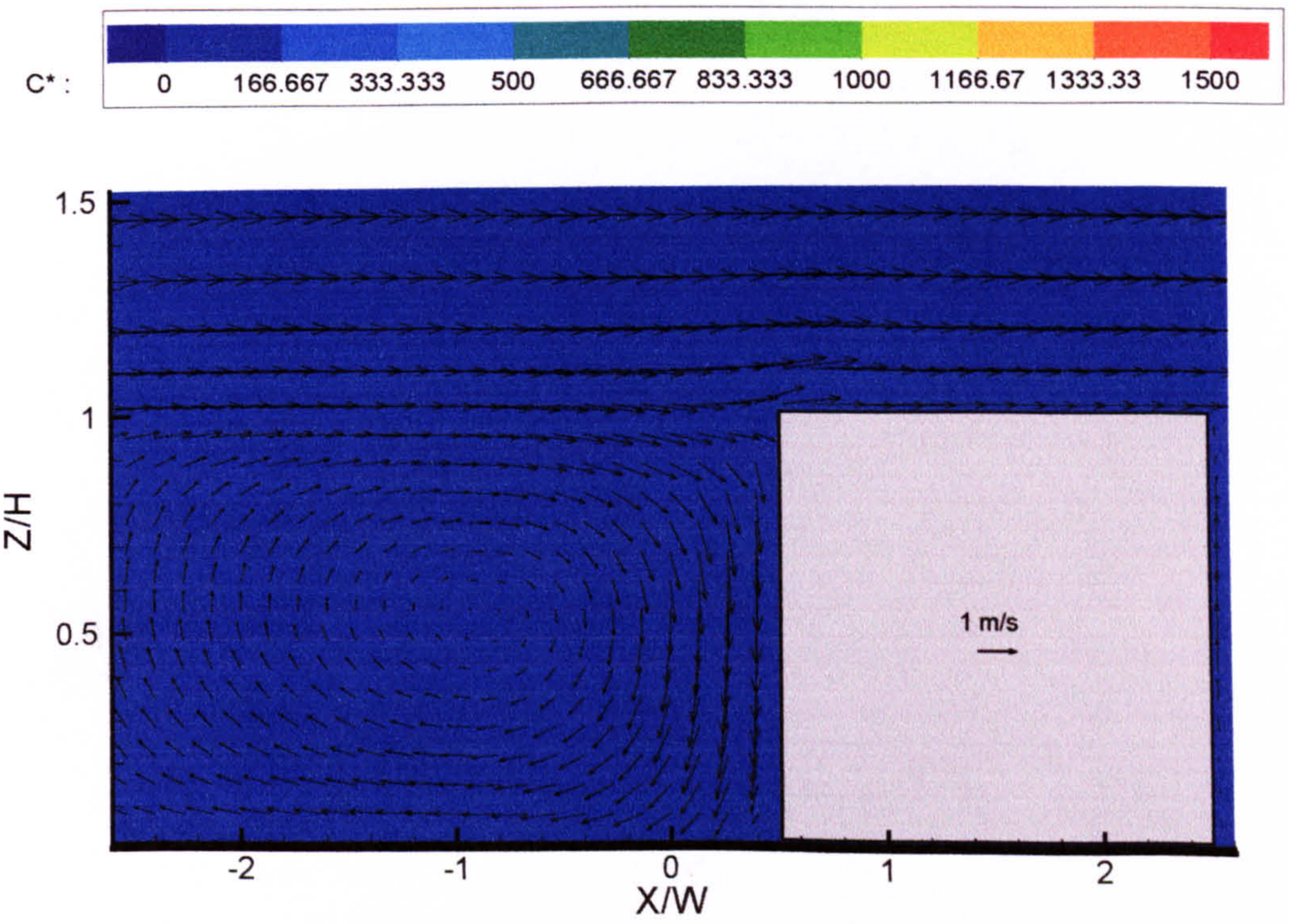

Figure 4.13g. Wind field and pollutant dispersion, as computed by MIMO for upwind building height of 0.0m (deep canyon).

4.2.4 Step-down notch results (deep case)

The step-down notch configuration is formed when the downwind building is lower in height from the upwind one. For this set of simulations the height of the downwind building was reduced in 10mm steps. The width of the street canyon was set at 30 mm thus the original configuration was that of a deep street canyon, (aspect ratio of ½).

In particular, a good examination of the results leads to the following main remarks:

In Figure 4.14a where the downwind building is 50 mm high, a clear double vortex system can be identified. The main vortex covers approximately the top 1/3 of the street canyon total depth and is significantly stronger than the secondary counter-rotating vortex developed at the bottom. Thus, the main vortex has diminished in size compared to the deep building symmetric case. Maximum pollutant concentrations appear on the lower downwind building corner and the bottom, with a tendency to diffuse towards the upwind building wall.

In Figures 4.14b and c, where the building height reduces further to 30 mm, the following observations can be made:

- The main vortex has departed from the street canyon, and it is elongated covering almost the whole downwind building roof.

- The secondary vortex extends over the canyon depth producing increased updraft and downdraft velocities near the upwind and downwind building walls.

- The bottom cell of pollution is still apparent, while the overall pollution pattern indicates a diffusion tendency from the upwind to the downwind building wall.

Furthermore, in Figures 4.14d and e, where the downwind building height reduces further to 10 mm, the following remarks can be made:

- The main vortex elongates further covering the whole of the downwind building roof, while its centre moves further downstream. The vortex starts to merge with the one downstream, creating an air mass transportation channel from the canyon downstream to the area above the downwind building.

- The pollutant cell remains at the bottom of the cavity, while a better dispersion pattern prevails over the canyon.

Finally, it was thought necessary to present the case where no downwind building existed, where certain similarities with section 4.2.2 were observed. As seen from Figure 4.14f, a main vortex extending across the created greater canyon area is established. The pollution cell has now shifted to the lower upwind building corner.

The main conclusion of this effort is that the characteristics of the flow field established and the pollutant dispersion pattern are similar to those in section 4.2.3. Small differences related to the dispersion strength inside the canyon are identified indicating here a lower level of pollution.

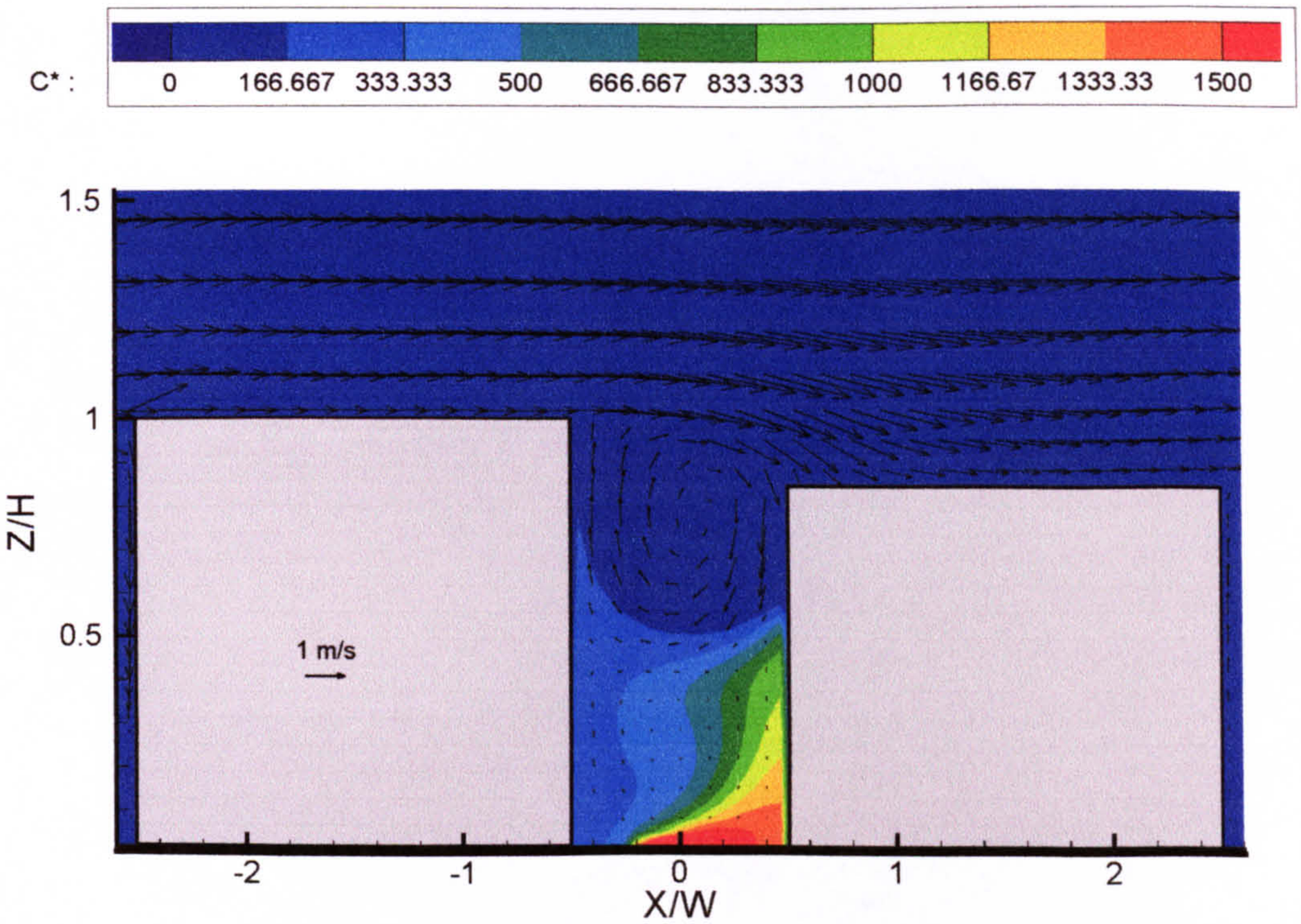

Figure 4.14a. Wind field and pollutant dispersion, as computed by MIMO for downwind building height of 0.05m (deep canyon).

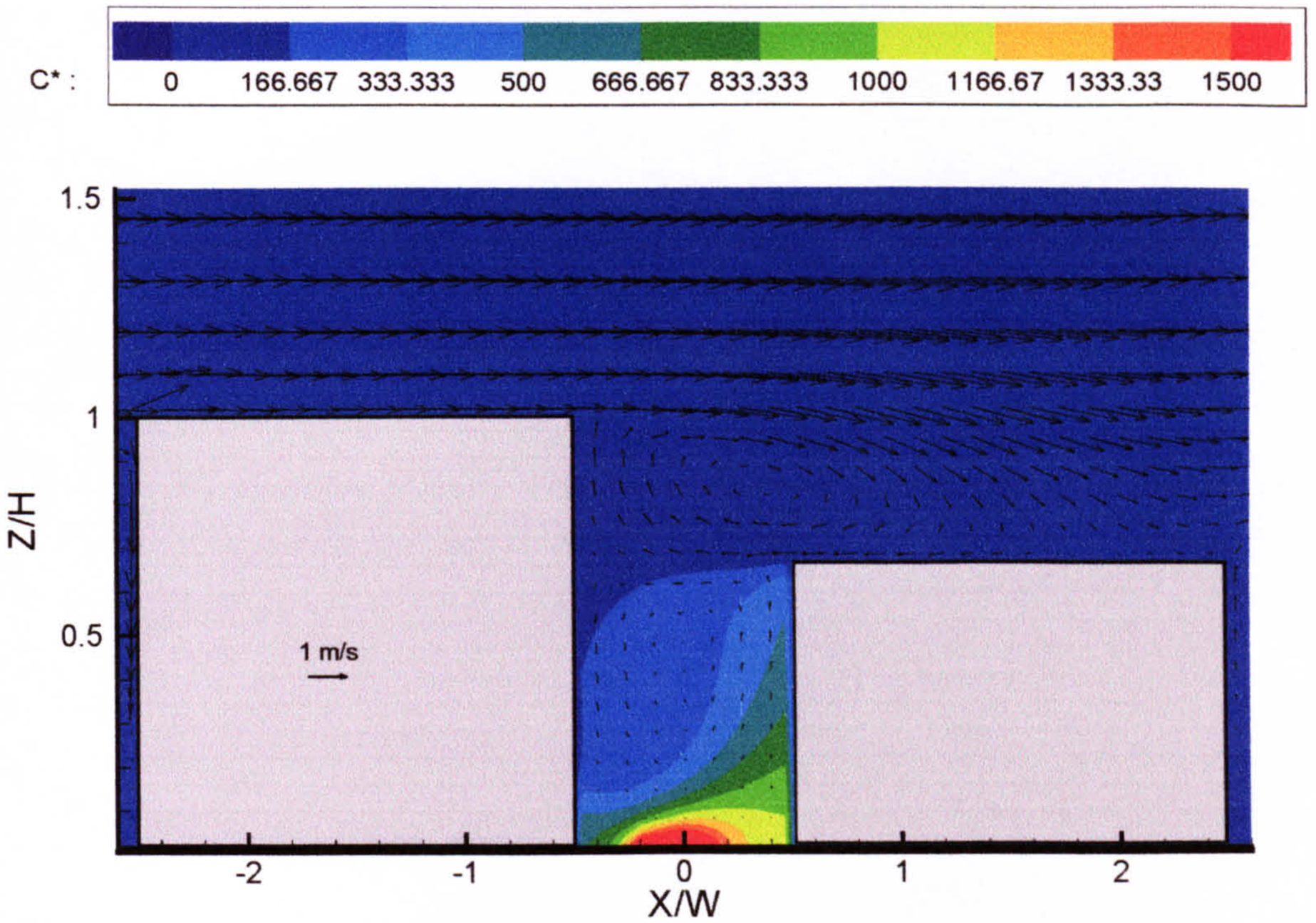

Figure 4.14b. Wind field and pollutant dispersion, as computed by MIMO for downwind building height of 0.04m (deep canyon).

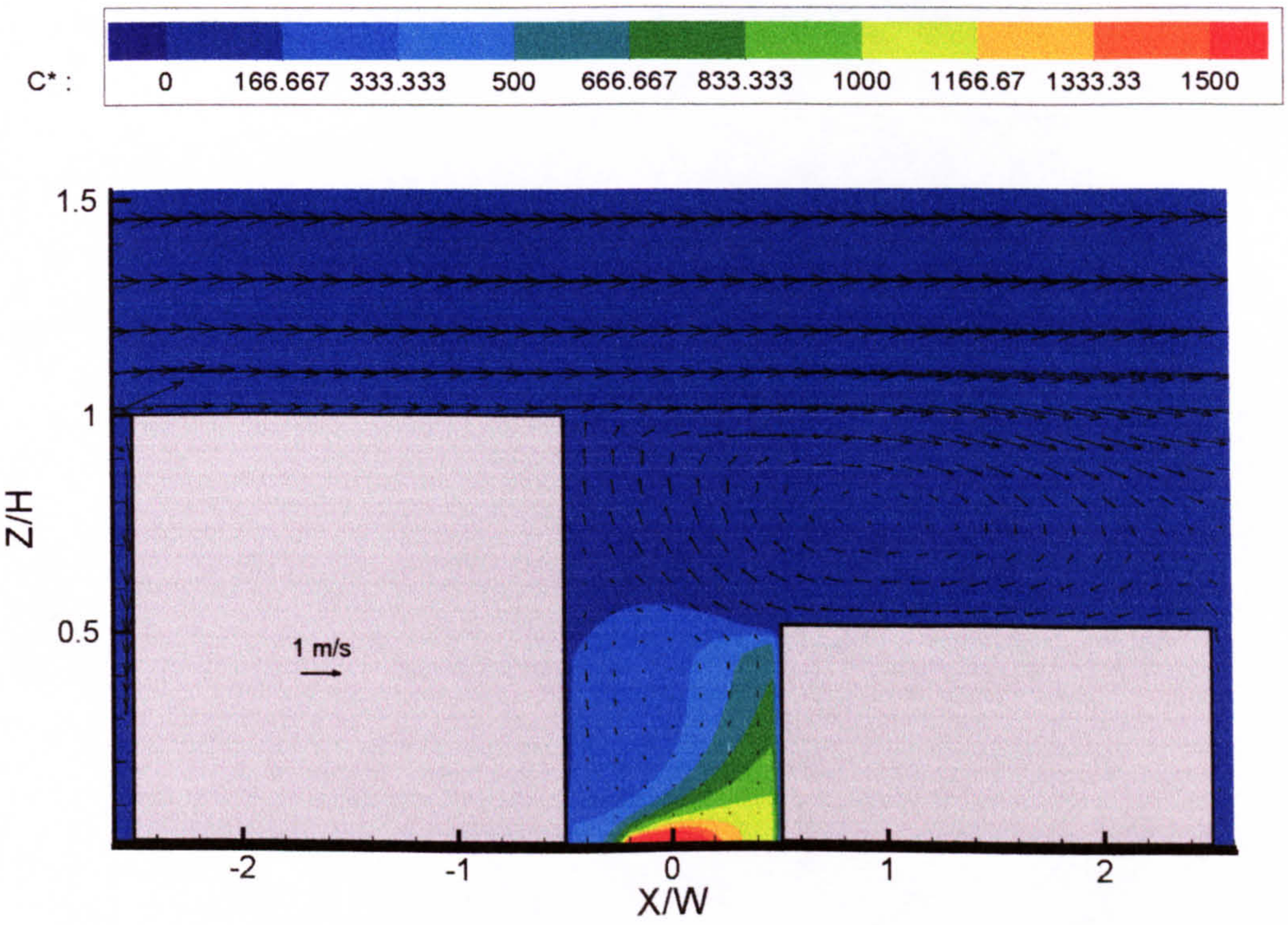

Figure 4.14c. Wind field and pollutant dispersion, as computed by MIMO for downwind building height of 0.03m (deep canyon).

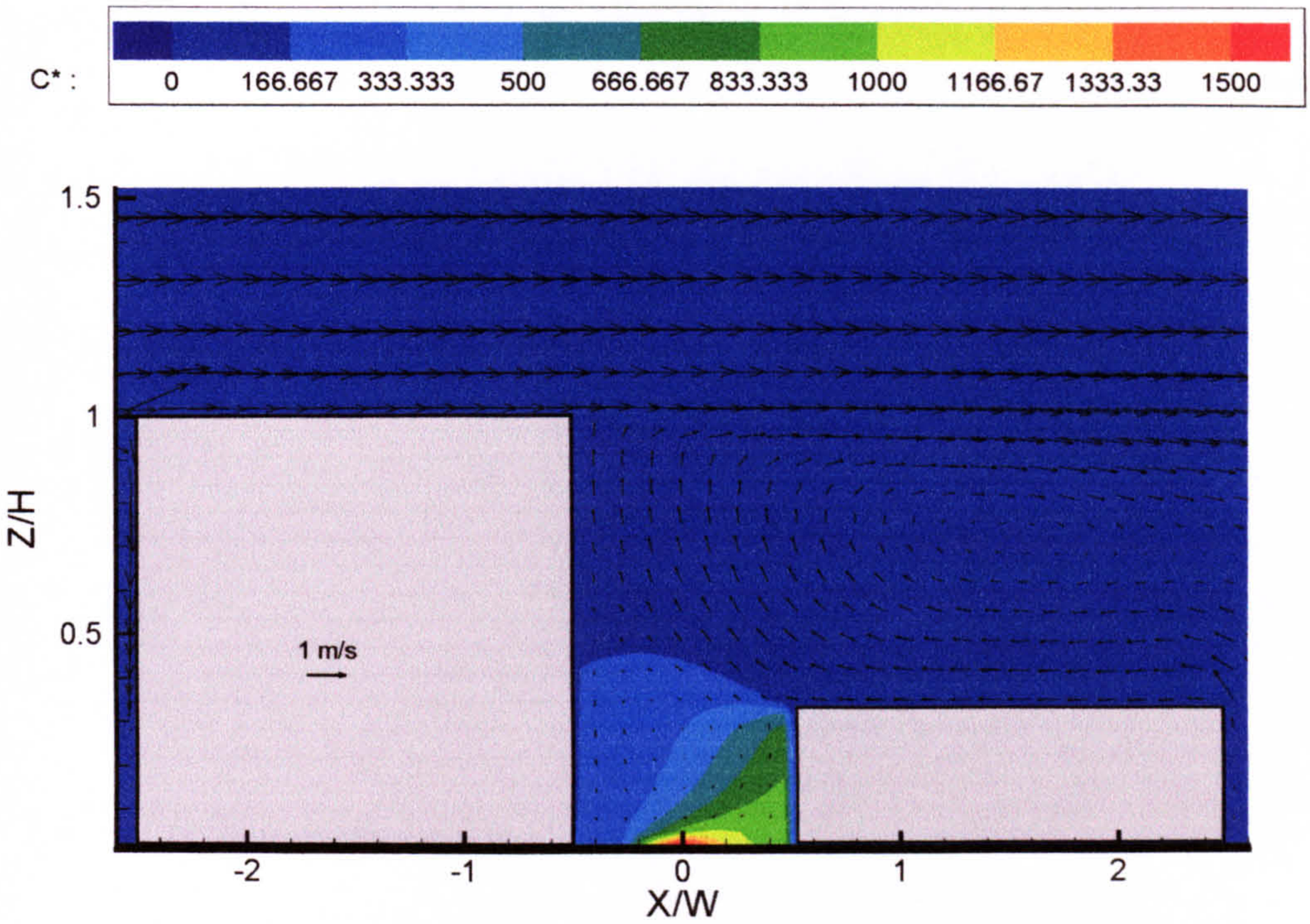

Figure 4.14d. Wind field and pollutant dispersion, as computed by MIMO for downwind building height of 0.02m (deep canyon).

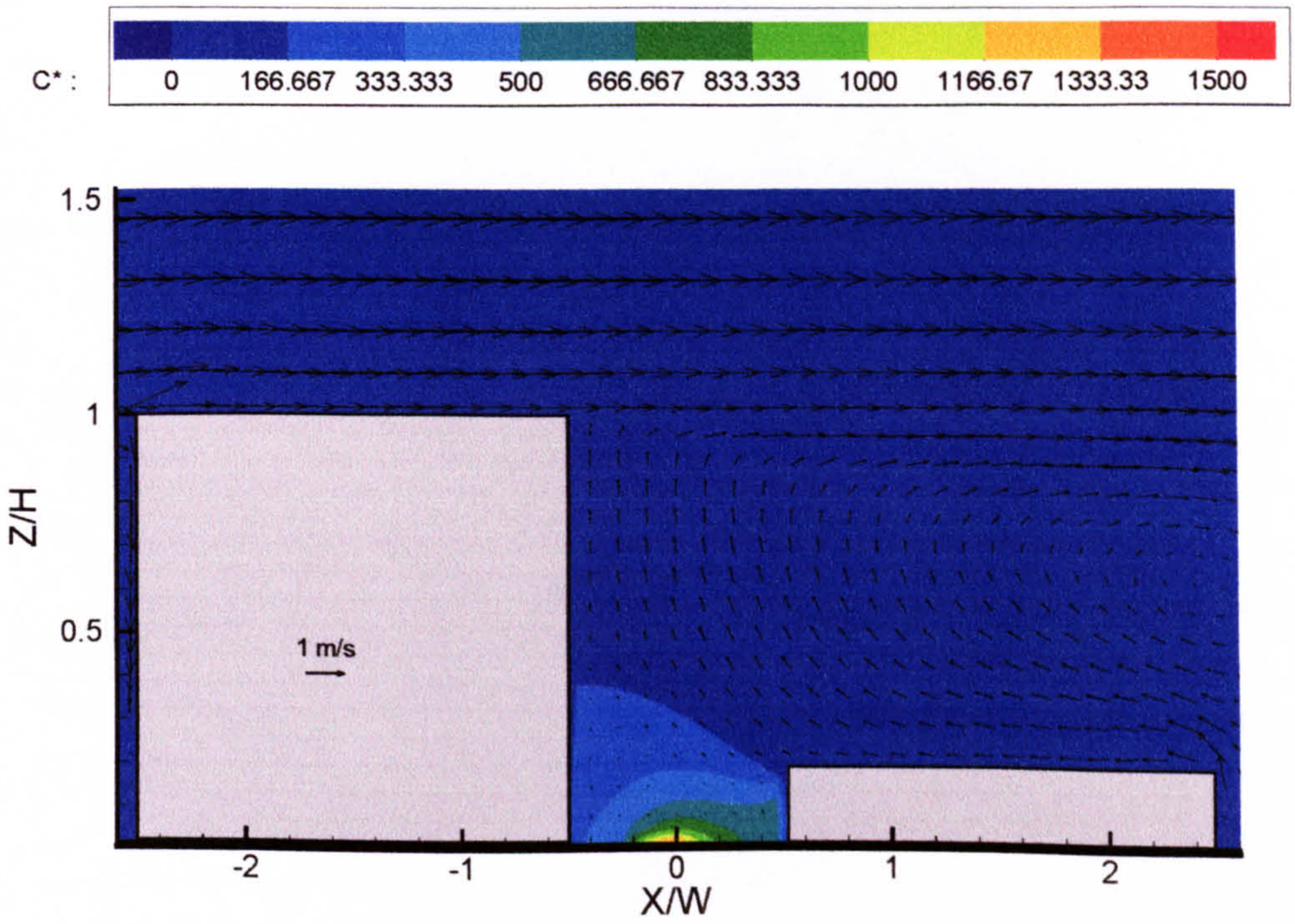

Figure 4.14e. Wind field and pollutant dispersion, as computed by MIMO for downwind building height of 0.01m (deep canyon).

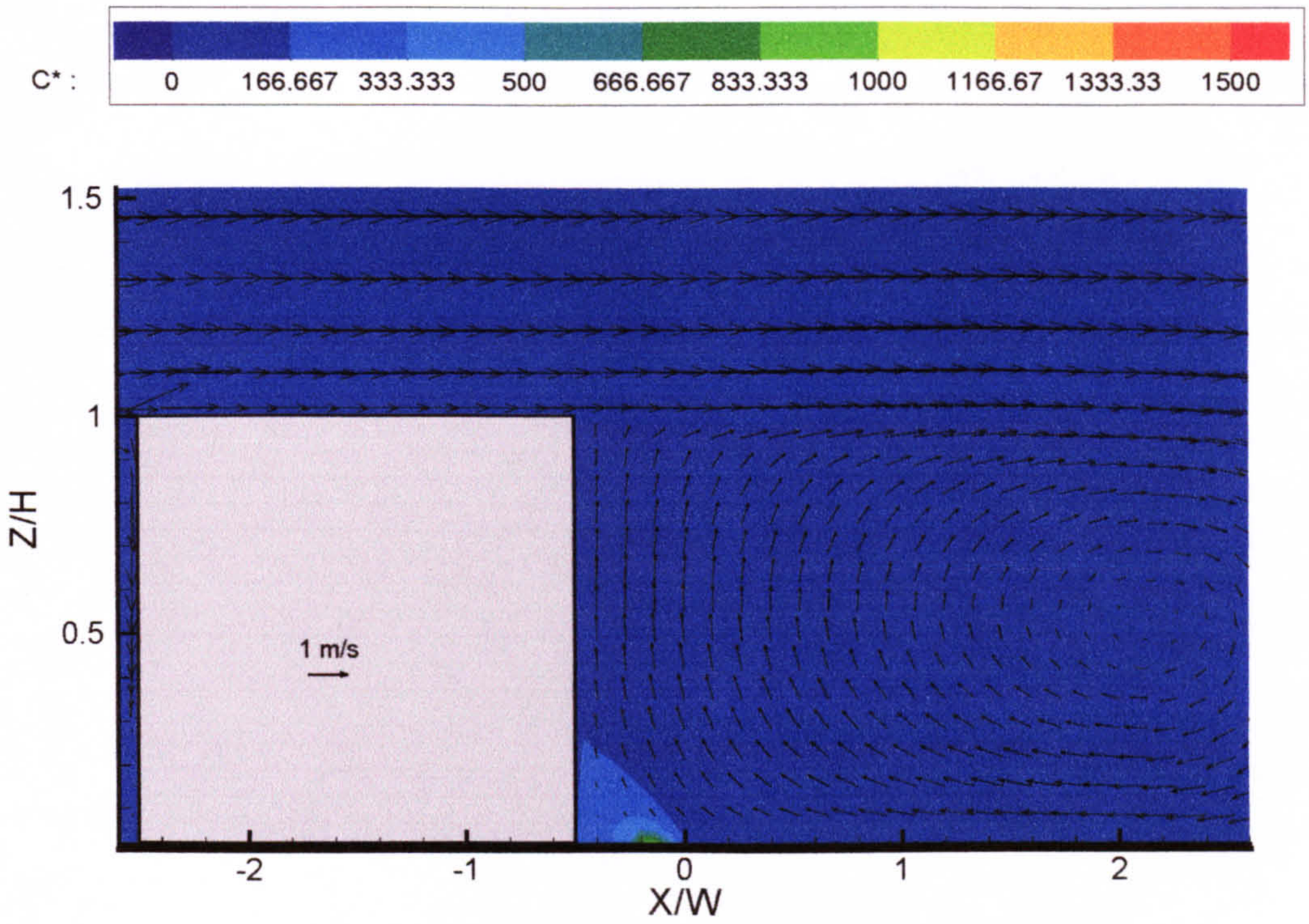

Figure 4.14f. Wind field and pollutant dispersion, as computed by MIMO for downwind building height of 0.0m (deep canyon).

4.2.5 Aspect ratio effect on dispersion

Following the previously presented cases, where two different aspect ratios were examined, (0.5, i.e. deep canyon, and 1, i.e. square canyon), it was thought necessary to further investigate cases of higher aspect ratios (wider streets). In this respect, two different street canyon configurations were examined, (aspect ratio of 3 and 1.5).

For the wide street canyon case, a main vortex forms whose centre is shifted towards the downwind building side of the street and is elongated along the horizontal. A minor vortex barely seen is formed at the lower upwind building corner, Figure 4.15a. In case a pollution source is placed close to the upwind building side, the pollutants disperse better than for the square canyon case, but still there remain high levels on the upwind building wall. If on the other hand the source is placed close to the downwind building, Figure 4.15b, a better dispersion pattern is formed, covering the major part of the street canyon area from the dispersion point until the upwind building wall.

If an aspect ratio of 1.5 is selected and the pollutant source is as for Figure 4.15a and 4.14b respectively, an almost identical flow field and pollution dispersion pattern is formed.

Concluding, the overall aspect ratio investigation the following main points are underlined:

- A single vortex extending across the street canyon with elongated shape and lower velocities is observed mainly for the wider canyons, (aspect ratio of 3).

- The wider street canyons are ventilated better and pollution levels are lower.

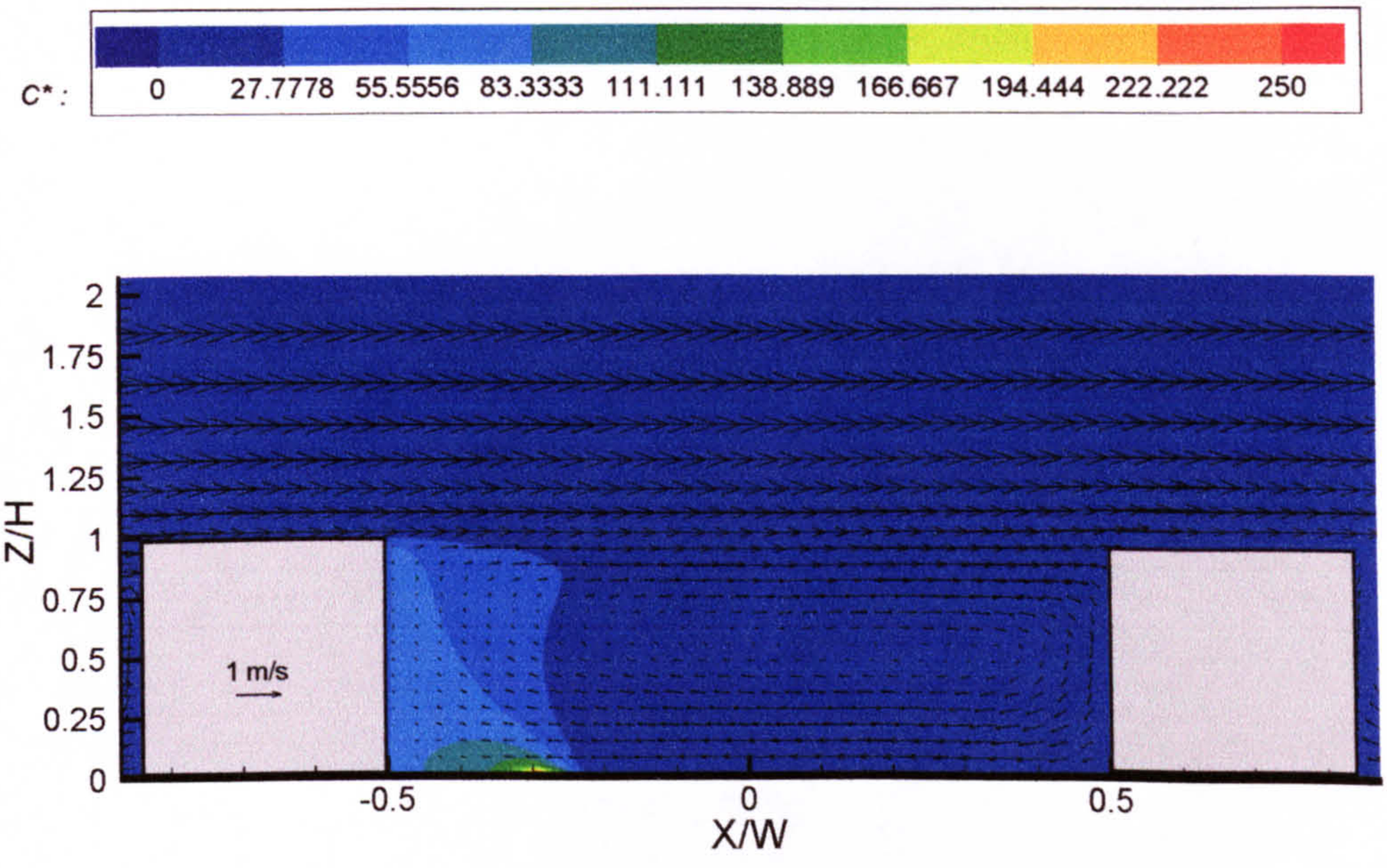

Figure 4.15a. Wind field and pollutant dispersion, from the upwind building side as computed by MIMO for the aspect ratio of 3.

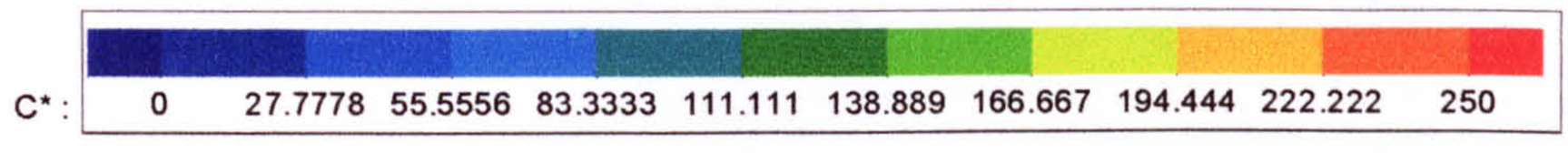

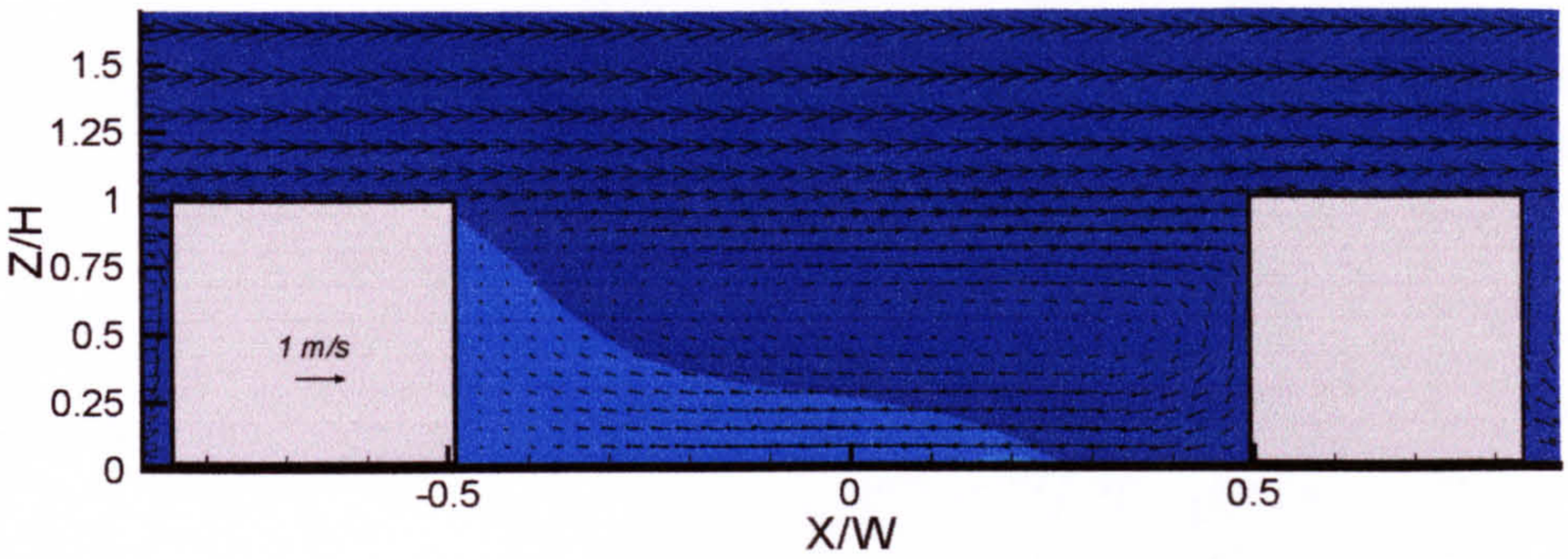

Figure 4.15b. Wind field and pollutant dispersion, from the downwind building side as computed by MIMO for the aspect ratio of 3.

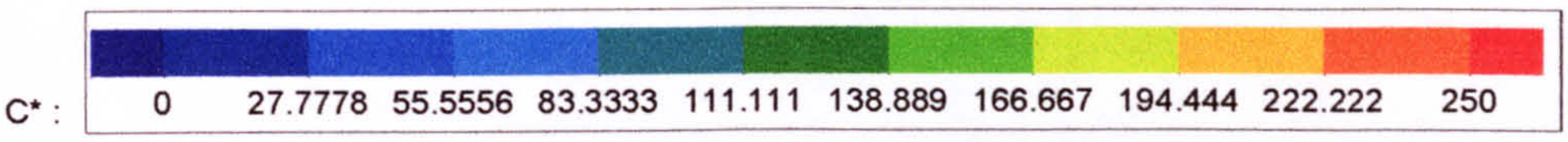

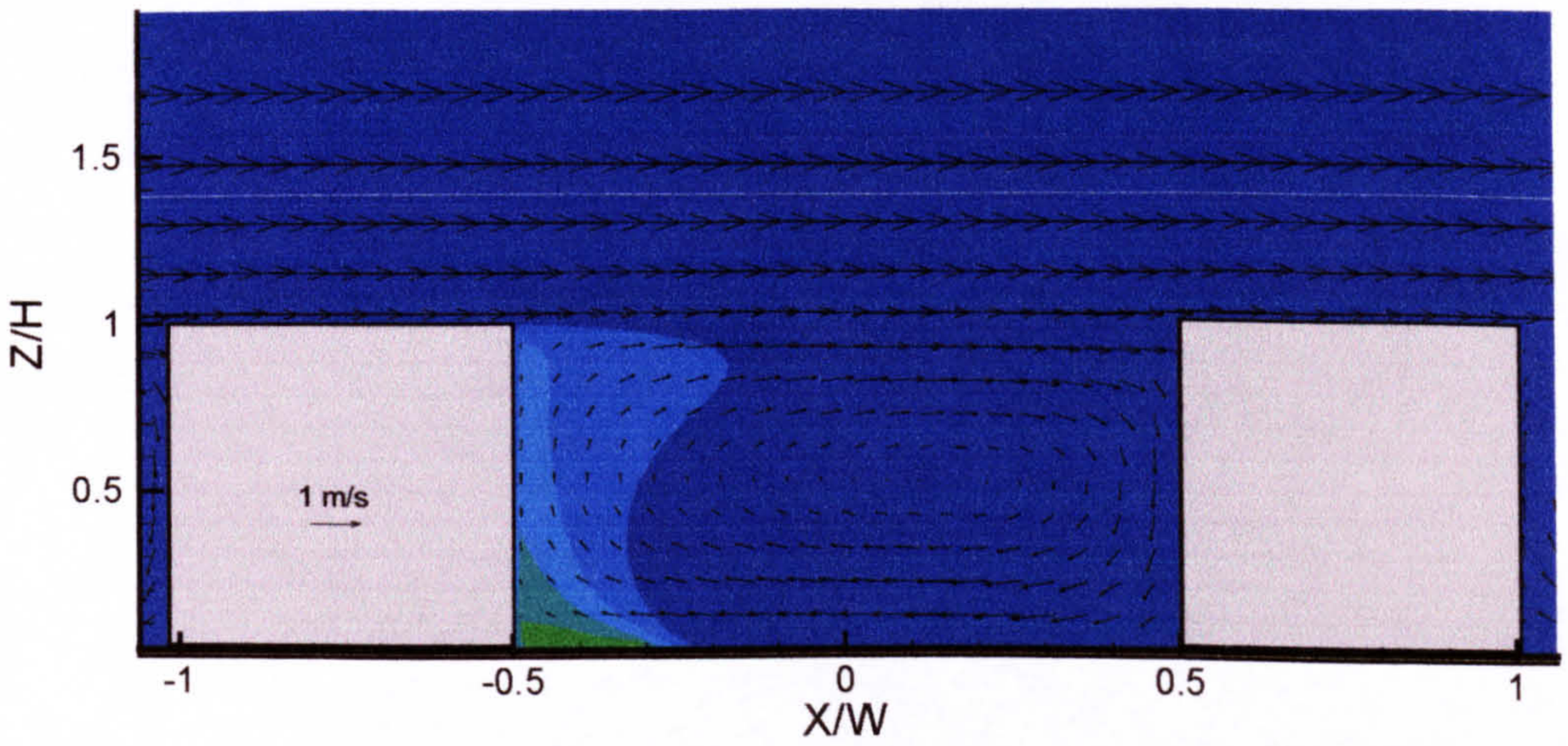

Figure 4.15c.Wind field and pollutant dispersion, from the upwind building side, as computed by MIMO for the aspect ratio of 1.5.

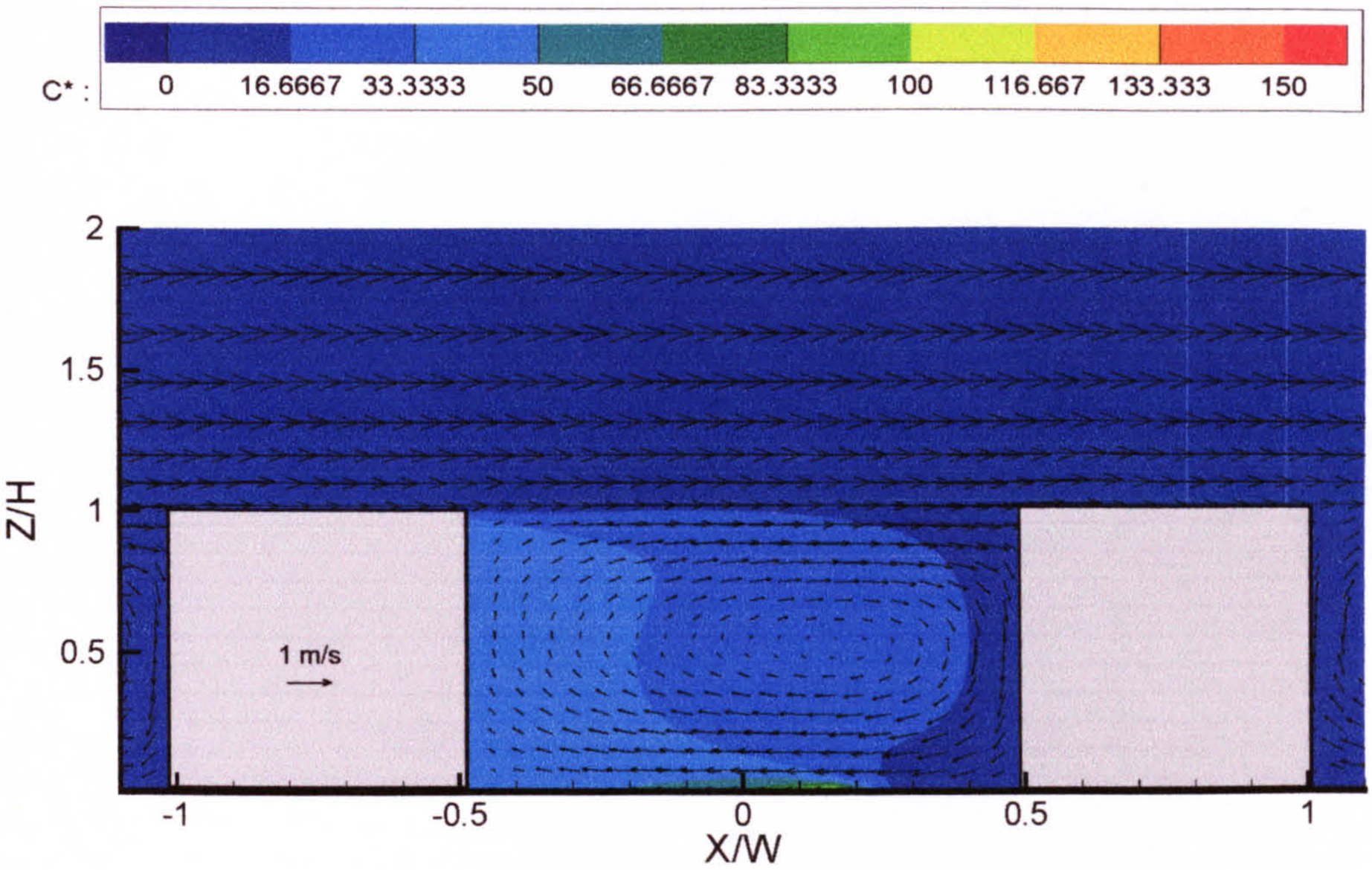

Figure 4.15d.Wind field and pollutant dispersion, from the downwind building side, as computed by MIMO for the aspect ratio of 1.5.

In the Tables presented below all the results obtained from the case studies performed in section 4.2 are grouped conveniently. Measurements were taken from the roof of the upwind building (up-roof), the upwind building wall (up-wall), the downwind building wall (down-wall) and the downwind building roof (down-roof) at the measurement positions indicated in Figure 4.2. In all the tables the first column indicates the measurement position in millimetres (see Figure 4.2), while the results from the wind tunnel experiment are given in the second column. It must be stressed at this point that the wind tunnel experimental results are only for the square and deep symmetric street canyon cases (upwind building height equals downwind building height), as no experiments were carried out for step-up or step-down notch configurations. However, they are included in the Tables as a source of reference. From the third until the last column of each table the results obtained from the numerical simulations are presented for different ratios of upwind to downwind building height, $\mathbf{H_u/H_d}$ or $\mathbf{H_d/H_u}$ depending on which building is diminished in height.

The dimensionless concentrations computed by MIMO for the **upwind building roof** for the **square step-up** and **step-down notches,** and the **deep step-up** and **step-down notches**, are presented in Tables 4.1, 4.2, 4.3 and 4.4 respectively. The results from the model calculations are extracted from the roof of the upwind building, while when the upwind building height is set to zero, results are extracted from the floor along the location where the upwind building used to be.

From the tables it becomes obvious that for both the **square** and **deep step-up** notch cases there is some pollutant escaping the canyon from the upwind building roof when the upwind building height is less than half the downwind building height. This comes in agreement with the wind and pollutant dispersion fields produced by the model, which indicate the formation of a return flow over the roof of the upwind building and into the canyon upstream. The concentration of pollution exiting from this side increases with decreasing upwind building height. On the contrary, for both the **square** and **deep step-down** notch cases no concentration escapes form the upwind roof since the pollutants are contained inside the street canyon by the vortex established. While the downwind building height is diminished the pollutants concentrate close to the source of emission and the lower upwind building corner, for the square configuration, and the downwind side for the deep configuration.

Position	Measured	$H_u/H_d=1$	$H_u/H_d=5/6$	$H_u/H_d=2/3$	$H_u/H_d=1/2$	$H_u/H_d=1/3$	$H_u/H_d=1/6$	$H_u/H_d=0$
15	0	0	0	0	0.16	6.75	17.63	21.72
30	0	0	0	0	0.44	9.23	20.28	23.23
45	0	0	0	0.01	1.81	14.74	25.09	25.35

Table 4.1. Dimensionless concentrations as computed by MIMO for the roof of the upwind building for the square step-up notch configuration.

Position	Measured	$H_d/H_u=1$	$H_d/H_u=5/6$	$H_d/H_u=2/3$	$H_d/H_u=1/2$	$H_d/H_u=1/3$	$H_d/H_u=1/6$	$H_d/H_u=0$
15	0	0	0	0	0	0	0	0
30	0	0	0	0	0	0	0	0
45	0	0	0	0	0	0	0	0

Table 4.2. Dimensionless concentrations as computed by MIMO for the roof of the upwind building for the square step-down notch configuration.

Position	Measured	$H_u/H_d=1$	$H_u/H_d=5/6$	$H_u/H_d=2/3$	$H_u/H_d=1/2$	$H_u/H_d=1/3$	$H_u/H_d=1/6$	$H_u/H_d=0$
15	2	0	0	0.004	7.74	27.04	33.20	32.87
30	1	0	0	0.034	11.47	29.93	35.83	34.78
45	1	0	0	0.381	19.21	37.57	40.60	37.83

Table 4.3. Dimensionless concentrations as computed by MIMO for the roof of the upwind building for the deep step-up notch configuration.

Position	Measured	$H_d/H_u=1$	$H_d/H_u=5/6$	$H_d/H_u=2/3$	$H_d/H_u=1/2$	$H_d/H_u=1/3$	$H_d/H_u=1/6$	$H_d/H_u=0$
15	2	0	0	0	0	0	0	0
30	1	0	0	0	0	0	0	0
45	1	0	0	0	0	0	0	0

Table 4.4. Dimensionless concentrations as computed by MIMO for the roof of the upwind building for the deep step-down notch configuration.

The figures in Tables 4.5, 4.6, 4.7 and 4.8 were extracted from the vicinity of the upwind building wall. The figures highlighted with the violet colour indicate that the pollutant concentration was extracted along an imaginary line extending above the upwind building since it was lower than the location where the measurement was performed (see Figure 4.2 for measurement positions).

For the **square** and the **deep step-up** notch cases the numbers confirm the behaviour recognised both via the velocity and concentration plots and Tables 4.1 and 4.3. When the upwind building is reduced in height, the pollution cell is concentrated close to the

lower upwind building corner. However, when the upwind building height is half the downwind building height, the return flow established transports pollutants from the step-up notch to the canyon upstream thus, increasing concentration along the upwind wall.

When a **square** and **deep step-down** configuration exists the pollutants seem to oscillate between the upwind and downwind sides of the street canyon, which explains the variations observed on the concentration levels. Concerning the **square** canyon the pollution levels remain almost the same presenting a 5% decrease. When a **deep** canyon exists the variations observed are more pronounced, firstly the concentration levels increase by about 40% and then decrease by about 60%.

Position	Measured	$H_u/H_d=1$	$H_u/H_d=5/6$	$H_u/H_d=2/3$	$H_u/H_d=1/2$	$H_u/H_d=1/3$	$H_u/H_d=1/6$	$H_u/H_d=0$
4	78	62	1.52	0.94	2	4.50	6.50	7.82
15	88	70	71.35	8.31	7	9.78	10.82	10.94
30	97	69	66.62	65.35	30.82	23.30	19.08	15.15
45	116	86	80.93	77.03	67.86	49.11	32	21

Table 4.5. Dimensionless concentrations as computed by MIMO for the upwind building wall for the square step-up notch configuration.

Position	Measured	$H_d/H_u=1$	$H_d/H_u=5/6$	$H_d/H_u=2/3$	$H_d/H_u=1/2$	$H_d/H_u=1/3$	$H_d/H_u=1/6$	$H_d/H_u=0$
4	78	62	72	74	62.56	54.60	56	50
15	88	70	69.5	77	68.04	59.80	60.93	54.56
30	97	69	60	83.5	77.87	68.72	71	62.89
45	116	86	78	105	92.62	80.96	90	78.22

Table 4.6. Dimensionless concentrations as computed by MIMO for the upwind building wall for the square step-down notch configuration.

Position	Measured	H_u/H_d=1	H_u/H_d=5/6	H_u/H_d=2/3	H_u/H_d=1/2	H_u/H_d=1/3	H_u/H_d=1/6	H_u/H_d=0
4	115	152.28	1.71	5.72	8	10.04	10.66	11.82
15	113	146.10	128.14	22.28	23.16	18	15	14.50
30	117	145.14	157.87	138	70	38.41	19.42	15.12
45	125	271.30	342.15	299.54	198.05	100.96	45.76	15.94

Table 4.7. Dimensionless concentrations as computed by MIMO for the upwind building wall for the deep step-up notch configuration.

Position	Measured	H_d/H_u=1	H_d/H_u=5/6	H_d/H_u=2/3	H_d/H_u=1/2	H_d/H_u=1/3	H_d/H_u=1/6	H_d/H_u=0
4	115	152.28	12	90	75	73.56	69.71	51.75
15	113	146.10	122.96	110.49	97.43	83.92	78.89	63.41
30	117	145.14	200	138.17	134.36	122.97	113.67	73.77
45	125	271.30	254.58	150.96	155.66	180.37	184.21	73.77

Table 4.8. Dimensionless concentrations as computed by MIMO for the upwind building wall for the deep step-down notch configuration.

In Tables 4.9, 4.10, 4.11 and 4.12 the concentration levels obtained from the vicinity of the downwind building wall are presented for the **square** and **deep step-up** and **step-down** cases. When a step-up notch configuration is formed the flow established urges the pollutants towards the upwind building side of the canyon and also better ventilation is accomplished. With lowering gradually the upwind building the already low concentrations for the **square** case (approximately 50% lower than for upwind building wall) become even lower as the pollutants are "sucked" upstream. The pollutants are distributed almost evenly along the wall and their level drops by almost 70%. For the **deep** canyon case, it is reminded that the concentration peak is observed at the lower downwind building corner and the pollutants are distributed unevenly along the downwind building wall (concentration level at lower downwind building corner almost 7 times higher). In this case the concentration levels drop unevenly

from 7 times on the top of the downwind building corner to about 25 times on the lower downwind building corner.

The behaviour of the pollution cell is quite different when a step-down configuration is applied for the square and deep canyon configuration. In the case where a square canyon exists the concentration levels increase abruptly (4 to 5 times the initial concentration) at the lower downwind building corner when the upwind building is half the downwind building height. This situation is reversed when the upwind building is 10mm high or removed, when the flow in the step-down notch is unified with the flow of the canyon downstream. In the deep canyon case an interesting variation in the concentration levels is observed, firstly the concentration levels exhibit a significant increase at the lower downwind building corner (3 times higher than the initial concentration), when the downwind building is 50mm high. As its height reduces the concentration levels drop but to become 2 times higher from the symmetric case. At higher locations along the downwind building wall the pollutant levels drop since the flow established favours the assembly of the polluted mass at the lower downwind building corner. Pollutant levels drop dramatically when the downwind building is 10mm high or removed.

Position	Measured	$H_u/H_d=1$	$H_u/H_d=5/6$	$H_u/H_d=2/3$	$H_u/H_d=1/2$	$H_u/H_d=1/3$	$H_u/H_d=1/6$	$H_u/H_d=0$
4	28	30	15.68	11.85	10.20	9.28	7.25	6.47
15	33	33	22.20	15.25	13.51	11.57	8.59	7.27
30	41	32	25.56	18.55	18.34	14.65	10.12	8.06
45	43	30	25.65	19.77	21.16	17.39	11.26	8.49

Table 4.9. Dimensionless concentrations as computed by MIMO for the downwind building wall for the square step-up notch configuration.

Position	Measured	H_d/H_u=1	H_d/H_u=5/6	H_d/H_u=2/3	H_d/H_u=1/2	H_d/H_u=1/3	H_d/H_u=1/6	H_d/H_u=0
4	28	30	18.43	15.18	16.55	16.66	15.71	16.38
15	33	33	30.94	23.21	19.49	18.24	16.38	16.82
30	41	32	34.07	21.82	19.37	14.50	11.77	12.31
45	43	30	32.97	24.13	144.34	122.11	9.35	9.26

Table 4.10. Dimensionless concentrations as computed by MIMO for the downwind building wall for the square step-down notch configuration.

Position	Measured	H_u/H_d=1	H_u/H_d=5/6	H_u/H_d=2/3	H_u/H_d=1/2	H_u/H_d=1/3	H_u/H_d=1/6	H_u/H_d=0
4	44	49.16	23	19.38	16.38	10.37	8.98	8.91
15	62	68.86	37.60	29.38	20.79	12.89	10.28	10
30	172	180	42.30	47.23	42.47	18.82	11.74	10.98
45	300	323.15	191.60	109.91	156.56	58.20	12.80	11.32

Table 4.11. Dimensionless concentrations as computed by MIMO for the downwind building wall for the deep step-up notch configuration.

Position	Measured	H_d/H_u=1	H_d/H_u=5/6	H_d/H_u=2/3	H_d/H_u=1/2	H_d/H_u=1/3	H_d/H_u=1/6	H_d/H_u=0
4	44	49.16	34.84	33.00	31.55	31.82	30	25
15	66	68.86	41.89	29.74	24.53	29.28	31.46	24.56
30	172	180	442.18	399.36	98.45	24.35	27.43	16.56
45	300	323.15	904.03	627.35	673.11	598.17	53.28	12.37

Table 4.12. Dimensionless concentrations as computed by MIMO for the downwind building wall for the deep step-down notch configuration.

The concentration levels identified on the downwind building roof are low for the symmetric configuration, given in Tables 4.13, 4.14, 4.15 and 4.16. In the case where a step-up notch is created the quantity of pollutants exiting the canyon above the

downwind building roof is reduced to less than half. This happens because of the wind field established, which transports the pollutants backwards towards the canyon upstream. When a step-down notch exists, the polluted air mass exiting the canyon remains almost constant, since in this case the wind field established favours such behaviour.

Position	Measured	$H_u/H_w=1$	$H_u/H_d=5/6$	$H_u/H_d=2/3$	$H_u/H_d=1/2$	$H_u/H_d=1/3$	$H_u/H_d=1/6$	$H_u/H_d=0$
15	25	12	8.16	6.49	5.97	5.48	4.90	4.60
30	21	10	7.04	5.56	5.15	4.78	4.37	4.16
45	19	9	6.06	4.96	4.61	4.37	4	3.84

Table 4.13. Dimensionless concentrations as computed by MIMO for the downwind building roof for the square step-up notch configuration.

Position	Measured	$H_d/H_u=1$	$H_d/H_u=5/6$	$H_d/H_u=2/3$	$H_d/H_u=1/2$	$H_d/H_u=1/3$	$H_d/H_u=1/6$	$H_d/H_u=0$
15	25	12	11.45	13.65	11.15	9.29	7.69	6.87
30	21	10	9.38	10.47	9.40	8.22	7.05	6.59
45	19	9	8.07	9.01	8.24	7.23	6.42	6.37

Table 4.14. Dimensionless concentrations as computed by MIMO for the downwind building roof for the square step-down notch configuration.

Position	Measured	$H_u/H_d=1$	$H_u/H_d=5/6$	$H_u/H_d=2/3$	$H_u/H_d=1/2$	$H_u/H_d=1/3$	$H_u/H_d=1/6$	$H_u/H_d=0$
15	33	12.61	9.66	8.33	7.39	6.28	5.98	6.03
30	25	10.32	7.95	6.96	6.31	5.41	5.24	5.31
45	22	8.79	6.66	5.94	5.48	4.93	4.81	4.89

Table 4.15. Dimensionless concentrations as computed by MIMO for the downwind building roof for the deep step-up notch configuration.

Position	Measured	H_d/H_u=1	H_d/H_u=5/6	H_d/H_u=2/3	H_d/H_u=1/2	H_d/H_u=1/3	H_d/H_u=1/6	H_d/H_u=0
15	33	12.61	15.66	15.31	11.78	10.37	10.03	11.52
30	24	10.32	10.89	11.51	9.97	9.44	9.63	11.40
45	22	8.49	8.94	9.53	8.67	8.77	9.39	11.24

Table 4.16. Dimensionless concentrations as computed by MIMO for the downwind building roof for the deep step-down notch configuration.

In Tables 4.17 and 4.18 the pollutant concentration levels reached, when the streets are made wider, on the upwind building wall are lower even though the emission source is quite close to this side of the street. On the downwind building wall pollution is distributed evenly with respect to height, and is of very low concentration, except for the square canyon case (see Table 4.10). The flow field established favours accumulation of pollutants at the upwind building side of the street and the wider canyon gives rise to higher wind velocities. When the pollution source is placed close to the downwind building wall, concentrations measured on the downwind building side are quite lower for the wider streets than for the square canyon. Furthermore, they are evenly distributed with height and the same holds true for the upwind building wall where, pollutant concentration is of the order of 50.

Position	Measured	H/W=1	H/W=1/3	H/W=2/3
4	78	62	50	55
15	88	70	55	61
30	97	69	65	68
45	116	86	70	85

Table 4.17. Dimensionless concentrations computed by MIMO for different aspect ratios when the emission source is placed close to the upwind building.

Position	Measured	H/W=1	H/W=1/3	H/W=2/3
4	28	30	15	21
15	33	33	16	15
30	41	32	18	24
45	43	30	14	25

Table 4.18. Dimensionless concentrations computed by MIMO for different aspect ratios when the emission source is placed close to the downwind building.

4.2.6 Effect of upwind characteristics

In this part of the work completed all the input parameters were kept the same (velocity, turbulent kinetic energy and dissipation) and so did the computational domain for both the square and the deep canyon configurations. Furthermore, the wall treatment scheme was the Sondak and Pletcher one as suggested in section 4.1.6. In this part the effects of the upwind (from the source) conditions were studied. The computational domain was kept the same, i.e. it contained five street canyons. The **emission source** was **placed** primarily in the first street canyon of the domain, that is the **inlet street canyon**. The width of the upwind building is half the street canyon width. Secondly the source of emissions is placed in the **middle street canyon** (i.e. its original placement), simulating thus, the addition of two more street canyons excluding the inlet building. Finally, the **emission source** was placed at the **last street canyon** of the computational domain and so another two street canyons were added. This procedure was performed for both the square and the deep street canyon configurations.

In Figure 4.16 a comparison between the measured and calculated concentrations is presented for the square canyon configuration. The calculated concentrations are coded as follows: 'first' canyon is the one with no street canyons placed upstream, 'third' canyon is the case where there exist two upstream canyons, 'fifth' canyon is the one with four canyons upstream. The obtained results indicate that concentration of pollutants in the 'first' canyon is quite lower than in the 'third' canyon, which in turn is lower than the calculated concentrations in the 'fifth' canyon.

Figure 4.17 shows the comparison between the computed concentrations for the deep canyon case for the first, third and fifth canyons and also of the measured concentrations. At the first measuring point, which is 4mm below the top of the upwind building the lowest concentration is recorded at the first canyon and the highest at the fifth canyon. Moving along the street canyon concentrations become almost equal with very small deviations. Nevertheless, it can be concluded that the first canyon is ventilated better than the other two but only for the top part.

The results obtained above may lead to two important conclusions:

- The placement of buildings on the flow leads to the development of an internal boundary layer, which means that the flow shifts above the buildings and the air exchange between the flow within the street and the outer flow is impeded. This explains the fact that pollutants are dispersed better out of the 'first' canyon and then worse out of the 'third' and 'fifth' canyons as a result of the gradual development of the internal boundary layer and the decoupling from the flow above. This is also supported by Kastner-Klein and Plate (1999).
- When a deep street canyon configuration is realised the situation described above does not influence significantly dispersion of pollutants out of the streets due to the complex flow field developed, which isolates the lower part of the street where the pollutants are emitted from the upper part.

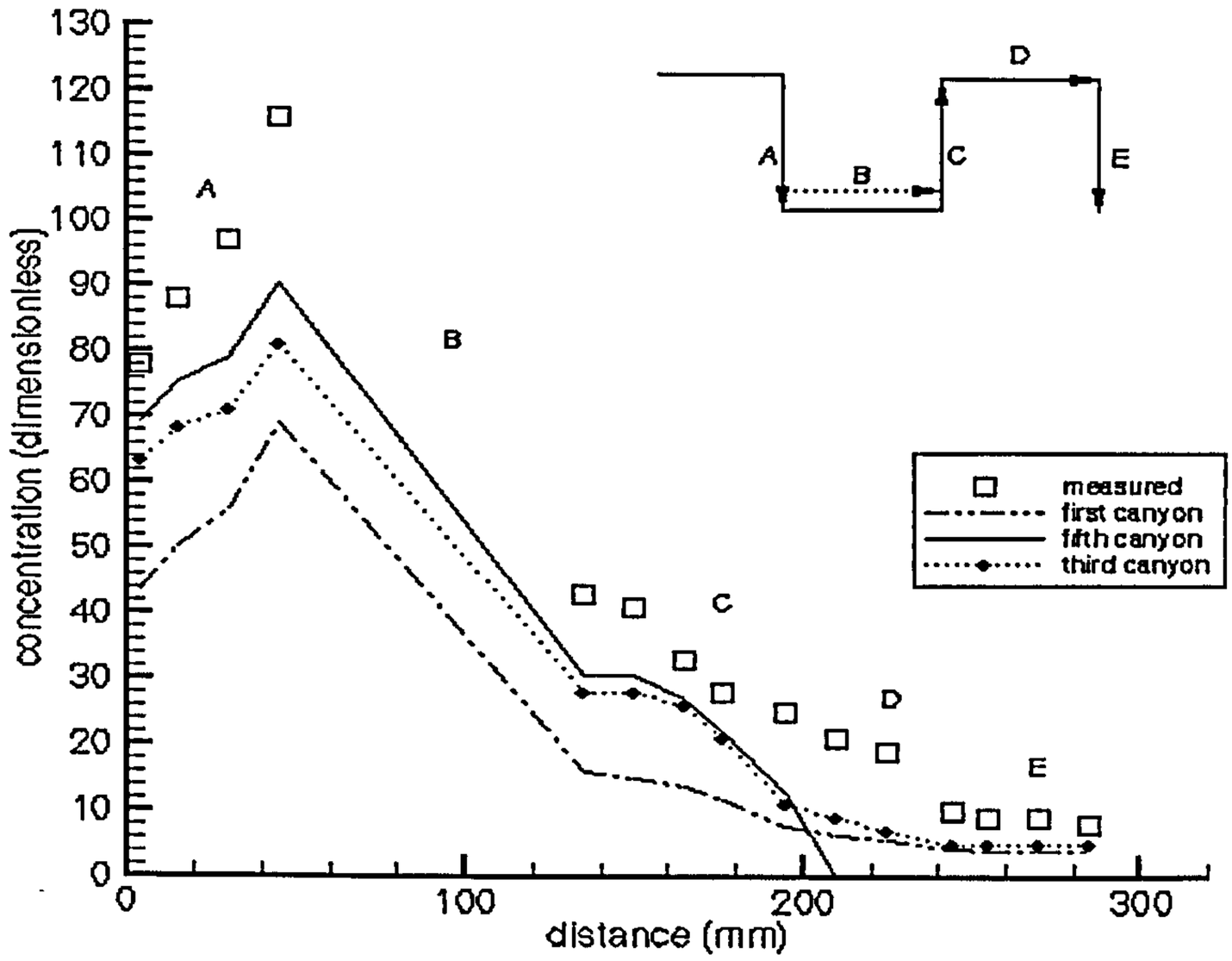

Figure 4.16. Comparison of concentrations for the square canyon cases.

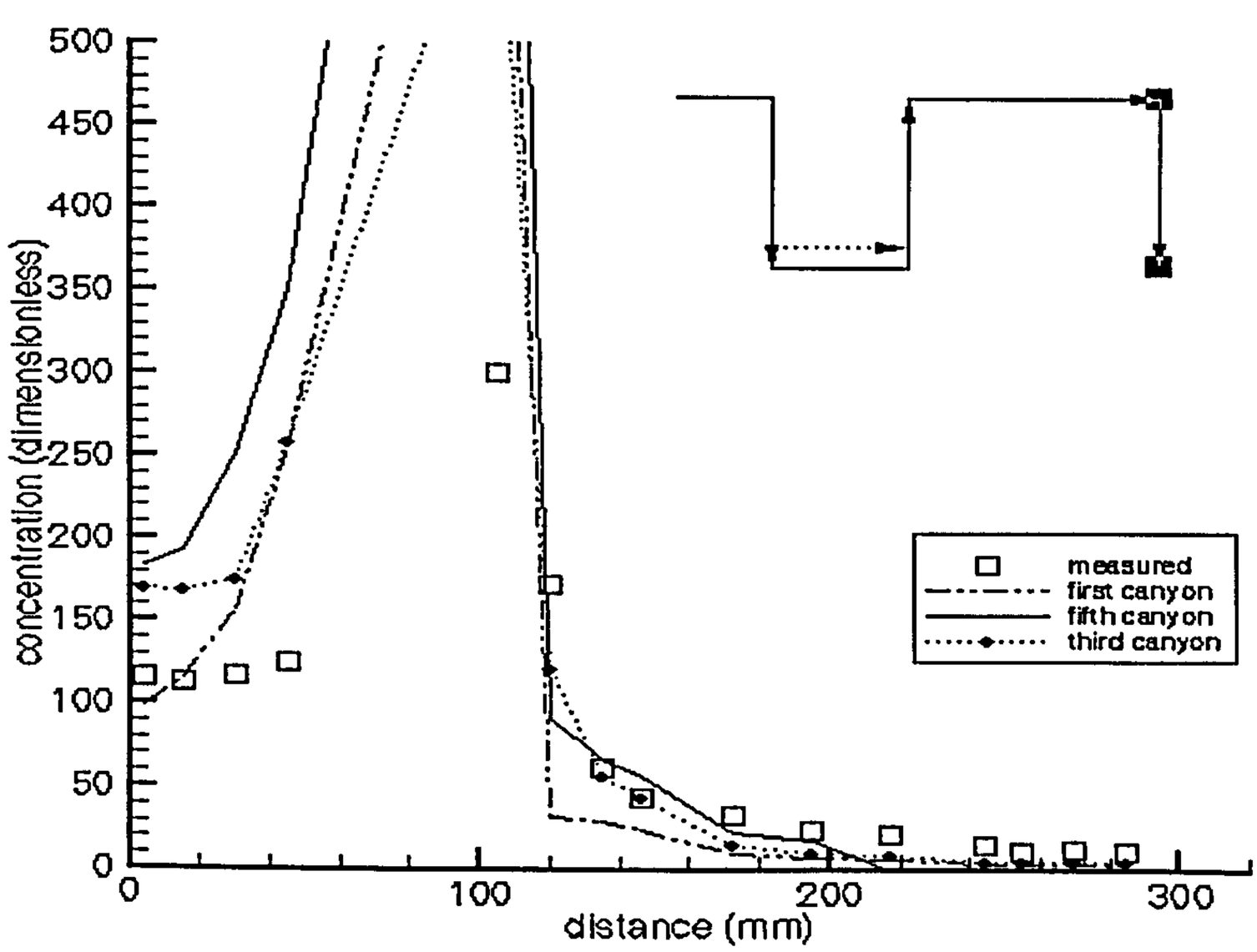

Figure 4.17. Comparison of concentrations for the deep canyon cases.

5 Fast Chemistry

The emission of a variety of pollutant gases, e.g., nitrogen oxides (NO_x), and volatile organic compounds (VOC's), into the troposphere may present a health risk either directly, or as a result of their oxidation. This can lead to a variety of secondary oxidised products, many of which are potentially more harmful than their precursors. Because much of the chemistry is driven by the presence of sunlight, the oxidised products are commonly referred to as secondary photochemical pollutants and include photochemical oxidants such as ozone, O_3. The production of elevated levels of O_3 at ground level is of particular concern, since it is known to have adverse effects on human health, vegetation and materials, (PORG, 1997). Established air quality standards for O_3 are frequently exceeded and the formulation of control policies is therefore a major objective of environmental policy. Nevertheless, other pollutants that are formed on local or regional scales in the PBL may also have direct impacts (e.g., PAN), and play wider roles in atmospheric chemistry.

Photochemical air pollution first identified in Los Angeles in the 1940's, is now a widespread phenomenon in many of the world's population centres. Consequently, considerable attention has been given to identifying and quantifying chemical processes leading to the generation of O_3 and other secondary photochemical pollutants in the PBL. This has involved the laboratory study of many hundreds of chemical reactions and a significant amount of evaluated chemical kinetics and photochemical data have been made available, (e.g., Atkinson et al., 1997a,b; DeMore et al., 1997).

5.1 Introductory remarks

Reactions taking place in the troposphere generate secondary pollutants such as O_3. NO is oxidised rapidly to NO_2 by O_3, this explains low O_3 concentrations close to sources of NO_x such as streets. NO_2 then breaks down photochemically under the action of ultra-violet light to generate NO and atomic oxygen ($O^{\cdot}$). The latter combines with molecular oxygen, (O_2) to produce O_3. The presence of peroxy radicals derived from atmospheric reactions of hydrocarbons, (HC) and other organic compounds ensures that NO is oxidised back to NO_2 without loss of O_3. Thus an

ozone-generating series of reactions is established. The formation of O_3 typically occurs as polluted air drifts away from sites of production including urban areas. O_3 may be present at large distances from sources of NO_2 and HC (Jenkin and Clemitshaw, 2000).

Daytime interconversion of NO and NO_2

NO_x are released into the troposphere from a variety of biogenic and anthropogenic sources, (Logan, 1983; IPCC, 1995; Lee et al., 1997b). Approximately 40% of the global emissions, and the largest single source, results from the combustion of fossil fuels, which almost exclusively leads to emission directly into the PBL, mainly in the form of NO. A small fraction (generally 10% or less) may be released as NO_2 (PORG, 1997), or is produced close to the point of emission from the termolecular reaction of NO with O_2:

$$2NO + O_2 \rightarrow 2NO_2 \qquad (5.1)$$

The rate of this reaction is strongly dependent on the NO concentration, furthermore it was suggested by Bower et al., (1994), that reaction (5.1) may occur under stagnant, low temperature winter conditions. Thus, at high levels typical of those close to points of emission, the rate of conversion of NO to NO_2 is rapid (eg. ca. 0.5% s^{-1} at 1000ppmv NO), but the significance of the above reaction decreases dramatically as NO is diluted, with a fractional conversion rate of only $5*10^{-6}s^{-1}$ at 1 ppmv NO. Under most tropospheric conditions, the above reaction is insignificant, and the dominant pathway by which NO is converted to NO_2 is through the reaction with O_3:

$$NO + O_3 \rightarrow NO_2 + O_2 \qquad (5.2)$$

At a typical boundary layer concentration of 30ppbv O_3, this reaction occurs on a timescale of approximately 1 min. During daylight hours, however, NO_2 is converted back to NO as a result of photolysis, which also leads to the regeneration of O_3 as follows,

$$NO_2 + h\nu(\lambda < 420\text{nm}) \rightarrow NO + O(^3P) \qquad (5.3)$$

$$O(^3P) + O_2(+M) \rightarrow O_3(+M) \qquad (5.4)$$

Where M is a third body, most commonly N_2. Thus, reactions (5.2, 5.3 and 5.4 above) constitute a cycle with no net chemistry. In the absence of competing interconversion reactions, this cycle leads to a photostationary state in which the concentrations of NO and NO_2 are related to the O_3 concentration by the following expression:

$$[O_3] = (J_3[NO_2]/k_2[NO]) \qquad (5.5)$$

where J_3 is the rate of NO_2 photolysis and k_2 is the rate coefficient for the reaction of NO with O_3. As a result of this rapid interconversion, the behaviour of NO and NO_2 is highly coupled, and they are usually collectively referred to as NO_x. The lifetime of NO_2 with respect to photolysis in the ABL depends on latitude, season and time of day.

Transport and dispersion processes are not the only factors affecting relationships between emissions and ambient concentrations. Chemistry plays a crucial role in transformation of pollutants resulting in degradation of some species and formation of others. Considering transport of pollution on a larger scale, when the transport times involved are of the order of hours or even days, hundreds of chemical reactions must often be considered in order to account for the chemical composition of the air. The situation is quite different when dealing with processes in street canyons. Due to the very short distances between the sources and receptors, only the fastest chemical reactions can have any significant influence on the transformation processes in the street canyon air. It means that most of the pollutants emitted from traffic can be considered as inert components for which chemical transformations inside the street canyon are unimportant. Such inert compounds on these time scales are carbon monoxide (CO) and HC, which actually constitute the main composition of car exhaust gases, (Berkowicz et al., 1997).

Transport and chemical reactions and kinetics, has been the subject of study of many researchers recently. Computer models, such as the Urban Airshed Model (UAM), EPA, (1990), the Californian Grid Model (CALGRID), Yamartino et al., (1992) and

Stern and Yamartino, (2000), MARS and MUSE (Moussiopoulos et al., 1995; Sahm et al., 1997), the Atmospheric Dispersion Modelling System, (ADMS), Carruthers, et al., (1996) have provided a useful means of assembling these processes, and describing the likely behaviour and inter-conversion of various atmospheric pollutants. Such models play a central role in policy development and implementation, Moussiopoulos et al., (1996). Furthermore, this work has also been driven, by the need to interpret the results of field studies on atmospheric processes. Finally, it must be mentioned that an enormous variety of observational data has become recently available for molecular and free radical species involved in atmospheric chemical processes in both polluted and clean environments, Karppinen et al., (1997), Olesen, (1995), Karppinen et al., (2000).

5.2 MIMO Photochemical Routine

The MIMO Photochemical Routine, (MIPHOR) was designed to simulate the fast chemical reactions, which take place immediately after emission of NO_x in the street canyon regime. It was also planned to quantify the effects of photochemistry on the NO_2 concentrations in this environment, since NO_2 is considered to be harmful to human health, WHO[1]. Taking into account pollutant residence time in street canyons and the fact that fast chemistry needs approximately one to two minutes to reach a steady state, it was thought reasonable to consider only the photochemical cycle.

A semi-implicit treatment scheme of source terms due to chemical transformations is implemented. The reactions involving $NO - NO_2 - O_3$ were thus included in MIMO. A source term linearisation was performed in order to calculate the increase or decrease of each chemical's concentration. Taking this into account a module for the coupled treatment of fast chemical reactions within street canyons has been developed. The rate of change of the concentrations of NO, NO_2, and O_3 in the street can be approximated by the following equations, (5.6, 5.7 and 5.8 respectively):

---

[1] http://www.who.int/environmental_information/Air/Guidelines/ann4.htm

$$\frac{d[NO]}{dt} = -k[NO]\cdot[O_3] + J[NO_2] \quad (5.7)$$

$$\frac{d[NO_2]}{dt} = k[NO]\cdot[O_3] - J[NO_2] \quad (5.8)$$

$$\frac{d[O_3]}{dt} = -k[NO]\cdot[O_3] + J[NO_2] \quad (5.9)$$

where k(ppb-1s-1) is the rate coefficient of the reaction between NO and O_3, J(s-1) is the photodissociation coefficient for NO_2.

These equations are then embodied to the transport equations of MIMO, as source terms due to chemistry, using a simple integration rule.

5.3 MIPHOR results

Different background values for O_3 are assumed while no background values for NO and NO_2 are provided. NO and NO_2 sources at street level are used in order to simulate heavy NO_x traffic emissions. The NO_x emission rate was assumed to be 1250μg/m^3sec and O_3 background concentrations ranged from 30 ppb to 70 ppb. The proportion of NO_x emitted as NO was set to 5% following the suggestions of other researchers. The computational domain, inflow profiles and boundary conditions used for this set of simulations were those from sections 4.1.2 and 4.1.3 respectively. Emission of pollutants was assumed to be released at the third street canyon (urban cell) downstream. The flow field and pollutant dispersion patterns observed are identical to those of section 4.1.6. Additionally, as far as the O_3 inflow profile is concerned, it was assumed that its concentration was steady at the boundaries of the canyon as an initial state.

5.3.1 Night-time chemistry

In Figures 5.1, 5.2 and 5.3 the initial distribution of NO_x, NO and NO_2 respectively, is presented. Maximum concentrations are observed at the upwind building wall of the street and minimum at the downwind building side of the street.

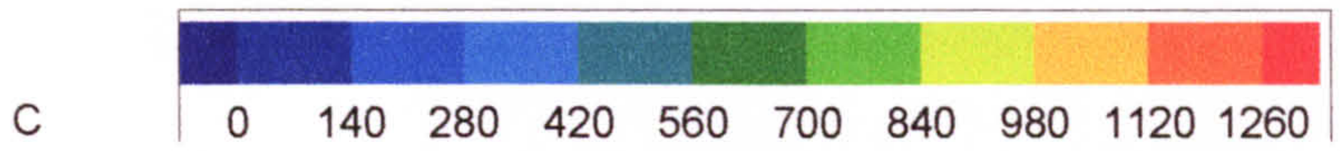

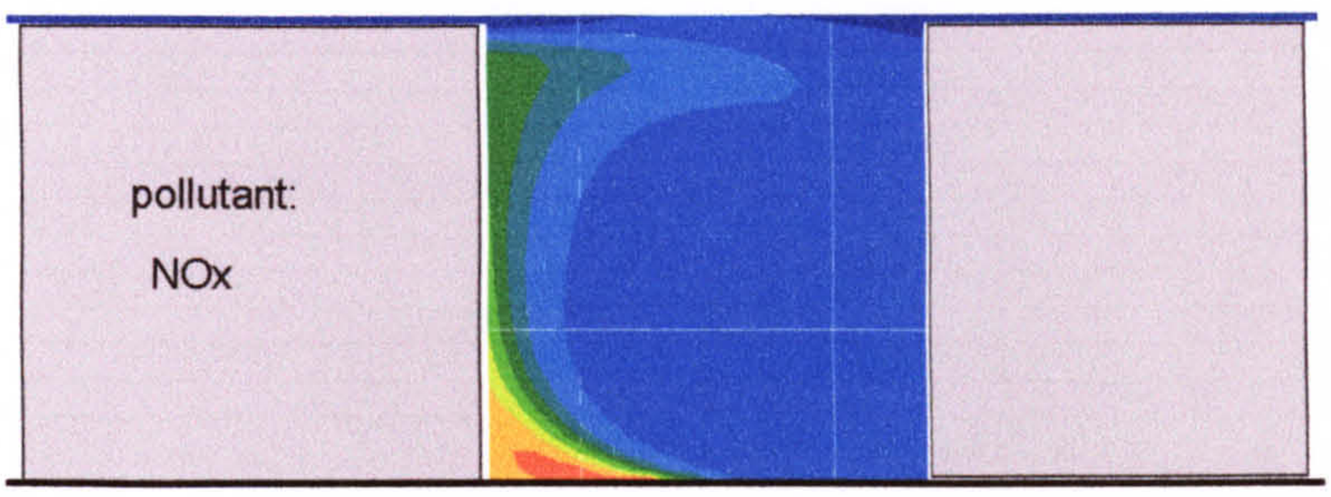

Figure 5.1. Distribution of total NO_x along the street before fast chemistry is activated, C in $\mu g/m^3$.

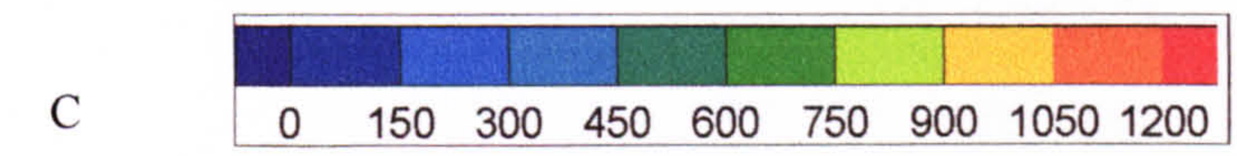

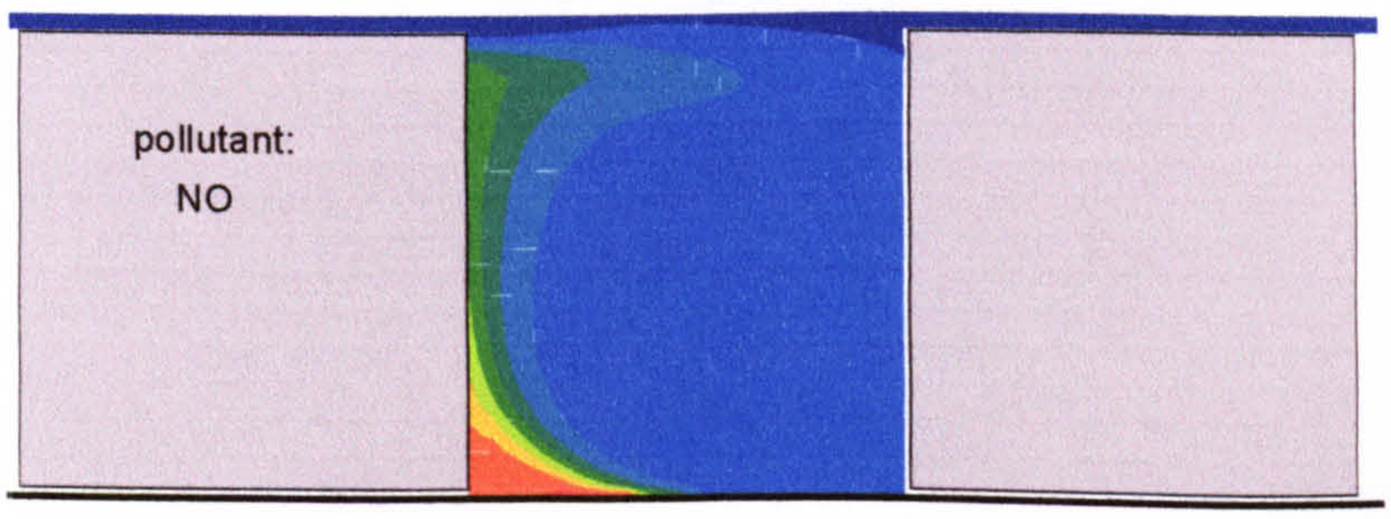

Figure 5.2. Distribution of total NO along the street before fast chemistry is activated, C in $\mu g/m^3$.

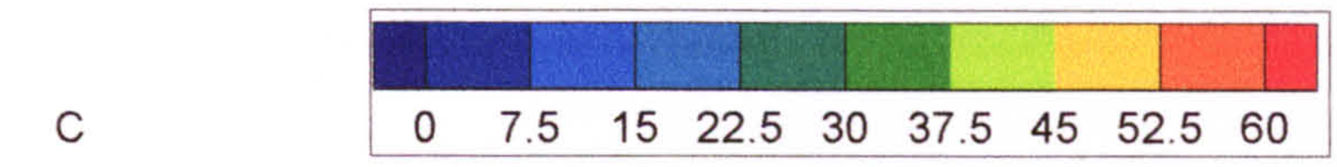

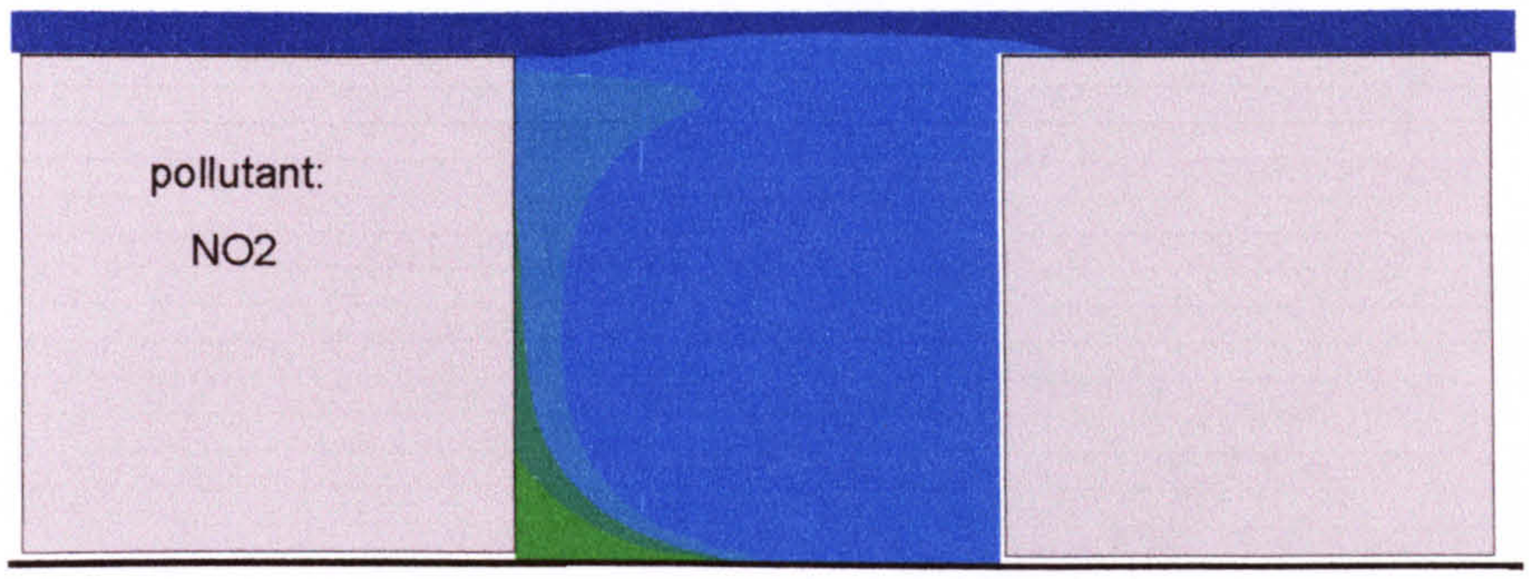

Figure 5.3. Distribution of total NO_2 along the street before fast chemistry is activated C in $\mu g/m^3$.

In Figure 5.4 the NO_2 concentration graph after fast chemistry has been activated with a background value of O_3 set to 40ppb is presented. From the graph one may deduce that NO_2 has increased significantly along the whole canyon domain. In Figure 5.5 the remaining O_3 concentration field established after fast chemistry has acted, indicates that it has been almost entirely depleted taking into account that its initial uniform value was assumed to be 40 ppb.

In Figure 5.6 a very interesting graph is presented, which depicts the NO_2/NO_x % ratio, i.e. how much has NO_2 increased related to NO_x. This leads to the conclusion that NO_2 presents a higher increase on the windward rather than on the leeward side of the street canyon.

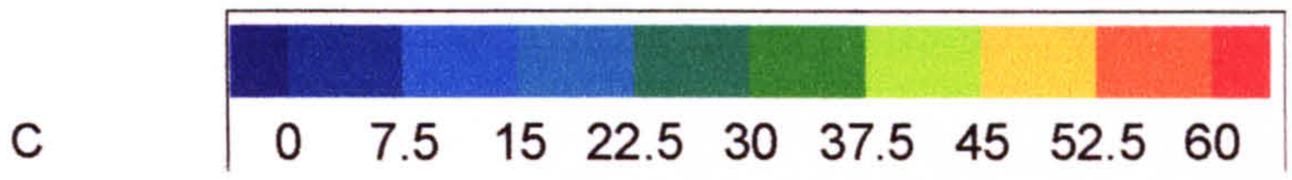

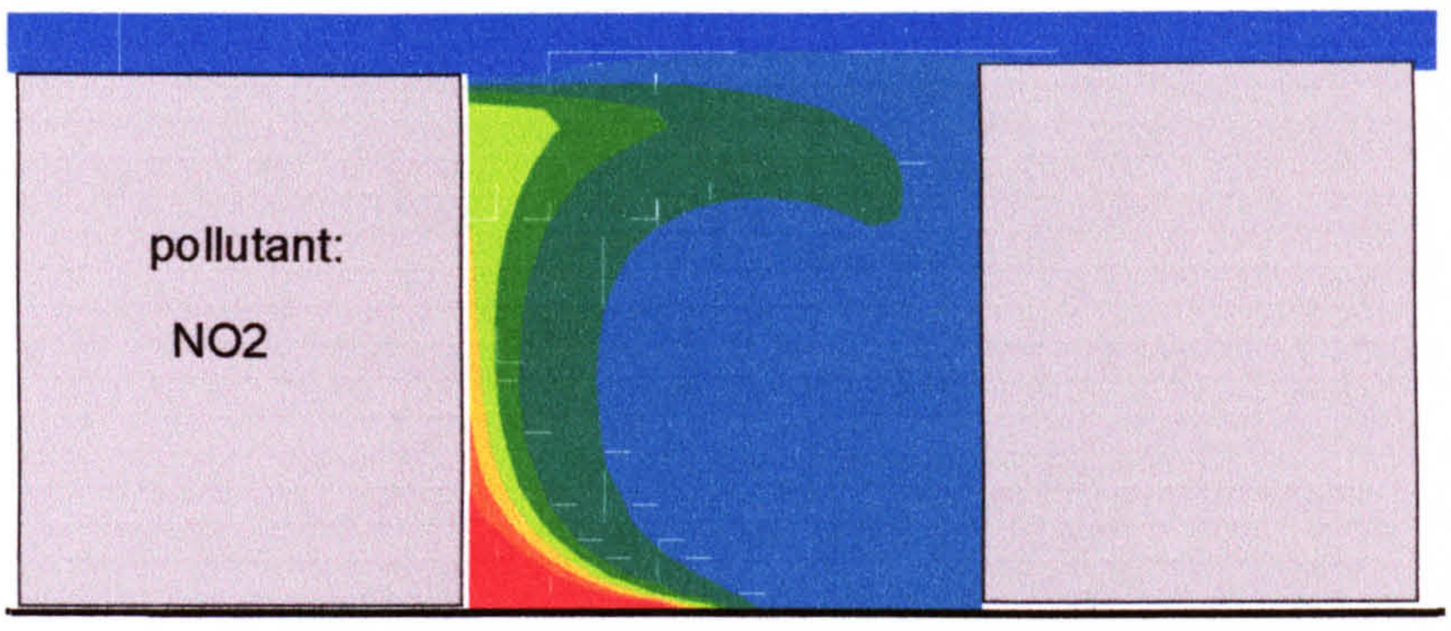

Figure 5.4. Distribution of total NO_2 along the street after fast chemistry is activated C in $\mu g/m^3$.

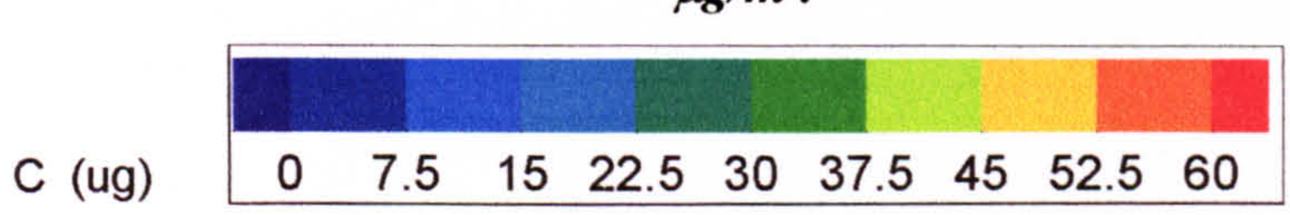

Figure 5.5. ***Distribution of total O_3 along the street after fast chemistry is activated C in $\mu g/m^3$.***

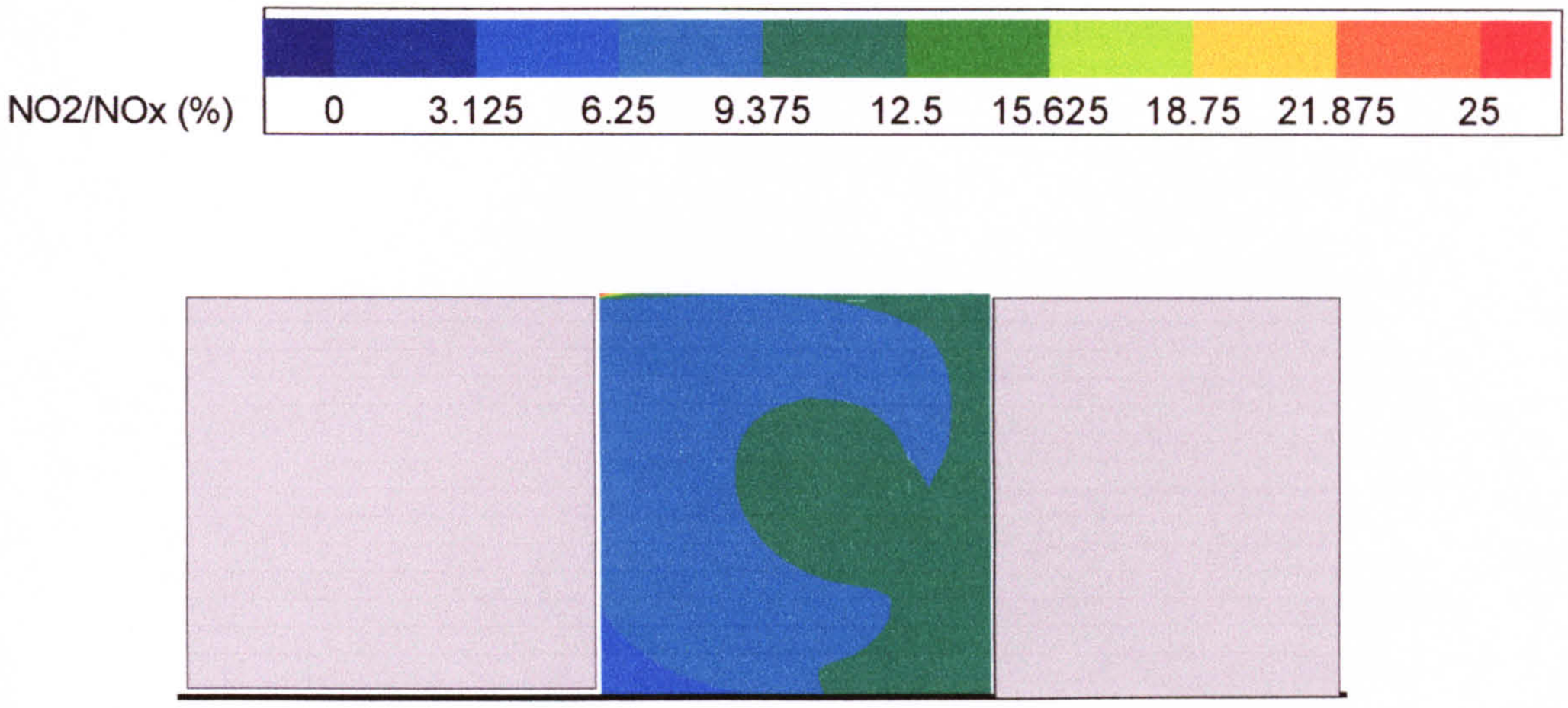

Figure 5.6. NO_2/NO_x ratio formed after fast chemistry is activated indicating percentage increase of NO_2.

In Figures 5.7, 5.8 and 5.9 the effect of the chemical reactions taking place immediately after emission is clearly seen for the leeward wall, the centre of the cavity and the windward wall respectively. In this case, no photolysis process of NO_2 takes place so in equations 5.7, 5.8 and 5.9, the photolysis rate is set to zero.

The NO_2/NO_x ratio rises in an almost uniform manner as the background O_3 concentration rises. As is illustrated from the reactions given above, the oxidation of NO with O_3 acts as a source of NO_2 and as there is no destruction of NO_2 since no photolysis occurs. Also there is a 6% increase of its concentration as the background concentration of O_3 increases. Moving towards the centre of the cavity the NO_2/NO_x ratio presents an even larger increase of the order of 30% for a background concentration of O_3 of 70ppb. This dramatic increase may be explained by the lower wind velocity observed at the middle of the canyon, which enhances good mixing and diffusion of pollutants. Thus, fresh air mass reaches the area and more NO_2 is produced. At the windward wall the NO_2/NO_x ratio rises even higher, but not dramatically higher than that at the centre of the cavity. This may be explained by the fact that recirculating chemicals which did not have time to react at the leeward wall due to the high wind velocity react locally. Furthermore, fresh O_3 enters the street canyon from above the cavity (Assimakopoulos et al., 2001).

Work already completed with CFX-TASCflow for night-time conditions allowed quantifying the O_3 depletion and the significant increase of the NO_2 concentration due

to oxidation of NO with O_3. Similar calculations performed with the CFD code TASCflow revealed the same behaviour, (Moussiopoulos et al., 1998). Earlier work completed by Berkowicz et al., 1996, using the street model OSPM, and considering three different ozone background concentrations showed that with increasing ozone concentrations NO_2 increases by almost 20%, depending on NO_x emitted by automobiles, Palmgren et al., 1996.

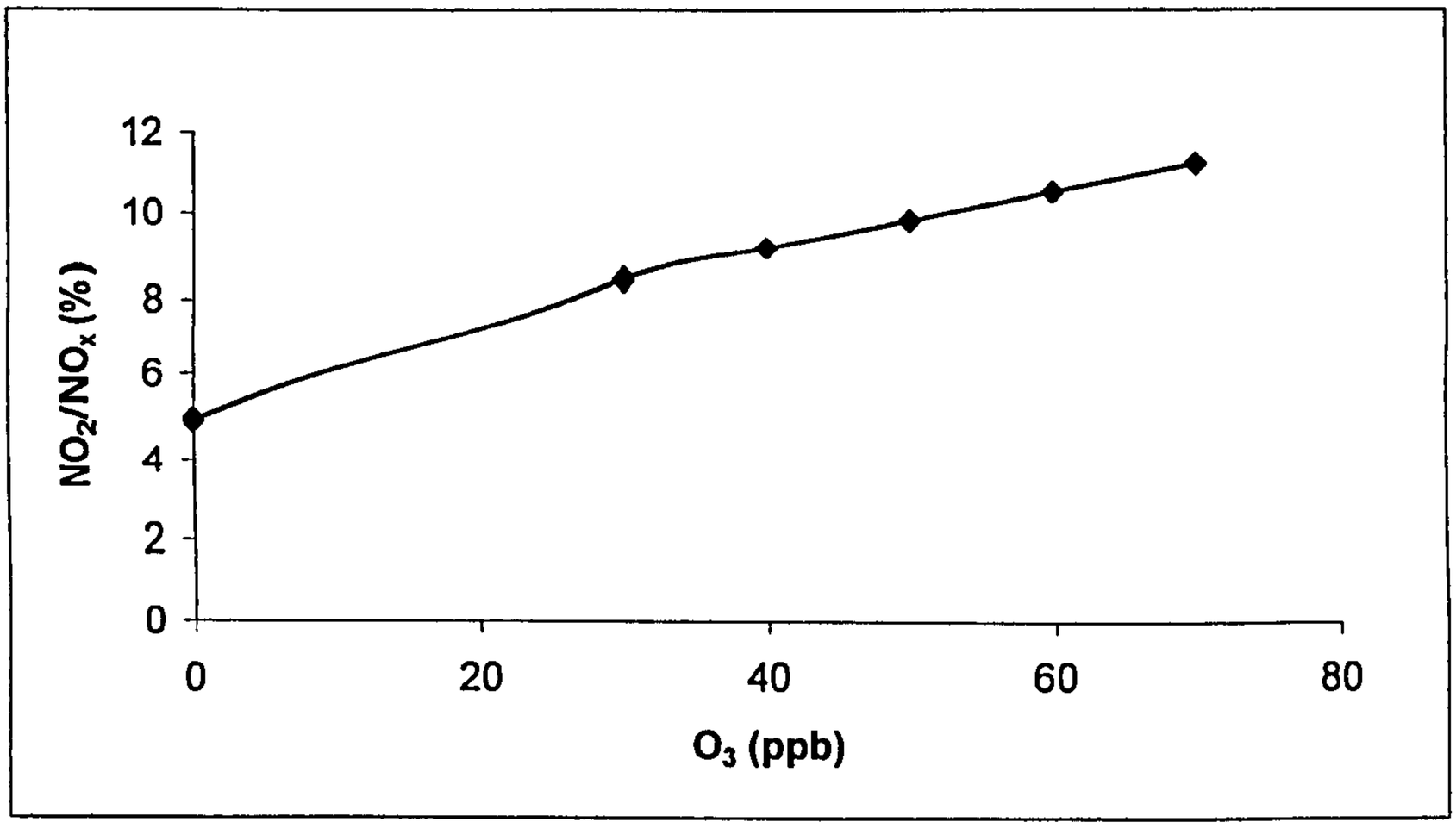

Figure 5.7. Average NO_2/NO_x ratio versus background O_3 concentration as computed by MIMO for the upwind building wall.

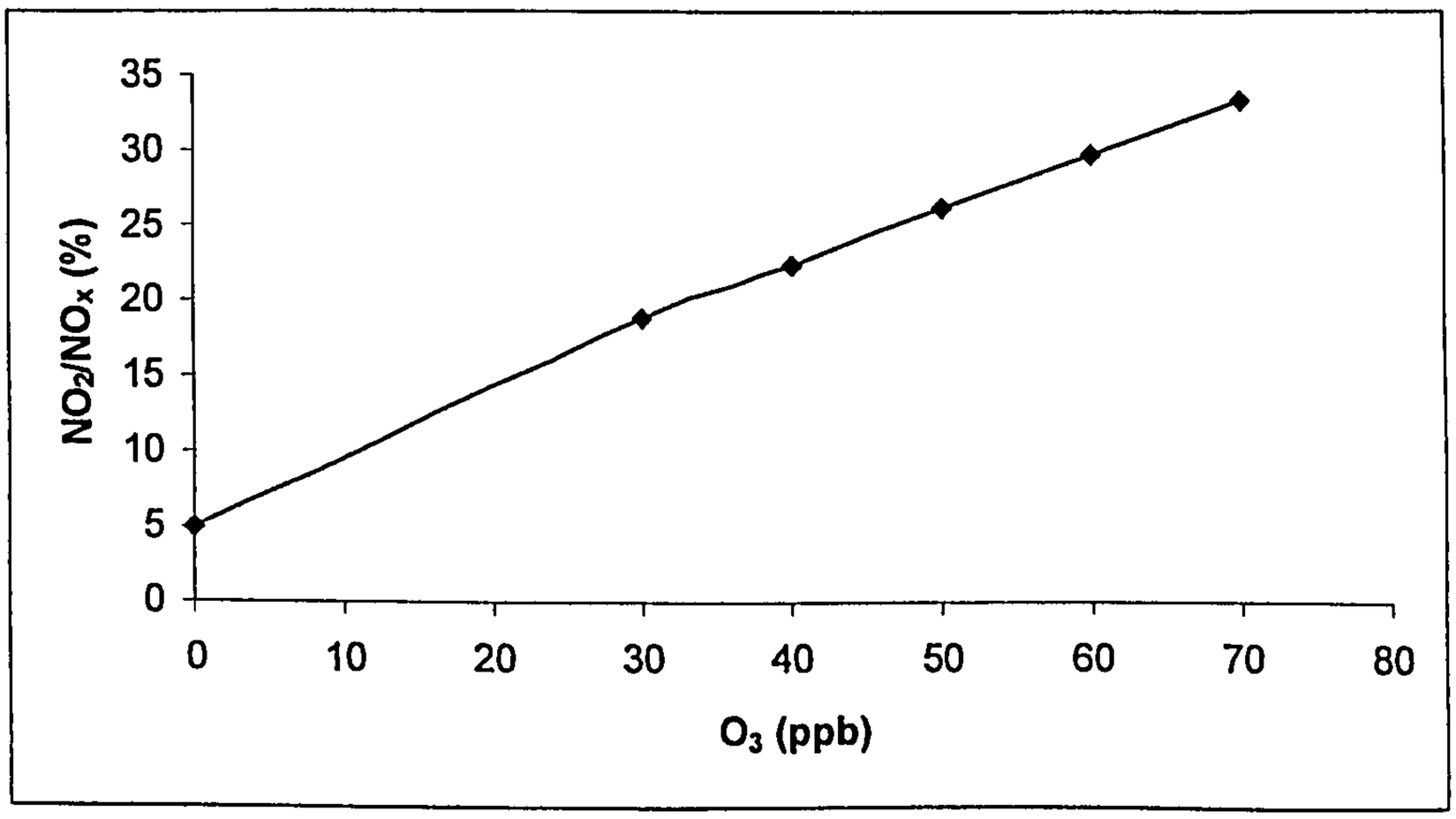

Figure 5.8. Average NO_2/NO_x ratio versus background O_3 concentration as computed by MIMO for the centre of the canyon.

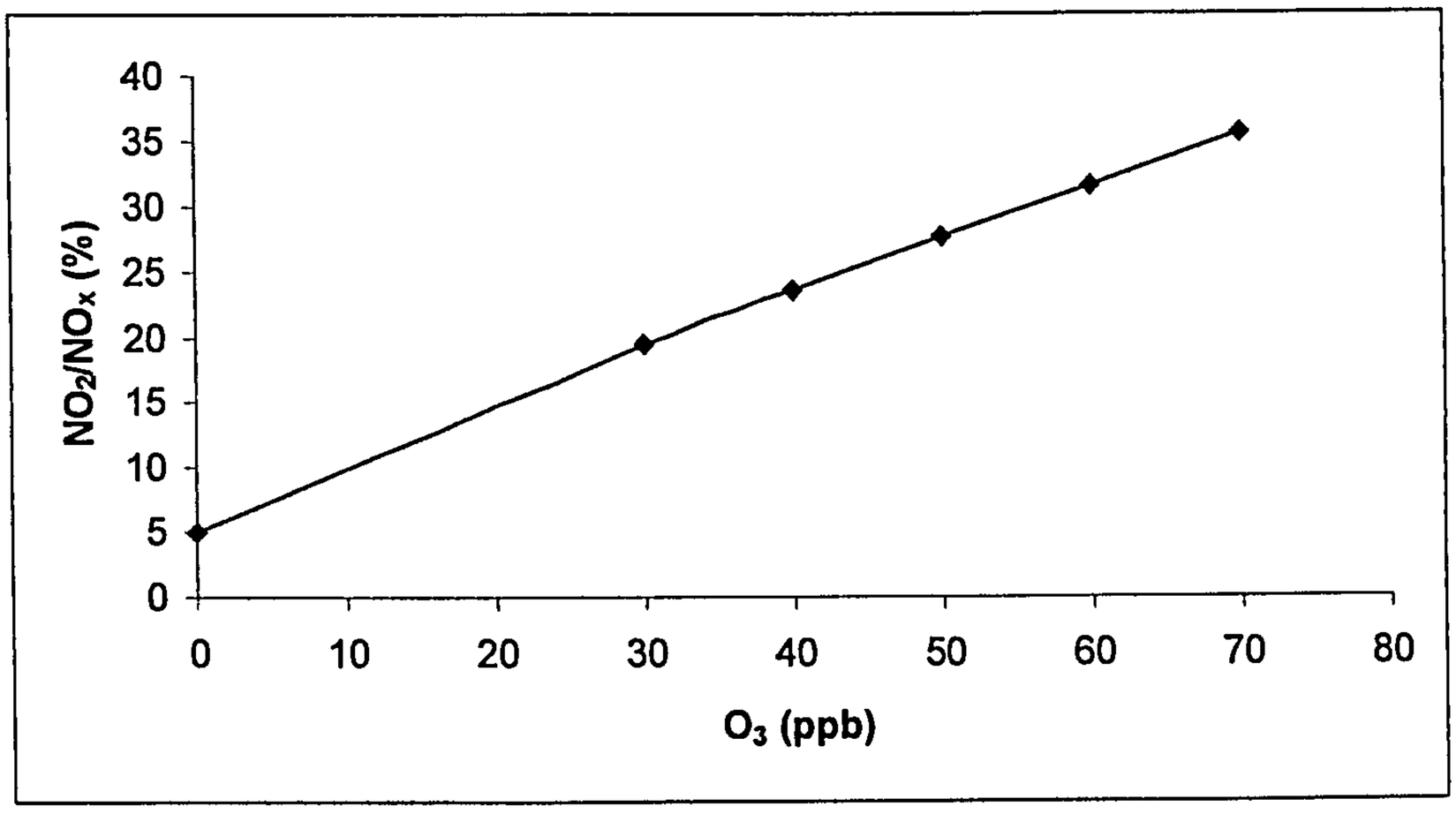

Figure 5.9. Average NO_2/NO_x ratio versus background O_3 concentration as computed by MIMO for the downwind building wall.

5.3.2 Day-time chemistry

In Figures 5.10,5.11 and 5.12 the effect of the chemical reactions during daytime conditions is clearly seen for the leeward wall, the centre of the cavity and the windward wall locations, respectively.

As seen from the Figures, the NO_2/NO_x ratio rises here again in an almost uniform manner as the background O_3 concentration increases. Although photolysis of NO_2 takes place, there is not a great difference in the observed ratios compared to night-time chemistry. However, it becomes clear that the same logic applies as far as the trapping of pollution at the leeward wall and the improved ventilation regime that prevails in the other locations of the canyon. It is also important to note that the overall reduction of the average NO_2/NO_x ratio of daytime compared to night-time, is of the order of 9%.

Finally according to Figure 5.13 the overall NO_2/NO_x ratio increases linearly with respect to increasing background ozone concentration.

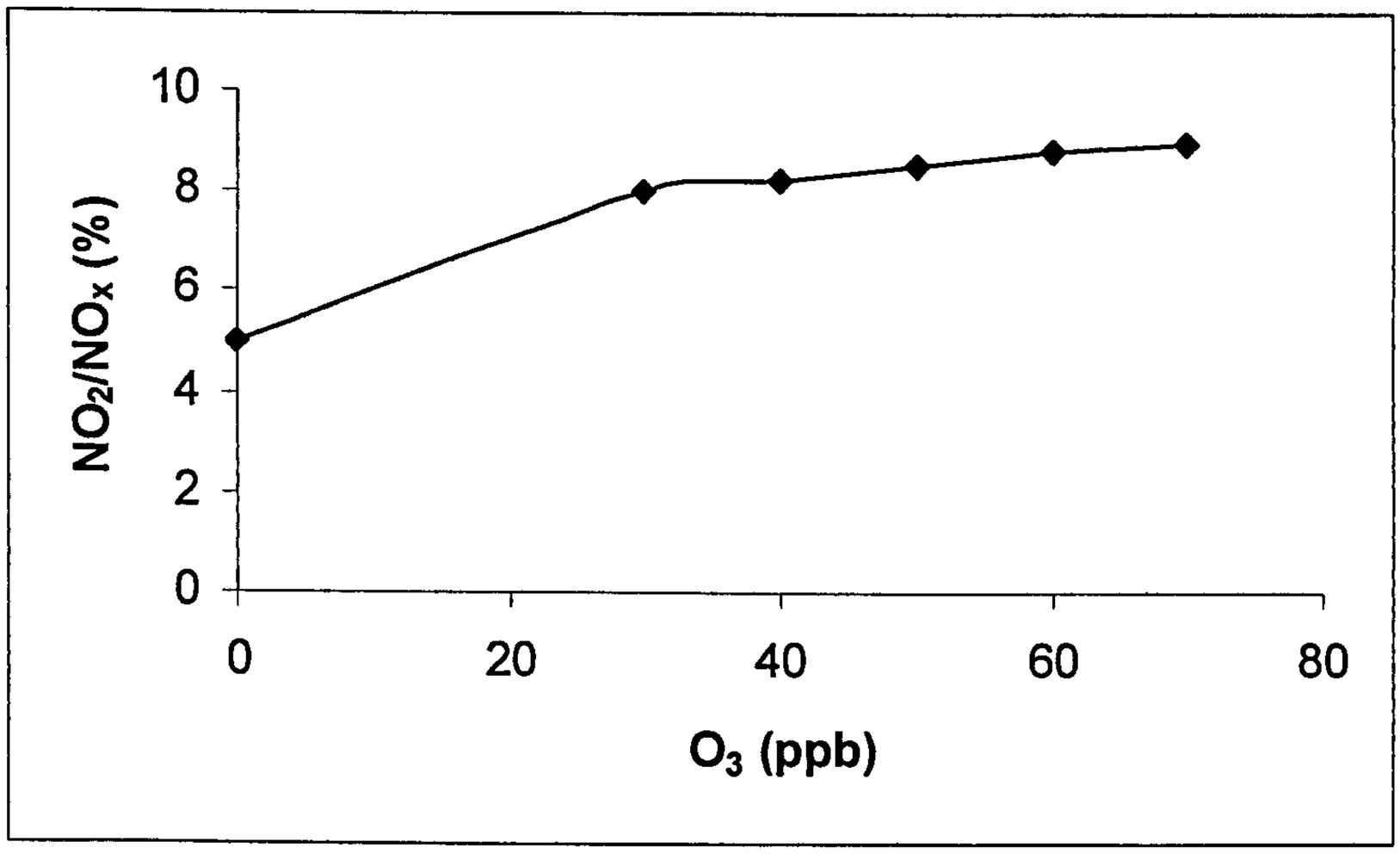

Figure 5.10. Average NO_2/NO_x ratio versus background O_3 concentration as computed by MIMO for the upwind building wall.

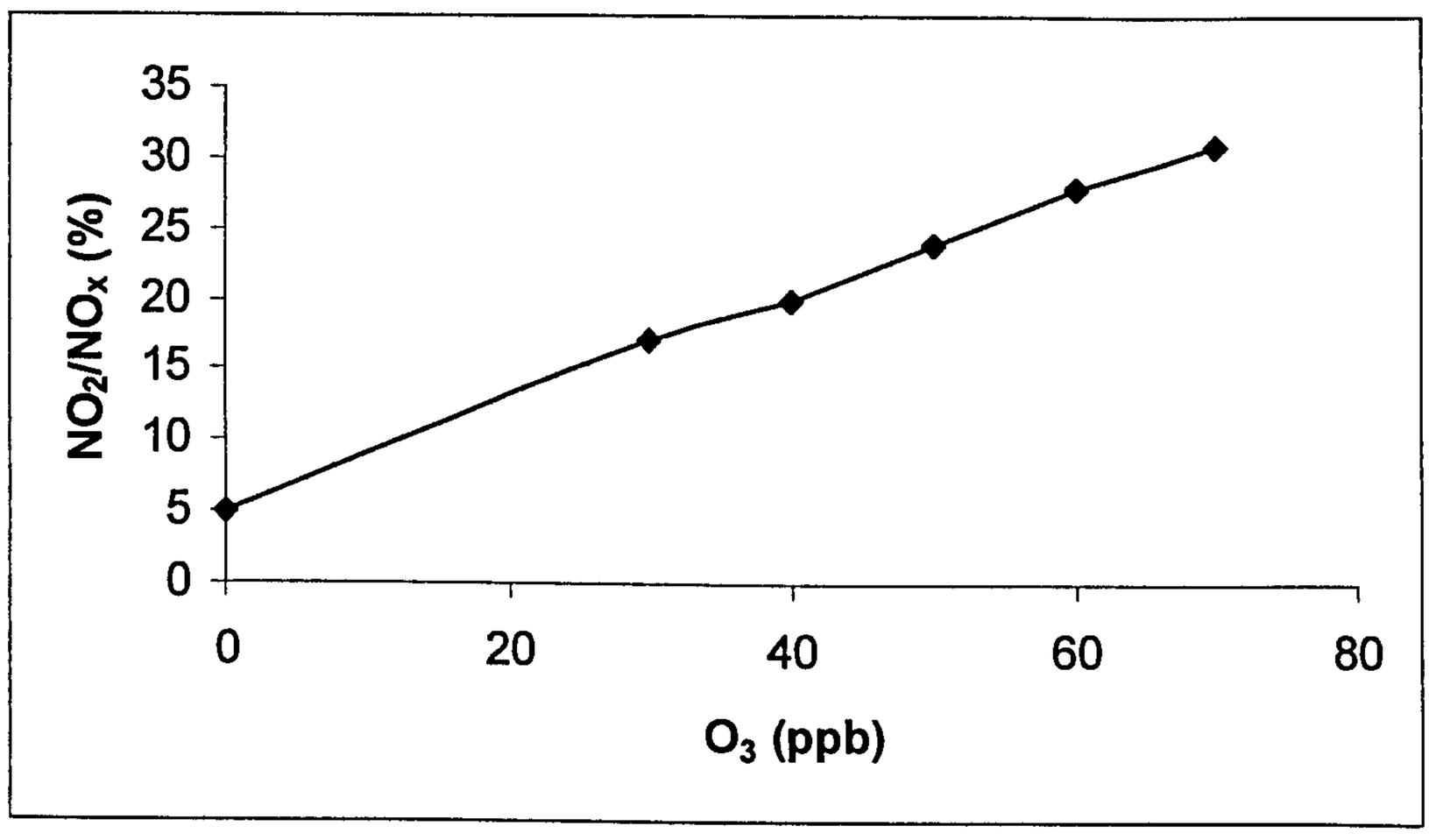

Figure 5.11. Average NO_2/NO_x ratio versus background O_3 concentration as computed by MIMO for the centre of the canyon.

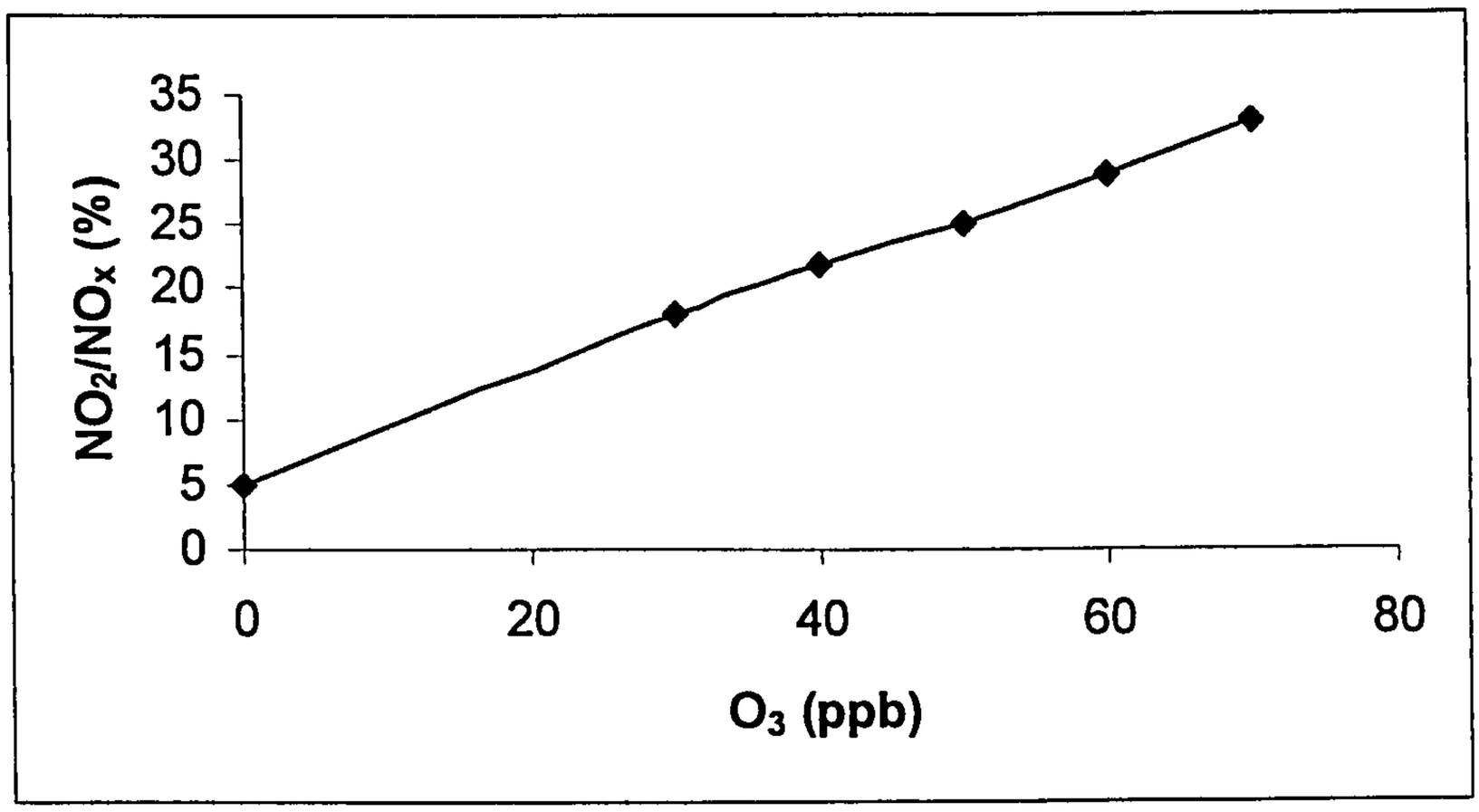

Figure 5.12. Average NO_2/NO_x ratio versus background O_3 concentration as computed by MIMO for the downwind building wall.

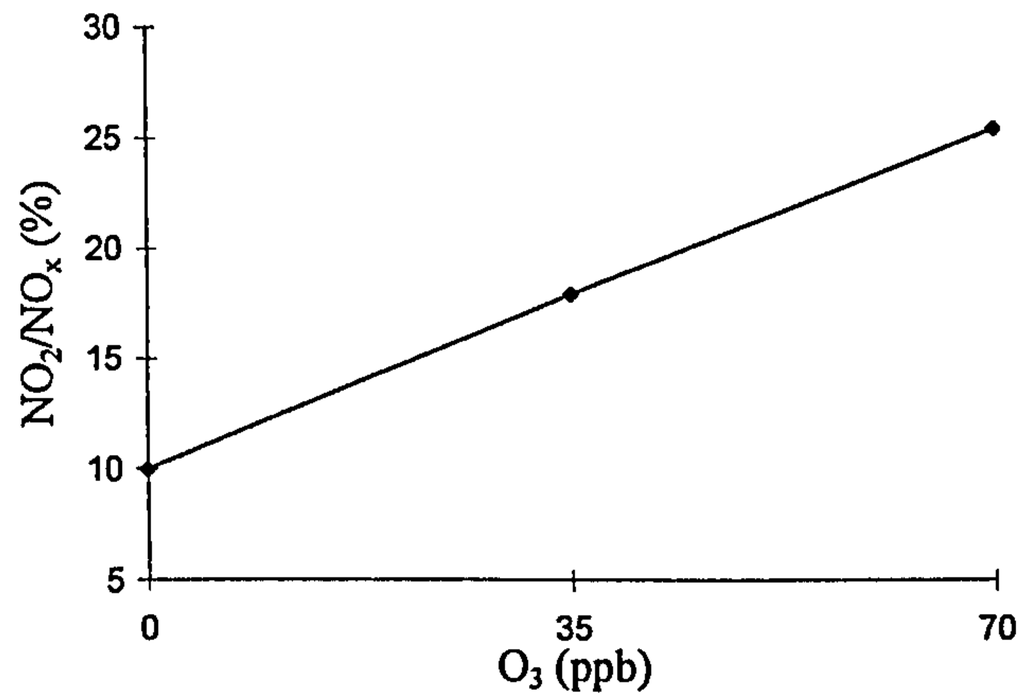

Figure 5.13. NO_2/NO_x ratio varying with background ozone concentration, averaged across the street canyon domain.

5.4 Concluding remarks

A fast chemistry module was created and embodied with MIMO in order to study the effects on the concentration of NO_2. From this effort the following main preliminary conclusions can be drawn:

- With a steady background O_3, NO_2 concentration rises. The relationship between the NO_2/NO_x ratio is almost linear and increasing with increasing O_3. This applies for both night and daytime conditions.

- The NO_2/NO_x ratio varies along the canyon rising from the upwind building wall to the downwind building wall. In the location of maximum pollution, the upwind building wall, the NO_2/NO_x ratio is lower compared to that at the center and downwind building wall locations. This could be explained by the fact that this location of the street canyon is characterized by weak ventilation, which leads to a limited O_3 feed and trapping of pollutants. Both in the center and windward wall locations, the NO_2/NO_x ratio is higher, since these areas are characterised by good mixing conditions and better feeding of fresh pollutants. This applies for both night and daytime conditions.

- The average NO_2/NO_x ratio for daytime conditions is lower than for the night-time case by approximately 9%.

- It is important to note that at the 'pedestrian' level, i.e., one to two metres above street level and across the canyon width, it is the upwind building wall (upwind building side) that presents the highest increase in NO_2 levels, rather the downwind building wall (downwind building side). However, in average terms this is completely reversed since as seen from the graphs presented above NO_2 increases more on the downwind building wall rather than on the upwind building wall case.

6 Three-dimensional calculations

In reality not all street canyons are two dimensional in the sense that they are not infinitely long, or long enough to be considered as such. In most urban areas a main street is intersected at regular intervals with other smaller or bigger streets, thus giving rise to more complex wind field patterns than the ones met when a flow is considered to be two-dimensional. However, if the distance between two intersections is large enough that the effects from the edges are diminished the flow may be considered two-dimensional. Furthermore, it is recommended that CFD calculations commence with simpler, validated cases in order to evaluate a model's performance and then to progress to more complex cases.

In this chapter the results from three-dimensional runs performed with the microscale model MIMO are presented. The main objective here is to validate MIMO against available experimental data, and to perform a study of street geometry effect on the flow patterns. It must be noted here that the dataset made available for this work consist of wind field measurements in a wind tunnel environment. Thus, the computations and comparisons performed here focus on this aspect.

MIMO has already been validated against wind tunnel experimental data for simple three-dimensional geometries such as a single cube (Ehrhard et al., 1998 and 2000), a U-shaped building Goetting et al., (1997) and for full scale field experiments[1]. However, it has never been compared to wind tunnel experimental data from **complex** three-dimensional cases such as a finite array of square shaped buildings, Assimakopoulos et al., (2000). Thus, in the following sections a description of the wind tunnel experiment, the inflow profiles implemented and the obtained results is given.

It should also be mentioned here that a three-dimensional configuration better approaches the reality and covers the temporal and spatial dimensions of conventional mesoscale single cell. Thus, better resolution is achieved since microscale effects are taken into account for mesoscale modelling.

---

[1] http://www.dmu.dk/atmosphericenvironment/Trapos/main.htm

6.1 Description of wind tunnel experiment

The wind tunnel experimental data were taken from a database specially created by the Meteorological Institute of the University of Hamburg for validation of microscale dispersion models. This database is called CEDVAL (Leitl and Schatzmann, 1998), wherein a variety of wind tunnel experimental results are given. More information may be obtained at the following address: http://www.mi.uni-hamburg.de/cedval. The data selected were carried out in the BLASIUS wind tunnel at the Meteorological Institute of the University of Hamburg. A detailed description of the facility is given in Donat, 1995. Using modified Standen-Spires and a uniform LEGO-roughness a neutrally stratified atmospheric boundary layer was modelled at a scale of 1:200. Before the building models were mounted in the test section, the boundary layer flow was validated against flow measurements and full-scale data (ASME, 1995). The roughness length of the model was 0.0004 m and there was no offset height.

The regular array of street canyons consisted of 56 square-shaped building rings mounted in rows of 4 rings across the wind tunnel (see Figures 6.1 and 6.2). The square rings' dimensions were 250 x 250 x 60 mm. Upstream of the measurement area, 7 rows have been set-up establishing a sufficient long fetch of buildings. The width lateral street canyons was set 1 building height, H = 60mm, which is also the characteristic length scale of the experiment. The aspect ratio of the streets is thus H/W=1.

The characteristics of the approaching flow are thus formulated according to the above model set-up, with a friction velocity of 0.37772 m/s and a power law exponent α=0.22. Furthermore, the vertical profiles for the approaching horizontal velocity, the turbulent kinetic energy and its dissipation were provided.

Data were acquired in two horizontal and three vertical measurement planes. Velocity measurements were performed using Laser Doppler Velocimetre, LDV.

6.2 Computational domain

The layout utilised for this experiment suggested a very large grid size since, the number of buildings was large (4 rows of 14 buildings each), and their dimension and separations was in the millimetre scale (Figure 6.1 and Figure 6.2). This would imply

the construction of a grid with approximately 270 x 110 x 40 cells, i.e. 1,188,000. The computational power required would be extremely high in order to produce convergence. However, this kind of computational power was not available and the cost of time would be too big to make this feasible for application. Besides, the current experimental set-up served for other purposes from the experimental point of view, since it was necessary to create an urban roughness profile, before reaching the measurement area. In addition to that, sufficient distance should be kept from the side-walls in order to prevent any reflection back into the measurement region.

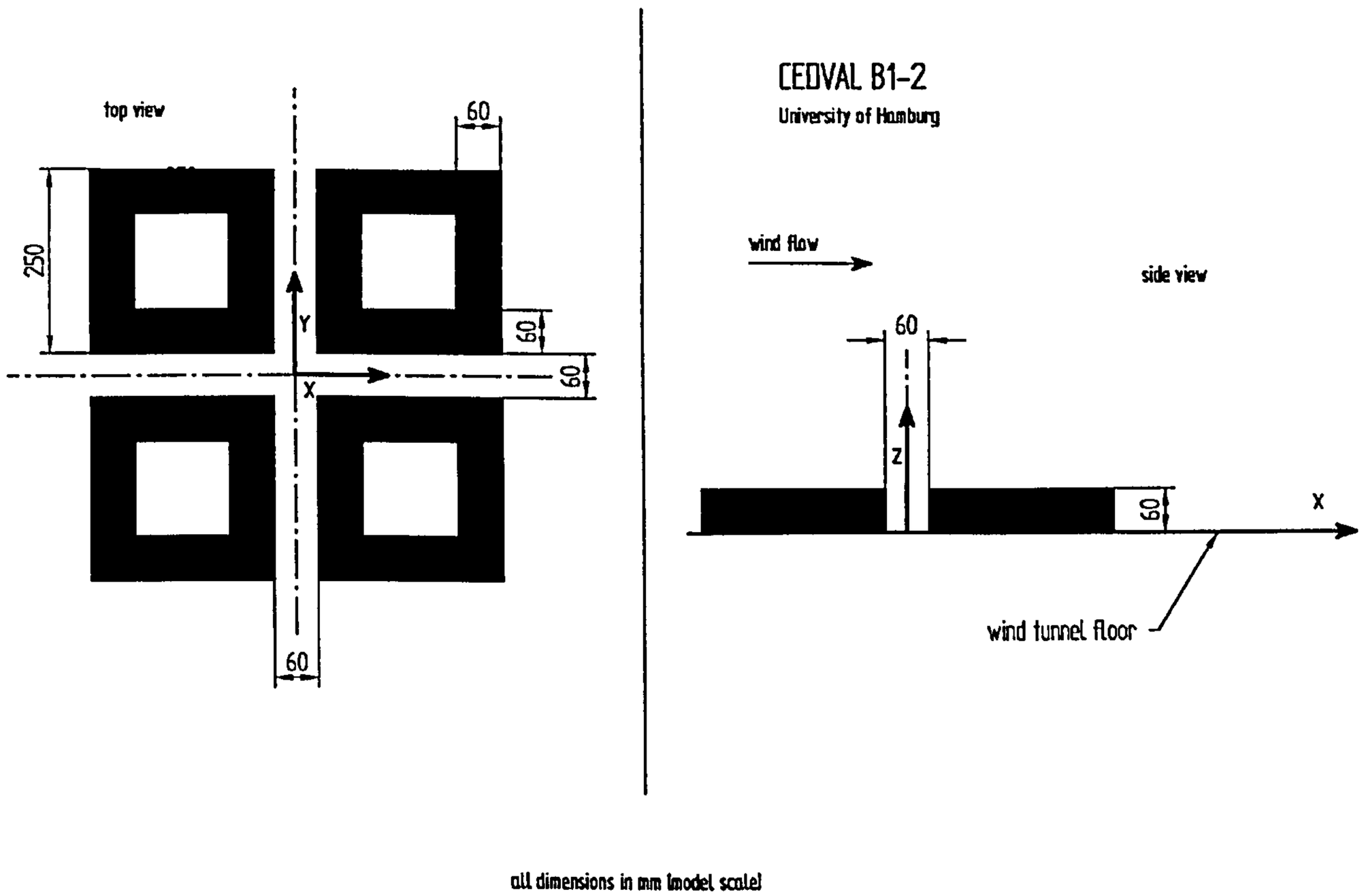

Figure 6.1. Plan view (left) and side view (right) of the square buildings indicating their dimensions.

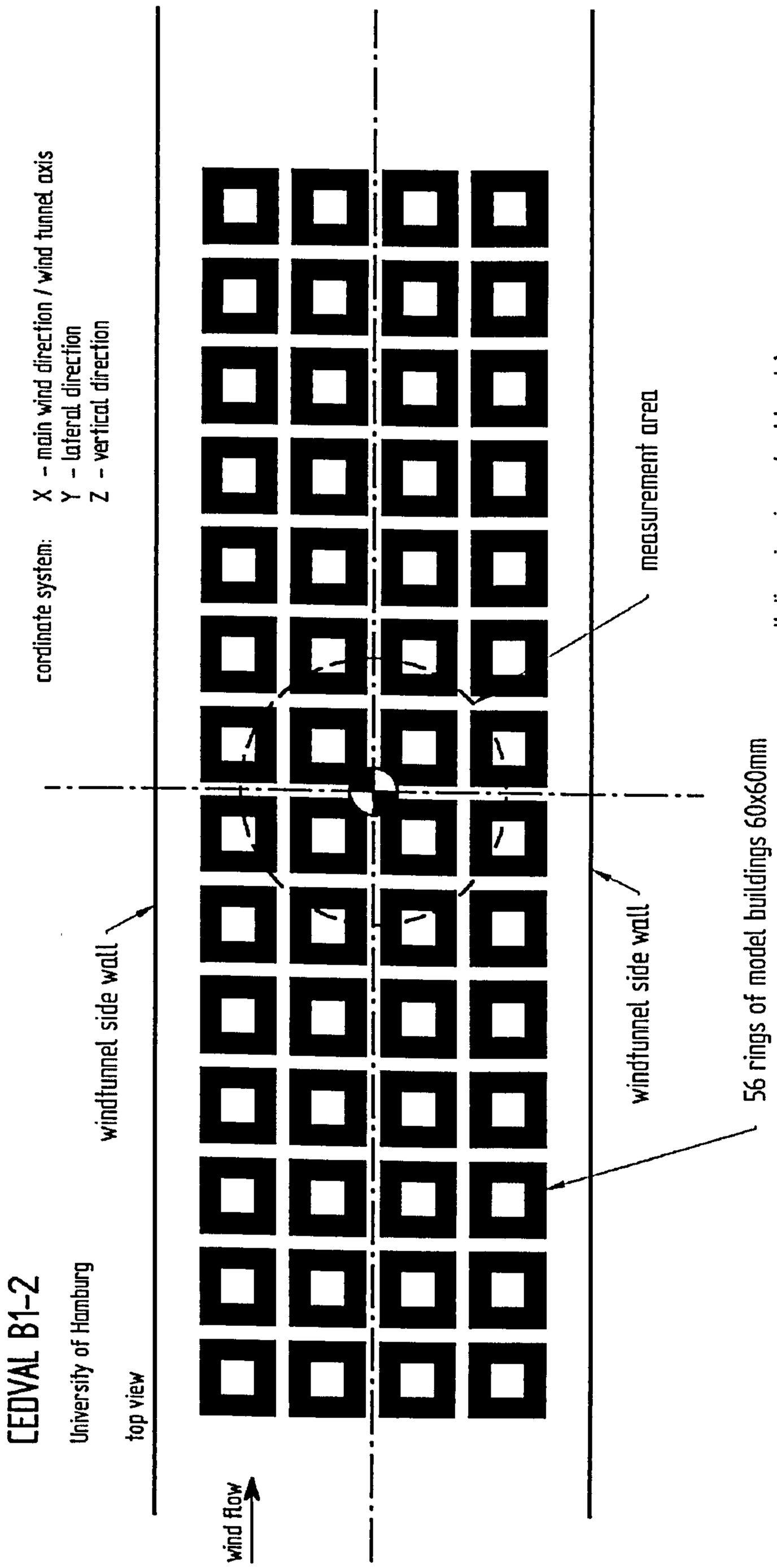

Figure 6.2. Plan view of the experimental layout.

Nevertheless, from the modelling point of view only a few buildings upstream would be necessary, to achieve a stable internal boundary layer and to be far enough from the inlet boundary.

In view of the above considerations the computational domain constructed included two rows of six buildings each, keeping a distance of 5H, 13H and 5H from the inlet, outlet and lateral boundaries respectively (Figure 6.3). The computational domain consisted of 180 x 72 x 38 grid cells (only 492,480 cells), while the minimum cell size is 0.006 x 0.006 x 0.004 m.

The experimental set-up, as mentioned above consisted of square rings of buildings, which would serve to make some "backyard' concentration measurements, since the hollow part of the structure represented the backyard of a domestic building bounded from all sides. However, no such measurements were made available and for simplification purposes it was assumed that the buildings were not hollow.

The main street extends along the x-axis, intersected regularly by side streets, which extend along the y-axis, as seen in Figure 6.3. Both the main street and the side streets have the same width, e.g. 60 mm.

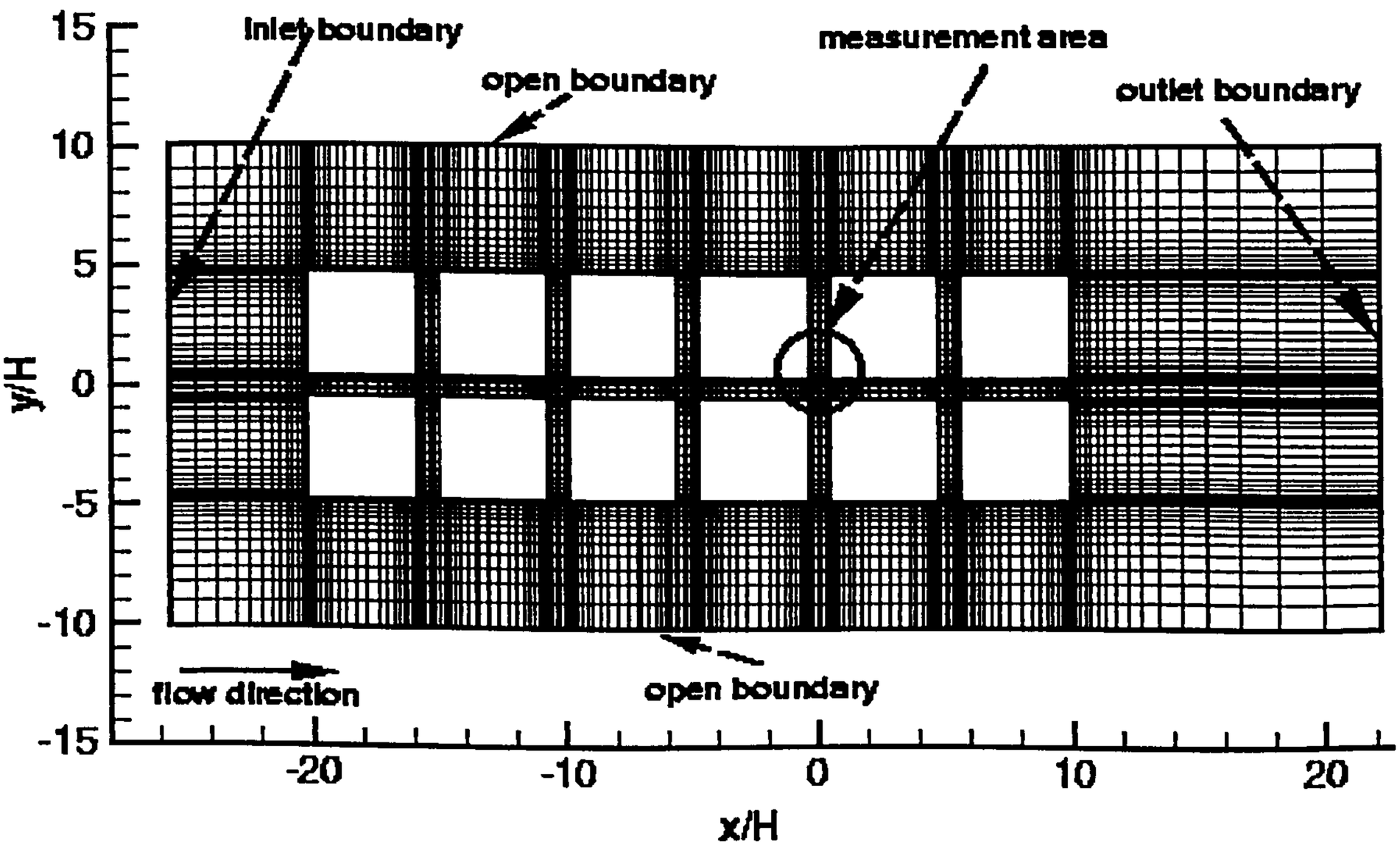

Figure 6.3. Plan view of the computational domain.

6.3 Inflow profiles and Boundary Conditions

Although, certain measured vertical profiles of the horizontal velocity, u and the turbulent kinetic energy, k were available, theoretical inflow profiles were calculated. This was thought necessary since the measured kinetic energy values were not of good quality, presenting a rather unexpected and difficult to explain profile shape. Thus, the friction velocity $u^*=0.37772$ m/s, the roughness $z_o=0.0004$ m and the profile exponent $\alpha=0.22$ were used from the experiment and the inflow profiles were derived as follows:

- The velocity was computed using the power law,

$$u = U_{ref}\left(\frac{z}{z_{ref}}\right)^{\alpha}$$ where U_{ref}= 6m/s, and z_{ref}= 0.4 m.

- The turbulent kinetic energy was given a uniform inflow profile,

$$k = \frac{u^{*2}}{\sqrt{c_\mu}}$$ where the empirical constant, c_μ=0.09

- The dissipation was set equal to,

$$\varepsilon = \frac{u^{*3}}{\kappa z}$$ where $\kappa = 0.41$ is von Karman's constant.

The inlet is located along the y-axis from the left side as seen from Figure 6.3. The inflow profiles adopted for the horizontal velocity, the turbulent kinetic energy and its dissipation are given in Figures 6.4, 6.5 and 6.6 respectively.

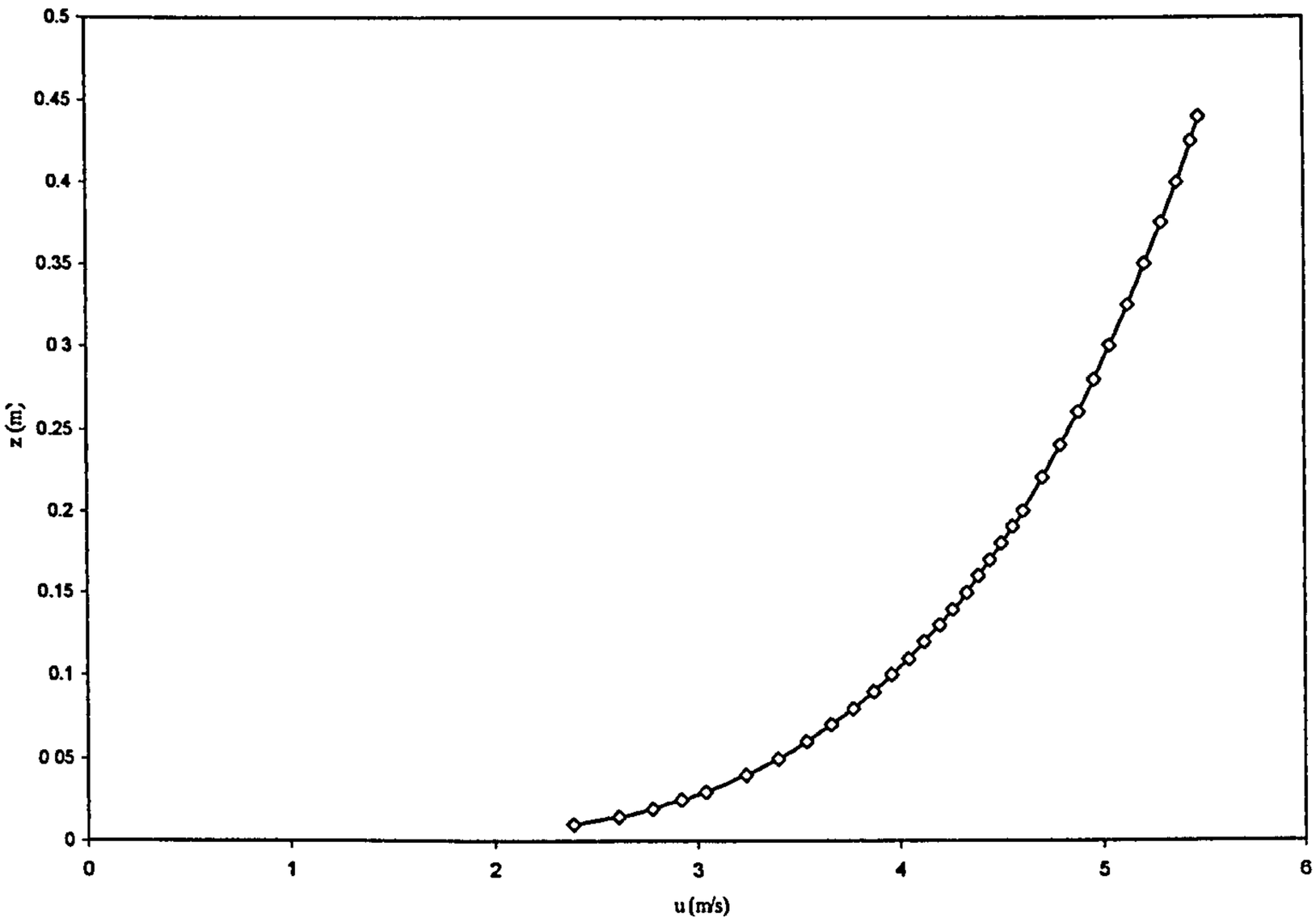

Figure 6.4. Plot of the inflow profile of the horizontal velocity.

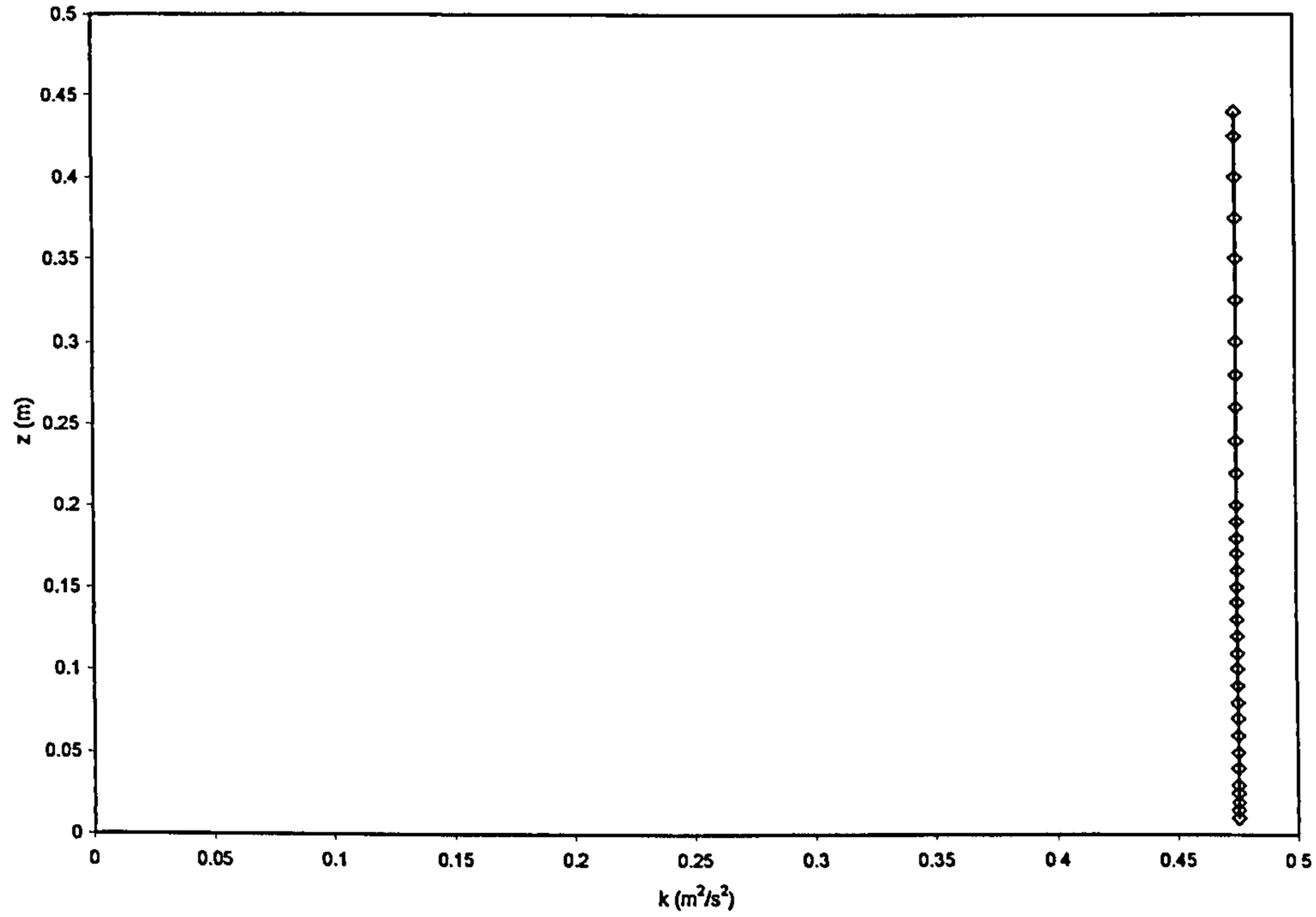

Figure 6.5. Plot of the inflow profile of the turbulent kinetic energy.

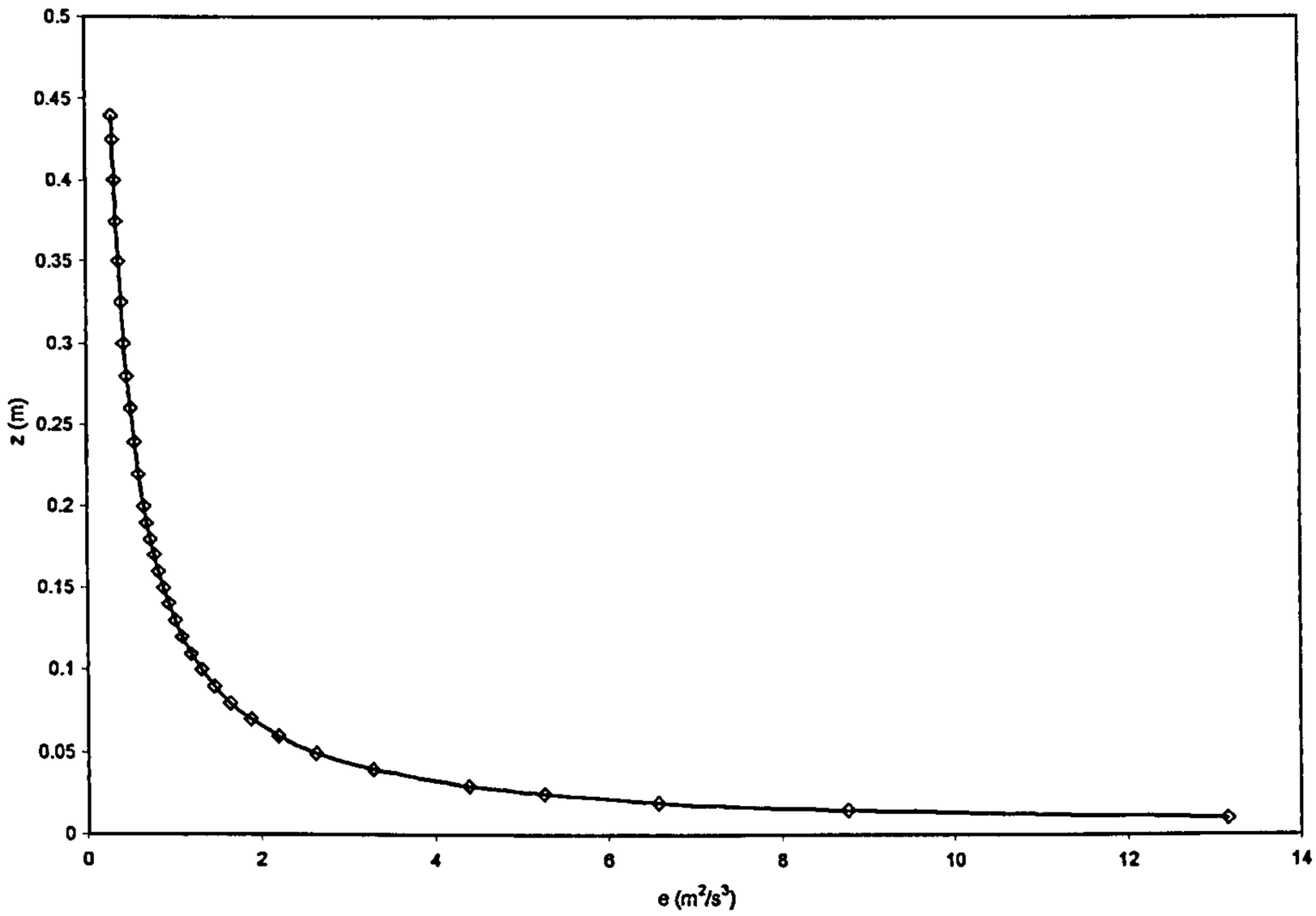

Figure 6.6. Plot of the inflow profile of the rate of dissipation of turbulent kinetic energy.

The boundary conditions implemented in this case are the following:

- **Inlet boundary:** All variable values and parametres are known at the inlet following the definition of the problem from the relevant experimental data and theoretical empirical relationships. Thus, Dirichlet boundary conditions were implemented at all surfaces characterised as inlet. This should be placed a satisfactory distance from the area of interest, (the beginning of the building cluster), so that the results are not influenced and the IBL has evolved. In any case, special care should be taken if the inlet is close to the area of interest so that estimation of the inlet profiles is correctly done. The inlet boundary is shown in Figure 6.3.

- **Outlet boundary:** The outlet is placed where inflow of air is not expected and preferentially a great distance away from the area of interest. The variable values are ususally unknown, thus Neumann boundary conditions are implemented. A fundamental characteristic of all outlet boundaries is that the flow of all variables should satisfy the mass conservation condition. The gradients of all variables

vertical to the surface of the outlet boundary are set to zero. The outlet boundary is depicted in Figure 6.3.

- **Symmetry boundary:** On a symmetry plane the following conditions prevail: a) Zero vertical velocity (i.e., w) and b) Zero gradient of the variables vertical to this plane. The top of the computational domain is considered to be a symmetry boundary, where the vertical velocity, the induction and dispersion go to zero. From the point of view of physics the top domain represents the inversion layer thus the top of the boundary layer where no vertical movements take place.

- **Wall boundary:** On an impermeable wall both the vertical as well as the horizontal components of the velocity vector are zero. Thus, dispersion is the only mechanism for transfer of momentum and energy. The turbulent kinetic energy is also zero, but the rate of dissipation reaches infinity. The wall function employed for the representation of the flow is Sondak and Pletcher (as described in section 4).

When the wind comes from different compass directions above the roofs, the wind vector at roof level may be analysed in along and perpendicular to the street axis velocities respectively. The perpendicular component will equal the wind speed at roof level, when the incoming wind is normal to the street, and zero when it is parallel to it. The opposite holds true for the parallel case.

6.4 Results

The microscale model MIMO was applied in order firstly to validate its performance against a complex computational domain and secondly to study the three-dimensional characteristics of wind flow close and far away from an intersection, inside a street canyon. Variables x, y, and z were made dimensionless by dividing by the building height (H), and the velocity u by dividing by U_{ref}. The pointed area in Figure 6.3 was the one selected for comparison of measurements and computed results from MIMO. More specifically the location x/H = 0, y/H, where measurements for the horizontal velocity were taken at different heights, was selected. This is inside a street canyon whose axis is perpendicular to the wind direction and at a distance to the centre line of the main canyon.

From the results shown in Figure 6.7 it can be seen that the agreement between computed and measured horizontal velocities is very good. The measurement area is located near the street intersection, where the wind field established is quite complicated (Figure 6.8). The agreement between measured and computed wind filed is also obvious from Figure 6.9, which depicts the flow field established during the experiment. The flow is parallel to the axis of the main-street and perpendicular to the axis of the side-street. The flow seems steady away form the intersection, but at the intersection it is disturbed by a recirculation vortex-like structured flow emerging from the side-street and oriented towards the leeward corner of the side-street. The flow is symmetric as the same pattern occurs from both sides of the main-street. Moving from location A to location B along the side-street, the wind gradually rotates and blows from the windward to the leeward wall of the side-street, at approximately y/H=1.4, changing direction again and blowing at an angle from the windward to the leeward wall, tending to become parallel to the axis of the street. Thus it flows in a corkscrew-like manner.

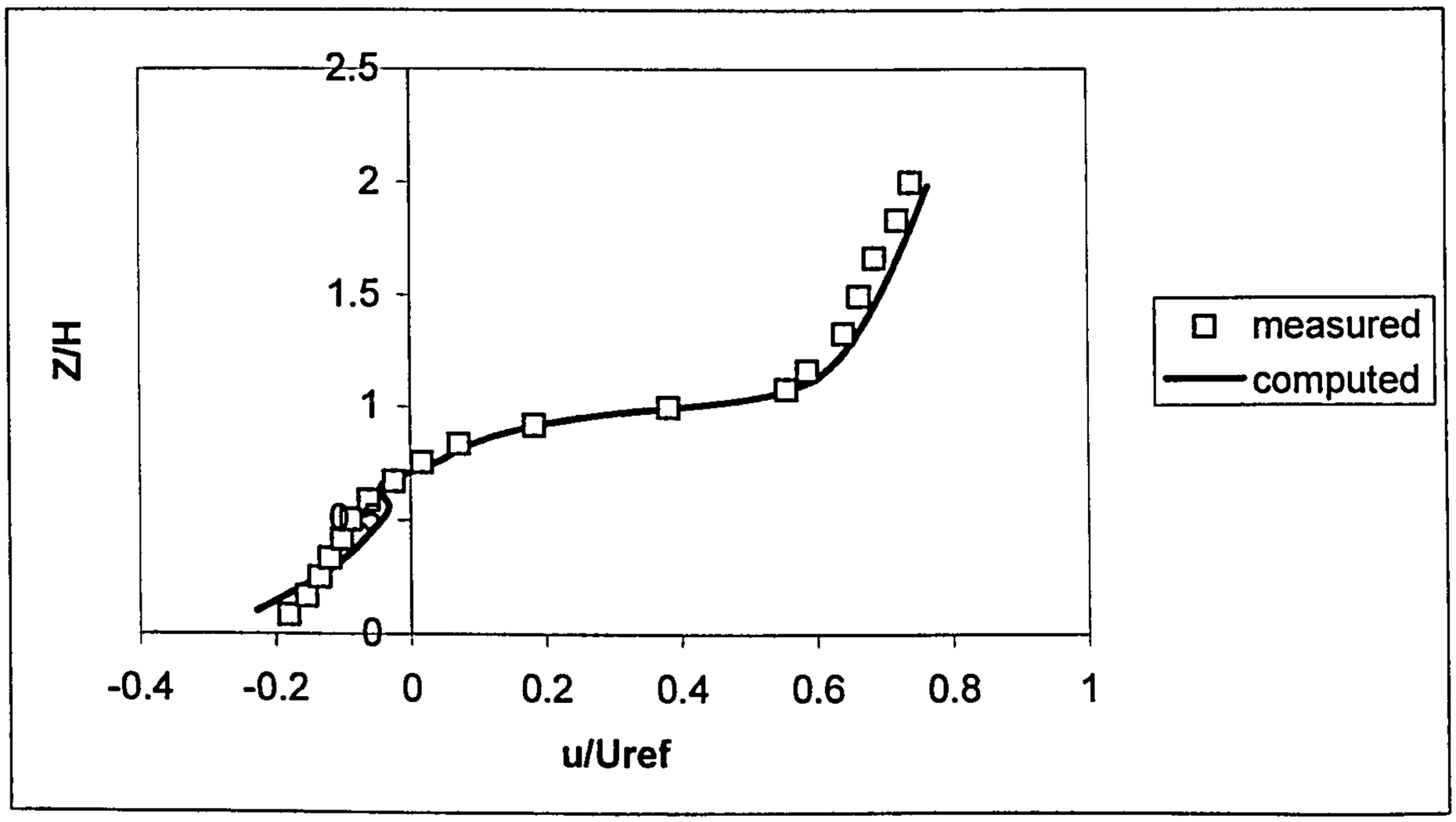

Figure 6.7. A comparison of measured vertical profile of velocity against vertical profile of velocity as computed by MIMO.

In Figures 6.10 and 6.11 a side view of the wind field developed at locations A and B respectively is given. At location A, a main vortex is established, whose centre is tilted towards the lower windward corner, obviously affected by the presence of the intersection. However, at location B, the main vortex established is centred and is identical to the wind field evolved for a two-dimensional street canyon. Thus, the distance from the intersection is large enough to affect the wind field.

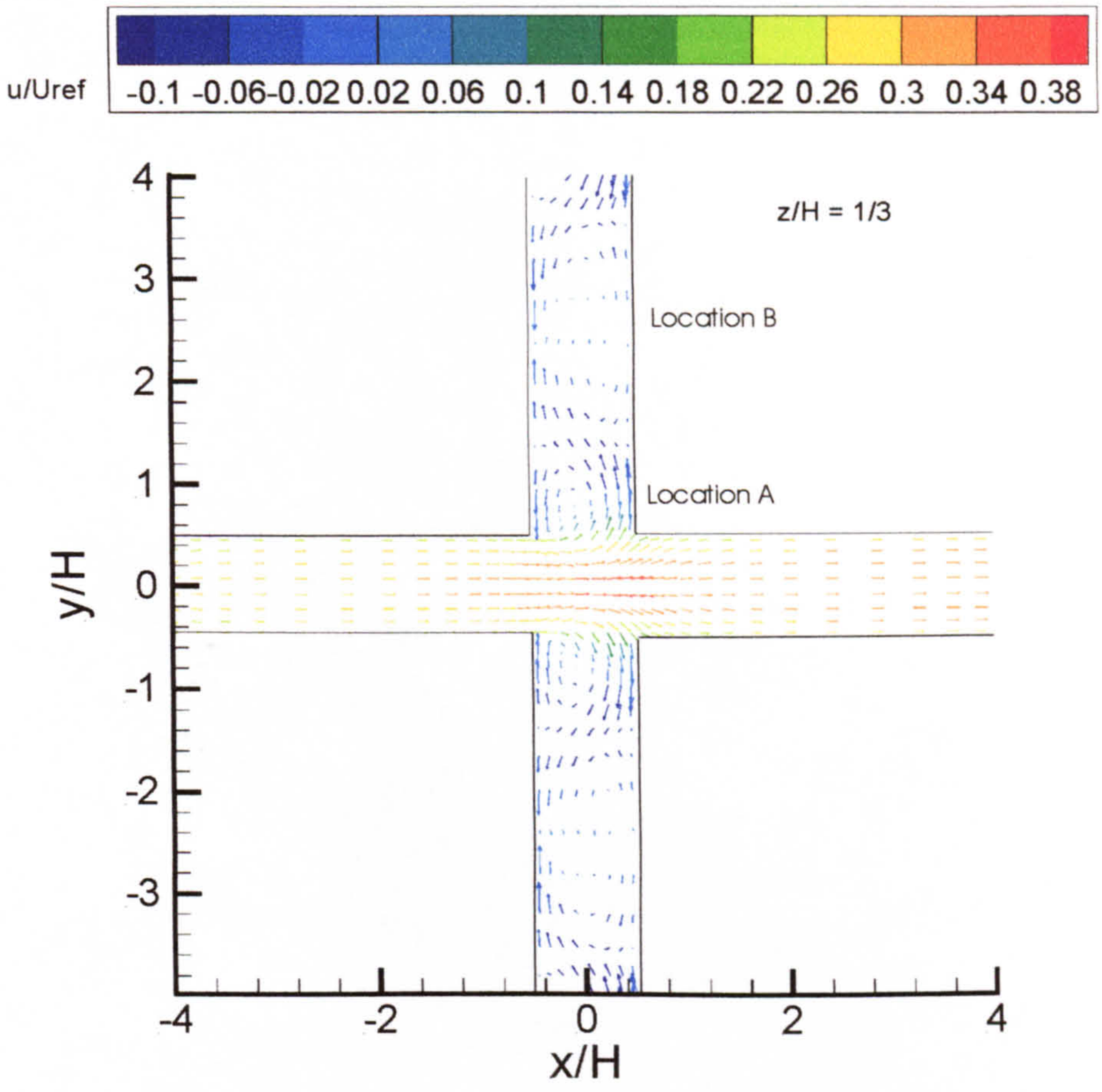

Figure 6.8. Computed flow field established at a height of Z/H=1/3.

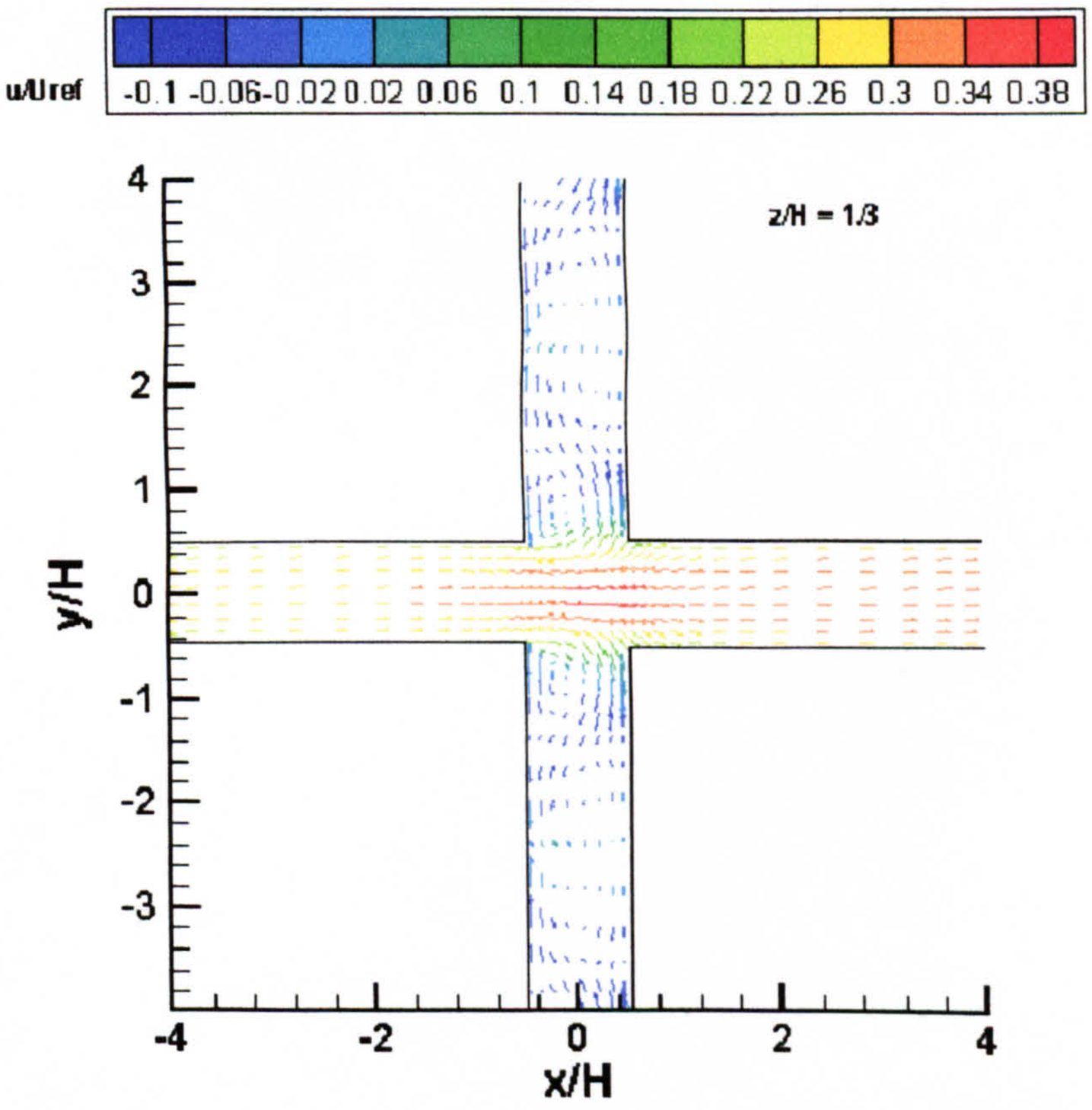

Figure 6.9. Measured flow field established at a height of Z/H=1/3.

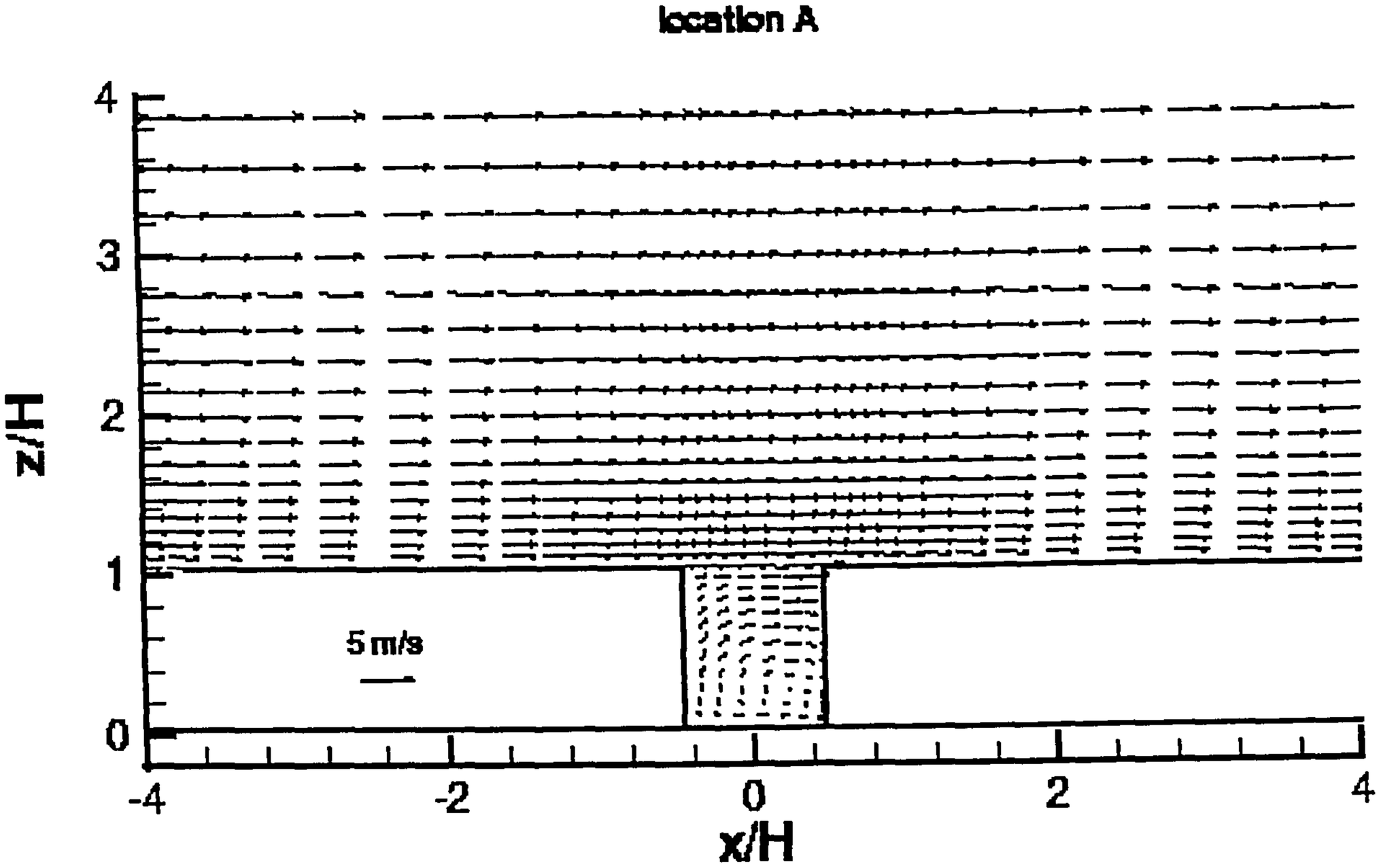

Figure 6.10. Side view of wind field established at location A.

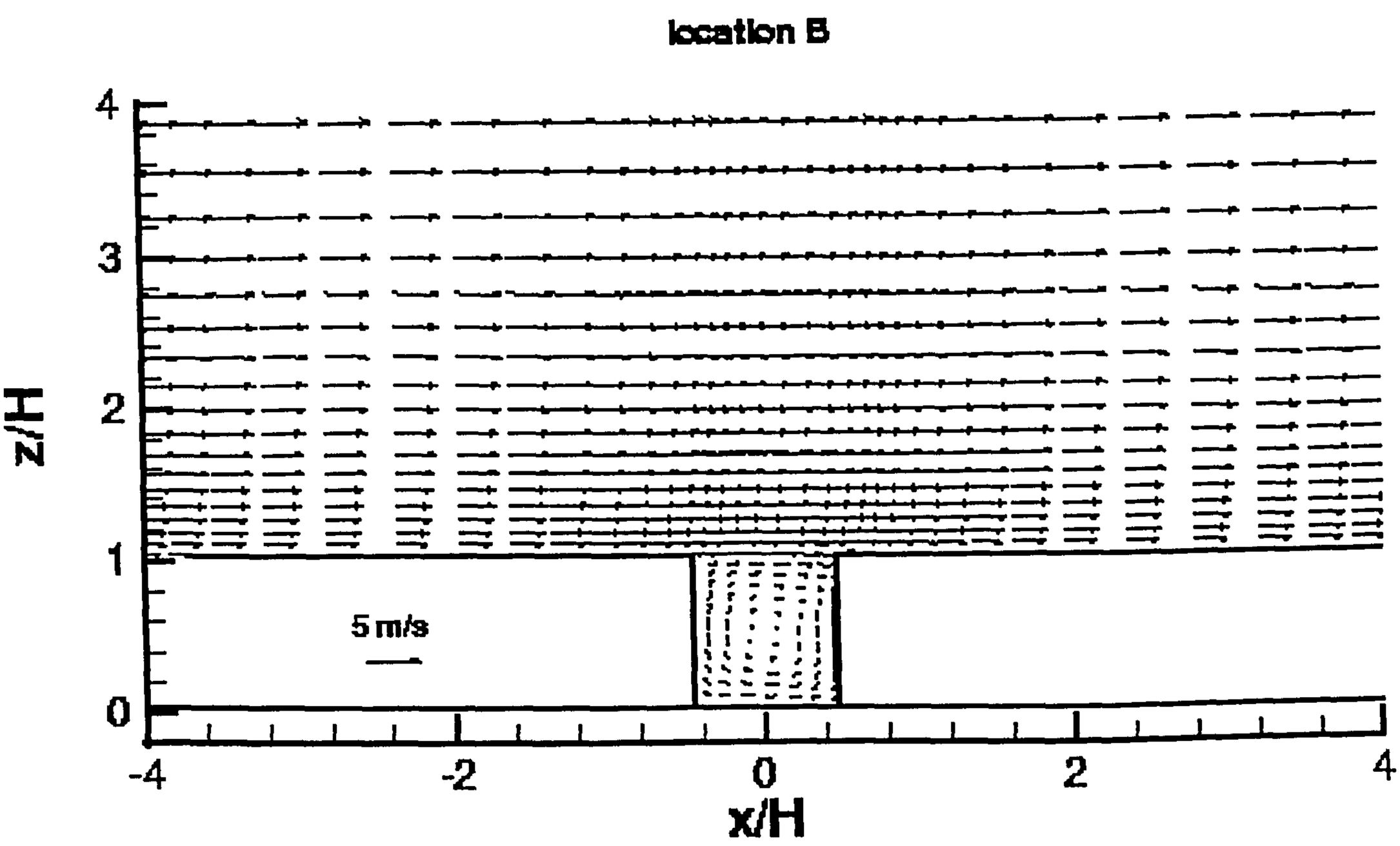

Figure 6.11. Side view of wind field established at location B.

Concluding, it is important to note that MIMO performed very well even after the simplifications were made. The three-dimensional nature of a street canyon produces corkscrew-like vortices and thus a more complicated wind field. Furthermore, the concept of the two-dimensional street-canyon is true as long as its length is 3 to four times larger than its width.

An additional case, using a 45 degrees angle, to the x-axis, wind direction, (i.e. two equal components at a 90 degrees angle), was considered. The wind was blowing from the lower left-hand corner of Figure 6.12 towards the upper right-hand corner of the Figure. For symmetry reasons a third row of buildings was added to the initial configuration and three columns were subtracted, in order not to exceed the computational limits of the model. The lower x-axis boundary was thus, made an inlet boundary together with the already specified lest hand side y-axis inlet boundary. The measurement area was chosen to be at the second intersection downstream. The idea behind this case study was to observe two incident and turbulent flows in the middle of the street canyon arrangement. This was thought of importance since, such a condition could easily be met in practice. The obtained results were in a way expected since a mirror-like performance was identified downwind on both axes. Figure 6.12 shows graphically this behaviour presenting two elongated weak vortices starting from the intersection and extending downwind on both axes.

The particular wind angle selected, i.e. 45 degrees, may be considered as a symmetric case as well as the perpendicular incident wind case studied at the beginning of this chapter. From a wind tunnel experiment conducted by Scaperdas, 2000, it was found that the flow was bi-stable 'switching sides', unlike the computational results obtained in this case. However, no computational results were given by Scaperdas, 2000 and thus, one may conclude that since the model tends to produce average profiles and instantaneous, steady wind fields the results of the case presented in this chapter are valid and reasonable.

It is also of interest to observe the comparison of the simulated results for this case against the simulated results for the case above, for the vertical profiles of the velocity at the two entrances of the street canyon. Surprisingly enough, the two profiles are identical and coincide (Figure 6.13).

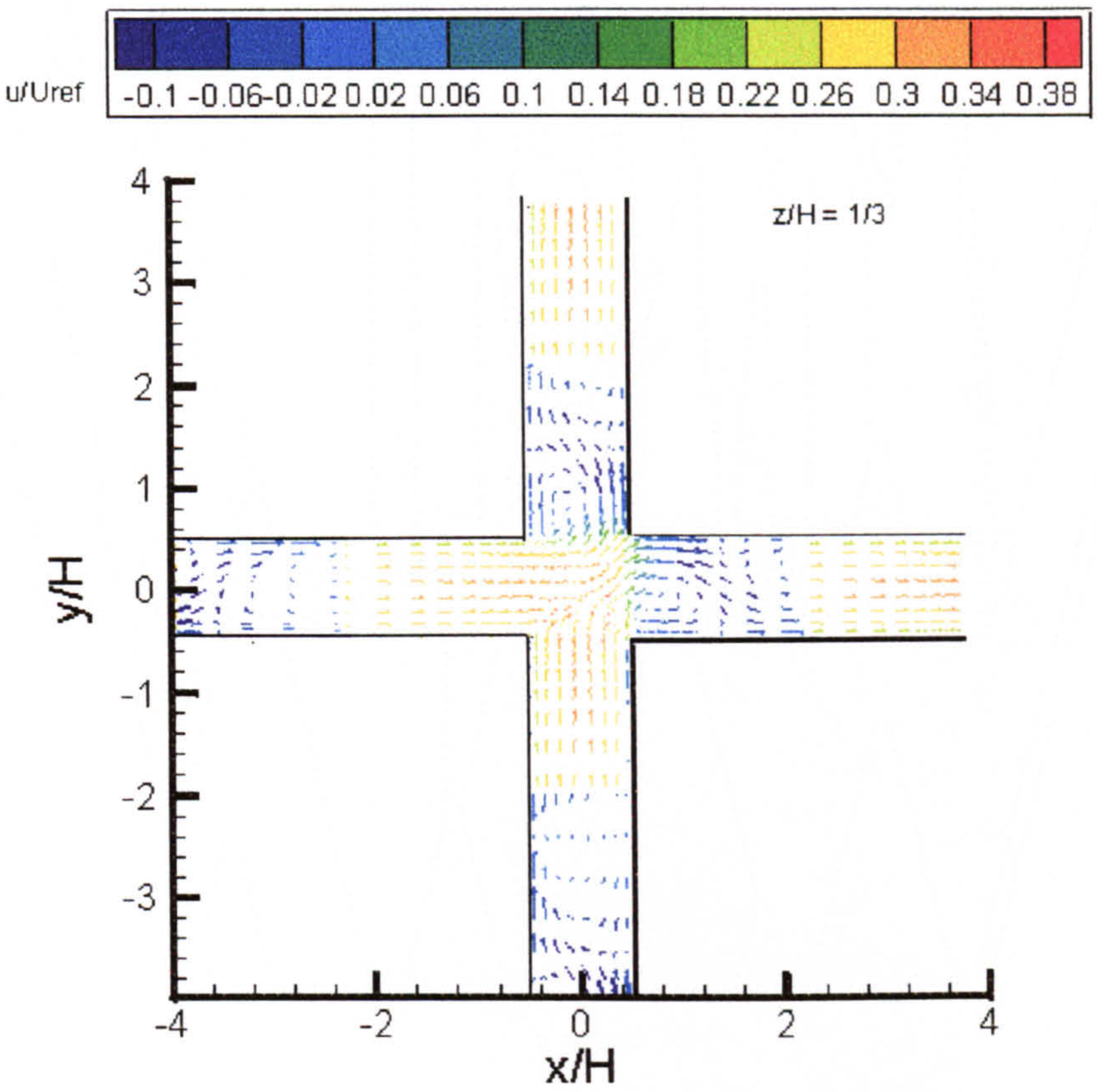

Figure 6.12: Flow field established at a height of Z/H=1/3.

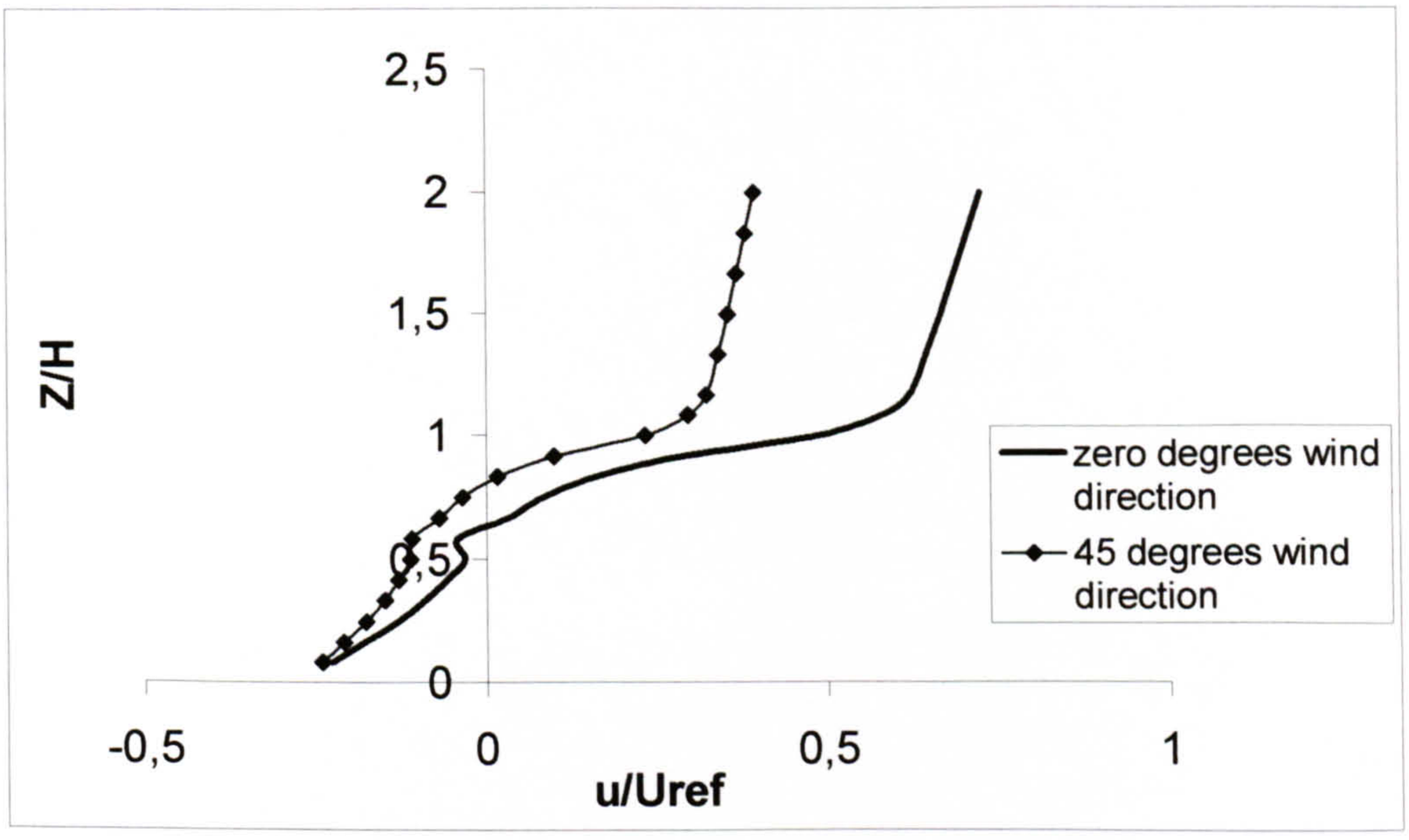

Figure 6.13: Simulated vertical profile of velocity for wind at angle of 45 degrees against vertical profile of velocity for zero degrees wind direction.

7 Mesoscale calculations- The London case

The purpose of the mesoscale calculations presented here, is to study the dispersion of pollutants (inert as a commencing point) above an urban cluster such as London. In particular it is of importance to study the dispersion patterns with a well-documented model over a thoroughly monitored area. Such an investigation could help in identifying, certain simulation limitations of the mesoscale modelling with ultimate purpose to implement a microscale model such as MIMO in order to provide the mesoscale one with the appropriate boundary conditions and pollutant vertical fluxes.

Having studied dispersion patterns in the small scale, it became evident that on a local scale the shape and distribution of buildings gave rise to local circulation systems, highly dependent on any changes made to the geometrical configuration of the specific area. It must be argued here that when the synoptic circulation is sufficiently stronger, such as to overtake any small-scale activity, then the building geometry effects are minimised.

The general differences between the mesoscale and microscale can be summarised as follows:

- A mesoscale model uses parameterisations that enable it to model flow above various types of ground. Thus, an urban area inside the computational domain is represented by an aerodynamic roughness value without taking into account any special features of the city. On the other hand, a microscale model does take into account building geometry.

- A mesoscale model takes into account bigger turbulent formations (eddies), whereas a microscale model resolves smaller eddies which play an important role especially in the vicinity of buildings.

- A mesoscale model can provide with information relating to general circulation patterns, thus the effect of an urban area to the wind field characteristics is included. The microscale can not resolve wind flow patterns in this dimension, but focuses on the effect of a cluster of buildings on the wind field.

Following the above and in order to fulfil the purposes of the present study the mesoscale model MEMO run coupled to the Eulerian trajectory model incorporating the necessary emission inventory, landuse and synoptic meteorological parameters, details of which will be presented in the following sections.

7.1 The non-hydrostatic mesoscale model MEMO

The prognostic mesoscale model MEMO has been developed by the Aristotle University Thessaloniki in collaboration with the Institute of Technical Thermodynamics of the University of Karlsruhe. This model belongs to the family of models designed for describing atmospheric transport phenomena in the local-to-regional scale, frequently referred to as mesoscale air pollution models.

It has been already successfully applied for various European airsheds including the Upper Rhine Valley and the areas of Basel, Graz, Barcelona, Lisbon, Madrid, Milan, London, Cologne, Lyon, The Hague, Athens (Moussiopoulos, 1995a; Moussiopoulos, 1995b; Moussiopoulos and Papagrigoriou, 1997) and Thessaloniki. In the following, a complete description of MEMO is given in brief outlines. More details are to be found elsewhere, (Flassak 1990), (Moussiopoulos et al. 1995).

7.1.1 Model Equations

The prognostic mesoscale model MEMO describes the dynamics of the atmospheric boundary layer. In the present model version, the air is assumed to be unsaturated. The model solves the continuity equation for momentum and several transport equations for scalars (including the thermal energy equation and, as options, transport equations for water vapour, the turbulent kinetic energy and pollutant concentrations).

The conservation equations solved in MEMO are the following:

$$\frac{\partial(\rho u)}{\partial t}+\frac{\partial(\rho uu)}{\partial x'}+\frac{\partial(\rho vu)}{\partial y'}+\frac{\partial(\rho wu)}{\partial z'}=-\frac{\partial \hat{p}}{\partial x'}+R_u+C_u \qquad (7.1)$$

$$\frac{\partial(\rho v)}{\partial t}+\frac{\partial(\rho uv)}{\partial x'}+\frac{\partial(\rho vv)}{\partial y'}+\frac{\partial(\rho wv)}{\partial z'}=-\frac{\partial \hat{p}}{\partial y'}+R_v+C_v \qquad (7.2)$$

$$\frac{\partial(\rho w)}{\partial t}+\frac{\partial(\rho uw)}{\partial x'}+\frac{\partial(\rho vw)}{\partial y'}+\frac{\partial(\rho ww)}{\partial z'}=-\frac{\partial \hat{p}}{\partial z'}+R_w+C_w-\hat{\rho}\cdot g \qquad (7.3)$$

$$\frac{\partial \rho}{\partial t}+\frac{\partial(\rho u)}{\partial x'}+\frac{\partial(\rho v)}{\partial y'}+\frac{\partial(\rho w)}{\partial z'}=0 \qquad (7.4)$$

$$\frac{\partial(\rho\psi)}{\partial t}+\frac{\partial(\rho u\psi)}{\partial x'}+\frac{\partial(\rho v\psi)}{\partial y'}+\frac{\partial(\rho w\psi)}{\partial z'}=R_\psi+C_\psi \qquad (7.5)$$

where, x', y' and z' represent the Cartesian co-ordinates and u, v and w are wind velocity components in the x', y' and z' directions respectively. ψ is any scalar (e.g. the potential temperature θ or the turbulent kinetic energy E).

In the conservation equations R_u, R_v, R_w and R_ψ represent turbulent diffusion, while C_u , C_v and C_w represent the volumetric Coriolis force components ($\underline{C} = 2\rho\cdot\underline{\Omega}\times\underline{v}$). The source/sink terms Q_ψ depend on the transported scalar quantity: For the potential temperature this term includes anthropogenic heat emission and the divergence of radiative fluxes, for the turbulent kinetic energy it contains the shear and buoyancy production rates as well as the dissipation rate.

Following the common practice in mesoscale models, variables are split into base-state parts (denoted by overbars) and mesoscale perturbations (marked by a hat). By definition, the base-state parts of the wind velocity components are taken as zero. For the thermodynamic variables the separation yields

$$p = \bar{p}(z') + \hat{p}(x',y',z',t) \qquad (7.6)$$

$$\rho = \bar{\rho}(z') + \hat{\rho}(x',y',z',t) \qquad (7.7)$$

$$\theta = \bar{\theta}(z') + \hat{\theta}(x',y',z',t) \qquad (7.8)$$

In order to accelerate the convergence of the solution of the elliptic equation for pressure (see below), the mesoscale pressure perturbation is split into three components:

$$\hat{p} = p_g + p_h + p_{nh} \qquad (7.9)$$

The first term on the right-hand-side of this equation accounts for a large-scale horizontal pressure gradient in the considered mesoscale domain. The hydrostatic part, i.e. the second term on the right-hand-side of Eq. (7.9), is obtained by integrating the hydrostatic equation:

$$\frac{\partial p_h}{\partial z'} = -\hat{\rho}\cdot g = -[\rho - \bar{\rho}(z')]\cdot g \qquad (7.10)$$

where ρ follows from the ideal gas law. The last term on the right-hand-side of Eq. (7.9), the non-hydrostatic part is computed implicitly by solving for the elliptic pressure equation.

7.1.2 Transformation to Terrain-Following Coordinates

The lower boundary of the model domain coincides with the ground. Because of the inhomogeneity of the terrain, it is not possible to impose boundary conditions at that boundary with respect to Cartesian coordinates. Therefore, a transformation of the vertical coordinate to a terrain-following one is performed:

$$\eta \equiv H\cdot\frac{z'-h(x',y')}{H-h(x',y')} \qquad (7.11)$$

H and h (x',y') are the (temporally and spatially constant) height of the model top boundary and the altitude at the location (x',y'), respectively. To allow for non-equidistant mesh-sizes, in order to achieve a better resolution near the ground, the additional transformation x = x (x'), y = y (y'), z = z (η) is employed, where x (x'), y (y') and z (η) represent arbitrary monotonic.

7.1.3 Numerical Solution of the Equation System

The discretised equations are solved numerically on a staggered grid. Temporal discretisation of the prognostic equations is based on the explicit second order Adams-Bashforth scheme. There are two deviations from the Adams-Bashforth scheme: The first refers to the implicit treatment of the non-hydrostatic part of the mesoscale pressure perturbation p_{nh}. To ensure non-divergence of the flow field an elliptic equation is solved. The elliptic equation is derived from the continuity equation wherein velocity components are expressed in terms of p_{nh}. It should be

noted that since the elliptic equation is derived from the discrete form of the continuity equation and the discrete form of the pressure gradient conservativity is guaranteed. The discrete pressure equation is solved numerically with a fast elliptic solver in conjunction with a generalized conjugate gradient method. The fast elliptic solver is based on fast Fourier analysis in both horizontal directions and Gaussian elimination in the vertical direction.

The second deviation from the explicit treatment is related to the turbulent diffusion in vertical direction. In case of an explicit treatment of this term, the stability requirement may necessitate an unacceptable abridgement of the time increment. To avoid this, vertical turbulent diffusion is treated using the second order Crank-Nickolson method.

The advective terms are computed by implementing a 3-D second-order total-variation-diminishing (TVD) scheme.

7.1.4 Parameterisations

Turbulence and radiative transfer are the most important physical processes that have to be parameterised in a prognostic mesoscale model. In the MEMO model radiative transfer is calculated with an efficient scheme based on the emissivity method for long-wave radiation and an implicit multi-layer method for short-wave radiation.

The diffusion terms in Eqs. (1-3) and (5) may be represented as the divergence of the corresponding fluxes. For turbulence parameterisations K-theory is applied. In case of MEMO turbulence can be treated either with a zero-, a one- or a two-equation turbulence model.

For most applications a one-equation model is used, where a conservation equation for the turbulent kinetic energy E is solved. The eddy viscosity K_m follows from

$$K_m = c_k \, l \sqrt{E} \qquad (12)$$

where a length scale (the so-called mixing length) is needed:

$$l = \left[\frac{1}{l^{\infty}} + \frac{1}{\kappa [z' - h(x', y')]} \right]^{-1} \qquad (13)$$

(κ: von Kármán constant). In MEMO the limiting value l^{∞} is given by $l^{\infty} = \max\left(30\,m\,,\, 0.00027 \left| \underline{v}_g \right| / f \right)$.

The eddy diffusivity K_ψ can be calculated from the turbulent Prandtl number $Pr_t \equiv K_m / K\psi$. The turbulent Prandtl number is given by

$$Pr_t = \begin{cases} 1 & ;\ z' - h(x', y') \geq z_D \\ \left[1.35 - 0.35 \dfrac{z' - h(x', y')}{z_D} \right] & ;\ z' - h(x', y') < z_D \end{cases} \qquad (14)$$

(typically z_D = 1000 m).

7.2 Initial and Boundary Conditions

In the prognostic model MEMO initialisation is performed with suitable diagnostic methods: A mass-consistent initial wind field is formulated using an objective analysis model; scalar fields are initialised using appropriate interpolating techniques. Data needed to apply the diagnostic methods may be derived either from observations or from larger scale simulations.

Suitable boundary conditions have to be imposed for the wind velocity components u, v, w, the potential temperature θ and pressure p at all boundaries. At open boundaries, wave reflection and deformation may be minimised by the use of so-called '*radiation conditions*'. As the original formulation of the radiation conditions merely allows disturbances to propagate out through the boundary, but does not allow information from outside to be imposed at the boundary expanded radiation conditions at lateral boundaries are used:

$$\frac{\partial \phi}{\partial t} = -C\frac{\partial \phi}{\partial n} + \frac{\partial \phi^s}{\partial t} + C\frac{\partial \phi^s}{\partial n} \qquad (15)$$

Where n is the direction perpendicular to the boundary and C the phase velocity that includes wave propagation and advection. C is calculated for every variable ϕ from known values from the interior of the computational domain. Eq. (15) differs from the standard formulation of the radiation condition by the last two terms describing the temporal and spatial change of the undisturbed large scale environment. This information can be specified to the model using either measurements or results of larger scale simulations.

According to the experience gained so far with the model MEMO, neglecting large scale environmental information might result in instabilities in case of simulations over longer time periods.

For the non-hydrostatic part of the mesoscale pressure perturbation, homogeneous Neumann boundary conditions are used at lateral boundaries. With these conditions the wind velocity component perpendicular to the boundary remains unaffected by the pressure change.

At the upper boundary Neumann boundary conditions are imposed for the horizontal velocity components and the potential temperature. To ensure non-reflectivity, a radiative condition is used for the hydrostatic part of the mesoscale pressure perturbation p_h at that boundary. Hence, vertically propagating internal gravity waves are allowed to leave the computational domain. For the non-hydrostatic part of the mesoscale pressure perturbation, homogeneous staggered Dirichlet conditions are imposed. Being justified by the fact that non-hydrostatic effects are negligible at large heights, this condition is necessary, if singularity of the elliptic pressure equation is to be avoided in view of the Neumann boundary conditions at all other boundaries.

The lower boundary coincides with the ground (or, more precisely, a height above ground corresponding to its aerodynamic roughness). For the non-hydrostatic part of the mesoscale pressure perturbation, inhomogeneous Neumann conditions are imposed at that boundary. All other conditions at the lower boundary follow from the assumption that the Monin-Obukhov similarity theory is valid. With the exception of

water surfaces (where the temperature is specified) the surface temperature is calculated from the non-linear heat balance equation

$$R\downarrow_O - R\uparrow_O + S\downarrow_O - S\uparrow_O - Q_S - Q_O - L_O - Q_a = 0 \qquad (16)$$

(R: long-wave, S: short-wave radiative fluxes ($R\uparrow_O \sim T_O^4$); Q_S heat flux to the soil; Q_O, L_O: sensible and latent heat to the atmosphere; Q_a: anthropogenic heat flux), which is solved using a Newton iteration technique. Radiative fluxes follow from the above mentioned radiation scheme. For the calculation of the soil temperature, a one-dimensional heat conduction equation for the soil is solved. The specific humidity at the surface (needed even in the case that the transport equation for water vapour is not included in the model) is computed from

$$q = \Psi q_s + (1-\Psi) q_2 \qquad (17)$$

where Ψ is the evaporation parameter varying between 0 and 1 (water: $\Psi = 1$, dry soil: $\Psi = 0$), q_S is the saturation humidity and q_2 is the humidity computed at the lowermost grid level above ground.

The one way interactive nesting facility is possible within MEMO. Thus, successive simulations on grids of increasing resolution are possible. During these simulations, the results of the application to a coarse grid are used as boundary conditions for the application to the finer grid (Kunz and Moussiopoulos, 1995).

7.3 Eulerian dispersion model

For the calculation of inert pollutant dispersion, a specially adjusted Eulerian dispersion model, TRAPPA model, was integrated into MEMO. The finite volume discretisation procedure is followed, which is conservative. By a non-equidistant grid level distribution in the vertical direction a better resolution near the ground is achieved. For a better formulation of boundary conditions at the lower boundary, which essentially coincides with the ground, the model TRAPPA uses the transformation to terrain-following coordinates adopted in the model MEMO. Advective terms are treated with the Flux Corrected Transport Adams-Bashforth scheme. Vertical turbulent diffusion is treated using the second order Crank-

Nickolson method. The dry deposition process is described with the "big-leaf" multiple resistance model concept.

7.4 Calculations performed

7.4.1 Area of investigation and emission inventory

MEMO ran nested, for this reason the coarse grid was set at 100 x 100 km and the finer at 50 x 50 km, centred over London. The greater area of interest is depicted in Figure 7.1a. This Figure is taken from CORINE with permission of the EEA.

As seen from this Figure, a 50 x 50 km^2 area includes the densely built central London area, the suburbs and a good part of rural area. A more detailed observation indicates that London maintains unusual for many European cities, environmental characteristics. In fact even the densely built area is not continuous and is interrupted by parks, squares and regions of different air pollution emission types. Such a large area, which presents variability in land use, although maintains a relatively simple morphology, creates the need for accurate roughness mapping and a representative emission inventory.

For this purpose, as far as the roughness mapping is concerned, it was decided to use information given by CORINE coupled with mainly ground truth detailed data provided by SATURN partner Dr. Ranjeet Sokhi (private communication).

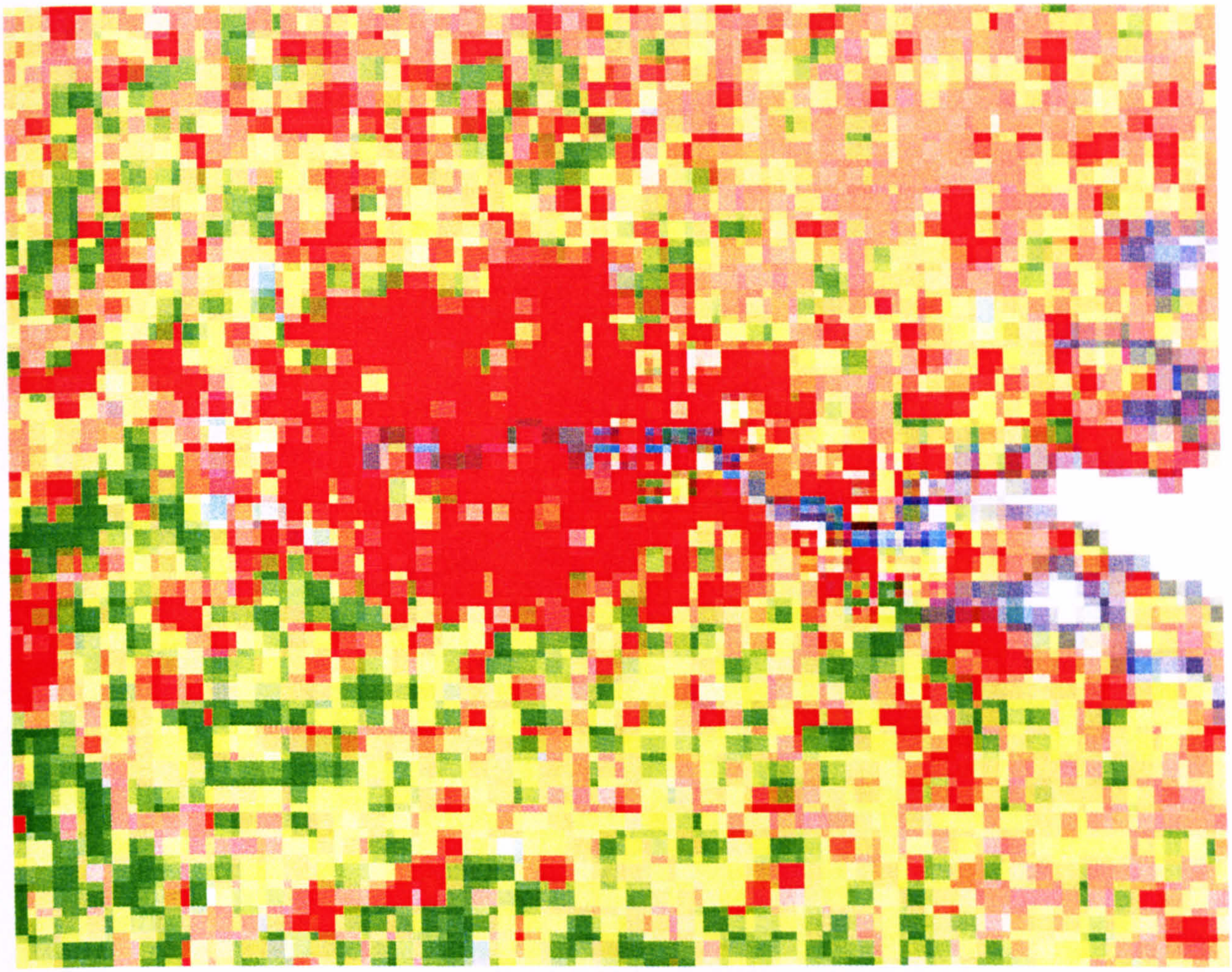

Figure 7.1.a The CORINE Level 3 classification for the London greater area

LEGEND FOR CORINE LEVEL 3 CLASSIFICATION

- Continuous urban fabric
- Discontinuous urban fabric
- Industrial or commercial units
- Road and rail networks and associated land
- Port areas
- Airports
- Mineral extraction sites
- Dump sites
- Construction sites
- Green urban areas
- Sport and leisure facilities
- Non-irrigated arable land
- Permanently irrigated land
- Rice fields
- Vineyards
- Fruit trees and berry plantations
- Olive groves
- Pastures
- Annual crops associated with permanent crops
- Complex cultivation patterns
- Land principally occupied by agriculture, with significant areas of natural vegetation
- Agro-forestry areas
- Broad-leaved forest
- Coniferous forest
- Mixed forest
- Natural grassland
- Moors and heathland
- Sclerophyllous vegetation
- Transitional woodland-scrub
- Beaches, dunes, sands
- Bare rocks
- Sparsely vegetated areas
- Burnt areas
- Glaciers and perpetual snow
- Inland marshes
- Peat bogs
- Salt marshes
- Salines
- Intertidal flats
- Water courses
- Water bodies
- Coastal lagoons
- Estuaries
- Sea and ocean

Figure 7.1.b

Other significant model parameters are:

- Space resolution: The space resolution in the present model configuration, allows for a 1 x 1 km cell size. This cell size coincides with the maximum domain size MIMO can support.

- Horizontal eddy diffusion coefficient finally was selected to be 10,000 m^2s^{-1}. This value was empirically selected by the technical support group of the Laboratory of Heat Transfer considering the topography and the roughness of the area under investigation.

The emission inventory for London was provided by the London Research Centre as well as the emission factors, which represent weekend circulation. It must be noted here that the case study was chosen considering the "good" emission inventory data, which referred to the weekend and to the suitable meteorological conditions, necessary to support the creation of high air pollution concentrations. The case study day was the 31st of July 1999.

The emission inventory included ground sources of NO_x such as cars, industrial activity and other minor ones, and stack sources such chimneys and other elevated ones. These were divided into 5 layers above the ground as requested by MEMO. NO_x emitted from the stacks, had a vertical exit velocity and was hotter than the surrounding air, thus diffusion commenced at a greater height than the stack height. For this reason the effective height DH was computed following Holland's semi-empirical law:

$$DH = \frac{(1.5 \times V_s \times D + 4 \times 10^{-5} (m^3/cal)\, Qh)}{u}$$

Where: Vs is the evit velocity of the effluent (m/s), D is the stack diameter (m), Qh is the heat released in calories/sec and u is the wind velocity at that height (m/s). The effective height calculated is added to the original stack height for each case.

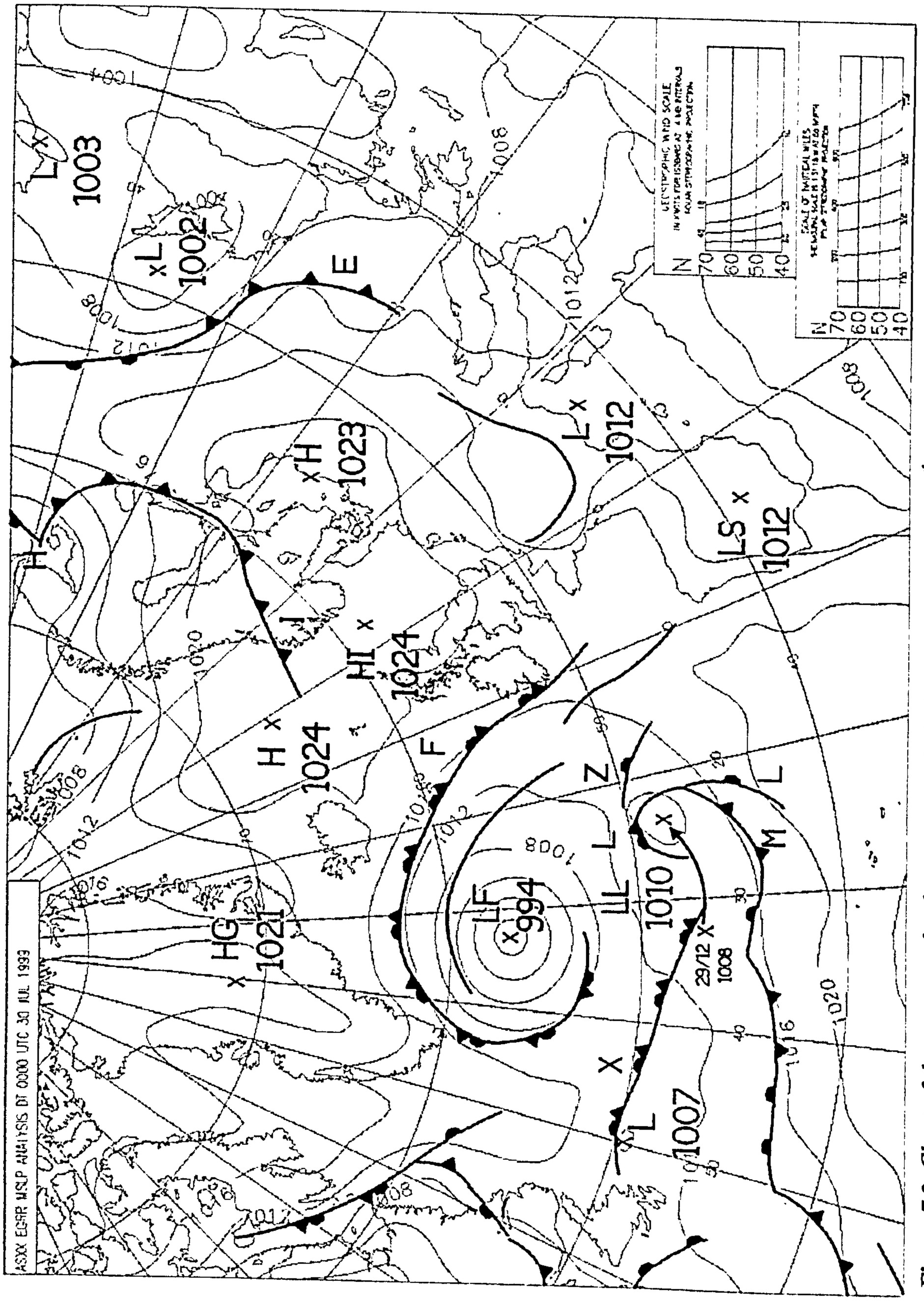

Figure 7.2 Chart of the mean sea level pressure analysis for 00:00LST on the 30th of July 1999.

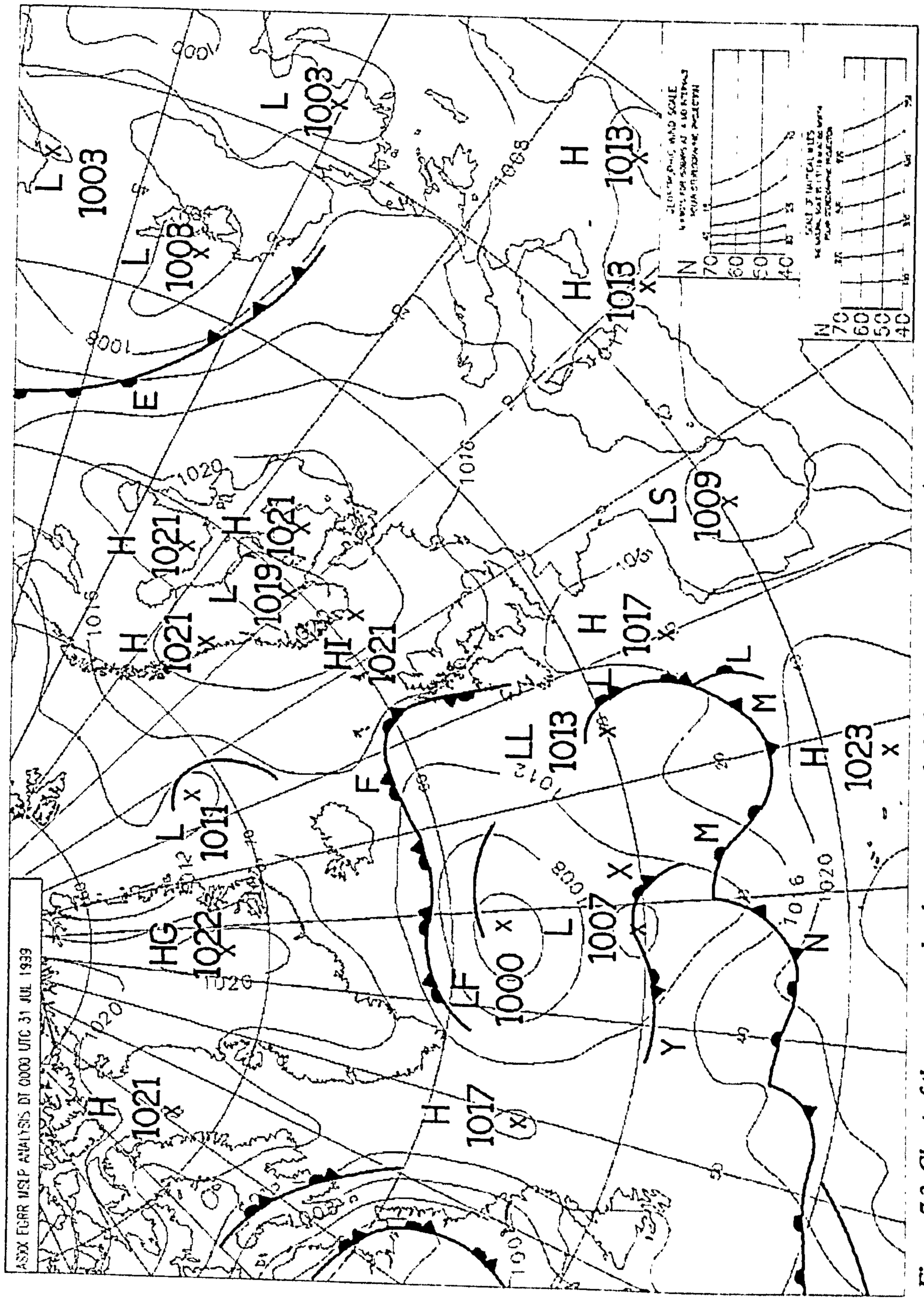

Figure 7.3 Chart of the mean sea level pressure analysis for 00:00LST on the 31st of July 1999.

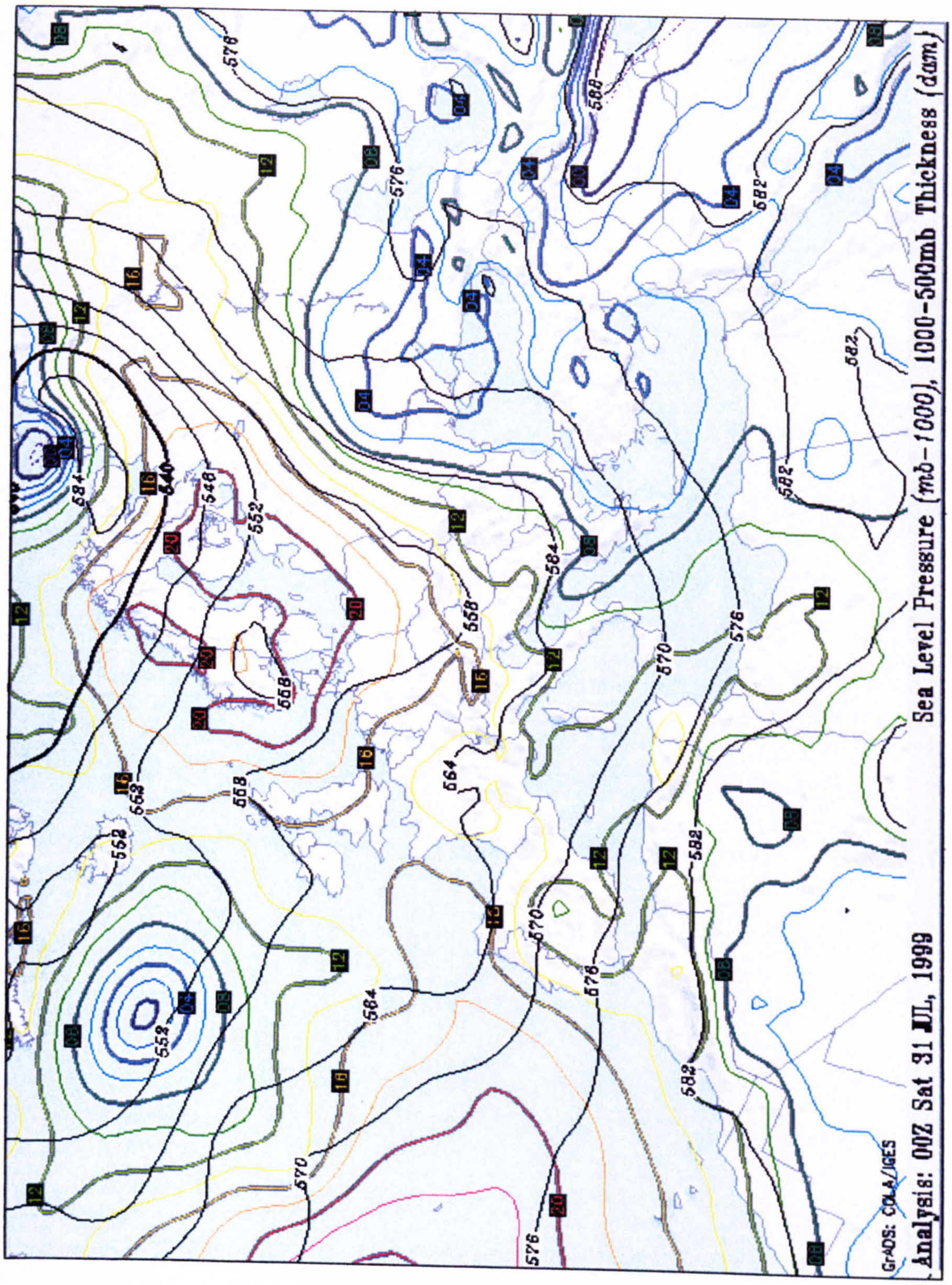

Figure 7.4 Analysis of the 1000-500hPa thickness layer of the 31st of July 1999 at 00:00LST.

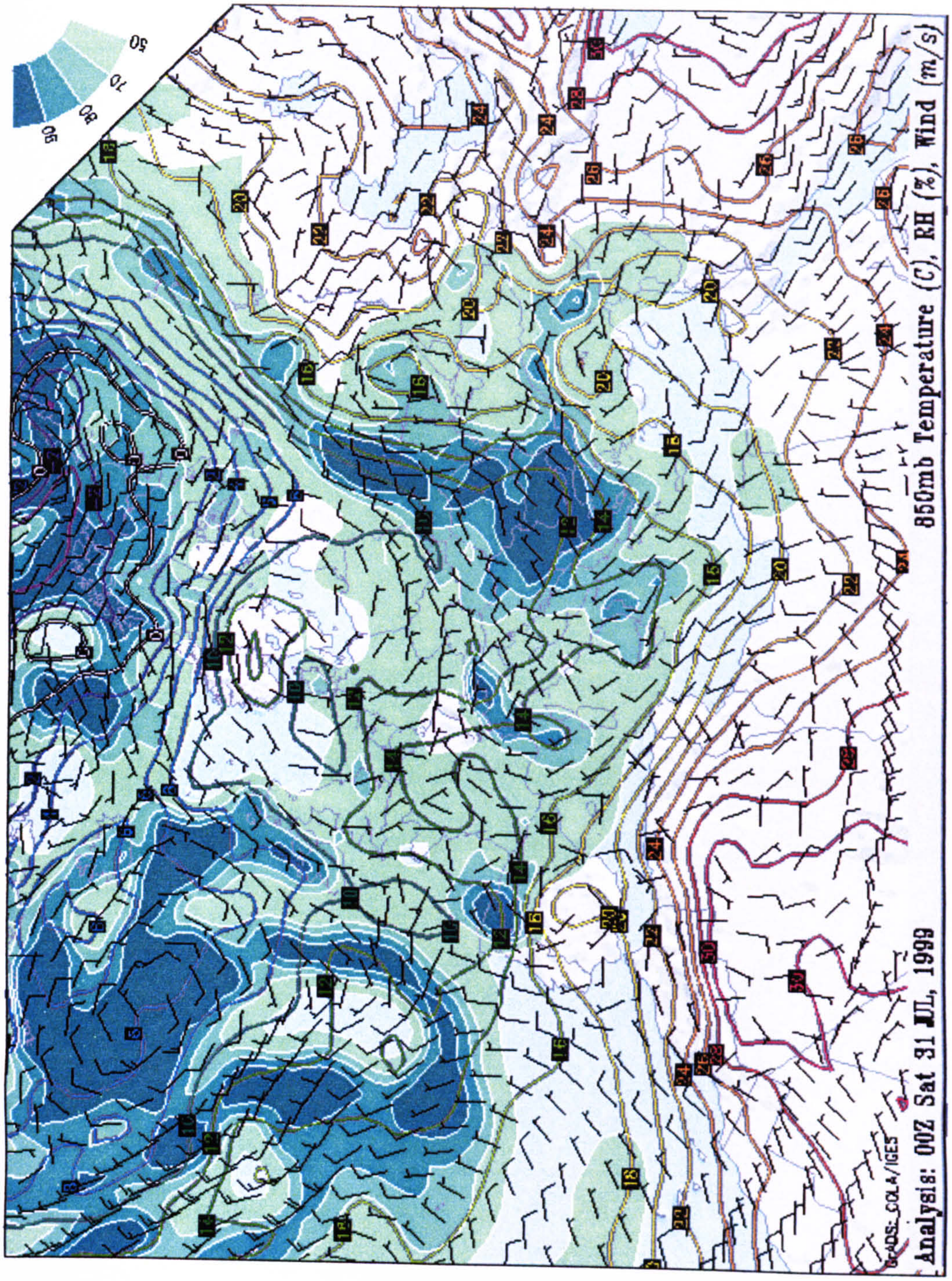

Figure 7.5 Analysis of Temperature, Relative Humidity and Wind of the 31st of July 1999 at 00:00LST.

7.4.2 Background meteorological information

The MEMO model as was mentioned above, used for initialising boundary conditions from the large scale model EMEP-MSCW[1]. These included, wind velocity at a height of 600m, temperature and temperature gradient in order to create a profile, wind direction and humidity. In particular, the synoptic meteorological conditions that prevailed during the case study time period are presented in Figures 7.2, 7.3, 7.4 and 7.5.

A good observation of these figures revealed the following main meteorological conclusions:

- On the 30th of July, 1999 at 00 LST (or 00 UTC), the surface atmospheric circulation over the British isles was characterised by a large scale anticyclone covering the North Sea and Scandinavia, with central mean sea level pressure of 1024hPa, (Figure 7.2). This type of circulation induced weak synoptic wind over southern England, blowing mainly form the easterly sector. In the west an occluded front, which is part of a Atlantic deep low pressure system, approached Ireland, evidencing the warm air advection being performed over Atlantic over at that time. The weak wind regime caused limited vertical extend of the mixing layer and, in association with the clear sky conditions, facilitated the accumulation of air pollutants in the lower tropospheric layers and the formation of poor dispersion conditions over the GLA.

- On the 31st of July, (00 LST), the front had moved northwards, being located over northern Ireland and Scotland on the 31st of July without influencing the fair weather conditions over southern England, (see Figure 7.3).

- As the anticyclonic circulation continued to predominate, the surface wind remained weak, however it had shifted to the southerly sector. The progressive warm air advection over northern Europe caused the establishment of warm air masses over the British Isles and Scandinavia. These can be clearly seen from the 1000-500 hPa thickness chart, in Figure 7.4. It is indicative that the

[1] http://projects.dnmi.no/~emep/

mean daily surface temperature in London was relatively high for the season. Furthermore, due to the enhanced moisture of the advected warm air masses, the 850 hPa relative humidity (RH), increased over the British Isles and mainly over the southern coast, where it reached a value in the range of 70-80 %, Figure 7.5. The high temperatures in association with the increased humidity, further contributed to the degradation of the air quality conditions over the GLA during the case study day.

7.4.3 London Air Pollution Monitoring Network

The London Air Pollution Monitoring Network, (LAPMN), is a "measuring organization" with nearly 30 years operating experience. During this time period the network has expanded and modernised following the technological developments and the scientific needs to better cover the Greater London Area, (GLA). Nowadays the network consists of 30 well-distributed stations, which monitor a variety of air pollutants. All stations are networked and their data are centrally recorded and quality controlled before made available to the public. These stations are classified in accordance with well-accepted categorization procedures in seven types, (e.g. roadside, urban background, urban centre, suburban etc). This categorisation must be carefully considered before using their data.

Detailed information and data archives can be found in the following web address, http://www.aeat.co.uk/netcen/airqual/data/sitelon.html.

For the needs of the present thesis, seven monitoring stations were selected which are equipped to measure NO_x and O_3 concentrations with a significantly long time history of data. Their hourly estimates were used mainly for general validation purposes against the meso-scale model corresponding results. It should also be mentioned that the selected stations cover all types of monitoring areas in the city centre and the suburbs.

In Figure 7.6 the GLA map is illustrated together with the locations of the selected monitoring stations.

Map of Greater London

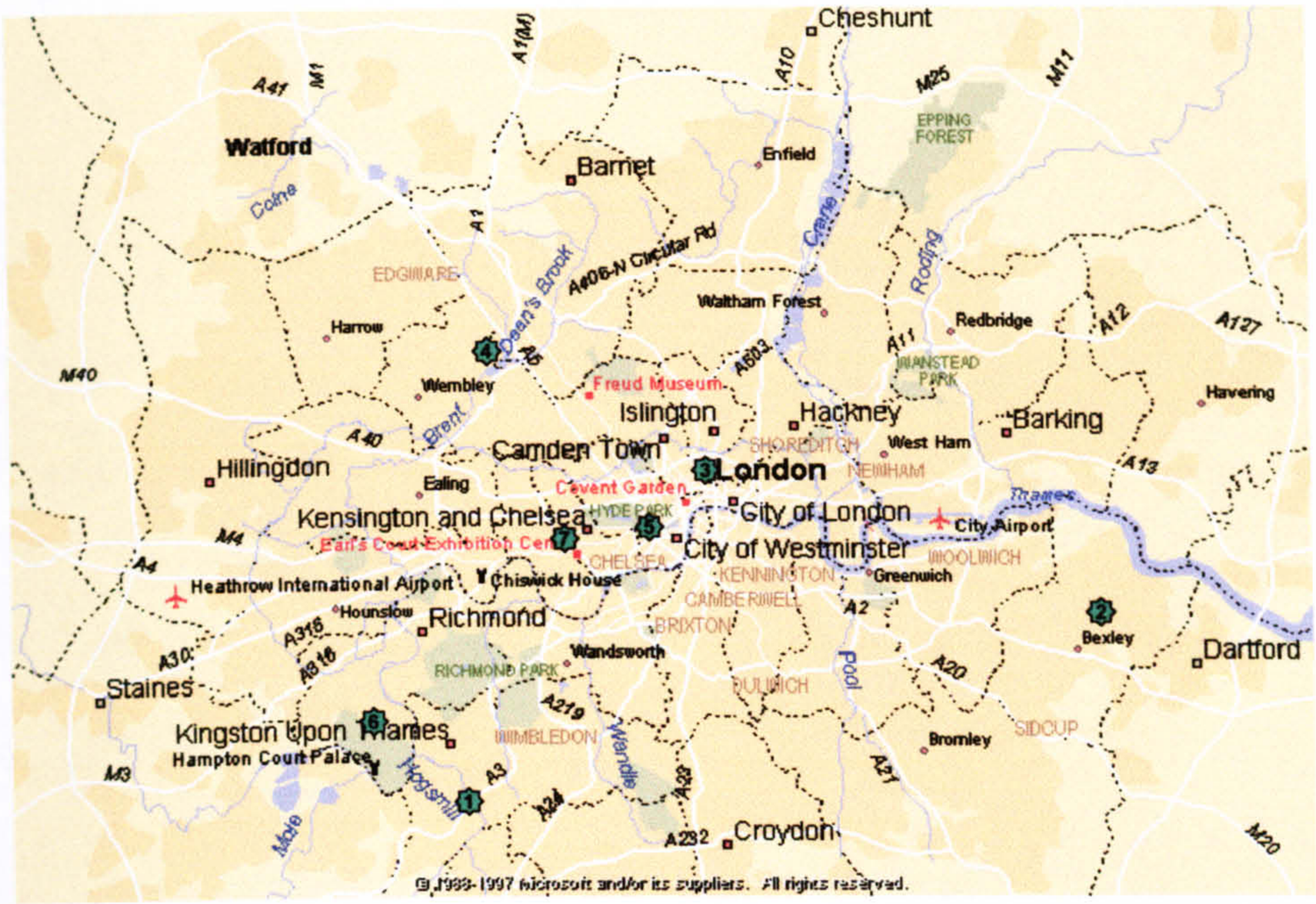

Monitoring Sites in London:

1) London A3 Roadside
2) London Bexley
3) London Bloomsbury
4) London Brent
5) London Bringe Place
6) London Teddington
7) West London

Figure 7.6: Map of the Greater London Area indicating the locations of the selected monitoring stations.

7.4.4 MEMO results

Based on the input data described above, MEMO performed the wind field reconstruction and the NO_x concentrations for the 30th and 31st of July 1999. The results are plotted in figures 7.7 and 7.8 respectively. According to the results, one can draw the following conclusions:

A) 30/7/1999

- 04 LST: The Figure is practically divided into two parts. In the upper part the wind blows mainly from the North-East direction with intensities lower than 3 m/s. In the bottom part the wind changes direction and turns to the Eastern sector with relatively lower intensities. This characteristic is actually supported by the synoptic meteorological maps presented previously. It is important to note that in the middle of the picture and over the Eastern part the wind is even weaker with uncertain wind direction. This behaviour is attributed to the local topography. The overall assessment is that the wind field reconstruction is well depicted and matches perfectly with the meteorological synoptic conditions. As far as the NO_x concentrations is

concerned one can identify values varying in the range of 15 to 50 ppb approximately according to the MEMO calculations. These calculations also indicate an island of higher concentrations in the central part of London. These observations come in satisfactory agreement with the measurements of the LAPMN stations, some of which indicate higher concentrations at the centre of London (West London Station, Marylebone station etc.). Comparison of absolute hourly values will not be attempted because it would be totally unfair for the model since only one case is studied. The computed concentrations tend to drop while moving away form the centre towards the northern and southern parts of the domain. This is also observed from stations of LAPMN classified as background.

- 08 LST: As seen from the Figure, both the flow field and the air pollution concentrations are slightly altered in both general orientation and distribution in particular the wind field intensity is weaker giving rise to higher concentrations along the east to west main axis. Furthermore, it is worth noticing that in the very central area of the city, higher concentrations are observed. These observations together with the overall increase of the NO_x values are confirmed by LAPMN stations.

- 12 LST: At this time of day the overall NO_x concentration pattern is very much reduced indicating the lowest daily values according to the model calculations. However, a closer examination of the LAQMN stations data and especially those who provide background urban or suburban measurements (i.e. independent of main road local production), the same behaviour is identified.

- 16 LST: For part of the Figure, it is observed that the wind field is well formed with higher intensities, although it maintains the same general flow pattern (i.e. wind blowing from the eastern sector). These relatively higher intensities of the flow do not seem to diffuse polluted air masses and thus to reduce the final concentrations. On the contrary, air pollution has built and covers an area equivalent to that of 08 LST, with more or less the same pollution levels. Here again, the same trends are indicated by the representative LAPMN stations.

- 20 LST: At this time of day and although the winds are slightly stronger all over the computational domain, local air pollution activities take over. Thus, maximum daily concentrations appear over the city centre covering at the same time the biggest part of the area examined. Here again the same sort of performance is shown with only few deviations from the LAPMN. This is in a way very interesting especially since the model estimates are based on a chemically inert routine without considering major background transported pollutants in the computational domain.

- 24 LST: The description given for the previous case, (20 LST), in both meteorological and air quality terms, could fit to this time spell. However, the high air pollution city centre islands are now of lower concentrations and the overall NO_x polluted region is some how reduced. This was expected since the wind regime is similar to the previous case while the emissions are reduced.

B) 31/7/1999

Following the meteorological description given above, the second case study day, 31/7/1999 presents the same characteristics at least during the first twelve hours of the day. As it was mentioned in the description of the synoptic conditions previously, the only meteorological differences occurred when the anticyclone had shifted towards the south-eastern sector, producing warm and moist air masses over the south-eastern coast. These developments assisted the strengthening of the south-easterly wind flow, which shifted the polluted air towards the north. Taking into account this new meteorological pattern it is worth pointing out the following:

- 16 LST: The model estimates indicate that the upper half of the computational domain maintains a higher NO_x pollution regime; while over the city centre region the highest concentrations are observed. This is in agreement with the pollution trends indicated by the LAPMN and can be explained by the well-defined southerly flow, which transports the polluted air mass towards the north.

- 20 LST: During this time period and although the wind flow regime is stronger and well defined the concentrations estimated by the model present the worst disagreement with the LAPMN measurements. In fact the model NO_x estimates indicate a very dispersed pattern, which is not the case shown by the LAPMN. Significant differences on both maximum concentrations and trends are identified. These discrepancies can be explained by the fact that the model in its present arrangement can not easily model the thermal structure of the lower troposphere, which under the circumstances could be associated with low temperature inversions. These meteorological phenomena are of local nature and can only be measured by specific instrumentation operated close to the area of interest. This rather critical remark about the observed discrepancies is caused because of the good performance of the model and good agreement with measured data for all other cases.

- 24 LST: This is the final time period over which MEMO computed the wind field and the NO_x air pollution pattern over the area of interest. For this particular case one can identify similar computational behaviour with the one presented for the 16 LST results, with the exception that the wind is slightly stronger than for the 16 LST case. Here again the NO_x estimated concentrations are in fair agreement with the LAPMN corresponding measurements. Both the pollution levels and the general trend indicating a shifting of the polluted masses has taken place towards the north, is evidenced.

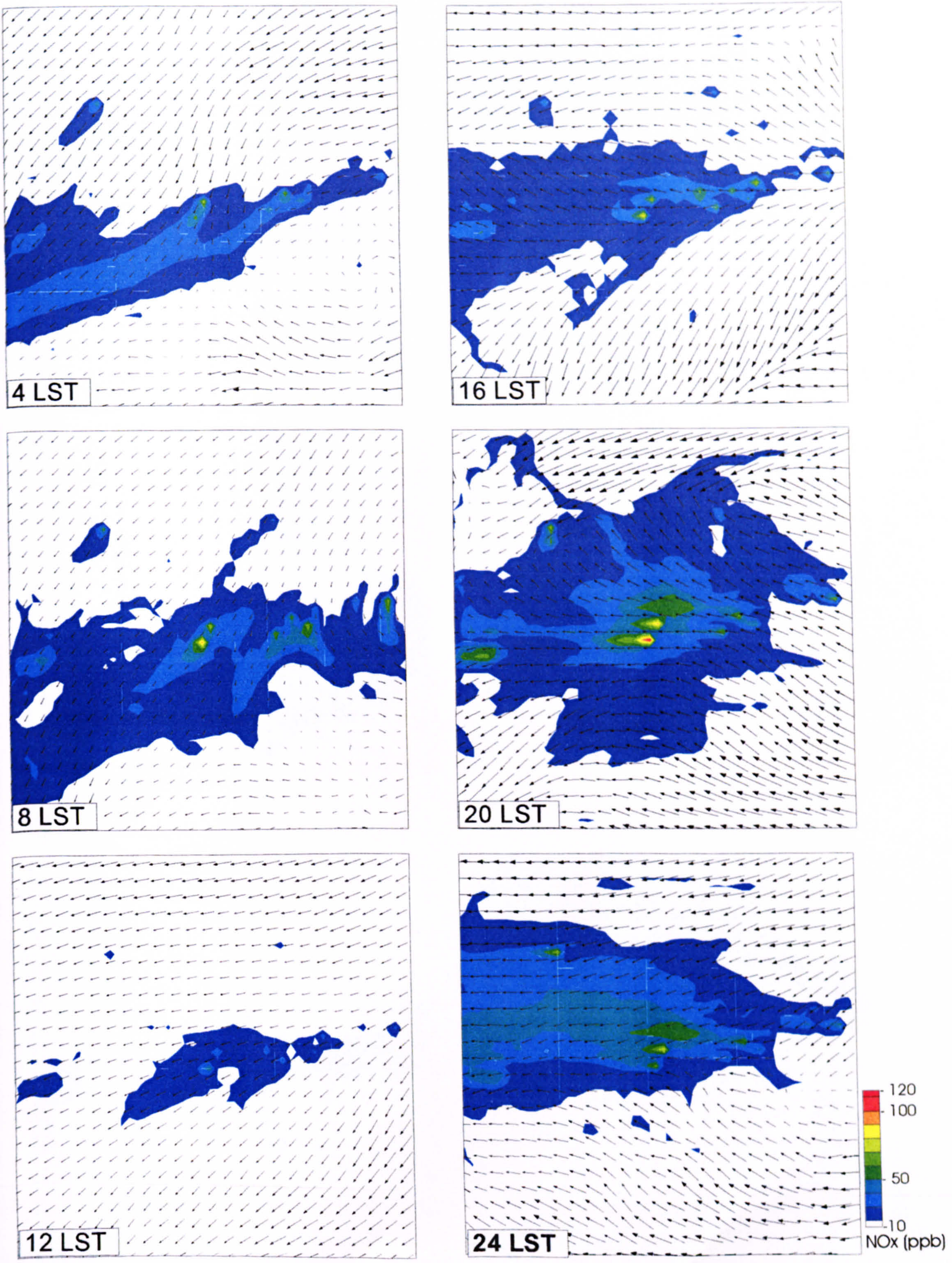

Figure 7.7: MEMO simulations of the wind field flows and NOx concentrations over the GLA on 30/7/99.

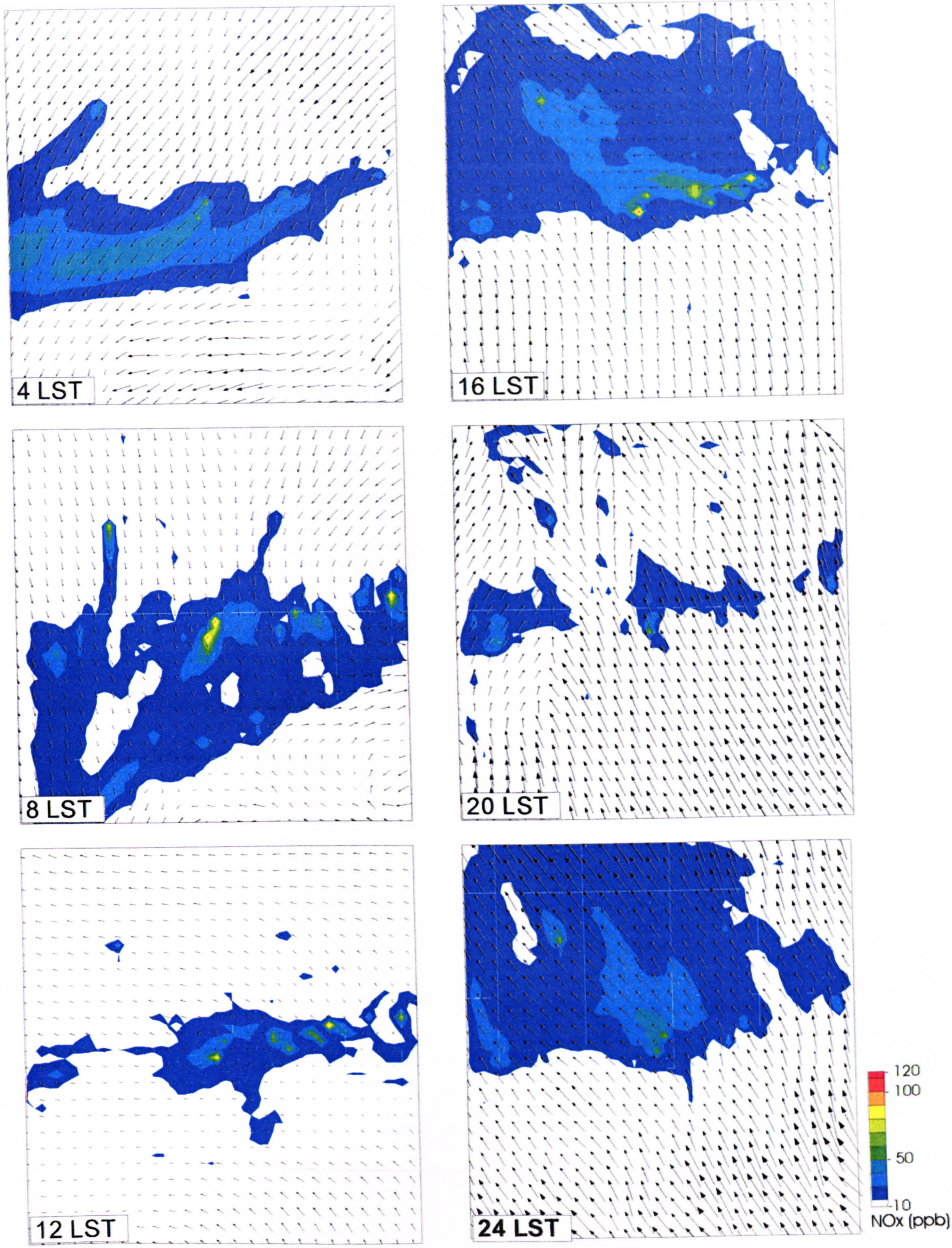

Figure 7.8: MEMO simulations of the wind field flows and NOx concentrations over the GLA on 31/7/99.

Following the above discussion, which was oriented towards a qualitative way, it was thought of importance to examine the obtained results in a more quantitative way. In this respect, seven stations of the LAPMN were selected covering urban, suburban and roadside environments and at the same time maintaining a complete time series of NO_x measurements, for the selected study. These stations are illustrated in Table 7.1 together with a brief description of their characteristics related to their location:

Station Name	Description
London A3 Roadside	Immediately alongside busy A3 Kingston by pass 2.5m from roadside. In suburban residential area.
London Bexley	Commuting centre park off Bridge Road in residential area of North End, suburban.
London Bloomsbury	Urban centre, land at Russell Square Gardens, 35m from kerbside.
London Brent	Urban background, located in the grounds of a school, 30m from a nearest road in a residential area with light industry.
London Bridge Place	Urban background, second floor office overlooking back street near Victoria Station.
London Teddington	Urban background, monitoring site at the National Physical Laboratory, close to parkland.
West London	Located in a municipal depot in a partially residential area bounded on all sides by major roads. 90m from Warwick Road, urban background.

Table 7.1. Brief description of characteristics of stations chosen for comparison purposes.

Four of the stations presented in the table above, which are not characterised by local air pollution regimes and at the same time cover both the central and the suburban London area, were chosen for comparison with MEMO-TRAPPA results. A time-series comparison is thus, attempted between hourly NO_x data measured at each one

of the four selected stations of the LAPMN and the corresponding computed NO_x concentrations.

In Figure 7.9 a comparison for Bexley, Bloomsbury, Brent and London Bridge is illustrated. A general characteristic of all plots is the variability of the NO_x concentrations, which cover a large range of values between 10 and nearly 200 ppb. This may be attributed to the selected case study, which as it was presented in more detail previously allows the formation of areas of high NO_x concentrations during selected time periods, due to the prevailing meteorological conditions. This variability is followed by the model estimates especially for the London Bridge, Bloomsbury and Brent stations. For the Bexley station however, this agreement is not as good. The discrepancy could be attributed to local conditions dominating since the monitoring station is located in a car park very close to a busy road. For the A3 roadside station a time series comparison is not attempted since both mean values and deviations differ significantly (between measured and computed values), and it seems that the model completely loses the very high values observed throughout the time series length of the station. At the same time this station is the only exception of extremely high values for all the LAPMN stations. This strongly indicates that an extremely high polluted local air mass biases the measurements of the station, taking under consideration the fact that it is situated at the side of a big, busy road.

Details of all measured and computed NO_x concentrations for the seven selected stations are presented in appendix A. In the same appendix results of the associated statistics are shown. These include both the standard deviation and the correlation coefficient between measured and computed concentrations for the stations. The correlation coefficient values, although were estimated using a relatively small number of points, satisfy the 99.8% confidence level and can be statistically accepted.

In Figure 7.10 a scatter diagram is presented of all pairs of values (measured-computed) of the case study for all seven stations selected. Here again, with the exception of A3 roadside, a good concentration of points is observed close to the 45 degrees line. It is also evident that MEMO-TRAPPA model tends to underestimate NO_x concentrations, which may be attributed to the fact that point measurements can not really be represented by a mesoscale model with the present settings. Additionally, the absence of an accurate background level of pollution given as input

to the model and the fact that the model integrates over a layer of 10m above ground and may also explain the underestimation. Nevertheless, the compute correlation coefficients and standard deviations indicate a very good overall performance of the model. In particular for the Bexley, London Bridge and Brent stations a correlation coefficient of 0.9 is achieved. Teddington and West London stations follow with a correlation coefficient of 0.8 and Bloomsbury station with a 0.7 one. Standard deviation values are also good ranging from 14 to 34, which is considered reasonable for the case. The only exception as mentioned above is the A3 roadside station.

The above quantitative results are considered very good and encourage further work during episodic weather conditions and other weekdays with different meteorological conditions and emission inventories.

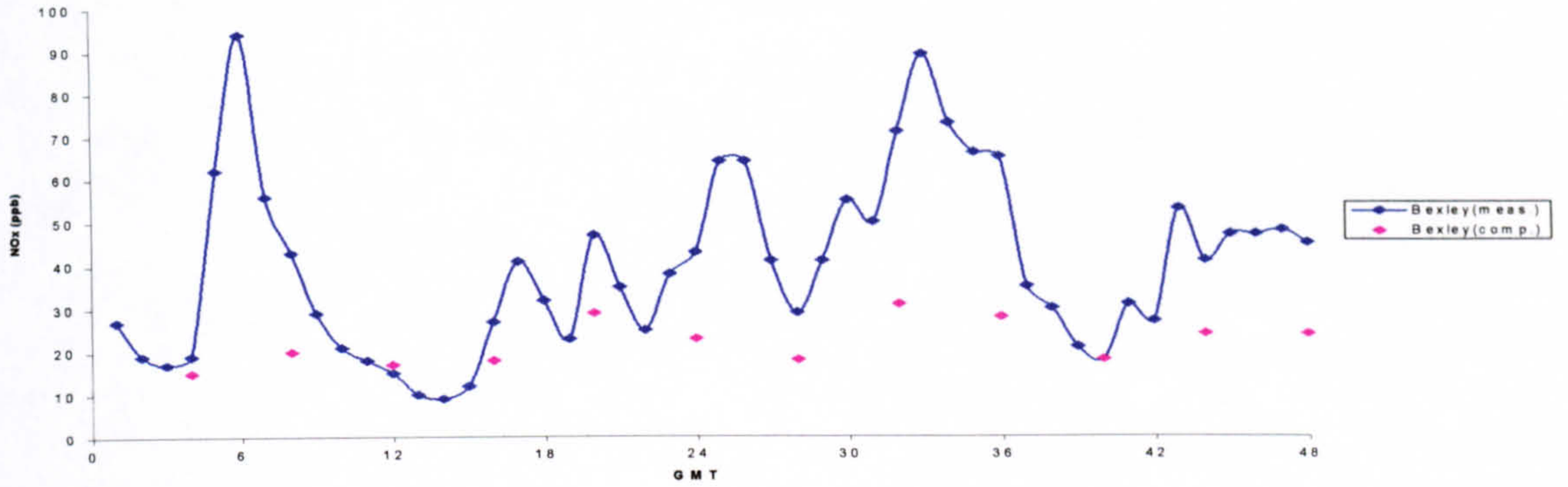

Figure 7.9: Hourly variation of NO_x concentrations for the 30th and the 31st of July 1999 for the stations of Bexley, Bloomsbury, Brent and London Bridge, (moving from the top downwards). The pink points indicate the computed concentrations.

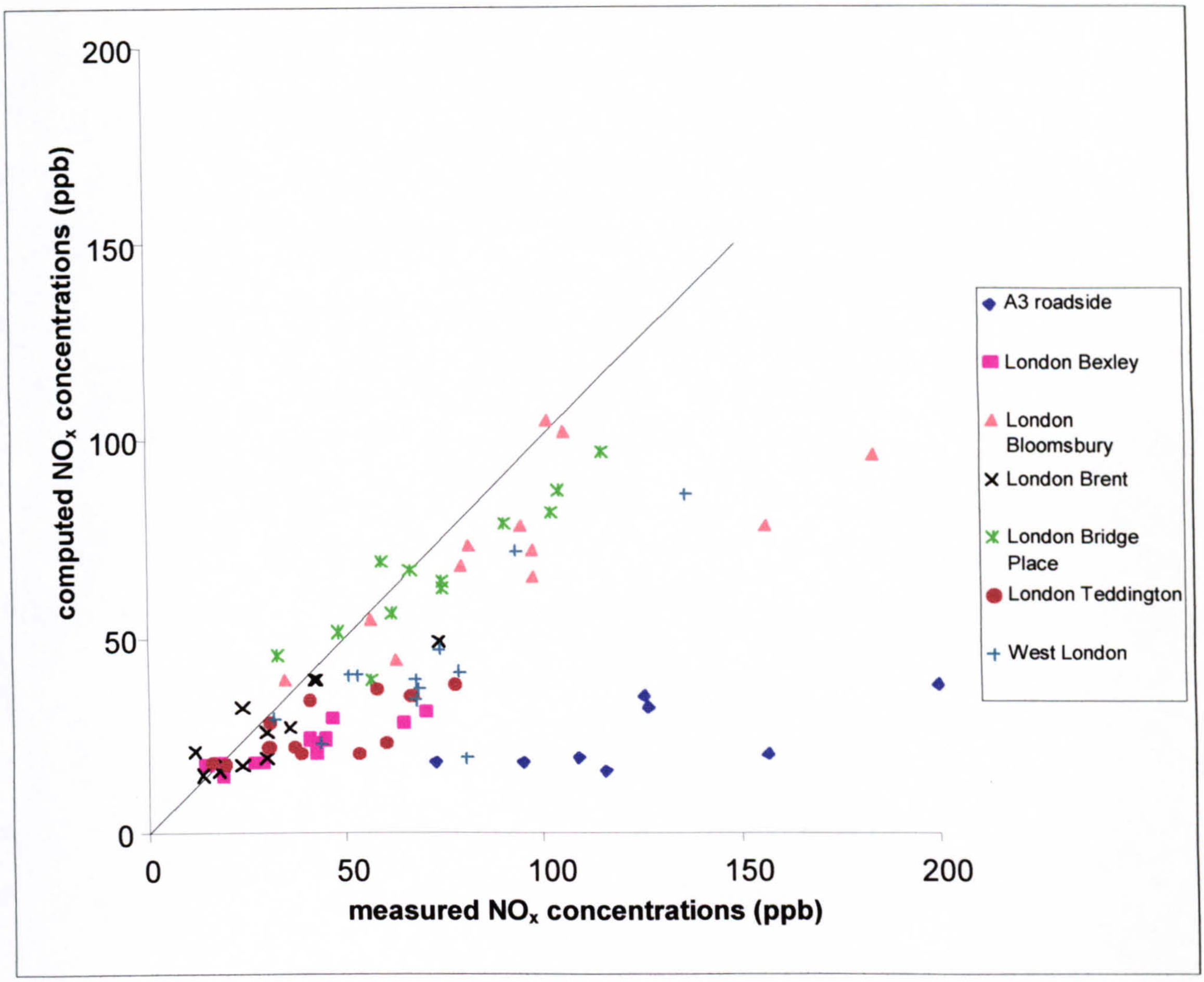

Figure 7.10: Scatter diagram of the computed NO_x concentrations against the LAPMN corresponding measurements for the 30th and the 31st of July 1999.

7.5 Preliminary conclusions

The conclusions that can be drawn from the work presented above are summarised below:

a. The combination of MEMO with TRAPPA provides a satisfactory tool with which one may study air quality and pollutant dispersion above urban areas. However, the performance of the modelling tool is limited by the fact that only one type of pollutant was considered and it was inert. Furthermore, as far as the thermal structure of the atmosphere is concerned it would have been better

if direct meteorological measurements especially of the temperature profile were available. This could further improve the performance of the model especially when meteorological conditions were such that radiation inversions and other local scale phenomena occurred.

b. Although, model estimates of air pollutant concentrations and in situ measurements can not easily be compared, at least for the case study days selected here, the obtained results were quite encouraging for the model. Especially during the first day, when local meteorological patterns were simpler than those of the second day, the comparisons were good with only few exceptions of measuring stations which maintained a very "local character" (e.g. roadside, kerbside). This sort of agreement was not repeated during the second day especially in the afternoon, evening and night hours, during which most probably local circulations, temperature inversions and other meteorological "localities" prevailed in certain areas of the computational domain. These are thought to be responsible for the major discrepancies observed between computed and measured concentrations.

c. Concerning the local circulations, these may be further analysed if a microscale model is employed to produce more accurate pollutant vertical fluxes and boundary conditions for the mesoscale model. In this case local meteorological information is required which could easily be obtained if specific instrumentation was placed in sight, e.g. tethered sonde facility, acoustic radars etc.

8. Discussion of results and suggestions for further work

8.1. Discussion of results

The degradation of air quality in urban and therefore, densely built and populated areas has become in the past decades a major problem. The concentration of activities including industry, transportation and energy generation, in and close to these areas results in high amounts of pollutants being emitted and consequently to poor air quality conditions.

Urban areas are characterised by the densely built streets (street canyons) and the geometric complexity, which significantly alter the wind flow field and the pollutant diffusion characteristics. Especially under low wind conditions, thus absence of synoptic circulation, almost stagnant conditions prevail at street level. As a result, pollutants emitted from traffic are trapped inside the street canyon, reaching levels much higher than those set by the EU and WHO.

This situation lead to the need for monitoring the air pollution levels in and around the city as well as the forecasting of episode days and the distribution of pollutants in the greater area of interest. Furthermore, it is of importance to identify the receptors especially in urban areas where, the distances between sources and receptors are relatively short.

To achieve these objectives it is necessary to plan and implement a representative air quality monitoring network as well as to select the proper modelling routines. **Mesoscale models** used so far could not be successful due to their spatial and temporal resolution, which were much larger than those required for the urban case.

Within that frame the work inspired here had two main objectives:

1. The selection, validation, development and use of a **microscale model** suitable to predict wind flow and pollutant dispersion and over a built area. The aim was to answer specific questions necessary for a deeper understanding of both the mechanisms of the flows and air pollution dispersion in the urban environment.

2. The selection of a validated mesoscale nested model to compute wind field and pollutant dispersion over different roughness terrains such as the Greater London Area. Furthermore an attempt was made to high light the limitations of mesoscale modelling in studying urban scale problems.

Along those lines of thought the present work led to the following main conclusions which are conveniently divided bellow into four main sections:

8.1.1. MIMO results, the 2 D case.

The microscale model MIMO was validated against available wind tunnel experimental data for a two-dimensional multiple street canyon case. The flow fields studied covered both the square and deep canyons cases, that is aspect ratios of 1 and ½ respectively. The wall treatment scheme implemented in MIMO, standard law of the wall by Launder and Spalding, was substituted by a relatively new law, Sondak and Pletcher. This wall treatment scheme is valid in all layers of the turbulent boundary layer formed between the wall and the flow above.

The obtained results indicated the presence of a single main vortex established in the **square canyon,** which results in a wind direction close to the source, from the windward to the leeward wall, thus indicating maximum concentration levels at the leeward wall. In the **deep canyon case** the corresponding main vortex covers approximately the top 2/3 of the street canyon total depth. On the contrary, almost stagnant conditions are established near the street level, due to the existence of a weak counter-rotating vortex. The location of maximum pollutant levels is now the windward wall, although high pollution is met along the almost stagnant area. This comes in good agreement with current literature.

Comparing the measured concentrations to the ones computed by MIMO, it was found that as for the square canyon case MIMO had underestimated, 15 –20%, the concentration levels, whereas for the deep canyon case it had underestimated by approximately the same percentage the pollutant concentrations.

The differences observed between the computed and measured non-dimensional concentrations, could be explained as follows:

- The experiment allowed for three-dimensional effects to develop. This was not the case for the two-dimensional set-up of the algorithm, which obviously, neglected the lateral component of the flow. This omission could easily lead to a 10-15% error, which is in many cases reported in full-scale atmospheric experiments.

- Experimental imperfections which, were pointed out by the same experimental team lead to 10-15% differences when the experiment was repeated in another laboratory.

- The profiles and the characteristics of the input flows used were purely statistical approximations of the real profiles used in the wind tunnel. This introduced errors, especially at the inlet region of the computational domain.

Having established a satisfactory two-dimensional performance, the two-dimensional computational set-up was maintained and the geometry of the central street canyon (the one studied above as well) was altered. This involved changing the height of the windward or leeward buildings and analysing the effect on the wind field and dispersion patterns. The interest in this type of analysis was brought up by the fact that the majority of street canyons are non symmetric. This geometrical variation produced interesting departures from the typical single or double vortex regime. In the framework of the geometry study, the following configurations were analysed:

Square canyon configuration

A) Step-up notch: When a step-up notch is created in general, ventilation of the street canyon is enhanced when the building height ratio becomes 0.5 or smaller. Until then pollutants accumulate at the leeward corner tending to expand towards the centre of the canyon. The vortex tends to remain intact until the flow form the upwind canyon intrudes in to the street passing over the lowered leeward building.

B) Step-down notch: For the step-down notch case, the obtained results presented a far more interesting and unexpected behaviour. As the building height ratio increases above 1, the location of maximum pollution concentration varies with the different windward building heights, shifting from one side of the canyon studied to the other. A secondary vortex appears when the building height ratio is almost 2. This is also of

importance since this vortex supports the formation of a localised air pollution concentration cell.

Deep canyon configuration

When a **step-up** notch configuration is created, the resulting wind field and pollutant dispersion patterns are clearer despite the existence of a double vortex system. The main vortex lifts up out of the canyon, almost stagnant conditions prevail at the bottom of the cavity and diffusion of pollutants occurs. Thus, pollutants do not indicate a preference to a certain location of the canyon and their concentration is almost uniform across the street width. There is a continuous weak circulation pattern observed at the bottom of the street canyon for all heights of the leeward building. The same sort of behaviour is established for the **step-down** notch configuration. Small differences related to the dispersion strength inside the canyon are identified indicating here a lower level of pollution. It can be concluded that in general a deep canyon configuration gives rise to higher pollutant concentration at street level and it seems to be disconnected from the flow above the street canyon. Changes in street geometry affect pollution levels however, high concentrations are still observed.

Thus, it is shown that the wind field and dispersion patterns are sensitive to the street canyon geometry and aspect ratio. More specifically, the aspect ratio plays an important role on the sensitivity of the wind field and dispersion of pollutants to the changes inflicted on the geometrical configuration. When a square canyon configuration prevails then it is extremely sensitive to the geometry. However, when a deep canyon configuration exists and the geometry is altered the wind field is relatively insensitive to the inflicted changes.

Aspect ratio variations

During the present investigation, it was found that both the shape of the flow in and above the street canyon as well as the pollutant dispersion patterns, are influenced by the different aspect ratios. For this reason different aspect ratios were chosen so that to cover most cases met in practice. In this respect street canyon aspect ratios were studied ranging from 3 to 0.5. The main conclusions reached were:

- A single vortex extending across the street canyon with elongated shape and lower velocities is observed mainly for the wider canyons, (aspect ratio of 3).

- The greater the aspect ratio, the better pollution dispersion pattern is established.

Based on the results obtained from the analysis performed here, the following general conclusion can be extracted. "In almost all cases within a canyon where traffic emissions occur, a local air pollution cell is created. This cell interacts weakly with the general background and the neighbouring cell flows. This situation is responsible for the slow development of an internal boundary layer and a new urban background **"airshed."**

8.1.2. The Fast Chemistry Module

A fast chemistry module was created and embodied in MIMO in order to study the effects on the NO_2 concentrations. From this study the following main preliminary conclusions can be drawn:

- With a steady O_3 background, NO_2 concentration rises. The relationship between the NO_2/NO_x ratio is almost linear and increases with increasing O_3. This applies for both night and daytime conditions.

- The NO_2/NO_x ratio varies along the canyon rising from the leeward to the windward wall. In the location of maximum pollution, the leeward wall, the NO_2/NO_x ratio is lower compared to that at the center and windward wall locations. This could be explained by the fact that this location of the street canyon is characterized by weak ventilation, which leads to a limited O_3 feed and trapping of pollutants. Both in the center and windward wall locations, the NO_2/NO_x ratio is higher, since these areas are characterised by good mixing conditions and better feeding of fresh pollutants. This applies for both night and daytime conditions.

- The average NO_2/NO_x ratio for daytime conditions is lower than for the night-time case by approximately 9%. Furthermore, for averaged NO_2/NO_x ratio across the canyon domain, a linear relationship exists with the background ozone concentration.

A main conclusion of the work presented here is that in an urban cell there is sufficient time for pollutants such as NO_2, NO and O_3 to react and therefore, to create high concentration of photochemical pollutants the majority of which are harmful to human health.

8.1.3. MIMO results, the 3D case.

In practice most street canyons may not be considered as two-dimensional since they are not infinitely long and are intersected at regular intervals by side streets. For this reason the model was modified to run for a three-dimensional configuration. The model was successfully validated against wind tunnel experimental data of a finite array of square buildings. It must be noted here that the square buildings were arranged in such a way that the main street was vertically intersected by a number of equally sized streets, thus producing a **highly complex urban cell.** Over such a complexity two main cases of flow were considered:

Wind perpendicular to the street canyon: The computational domain imposed by the experiment was difficult to implement and met limitations relevant to the computational power and CPU time required. This lead to certain compromises, which, after a careful study, did not affect the quality of the simulations. Based on the above the following interesting conclusions were reached:

- Close to a street intersection, corkscrew-like vortices develop, which retard slowly propagating down the street.
- The concept of a two-dimensional street-canyon can be true as long as its length is three to four times larger than its width.
- The two-dimensional flow, if met, develops at a distance of half-length away from the intersection.

Wind with a perpendicular and a parallel component to the street canyon:

8.1.4. The Inert MEMO Results.

The well-documented mesoscale model, MEMO, adjoined with the TRAPPA Eulerian dispersion model was employed for the need of the present work. The

chemistry was simplified to treat NO_x as an inert pollutant, i.e. a total oxidised N component with negligible deposition, with no background NO_x concentrations. Using a selected emission inventory, meteorological conditions likely to give air pollution episodes for the GLA (and a good representation of the surface roughness), the following conclusions were reached:

- The combination of MEMO with TRAPPA forms a satisfactory initial, qualitative platform with which one may study air quality and pollutant dispersion over urban areas. Thus, results taken from this approach can easily be used as a qualitative tool in order to decide about the general patterns of pollution over an urban and sub-urban environment. It may also be applied as an introductory tool for more specialised modelling platforms, which can cover smaller areas and will incorporate background pollution levels and active atmospheric chemistry (e.g. UAM, ADMS-Urban). However, the performance of this modelling tool is limited by the fact that only one type of pollutant was considered and it was inert. Furthermore, as far as the thermal structure of the atmosphere is concerned it would have been better if direct meteorological measurements especially of the temperature profile were available. This could further improve the performance of the model especially when meteorological conditions were such that radiation inversions and other local scale phenomena are present.

- Although, model estimates of air pollutant concentrations and in situ measurements, (which can take into account air quality and meteorological localities), can not easily be compared, at least for the case study day examined here, the obtained results were quite encouraging for the model. Especially during the first episode day, during which local meteorological patterns were simpler than those of the second day, the comparisons were good with only few exceptions of measuring stations which maintained a very "local character" (e.g. roadside, kerbside). This sort of agreement was not repeated during the second day especially in the afternoon, evening and night hours, during which, most probably, local circulations, temperature inversions and other meteorological "localities" prevailed in certain areas of the computational domain. These are thought to be responsible for the major discrepancies observed between computed and measured concentrations. Concerning the local circulations, these may be

further analysed if a microscale model is employed to produce more accurate pollutant vertical fluxes and boundary conditions for the mesoscale model. Finally, the local meteorological information required could easily be obtained if specific instrumentation is placed in sight, e.g. tethered sonde facility, acoustic radars etc. Data of this type can be introduced to mesoscale modelling platforms using the microscale "urban cell" approach described in section 4.

- In quantitative terms the model has slightly underestimated the corresponding network NO_x measurements. This is caused by the fact that short term high concentration values monitored by the in-situ instrumentation can not easily be identified by the model with the present spectral resolution. This causes the slight underestimation of the mean hourly values of the model. However, with the exception of the roadside station (A3), high correlation coefficients are observed for all cases examined in both the centre of London and the suburbs.

8.2. Suggestions for further work

In this final part of the thesis, a very brief mention will be made on the suggestions for further study that could be undertaken and seen as a continuation of the work presented here. In this line of thought the following suggestions can be made:

- It would have been useful if the in-canyon thermal structure was modelled. This could be done in MIMO if specific experimental data from field measurements were available. The data made available to scientists so far are scarce and maintain a very local character, which could not be easily incorporated in a general application routine. However, recent major European Union projects within the framework of City of Tomorrow[1] or similar, targeting towards the collection of real data from European cities are in-line and their results are expected to be made available soon.

- In the present work, the classic photochemical equilibrium was taken into account, without considering other pollutants which may affect significantly the secondary

[1] http://www.cordis.lu/eesd/ka4/projects.htm

production of pollutants and in general the chemical kinetics. Furthermore, no background levels for NO_x were considered. It is expected that the introduction of both background values for all pollutants including photochemistry, may aid significantly in the accuracy of the estimates presented here. Naturally, these improvements should be evaluated considering the cost of effort and the increased CPU time against the easy to operate routine, such as the one developed here. The latter is of importance since the majority of the end-users community maintains low skills in running high complexity models

- It will be of interest to see the result of the combination of a developed model systems (e.g. MIMO-MIPHOR), with mesoscale models (e.g. MEMO-TRAPPA) especially when high-resolution targets are aimed. Such a coupling of scales will create a powerful tool for studies over almost any terrain and under different meteorological conditions.

- Models such as MEMO-TRAPPA can be further improved for cases like the GLA, which although they look simple, maintain various delicate characteristics (e.g. land-use variability, ABL local flows etc.). It is proposed to include in the model routine, relative online information on the existing air quality state, synoptic meteorological conditions and relevant local ABL characteristics, (e.g. true mixing height, diffusion parameters etc.)

- It is important to study in depth the wind field and pollutant dispersion characteristics over a built area in order to study the effect of the outdoor air quality on the indoor environment. Current trends in research indicate that there exists a need to study both experimentally and numerically this field.

REFERENCES

Ashie, Y., Ca, V.T and Asaeda, T. (1999), '*Building canopy model for the analysis of urban climate.*', Journal of Wind Engineering and Industrial Aerodynamics, **81**, pp. 237-248.

ASME, LTR-LA-94, National Aeronautical Establishment, Ottawa, Canada Manual of Practice for Wind Tunnel Studies of Buildings and Structures, Draft - September 1995, Aerospace Division.

AssimakopoulosV., Moussiopoulos N. and ApSimon H.M. (2000), '*Effects of Street Canyon Geometry on the Dispersion Characteristics in Urban Areas*', 16th IMACS World Congress 2000, August 21-25 2000 Lausanne, Switzerland.

Assimakopoulos, V, ApSimon, H. and Moussiopoulos, N. (2001), '*Numerical modeling of dispersion of atmospheric pollution in and above urban canopies.*'7th Conference of Environmental Science and Technology, Syros 2-6 September, 2001.

Atkinson, R., Baulch, D.L., Cox, R.A., Hampson, R.F., Kerr Jr., J.A., Rossi, M.J, Troe, J. (1997a) *Evaluated kinetic and photochemical data for atmospheric chemistry; supplement V-IUPAC sub-committee on gas kinetic data evaluation for atmospheric chemistry.* Journal of Physical Chemistry Reference Data 26 (3), 521-1011.

Atkinson, R., Baulch, D.L., Cox, R.A., Hampson, R.F., Kerr Jr., J.A., Rossi, M.J, Troe, J. (1997b) *Evaluated kinetic and photochemical data for atmospheric chemistry; supplement V-IUPAC sub-committee on gas kinetic data evaluation for atmospheric chemistry.* Journal of Physical Chemistry Reference Data 26 (6), 1329-1499.

Bauer, W., Haag, O. and Hennecke, D.K. (1998), '*Comparison of Different Non-Linear Eddy Viscosity Models for Engineering Applications.*' ECCOMAS 98, John Wiley and Sons, Ltd.

Berkowicz R., Palmgren F., Hertel O., and Vignati E. (1996) '*Using measurements of air pollution in streets for evaluation of urban air quality-meteorological analysis and model calculations*'. The Science of the Total Environment 189/190, pp.259-265.

Berkowicz, R. Hertel, O., Sorensen, N.N., Michelsen, J.A. (1997) *'Modelling air pollution from traffic in urban areas.'* Proceedings from IMA meeting on Flow and Dispersion through Obstacles, University of Cambridge, 28-30 March 1994.

Boeft, den J., Eerens, H.C., Tonkelaar, den W.A.M. and Zandveldm P.Y.J. (1996) *CAR International: A simple model to determine city street quality,* Sci.Total Environ.,. 189/190, 321-326.

Bottema, M. (1999), '*Towards rules of thumb for wind comfort and air quality.*', Atmospheric Environment, 33, pp.4009-4017.

Bower J.S., Broughton G.F.J., Stedman J.R., and Williams M.L. (1994) *A winter NO_2 smog episode in the U.K.* Atmospheric Environment Vol.28, No.3, pp.461-475.

Boznar M., Mlakar P. (1995) *Neural networks- a new mathematical tool for air pollution modelling* Third International Conference on Air Pollution, Porto Carras, 26-29 September 1995, Vol. 1, pp. 259-266.

Buckland, A.T and Middleton, D.R. (1999), '*Nomograms for calculating pollution within street canyons.*', Atmospheric Environment, **33**, pp. 1017-1036.

Burr, C.R., Menter F.R., Grotjans, H. and Fruhauf, H.H (1998), '*Development of a Curvature Correction Method for the k-ε Turbulence Model*', ECCOMAS 98, John Wiley and Sons, Ltd.

Carruthers, D.J., Edmunds, H.A., Bennett, M., Woods, P.T., Milton, M.J.T., Robinson, R., Underwood, B.Y., Franclin, C.J. (1996) *Validation of the UK-ADAMS dispersion model and assessment of the performance relative to R91 and ISC using archive Lidar data.* Report Ref. DoE/HMIP/RR/95/022. The UK Environment Agency, London.

Carruthers, D.J., Singles, R.J., McHugh, C.A., Nixon, S.J. (1999) *Modelling urban air quality at high resolution using ADMS-Urban.* CERC, Cambridge, UK.

Croxford, B and Penn, A. (1998), '*Siting considerations for urban pollution monitors.*', Atmospheric Environment, Vol.32, No.6, pp. 1049-1057.

DeMore, W.B., Sander, S.P., Golden, D.M., Hampson, R.F., Kurylo, M.J., Howard, C.J., Ravishankara, A.R., Kolb, C.E., Molina, M.J. (1997) *Chemical kinetics and photochemical data for use in stratospheric modelling. Evaluation number 12. NASA panel for data evaluation.* Jet Propulsion Laboratory Report, 97-104.

DePaul F.T. and Sheih C.M. (1986) *Measurement of wind velocities in a street canyon.* Atmospheric Environment Vol.20, pp.455-459.

Delaunay, D.; Lakehal, D.; Barre, C. and Sacre, C. (1997), *Numerical and wind tunnel simulation of gas dispersion around a rectangular building.* Journal of Wind Engineering and Industrial Aerodynamics, Vol 67 & 68, pp.721-732.

Donat, J. *Windkanalexperimente zur Ausbreitung von Schwergas-strahlen.* Dissertation, University of Hamburg, Meteorological Institute, (1995).

Eerens, H.C., Sliggers, C.J. and van den Hout, K.D. (1993) *The Dutch method to determine city air quality,* Atmospheric Environment, 27B. 389-399.

Ehrhard J., Kunz R., and Moussiopoulos N. (1998) *A comparative study of two-equation turbulence models for simulating microscale wind flow.* 5th International Conference on Harmonisation within Atmospheric Dispersion Modelling, 18-21. May 1998, Rhodes, Greece.

Ehrhard, J. ''*Untersuchung linearer und nichtlinearer Wirbelviskositaetsmodelle zur Berechnung turbulenter Stroemungen um Gebaeude.*'', Ph.D. Thesis, University of Karlsruhe, 1999.

Ehrhard J., Khatib I.A., Winkler C., Kunz R. Moussiopoulos N. and Ernst G. (2000), '*The microscale model MIMO: development and assessment*', J. of Wind Engineering and Industrial Aerodynamics, 85, pp. 163-176.

EPA (1990) *Urban Airshed Model Research, studies of five cities,* Environmental Protection Agency, Triangle Park, North Carolina 27711.

Fenger, J. (1999), '*Urban air quality.*', Atmospheric Environment, **33**, pp. 4877-4900.

Ferziger, J.H. and Peric, M. (1997), '*Computational Methods for Fluid Dynamics.*', Springer-Verlag Berlin Heidelberg.

Flassak, T. *'Ein nicht-hydrostatisches Modell zur Berechnung der Dynamik der planetaren Grenzschicht.*, Fortschritt-Berichte *VDI*, Reihe 15, Nr.74, VDI-Verlag Duesseldorf, 1990.

Gardner, M.W. and Dorling S.R. (1999), '*Neural network modeling and prediction of hourly NO_x and NO_2 concentrations in urban air in London.*', Atmospheric Environment, **33**, pp. 709-719.

Gerdes, F. and Olivary, D. (1999), '*Analysis of pollutant dispersion in an urban street canyon.*', Journal of Wind Engineering and Industrial Aerodynamics, **82**, pp. 105-124.

Gayev, Y.A and Savory E. (1999), '*Influence of street obstructions on flow processes within urban canyons.*', Journal of Wind Engineering and Industrial Aerodynamics, 82, pp.89-103.

Goetting, J, Winkler, Ch., Rau, M., Moussiopoulos, N. and Ernst, G. (1997), '*Dispersion of a passive pollutant in the vicinity of a U-shaped building.*', Int. J. Environment and Pollution, Vol.8, Nos.3-6, pp.718-726.

Gossman, A.D. (1999), '*Developments in CFD for industrial and environmental applications.*', Journal of Wind Engineering and Industrial Aerodynamics, **81**, pp. 21-39.

Green, N.E, Etheridge, D.W. and Riffat, S.B. (2001), '*Location of air intakes to avoid contamination of indoor air: a wind tunnel investigation.*', Building and Environment, **36**, pp. 1-14.

Herbert, J.M., Johnson, G.T. and Arnfield J.A (1998), '*Modelling the thermal climate in city canyons.*', Environmental Modelling and Software, **13**, pp. 267-277.

Hotchkiss, R.S. and Harlow, F.H. (1973), '*Air pollution transport in street canyons*', EPA-R4-73-029.

Hoydysh W.G., and Dabberdt W.F. (1988) *Kinematics and dispersion characteristics of flows in asymmetric street canyons.* Atmospheric Environment Vol.22, No.12, pp.2677-2689.

Huang, h., Akutsu, Y., Arai, M and Tamura, M. (2000), '*A two-dimensional air quality model in an urban street canyon: evaluation and sensitivity analysis.*', Atmospheric Environment, 34, pp.689-698.

Hunter L.J., Johnson G.T., and Watson I.D. (1992) *An investigation of three-dimensional characteristics of flow regimes within the urban canyon.* Atmospheric Environment Vol.26B, No.4, pp425-432.

Hussain M. and Lee B.E. (1980) *An investigation of wind forces on three dimensional roughness elements in a simulated atmospheric boundary layer flow.* Report BS 56, Department of Building Science, Faculty of Architectural Studies, University of Sheffield.

IPCC (1995) *Climate Change 1994 – Radiative Forcing and Climate Change and an Evaluation of the IPCC IS92 Emission Scenarios.* Cambridge University Press, Cambridge, UK.

Jenkin, M.E. and Clemitshaw, K.C. (2000), '*Ozone and other secondary photochemical pollutants: chemical processes governing their formation in the planetary boundary layer.*', Atmospheric Environment, **34**, pp. 2499-2527.

Johnson G.T. and Hunter L. (1995) *A numerical study of dispersion of passive scalars in city canyons.* Boundary Layer Meteorology ,75:235-262.

Johnson, G.T. and Hunter, L.J. (1998), '*Urban wind flows: wind tunnel and numerical simulations-a preliminary comparison.*', Environmental Modelling and Software, **13**, pp. 279-286.

Johnson, G.T. and Hunter, L.J. (1999), '*Some insights into typical urban canyon airflows.*', Atmospheric Environment, **33**, pp. 3991-3999.

Jones W.P. and Launder B.E. (1972) *'The prediction of laminarisation with a two-equation model of turbulence'*, Int. J. Heat Mass Transfer, Vol. 15, pp. 301-314.

Kamenetsky E., and Vieru N. (1995) *Model of air flow and air pollution in urban canyons* (Research Note). Boundary-Layer Meteorology 73:203-206.

Karppinen, A., Kukkonen, J., Koskentalo, T., Elolahde, T. (1997), '*Comparison of dispersion model predictions and the results from an urban air quality measurement network.*', Power, H., Tirabassi, T., Brebbia, C.A. (Eds.), Air pollution. V. CMP, Southampton, pp. 405-411.

Karppinen, A., Kukkonen, J., Elolahade, T., Konttinen, M. and Koskentalo, T. (2000), '*A modelling system for predicting urban air pollution: comparison of model predictions with the data of an urban measurement network in Helsinki.*', Atmospheric Environment, **34**, pp. 3735-3743.

Karppinen, A., Kukkonen, J., Nordlund, G., Rantakrans, E., Valkama, I., (1998) *A dispersion modelling system for urban air pollution.* Finnish Meteorological Institute, Publications on Air Quality 28. Helsinki, 58p.

Kastner-Klein, P.; Fedorovich, E. and Plate, E. (1997) *"Gaseous pollutant dispersion around urban canopy elements: wind tunnel case studies"*, Int. J. Environment and Pollution, Vol.8, Nos. 3-6, pp.727-737.

Kastner-Klein, P. and Plate, E.J. (1999), '*Wind-tunnel study of concentration fields in street canyons.*' Atmospheric Environment, **33**, pp. 3973-3979.

Kastner-Klein, P., Fedorovich, E. and Rotach M.W. (1999), 'Organised and turbulent air motions in a wind tunnel model of a street canyon with and without moving vehicles.' 6th International Conference on Harmonisation within Atmospheric Dispersion Modelling, 11-14 October, 1999, Rouen, France.

Kim, S.E and Boysan, F. (1999), '*Application of CFD to environmental flows.*' Journal of Wind Engineering and Industrial Aerodynamics, **81**, pp. 145-158.

Kukkonen, J., Härkönen, J., Walden,J., Karppinen, A. and Lusa, K. (2001), *'Evaluation of the CAR-FMI model against measurements near a major road.'* Atmospheric Environment, Vol. 35, **5**, pp.949-960.

Kunz R. and Moussiopoulos N. (1995), '*Simulation of the wind field in Athens using refined boundary conditions.*' Atmospheric Environment Vol.29, No.24, pp.3575-3591.

Kunz R., Khatib I. and Moussiopoulos N. (1998), *'Coupling of Mesoscale and microscale models-An approach to simulate scale interaction'.* Environmental Modelling and Software, **15**, pp.597-602.

Lakehal D., Mestayer P.G., Edson J.B., and Anquetin S. (1995) *Eulero-Lagrangian simulation of raindrop trajectories and impacts within the urban canopy.* Atmospheric Environment Vol.29, No.23, pp.3501-3517.

Lakehal, D. and Rodi, W. (1997) *Calculation of the flow past a surface mounted cube with two-layer turbulence models.* Journal of Wind Engineering and Industrial Aerodynamics 67 &68, pp. 65-78.

Lakehal, D. (1998), '*Application of the k-ε model to flow over a building placed in different roughness sublayers.*', Journal of Wind Engineering and Industrial Aerodynamics, **73**, pp. 59-77.

Landsberg, H.E. (1981). *The Urban Climate.* Academic Press, New York.

Lanzani, G. and Tamponi, M. (1995), '*A microscale Lagrangian particle model for the dispersion of primary pollutants in a street canyon. Sensitivity analysis and first validation trials.*', Atmospheric Environment, Vol.29, No.23, pp. 3465-3475.

Launder, B.E.; Spalding, D.B. (1974) "*The Numerical Computation of Turbulent Flows*", Comp. Meth. App. Mech. Eng., 3, pp. 269-289.

Lee, R.L., Albrotton, D.L., Ermak, J. and Kim, J. (1997a), '*Computational fluid dynamics modelling for emergency preparedness and response.*', Environmental Modelling and Software, Vol. 12, No. 1, pp. 43-50.

Lee I.Y. and Park H.M. (1994) *Parameterisation of the pollutant transport and dispersion in urban street canyons.* Atmospheric Environment Vol.28, pp.2343-2349.

Lee, D.S., Kohler, I., Grobler, E., Rohrer, F., Sausen, R., Gallardo-Klenner, L., Olivier, J.J.G., Dentener, F.J. (1997b) *Estimation of global NO_x emissions and their uncertainties.* Atmospheric Environment 31 (12), 1735-1749.

Leitl, B.M. and Meroney, R.N. (1997) *Car exhaust dispersion in a street canyon. Numerical critique of a wind tunnel experiment* Journal of Wind Engineering and Industrial Aerodynamics, 67 & 68, pp. 293-304.

Leitl, B.; Schatzmann, M. 'CEDVAL - Compilation of Experimental Data for Validation of Microscale Numerical Dispersion Models', *Proc. 2nd East European Conference on Wind Engineering*, Prague, September 7-11,1998.

Logan, J.A. (1983) *Nitrgen oxides in the troposphere: global and regional budgets.* Journal of Geographical Research 88 (NC15), 785-807.

Louka, P., Belcher, S.E. and Harrison R.G. (2000), '*Coupling between air flow in streets and the well-developed boundary layer aloft.*' Atmospheric Environment, 34, pp.2613-2621.

Macdonald, R.W., Griffiths, R.F. and Hall, D.J. (1998), '*A comparison of results from scaled field and wind tunnel modelling of dispersion in arrays of obstacles.*', Atmospheric Environment, Vol. 32, No. 22, pp. 3845-3862.

Marquez, L.O. and Smith, N.C (1999), '*A framework for linking urban form and air quality.*', Environmental modelling and software, **14**, pp. 541-548.

Maurizi, A. (2000), '*Numerical simulation of turbulent flows over 2-D valleys using three versions of the k-ε closure model*', Journal of Wind Engineering and Industrial Aerodynamics, 85, pp.59-73.

Mayer, H. (1999), 'Air pollution in cities.', Atmospheric Environment, **33**, pp. 4029-4037.

Meroney, R.N, Leitl, B.M., Rafailidis, S. and Schatzmann M. (1999), '*Wind-tunnel and numerical modelling of flow and dispersion about several building shapes*', Journal of Wind Engineering and Industrial Aerodynamics, 81, pp.333-345.

Michallef, A., Deuchar, C.N. and Colls, J.J. (1998), '*Indoor and outdoor measurements of vertical concentration profiles of airborne particulate matter.*', The Science of the Total Environment, **215**, pp. 209-216.

Moussiopoulos N. (1995a) *The EUMAC Zooming Model, a Tool for Local-to-Regional Air Quality Studies.* Meteorology and Atmospheric Physics 57, 115-133.

Moussiopoulos N. (1995b) *Air pollution models as tools to integrate scientific results in environmental policy.* Third International Conference on Air Pollution, Porto Carras, 26-29 September 1995, Vol. 1, pp. 11-18

Moussiopoulos N., Sahm P., and Kessler CH. (1995) *Numerical simulation of photochemical smog formation in Athens, Greece-A case study.* Atmospheric Environment Vol.29, No.24, pp.3619-3632.

Moussiopoulos, N., Berge, E., Bohler, T., de Leeuw, F., Gronskei, K.E., Mylona, S. and Tombrou, M. (1996), *'Ambient air quality, pollutant dispersion and transport models.'* European Environment Agency, Topic Report 19, Air Quality. Copenhagen, pp 94.

Moussiopoulos N. and S. Papagrigoriou eds. (1997), Athens 2004 Air Quality, Proc. Int. Scientific Workshop *"Athens 2004 Air Quality Study"*, Zappion, 18/19 Feb. 1997.

Moussiopoulos, N., Theodoridis, G. and Assimakopoulos, V. (1998), *'The influence of fast chemistry on the composition of NOx in the emission input to atmospheric dispersion models'*, Proceedings from the EUROTRAC-2 Symposium 1998.

Nakamura Y., and Oke T.R. (1988) *Wind, temperature and stability conditions in an East-West oriented urban canyon.* Atmospheric Environment Vol.22, No.12, pp.2691-2700.

Oke T.R., (1987) *Boundary Layer Climates.* (2nd. Edition), Routledge Publ.

Oke, T.R., G.T. Johnoson, D.G. Steyn and I.D. Watson (1991). '*Simulation of Surface Urban Heat Islands under "Ideal" Conditions at Night – Part 2: Diagnosis and Causation*'. Boundary Layer Meteorology, Vol. 56, pp. 339-358.

Olesen, H.R. (1995), '*Datasets and protocol for model validation.*', International Journal of Environment and Pollution, **5**, pp. 693-701.

Oliveira, P.J and Younis, B.A. (2000), '*On the prediction of turbulent flows around full-scale buildings.*', Journal of Wind Engineering and Industrial Aerodynamics, **86**, pp. 203-220.

Pearce, W. and Baker, C.J. (1999), '*Wind tunnel on the dispersion of vehicular pollutants in an urban area.*', Journal of Wind Engineering and Industrial Aerodynamics, **80**, pp. 327-349.

Palmgren F., Berkowicz R., Hertel O., and Vignati E. (1996) *Effects of reduction of NO_x on the NO_2 levels in urban streets.* The Science of the Total Environment 189/190, pp.409-415.

Park, T.S. and Sung, H.J. (1995), '*A nonlinear low-Reynolds number k-ε model for turbulent separated and reattaching flows-I. Flow field computations.*', International Journal of Heat and Mass Transfer, Vol. 38, No. 14, pp. 2657-2666.

Pavageau, M. and Schatzmann, M. (1999), '*Wind tunnel measurements of concentration fluctuations in an urban street canyon.*', Atmospheric Environment, **33**, pp. 3961-3971.

Pearlmutter, D., Bitan, A. and Berliner, P. (1999), '*Microclimatic analysis of "compact" urban canyons in an arid zone.*', Atmospheric Environment, **33**, pp. 4143-4150.

Plate, E.J (1999), '*Methods of investigating urban wind fields-physical models.*', Atmospheric Environment, **33**, pp. 3981-3989.

PORG, (1997), '*Ozone in the United Kingdom'.* Fourth Report of the UK Photochemical Oxidants Review Group, Department of the Environment, Transport and the Regions, London.

Rafailidis S., and Schatzmann M. (1995) '*Concentration Measurements with different roof patterns in street canyons with aspect ratios B/H=1/2 and B/H=1*', Report, Meteorology Institute, University of Hamburg.

Rafailidis S., and Schatzmann M (1997) URL: *http://www.mi.uni-hamburg.de/technische_meteorologie/windtunnel/street02/overview.html*

Rafailidis S. (1997) *Influence of building areal density and roof shape on the wind characteristics above a town.* Boundary-Layer Meteorology 85:255-271.

Rafailidis S. (1998) *Using urban site measurements for model validation: Before starting, looking at the near-field geometry.* 5th International Conference on Harmonisation within Atmospheric Dispersion Modelling for Regulatory Purposes, Rhodes, 18-21 May 1998.

Reichardt,H. (1951) *'Vollstaendige Darstellung der turbulenten Geschwindigkeitsverteilung in glatten Leitungen"* ZAMM, 31, pp. 208-219

Rotach,M.W. (1995), '*Profiles of turbulent statistics in and above an urban street canyon.*' , Atmospheric Environment, Vol. 29, No. 13, pp. 1473-1486.

Sahm P., Kirchner F. and Moussiopoulos N. (1997), *Development and Validation of the Mul-tilayer Model MUSE - The Impact of the Chemical Reaction Mechanism on Air Quality Predictions, Proc. Int. 22nd NATO/CCMS "Technical Meeting on Air Pollution Modelling and its Application*", Clermont-Ferrand, France, June 2-6, 1997.

Scaperdas, A. and Colvile, R.N. (1999), '*Assessing the representativeness of minitoring data from an urban intersection site in central London, UK.*', Atmospheric Environment, **33**, pp. 661-674.

Scaperdas, A. (2000), '*Modelling air flow and pollutant dispersion at urban canyon intersections'* PhD Thesis, Univeristy of London.

SCAQMD (1994A), *'Air Quality Management Plan for the Antelope Valley'*, Appendix I-A, Air Quality Management Plan.

SCAQMD (1994B), *'Air Quality Management Plan for the Coachella-San Jacinto Planning Area'*, Appendix I-B, Air Quality Management Plan.

Sini J.F., Anquetin S., and Mestayer P.G. (1996) *Pollutant dispersion and thermal effects in urban street canyons.* Atmospheric Environment Vol.30, No.15, pp2659-2677.

Sondak, D.L.; Pletcher, R.H. "*Application of Wall Functions to Generalized Nonorthogonal Curvilinear Coordinate Systems*", AIAA J., 33 (1995), pp. 33-41.

Stern, R. and Yamartino, R.J. (2000), '*Evaluation and further application of the microscale photochemical model MICRO-CALGRID.*', 24th NATO/CCMS ITM on Air Pollution Modelling and its Application, May 15-19, 2000, Boulder, CO USA.

Stull, R.B. (1988), '*An Introduction to Boundary Layer Meteorology.*', Kluwer Academic Publishers.

Theodoridis, G. and Moussiopoulos, N. ''*Influence of building density and roof shape on the wind and dispersion characteristics in an urban area: A numerical study.*'' 2nd International Conference on Urban Air Quality, Madrid 3-5 March 1999, pp.79-80.

Theurer, W. (1999), '*Typical building arrangements for urban air pollution modelling.*', Atmospheric Environment, **33**, pp. 4057-4066.

Tombrou, M., Bossioli E., Lalas D. (1995) *Application of a Monte Carlo dispersion model in complex terrain* Third International Conference on Air Pollution, Porto Carras, 26-29 September 1995, Vol. 1, pp. 249-257.

Tombrou, M., Bossioli, E. and Lalas, D. (1998), *'An application of a simple Monte Carlo dispersion model in complex terrain.*', Environmental Modelling and Software, **13**, pp. 45-58.

Uehara, K., Murakami, S., Oikawa, S. and Wakamatsu, S. (2000), '*Wind tunnel experiments on how thermal stratification affects flow in and above urban street canyons.*', Atmospheric Environment, **34**, pp. 1553-1562.

Vakeva, M., Hameri, K., Kulmala, M., Lahdes, R., Ruuskanen, J. and Laitinen, T. (1999), *'Street level versus rooftop concentrations of submikron aerosol particles and gaseous pollutants in an urban street canyon.'*,Atmospheric Environment, Vol. 33, **9**, pp.1385-1397.

Versteeg H.K., and Malalasekera W., (1995) *An introduction to Computational Fluid Dynamics, The finite volume method.* Longman.

Vignati E., Berkowicz R., and Hertel O. (1996) *Comparison of air quality in streets of Copenhagen and Milan, in view of the climatological conditions.* The Science of the Total Environment 189/190, pp.467-473.

Winkler Ch. (1995) *'Mathematische Modellierung der quellnahen Ausbreitung von Emissionen'*, Fortschritt-Berichte VDI, Reihe 7, 268, VDI-Verlag Düsseldorf, pp. 142.

Yamartino, R.J. and Wiegand, G. (1986) *Development and evaluation of simple models for flow, turbulence and pollutant concentration fields within an urban street canyon,* Atmospheric Environment, 20, 2137-2156.

Yamartino, R.J., Scire, J.S., Carmichael, G.R. and Chang, Y.S. (1992) *The CALGRID mesoscale photochemical grid model 1: model formulation.* Atmospheric Environment 26A, 1493-1512.

Zoumakis M.N. (1995) *A note on average vertical profiles of vehicular pollutant concentrations in urban street canyons (Short Communication).* Atmospheric Environment Vol.29, No.24, pp.3719-3725.

date	GMT	measured A3	computed A3	measured Bexley	computed Bexley	measured Bloosmbury	computed Bloomsbury	measured Brent	computed Brent
7/30/99	4	127	32	19	15	35	39	19	17
	8	157	20	43	20	184	96	18	16
	12	95	18	15	17	98	72	14	15
	16	109	19	27	18	63	44	12	21
	20	269	30	47	29	106	102	43	39
	24	222	20	43	23	95	78	42	39
7/31/99	4	116	16	29	18	57	54	24	17
	8	200	38	71	31	102	105	36	27
	12	126	35	65	28	98	65	30	19
	16	73	18	18	18	82	73	24	32
	20	264	18	41	24	80	68	30	26
	24	205	20	45	24	157	78	74	49
STDEV		**66.47**	**7.75**	**17.82**	**5.23**	**40.89**	**21.09**	**17.05**	**11.11**
COR.COEF		**0.19**		**0.92**		**0.70**		**0.88**	

	GMT	London Brigde	London Bridge	Teddington	Teddington	West London	West London
7/30/99	4	33	45	41	34	51	40
	8	105	87	58.5	37	79	41
	12	57	39	38.7	20	53	40
	16	49	51	16.3	18	32	29
	20	75	62	31.3	28	68	39
	24	62	56	53.4	20	69	37
7/31/99	4	67	67	66.9	35	94	72
	8	116	97	78.1	38	137	86
	12	91	79	37.1	22	74	47
	16	60	69	19.6	17	44	23
	20	75	64	30.8	22	68	34
	24	103	82	60.3	23	81	19
STDEV.		**24.93**	**17.45**	**19.15**	**7.81**	**27.06**	**19.13**
COR.COEF.		**0.92**		**0.71**		**0.79**	

IMPERIAL COLLEGE LONDON UNIV.